

NASA

Technical

Paper

3111

December 1991

# Wind Tunnel Investigation of Vortex Flows on F/A-18 Configuration at Subsonic Through Transonic Speeds

Gary E. Erickson

(NASA-TP-3111) WIND TUNNEL INVESTIGATION OF VORTEX FLOWS ON F/A-18 CONFIGURATION AT SUBSONIC THROUGH TRANSONIC SPEED (NASA)  
166 p

CSCL 01A

N92-14968

H1/02

Unclas

0038018



**NASA  
Technical  
Paper  
3111**

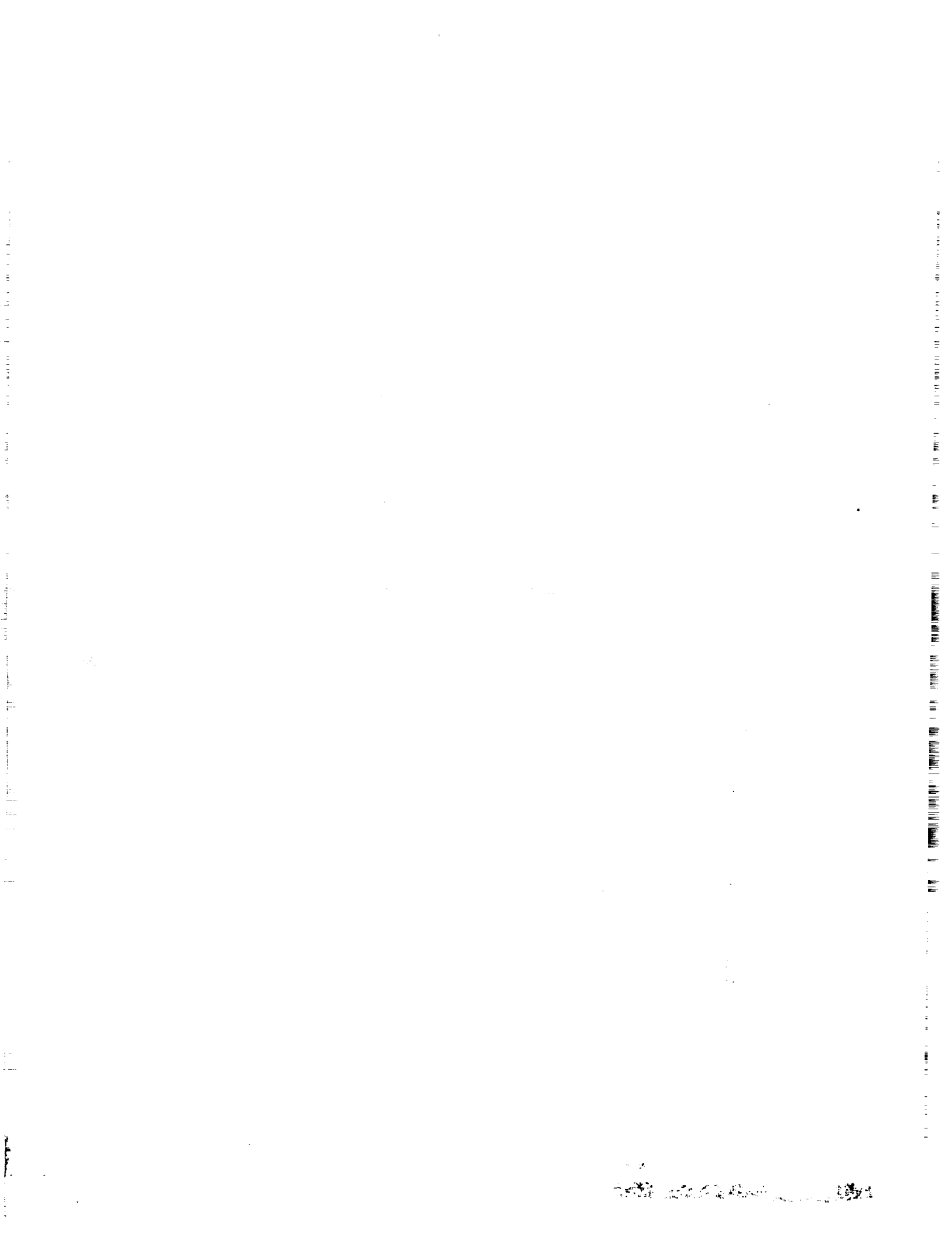
1991

**Wind Tunnel Investigation  
of Vortex Flows on F/A-18  
Configuration at Subsonic  
Through Transonic Speeds**

Gary E. Erickson  
*Langley Research Center  
Hampton, Virginia*



National Aeronautics and  
Space Administration  
Office of Management  
Scientific and Technical  
Information Program



## Symbols

B	swept, three-dimensional laminar separation bubble
BL	butt line, inches full scale (0.06 scale)
$b$	0.06-scale model reference wing span, 2.245 ft
$C_D$	drag coefficient, $\frac{\text{Drag}}{q_\infty S}$
$C_L$	lift coefficient, $\frac{\text{Lift}}{q_\infty S}$
$C_l$	body-axis rolling-moment coefficient, $\frac{\text{Rolling moment}}{q_\infty S b}$
$C_m$	pitching-moment coefficient referenced to $0.25\bar{c}$ , $\frac{\text{Pitching moment}}{q_\infty S \bar{c}}$
$C_n$	body-axis yawing-moment coefficient, $\frac{\text{Yawing moment}}{q_\infty S b}$
$C_p$	forebody surface static pressure coefficient, $\frac{p_{\text{local}} - p_\infty}{q_\infty}$
$C_{p,u}$	LEX upper surface static pressure coefficient, $\frac{p_{\text{local},u} - p_\infty}{q_\infty}$
$C_p^*$	pressure coefficient corresponding to local speed of sound, $\frac{2}{\gamma M_\infty^2} \left\{ \left[ \frac{(\gamma - 1)M_\infty^2 + 2}{\gamma + 1} \right]^{3.5} - 1 \right\}$
$C_Y$	side-force coefficient, $\frac{\text{Side force}}{q_\infty S}$
CFD	computational fluid dynamics
$\bar{c}$	0.06-scale model wing mean aerodynamic chord, 0.691 ft
DTRC	David Taylor Research Center
FS	fuselage station, inches full scale (0.06 scale)
HARV	High-Angle-of-Attack Research Vehicle
HATP	High-Angle-of-Attack Technology Program
Inbd.	inboard
LaRC	Langley Research Center
LE	leading edge
LEX	wing leading-edge extension
LP	laminar cross-flow separation pattern
LS	primary laminar separation
$l$	0.06-scale model length measured from nose to exhaust nozzle exit plane, 3.265 ft
$M_\infty$	free-stream Mach number
MHB	maximum half-breadth
NASA	National Aeronautics and Space Administration
Outbd.	outboard
$p_{\text{local}}$	local surface static pressure, lb/ft <sup>2</sup>
$p_{\text{local},u}$	local upper surface static pressure, lb/ft <sup>2</sup>

$p_{\infty}$	free-stream static pressure, lb/ft <sup>2</sup>
$q_{\infty}$	free-stream dynamic pressure, lb/ft <sup>2</sup>
R	location of reattachment
$Re_{\bar{c}}$	Reynolds number based on $\bar{c}$
S	0.06-scale model reference wing area, 1.440 ft <sup>2</sup>
SS	secondary separation
s	local semispan distance from LEX-fuselage junction to LEX leading edge, ft
TE	trailing edge
TP	turbulent cross-flow separation pattern
TRP	transitional cross-flow separation pattern
TS	primary turbulent separation
x	LEX vortex breakdown location measured from nose along model centerline, ft
y	distance along LEX local semispan, ft
$\alpha$	angle of attack, deg
$\beta$	angle of sideslip, deg
$\gamma$	ratio of specific heat constants
$\delta_{LE}$	leading-edge flap deflection angle measured normal to hingeline, positive leading edge down, deg
$\delta_{TE}$	trailing-edge flap deflection angle measured normal to hingeline, positive trailing edge down, deg
$\theta$	forebody cross-section angular location (0° is bottom dead center, positive is clockwise as seen from a front view), deg

## Summary

A wind tunnel experiment was conducted in the 7- by 10-Foot Transonic Tunnel at the David Taylor Research Center (formerly the Naval Ship Research and Development Center) of the wing leading-edge extension (LEX) and forebody vortex flows at subsonic and transonic speeds about a 0.06-scale model of the F/A-18. The primary goal was to improve the understanding and control of the vortical flows, including the phenomena of vortex breakdown and vortex interactions with the vertical tails. Laser vapor screen flow visualizations, LEX and forebody surface static pressures, and six-component forces and moments were obtained at angles of attack from  $10^\circ$  to  $50^\circ$ , free-stream Mach numbers from 0.20 to 0.90, and Reynolds numbers based on the wing mean aerodynamic chord from  $0.96 \times 10^6$  to  $1.75 \times 10^6$ . The wind tunnel results were correlated with in-flight flow visualization and handling qualities trends obtained by NASA using an F-18 High-Alpha Research Vehicle (HARV) and by the U.S. Navy and McDonnell Douglas Corporation on an F-18 airplane with LEX fences added to improve the vertical tail buffet environment. Key issues that were addressed include the sensitivity of the vortical flows to the Reynolds number and Mach number; the reduced vertical tail excitation, and the corresponding flow mechanism, in the presence of the LEX fence; the repeatability of data obtained during high-angle-of-attack wind tunnel testing of F/A-18 models; the effect of particle seeding for flow visualization on the quantitative model measurements; and the interpretation of off-body flow visualizations obtained with different illumination and particle seeding techniques.

## Introduction

Present-generation fighter airplanes such as the F/A-18 and the F-16 exploit vortex flows for enhanced maneuverability at high angles of attack and at subsonic and transonic speeds. The development, interaction, and breakdown of the vortices generated from the wing leading-edge extensions (LEX's) and fuselage forebodies and the interaction of the vortex flows with shock waves at the transonic speeds promote nonlinear aerodynamic and stability characteristics that are difficult to predict and control. In addition, the interaction of the vortical flows with vertical and horizontal tails can induce a severe tail buffet environment leading to structural fatigue. F-18 and F-16 derivatives and new-generation fighter airplanes will continue to employ vortex-lift concepts. As a consequence, the understanding, prediction, and control of these phenomena are essential to optimize airplane maneuverability and to reduce or eliminate

adverse vortex flow interactions with other airframe components.

NASA is conducting a High-Angle-of-Attack Technology Program (HATP) to provide design guidelines and new concepts for vortex control on advanced, highly maneuverable fighter airplanes. The program consists of wind tunnel testing of subscale models of complete aircraft configurations, subscale and full-scale models of airplane components, piloted simulations, development and validation of computational fluid dynamics (CFD) methods, and full-scale flight testing. The flight experiments are performed with a highly instrumented F-18 as a High-Alpha Research Vehicle (HARV) (fig. 1). The NASA HATP provides a unique opportunity for "closed-loop" correlations of the results from ground-based test facilities, CFD methods, and flight.

A fundamental issue in the NASA HATP is the sensitivity of the forebody and LEX vortical flows to Reynolds number and Mach number. The degree to which the vortical flows in subscale model wind tunnel testing represent the flow-field behavior in flight at full scale is of critical concern. Another issue is an apparent model scale effect (ref. 1), when discrepancies exist between the high-angle-of-attack stability characteristics of different scale models tested at the same Reynolds number in the same, or different, wind tunnel facilities. Model surface irregularities and the scale of the free-stream turbulence relative to the model size (ref. 2) are factors that may contribute to the development of global flow fields that are sufficiently different to affect the stability levels near maximum lift. Techniques for tripping the wind tunnel model boundary layers at high angles of attack to provide a consistent set of results and to properly represent the flight characteristics have yet to be developed. The development, interaction, and breakdown of the forebody and LEX vortices, their interaction with downstream airframe components such as the vertical and horizontal tails, and vortex-shock interactions are not fully understood.

The U.S. Navy and the McDonnell Douglas Corporation are also engaged in the development of concepts to improve the vertical tail buffet environment on the F/A-18 (ref. 3). The interaction of the burst LEX vortices with the twin vertical tails on the F/A-18 creates a buffet environment that is severe enough to cause structural fatigue. The excitation of the vertical tails occurs in the range of angle of attack from approximately  $16^\circ$  to  $44^\circ$ . The most critical effect of the burst vortices is manifested in the tail second, or outboard, bending and torsional mode. The second mode response is most severe in the range of angle of attack from approximately  $20^\circ$  to  $30^\circ$ .

The McDonnell Douglas Corporation and the Naval Air Systems Command conducted an extensive series of wind tunnel and flight experiments (ref. 3) aimed at reducing the vertical tail vibration environment at high angles of attack. The result of these efforts was the development of a streamwise fence mounted to the upper surface of the wing leading-edge extensions. These efforts culminated in a full-scale flight validation program featuring an F/A-18 with LEX upper surface fences. The fleet airplanes have been retrofitted with the LEX fences. Photographs of the fences installed on the F/A-18 airplane are presented in figure 2. The fences were demonstrated to significantly improve the vertical tail second bending and torsional mode response. Vertical tail accelerometer data obtained on the NASA F-18 HARV (ref. 4) are presented in figure 3. These results confirmed the significant reduction in the vertical tail buffet with the LEX fences installed. The improved vertical tail buffet environment, the minimal impact on the lateral-directional stability and aircraft performance, and the ease of implementation led to the selection of the LEX fences for installation on the fleet airplanes. The flow mechanism associated with the LEX fences was not identified during the wind tunnel and flight experiments. In addition, a forebody-LEX flow interaction occurred when the flight test nose boom and LEX fences were installed that led to degraded handling qualities near maximum lift. This effect was eliminated upon the removal of the nose boom. A determination of the corresponding flow-field interactions was not made during the LEX fence development program.

In support of these programs, and to address some of these issues, a cooperative experiment involving NASA, the U.S. Navy, and the McDonnell Douglas Corporation was conducted with a 0.06-scale model of the F/A-18 in the David Taylor Research Center (DTRC) 7- by 10-Foot Transonic Tunnel. The principal objective of the testing was to document the forebody and LEX vortex flow characteristics at subsonic and transonic speeds of the F/A-18 model with and without the LEX fences and a flight test nose boom. This objective was accomplished by conducting detailed off-body flow visualizations with a laser vapor screen technique and by measuring the forebody and LEX surface static pressures and model six-component forces and moments at free-stream Mach numbers from 0.20 to 0.90, Reynolds numbers based on the wing aerodynamic chord from  $0.96 \times 10^6$  to  $1.75 \times 10^6$ , and angles of attack from  $10^\circ$  to  $50^\circ$ . The present paper emphasizes the improved understanding of the forebody and LEX vortical flows from the laser vapor screen flow visualizations, correlations

of the off-body flows with the model surface pressures and forces and moments, and comparisons of the wind tunnel results to in-flight flow visualizations and handling qualities trends on the F/A-18 aircraft.

## Experimental Investigation

### Model Description and Test Apparatus

The testing was conducted with a 0.06-scale model of the F/A-18, which is illustrated in figure 4. The baseline configuration corresponded to the model with  $34^\circ$  leading-edge flap deflection,  $0^\circ$  trailing-edge flap deflection,  $-9^\circ$  horizontal stabilizer deflection,  $0^\circ$  rudder deflection, single-place canopy, and wingtip-mounted missiles. The model featured flow-through engine inlets and a distorted aft fuselage assembly to allow the installation of a sting between the twin exhaust nozzles.

The forward fuselage, consisting of the forebody, LEX's, and canopy, was removable and was instrumented to measure surface static pressures at 141 pressure orifices. The forebody pressures were measured at FS 107 (6.42), 142 (8.52), and 184 (11.04), whereas the pressures on the port and starboard LEX's were obtained at FS 253 (15.18), 296 (17.76), and 357 (21.42) on the upper surface only. The pressure ports at each station were selected to maximize the resolution in the vicinity of the vortical flows and in areas of expected large pressure gradients. The wind tunnel model forebody and LEX pressure measurement stations are indicated in figure 5. The fuselage station locations are identical to those on the NASA F-18 HARV (fig. 6). The pressure port locations at each fuselage station on the 0.06-scale model are a subset of those on the full-scale airplane.

LEX fences that were representative of those on the fleet airplanes were designed and fabricated. The fences are fixed devices mounted in a streamwise orientation on the upper surface of the LEX's. The fence is normal to the LEX surface at the fence leading edge (FS 378.17 (22.69)). This results in an angle relative to the vertical plane of symmetry of approximately  $25^\circ$ . This angular position was maintained along the length of the fence. The geometry details and location of the fences are provided in figure 7. The LEX fence concept was developed after the fabrication of the pressure-instrumented forward fuselage component. As a result, there were no LEX surface pressure orifices in the immediate vicinity of the fences. The aft pressure row on each LEX was situated 21.17 in. full scale (1.27 in. model scale) upstream of the fence leading edge.



The details of the flight test nose boom are presented in figure 8. The 0.06-scale model nose boom was representative of that used in the initial flights of the NASA F-18 HARV and during the early stages of the LEX fence flight validation program conducted by McDonnell Douglas and the Navy. The nose boom of the wind tunnel model did not include the angle-of-attack and sideslip vanes on the airplane nose boom.

The model six-component forces and moments were measured with an internally mounted strain-gauge balance. Angle-of-attack measurement devices were installed in the model support system, and the measurements were corrected for balance and sting deflection under load.

High angles of attack were obtained with the DTRC roll sting arrangement shown in figure 9. Angles of attack from  $10^\circ$  to  $20^\circ$  were obtained by pitching the model about the main support system boom pivot point. Rotating about the roll sting pivot point provided angles of attack from  $20^\circ$  to  $50^\circ$ . Within the latter angle-of-attack range, the model moved continuously upward through the test section, as sketched in figure 10. At an angle of attack of  $50^\circ$ , the model nose was approximately 12 in. from the tunnel ceiling.

The off-body flow visualization was conducted with a laser vapor screen technique (ref. 5). Water in sufficient quantity was injected into the settling chamber by using a spray nozzle which increased the relative humidity to create condensation within the vortical flows about the model. The vortex cross sections were visualized with an intense sheet of laser light. For contrast, the model and tunnel test section sidewalls were painted flat black. The condensation within the vortices was frequently observed along most of the vortex core length at subsonic speeds by using the wind tunnel test section lights located in the test section corner fillets. Previous NASA experiments in the DTRC facility with the vapor screen technique featured a laser light sheet directed from the right side of the tunnel test section (refs. 6 and 7). This approach was inadequate for the present application, since a large portion of the model flow field would be in the shadows created by the fuselage, canopy, and twin vertical tails. In addition, the upward movement of the model as the angle of attack increased made it impossible to track the flow field with a fixed set of optics in the test section window. Accordingly, the laser optics package was modified to allow the light-sheet generation from the tunnel ceiling. Locating the laser head in the low-pressure environment within the plenum surrounding the test section was precluded due to laser operational concerns. Instead, the 5-watt argon-ion

laser used in the present experiment was situated inside the wind tunnel control room. The beam was directed through an observation window, into the plenum, and to a series of mirrors mounted along the tunnel sidewall and ceiling. After passing through a beam contractor, it was then directed to an optics package consisting of a sheet generator and rotating mirror mounted inside a box beam directly above the test section. The laser light sheet was directed toward the model through a long, rectangular ceiling window that was offset slightly from the tunnel centerline. Two rotator stages in the optics package allowed the continuous variation of the light-sheet width and its location along the model. Since the light sheet swept along an arc, orthogonality of the light sheet with the model was precluded except at a preselected condition of  $\alpha = 30^\circ$  and the 50-percent wing chord station. This was an acceptable compromise in order to illuminate the entire model flow field through the ranges of angles of attack and sideslip.

The laser vapor screen flow visualizations in the present paper were documented with two color video cameras. A color video camera with remotely controlled zoom lens was mounted to a tilt/pan mechanism situated outside the test section. The flow field was observed through a window located downstream of the model as sketched in figure 10. A video camera having a fixed, 12.5-mm lens was mounted to the model sting support (specifically, to the sting adapter shown previously in fig. 9) and viewed directly between the twin vertical tails of the F/A-18 model. The field of view of this camera was fixed and was independent of the angles of attack and sideslip. Four additional video cameras and eight 70-mm and 35-mm still cameras were also mounted at selected locations in the tunnel sidewall and ceiling windows. However, none of these cameras tracked the model through the complete ranges of  $\alpha$  and  $\beta$ . The results obtained with the video camera units were superior and, consequently, still photographs were taken from the video monitor. These results are included in the present paper. The model pressures, forces, and moments were obtained with and without the camera mounted to the sting adapter. The upstream influence of the camera on the high-angle-of-attack flow field was found to be negligible.

### Wind Tunnel Facility and Test Conditions

The laser vapor screen results and model force, moment, and surface static pressure measurements that are presented in this paper were obtained in the DTRC (formerly NSRDC) 7- by 10-Foot Transonic Tunnel located in Bethesda, Maryland. The DTRC facility is a continuous-flow, closed-circuit facility capable of operating over a Mach number range

from 0.20 to 1.17 and an equivalent pressure altitude range from sea level to 40 000 feet. A complete description of the transonic wind tunnel is provided in reference 8. The 0.06-scale F/A-18 model with and without the LEX fences is shown mounted to the roll sting arrangement in the slotted test section in figure 11. Typical laser-illuminated vortical flows are also indicated in figure 11.

The test results were obtained at free-stream Mach numbers from 0.20 to 0.90. The angle of attack was varied in  $2.5^\circ$  increments from  $10^\circ$  to  $50^\circ$ . Pitch polars were obtained at sideslip angles of  $0^\circ$ ,  $4^\circ$ , and  $8^\circ$ . Sideslip "sweeps" in  $2^\circ$  increments from  $-10^\circ$  to  $+10^\circ$  were obtained at selected angles of attack and Mach numbers. The maximum free-stream dynamic pressure during the test was approximately  $250 \text{ lb/ft}^2$  due to a normal force limit of 1000 lb imposed on the DTRC roll sting arrangement. For free-stream Mach numbers from 0.20 to 0.40, the testing was conducted at atmospheric conditions. The tunnel was operated in the evacuated mode (ref. 8) at the higher Mach numbers. The tunnel stagnation pressure varied with the Mach number, ranging from approximately  $1250 \text{ lb/ft}^2$  at  $M_\infty = 0.60$  to  $750 \text{ lb/ft}^2$  at  $M_\infty = 0.90$ . The Reynolds number based on the wing mean aerodynamic chord  $Re_{\bar{c}}$  varied from approximately  $0.96 \times 10^6$  to  $1.75 \times 10^6$ .

The model force, moment, and surface pressure data were obtained on the baseline configuration under "dry tunnel" conditions at the outset of the experiment. Thereafter, the data were obtained simultaneously with the laser vapor screen flow visualizations. This allowed an assessment of the sensitivity of the quantitative measurements to the water injection.

The model featured boundary-layer trip strips on the forebody, LEX's, wings, tails, and inlet ducts. The trip strips were developed by McDonnell Douglas and consisted of epoxy cylinders that were bonded to the model surface. The epoxy cylinders had a nominal diameter of 0.050 in., spacing between cylinders of 0.025 in., and height of 0.0035 in. (0.06 scale). A trip ring was applied to the forebody about 0.40 in. (0.06 scale) from the nose tip, and a trip strip was installed along the entire forebody length at the bottom centerline. The trip strips on the LEX's, wings, tails, and inlet ducts were located 0.40 in. aft of the component leading edges.

## Discussion of Results

Representative results obtained in the DTRC 7- by 10-Foot Transonic Tunnel are presented in the following sections. The laser vapor screen flow vi-

sualizations are presented along with the model surface static pressure distributions and six-component forces and moments. The model without the fences and nose boom is referred to as the "baseline configuration." Comparisons are made of the wind tunnel flow-field observations and available in-flight flow visualizations on the NASA F-18 HARV. Experimental results from other F/A-18 model tests conducted by McDonnell Douglas and NASA are also used on a limited basis to support some of the conclusions of the present investigation.

The forebody pressures at FS 107 (6.42), 142 (8.52), and 184 (11.04) are shown as a function of angular position  $\theta$ , where the orientation is that of an observer standing in front of the model. A value of  $\theta$  of  $0^\circ$  corresponds to the bottom centerline;  $\theta$  increases in the clockwise direction. The LEX surface pressures at FS 253 (15.18), 296 (17.76), and 357 (21.42) are plotted against the local semispan distance  $y$  measured from the LEX-fuselage junction, normalized by the local distance  $s$  from the LEX-fuselage junction to the LEX leading edge. For the starboard LEX, values  $y/s$  of 0 and 1 correspond to the LEX-fuselage junction and LEX leading edge, respectively. Similarly, values of  $y/s$  of 0 and  $-1$  coincide with the port LEX-fuselage junction and LEX leading edge, respectively. Sketches of the LEX and forebody pressure orifice orientations are presented in figure 12. It is noted that the resolution of the LEX pressure distributions on the port and starboard sides was the same at FS 253 (15.18) but differed at FS 296 (17.76) and 357 (21.42). In addition, the pressure port density along the windward forebody surface was reduced in order to increase the pressure resolution in areas where the largest pressure gradients were expected, namely, near the maximum half-breadth (MHB) and on the lee side underneath the vortices.

The technical discussion is divided into five major sections. The first section compares the model pressure distributions obtained with and without water injection (for flow visualization) into the tunnel circuit. The second section addresses the repeatability of the data obtained from other wind tunnel models of the F/A-18. The forebody and LEX surface pressures on the 0.06-scale model tested in the DTRC facility are compared with previously unpublished data obtained on the same model in the Langley 14- by 22-Foot Subsonic Tunnel. The 0.06-scale model data are also compared with the results obtained in reference 9 with a 0.16-scale F/A-18 model in the Langley 14- by 22-Foot Subsonic Tunnel. The third, fourth, and fifth sections present the off-body flow visualizations, surface pressures, and forces and

moments obtained on the baseline configuration, the model with LEX fences, and the model with flight test nose boom, respectively.

### Effect of Water Injection on 0.06-Scale F/A-18 Model Surface Pressures

Figures 13 through 16 present the baseline model forebody and LEX surface static pressure distributions at  $M_\infty = 0.90$  and  $0.60$ , respectively, at selected angles of attack corresponding to conditions when the tunnel circuit was dry at the outset of the testing and to conditions when water was injected for the vapor screen flow visualizations. Water was injected into the tunnel in a sufficient amount to increase the relative humidity in the test section such that the water vapor condensed within the vortical flow regions above the model. The flow visualization run at  $M_\infty = 0.90$  was conducted first, since smaller amounts of water were required to achieve this effect. More water was required at  $M_\infty = 0.60$ . There was no instrumentation available in the tunnel to quantify the amount of moisture in the flow.

The region of principal concern was the forebody which, in contrast to the LEX, did not have fixed primary boundary-layer separation. The test data in figures 13 through 16 show essentially no effect, however, of adding water for flow visualization on the model pressure distributions. The forebody and LEX vortex strengths and locations were unaffected by the vapor screen seeding within the range of conditions considered in the present experiment. At angles of attack where LEX vortex bursting was known to occur over the LEX ( $\alpha = 30^\circ$  and greater), the vortex "footprints" or "signatures" were identical. This result is of importance to high-angle-of-attack testing, since it supports the simultaneous acquisition of off-body flow visualization and quantitative model data.

### F/A-18 Model Data Repeatability

Repeatability of data is a concern in high-angle-of-attack testing due to hysteresis and the sensitivity of the vortical flows to model surface irregularities, the model support system, blockage, wall interference, tunnel flow angularity, and free-stream turbulence (ref. 2). Repeat runs in the same wind tunnel entry can yield different results. Similarly, data from separate entries in the same facility, or in different wind tunnels, with a common model may fail to agree. Discrepancies often exist between results obtained on models of different scales tested in the same or different facilities.

These problems have arisen in the past several years during testing of the F/A-18 configuration. Of principal interest is the lateral stability near maxi-

mum lift, which occurs at an angle of attack of approximately  $40^\circ$ . Bursting of the LEX vortices dominates the flow about the LEX's and wings, and the forebody and LEX vortices interact with each other. The flow about the forebody of the F/A-18 can be sensitive to model surface irregularities, tunnel flow conditions, Reynolds number, and Mach number. It has been conjectured in reference 10 that even subtle differences in the primary boundary-layer separation along the forebody and, consequently, the forebody primary vortex strengths and locations may be amplified downstream as the forebody vortices interact with the LEX-wing flow field. Although the F/A-18 forebody shape is not conducive to the development of powerful vortices, they may be of sufficient strength to affect the flow field about the LEX's and wings and, hence, the lateral stability characteristics. Experience has shown that seemingly minor differences in LEX vortex burst locations in sideslip at high angles of attack can lead to large differences in the lateral stability levels of fighter aircraft models (ref. 11).

*Tunnel-to-tunnel comparisons.* Figures 17 and 18 present the forebody surface static pressures at angles of attack of  $40^\circ$  and  $50^\circ$ , respectively, obtained on the baseline 0.06-scale F/A-18 model tested in the DTRC 7- by 10-Foot Transonic Tunnel and the Langley 14- by 22-Foot Subsonic Tunnel. The Mach number and Reynolds number were identical in both tests ( $M_\infty = 0.20$ ,  $Re_c = 0.96 \times 10^6$ ). The forebody surface static pressure distributions are typically in good agreement. There is a stronger forebody vortex footprint at FS 107 (6.42) and  $\alpha = 50^\circ$  from the Langley 14- by 22-Foot Tunnel test, but this effect vanishes at FS 142 (8.52) and 184 (11.04). The model was painted flat black in the DTRC 7- by 10-Foot Tunnel test. This resulted in increased surface roughness in comparison with the glossy black finish on the model in the experiment in the Langley 14- by 22-Foot Tunnel. Although no boundary-layer trips were utilized during the 14- by 22-Foot Tunnel test, a boundary-layer trip ring near the nose and a trip strip along the bottom centerline were used during the DTRC testing. The differences in the paint finish and the trip arrangements may account for the different vortex footprints at  $\alpha = 50^\circ$  and FS 107 (6.42). The larger vortex footprint exhibited by the 14- by 22-Foot Tunnel data is consistent with a pressure distribution associated with laminar separation, where the relatively strong vortices formed by the laminar separation region are still close to the forebody. The much weaker footprint exhibited by the DTRC data is consistent with a transitional boundary layer. The overall data agreement is

encouraging, however. These results also suggest that the proximity of the model nose to the DTRC tunnel ceiling at  $\alpha = 50^\circ$  (12 in.) and model blockage were not significant factors at the low subsonic speeds.

The LEX surface pressures at  $\alpha = 40^\circ$  in figure 19 show reasonable agreement between the 0.06-scale model tests in the DTRC and Langley wind tunnels. At this angle of attack, vortex breakdown occurs near the second pressure row on the LEX (FS 296 (17.76)). The surface pressure signature of the burst LEX vortex is less pronounced in comparison with the unburst case. Despite the differences in the test facilities and support systems, the vortex breakdown behavior near maximum lift, as inferred from the surface pressure distributions, was repeatable. It is noted that the LEX surface pressure resolution was not the same in both model tests.

**Model-to-model comparisons.** The forebody surface pressures obtained on the 0.06-scale model in the DTRC tunnel and on the 0.16-scale F/A-18 in the Langley 14- by 22-Foot Subsonic Tunnel (ref. 9) are presented in figures 20 and 21 for angles of attack of approximately  $40^\circ$  and  $50^\circ$ , respectively. The free-stream Mach number in the 14- by 22-Foot Tunnel test of the 0.16-scale model was approximately 0.08, with a Reynolds number based on the wing mean aerodynamic chord of  $0.96 \times 10^6$ . This was identical to the Reynolds number on the 0.06-scale model at  $M_\infty = 0.20$  in the DTRC and Langley tests.

Significant differences exist between the forebody primary boundary-layer separation locations, vortex positions, and vortex strengths on the two models. The signatures of the forebody vortices are considerably stronger on the 0.16-scale F/A-18 at FS 107 (6.42) and 142 (8.52) and  $\alpha = 40^\circ$  and  $50^\circ$ . The stronger signatures are generally associated with more laminar flow. The reason why the flow is "more laminar" in nature for the 0.16-scale model is currently unknown, since both tests had the same nominal value of the Reynolds number. Some possible explanations include (1) lower tunnel free-stream turbulence at the lower velocities in the testing of the larger model, (2) smoother surface finish on the larger model, and (3) premature boundary-layer transition induced on the smaller model by the comparatively larger pressure orifices. The difference in the free-stream Mach number between the two tests is not the likely source of the data disparity. The data presented in figure 22, for example, which were obtained in the current experiment, indicate that the forebody vortex-induced suction pressures at FS 107

(6.42) and 142 (18.52) are insensitive to Mach numbers at  $M_\infty = 0.20, 0.40,$  and  $0.60$ .

Consistent with the forebody pressure distributions, the 0.16-scale model displays consistently higher LEX vortex-induced suction pressures. This effect is shown in figure 23 at  $\alpha = 40^\circ$  and may be due to the increased interaction of the forebody and LEX vortices on the larger scale model. The Mach number may also be a factor affecting the surface pressure comparisons. As discussed in later sections, in contrast to the forebody  $C_p$  distributions, the LEX vortex-induced surface pressures are sensitive to compressibility, even at very low Mach numbers. This effect is demonstrated in the next section of this paper. Nonetheless, these results suggest that the source of the model scale effect leading to different high- $\alpha$  stability levels on the two models (refs. 1 and 10) may be associated with the forebody flow development and the ensuing interaction of the forebody vortices with the LEX-wing flow field.

### Baseline 0.06-Scale F/A-18

**Vapor screen flow visualizations.** Figure 24 presents the laser vapor screen cross-flow visualizations obtained on the baseline model at  $\alpha = 20^\circ, 25^\circ, 30^\circ,$  and  $35^\circ$ ;  $M_\infty = 0.40$ ; and  $Re_c = 1.75 \times 10^6$ . The cross-flow patterns at each angle of attack are shown at fuselage stations that bracket the breakdown location. A stable vortex is manifested as a donut-shaped structure having low particle density along its axis and high particle density along the outer core. The breakdown phenomenon is discernible as an expansion, or flaring, of the core, which fills with water particles due to reverse flow along the axis. The vortex breakdown location at a given angle of attack was determined from the original videotapes of the laser vapor screen flow visualization. The model is viewed from a three-quarter right rear position.

The flow visualization results show the forward advance of the LEX vortex breakdown location as the angle of attack increases. At  $\alpha = 20^\circ$ , vortex breakdown occurs at FS 535 (35.1), which is slightly downstream of the intersection of the vertical tail leading edge and the fuselage (FS 525 (31.50)). The breakdown position moves to the junction of the LEX and the leading-edge flap hingeline (FS 434 (26.04)) at  $\alpha = 25^\circ$ . At  $\alpha = 30^\circ$ , core bursting is over the LEX at FS 381 (22.86), which is midway between the aft LEX pressure row (FS 357 (21.42)) and the LEX-wing-leading-edge junction. The latter is defined as the point of intersection of the leading edges of the LEX and wing when the wing flap is undeflected ( $\delta_{LE} = 0^\circ$ ). Vortex breakdown advances forward to FS 324 (19.44) at  $\alpha = 35^\circ$ , which is between the

second and third pressure rows (FS 296 (17.76) and 357 (21.42), respectively).

The LEX vortices on the F-18 HARV display a similar progression of vortex core breakdown with the angle of attack. Figure 25 shows in-flight visualizations from reference 12 taken with a wingtip-mounted 35-mm camera at angles of attack of approximately  $20^\circ$ ,  $25^\circ$ ,  $30^\circ$ , and  $34^\circ$ ,  $M_\infty \approx 0.3$ , and  $Re_{\bar{c}} \approx 13.5 \times 10^6$ . The sideslip angle in flight varied from approximately  $0.25^\circ$  to  $0.65^\circ$ . Smoke was injected into the vicinity of the vortex core from a port near the apex of each LEX. The smoke flow visualization technique employed on the HARV is described in detail in reference 13. It is noted that the wing flaps on the F-18 HARV are scheduled with the angle of attack and the Mach number, in contrast to the fixed deflection angles on the wind tunnel model ( $\delta_{LE} = 34^\circ$ ,  $\delta_{TE} = 0^\circ$ ). At  $\alpha = 20^\circ$ , the aircraft leading- and trailing-edge flaps are deflected to  $25^\circ$  and  $4^\circ$ , respectively. At  $\alpha = 25.6^\circ$  and greater, the flap settings in flight correspond to  $\delta_{LE} = 34^\circ$  and  $\delta_{TE} = 0^\circ$ , which coincide with the wind tunnel model. The vortex breakdown positions in flight at high Reynolds number agree well with the corresponding results obtained on the wind tunnel model at much lower Reynolds number. At  $\alpha = 20^\circ$ , where the flap settings are different on the wind tunnel model and the HARV, flow similarity may be imposed by the presence of the vertical tails in the paths of the vortices.

The LEX vortex breakdown positions obtained on the F-18 HARV (ref. 13) at  $M_\infty \approx 0.3$  and  $Re_{\bar{c}} \approx 13.5 \times 10^6$  and the 0.06-scale model at  $M_\infty = 0.4$  and  $Re_{\bar{c}} = 1.75 \times 10^6$  are plotted as a function of the angle of attack in figure 26. In the wind tunnel, a pulsing of the core, concurrent with the appearance of condensate within the core region, was defined as vortex breakdown. This was followed by an expansion of the vortex into a large, funnel-shaped, rotating flow. The density of condensed water vapor in this turbulent region was very high. The intersection of a line extending from the burst vortex to a surface normal on the model provided the breakdown location  $x$  measured along the centerline of the model from the nose. This value was then normalized by the model length  $l$  extending from the nose tip to the exhaust nozzle exit plane. The flight results are presented in a similar manner. The wind tunnel results obtained with the laser vapor screen method fall within the band of flight data obtained with natural condensation and smoke injection techniques.

The LEX vortex trajectories and breakdown locations observed in the wind tunnel were similar at  $M_\infty = 0.60$ . Representative results obtained from

a three-quarter, right rear position at  $\alpha = 20^\circ$  are shown in figure 27. The details of the cross-flow structure are sensitive to the Mach number, however. The extent of the vortical flow region that is illuminated by the laser light sheet in figure 27 is larger at the higher Mach number. This is indicated by a growth of the hollow core and a more extensive region of condensed water vapor outside the core. Illumination of the vortical flows with only the test section lights also revealed a larger system of vortices.

The LEX vortex structure and breakdown behavior at  $M_\infty = 0.60$  are shown from a different perspective in the photographs in figures 28 through 33, which were taken from the model sting-mounted camera looking directly upstream between the twin vertical tails. In each figure, the cross-flow patterns are presented at a fixed light-sheet position at selected angles of attack. The light-sheet locations range from FS 357 (21.42) (aft pressure row on the LEX's) in figure 28 to FS 567 (34.02) (near the wing-trailing-edge-fuselage junction) in figure 33. At  $\alpha = 15^\circ$  and  $17.5^\circ$ , the LEX vortices are stable at all stations and pass outboard of the vertical tails. The growth of the vortices and their inboard and upward migration as the angle of attack increases from  $15^\circ$  to  $17.5^\circ$  are particularly apparent at the aft stations. At  $\alpha = 20^\circ$ , the vortices continue their migration and burst near the vertical tail (fig. 33). The vortex breakdown at  $\alpha = 25^\circ$  is clearly illustrated beginning at FS 450 (27.00) (fig. 30). Farther aft, the expanded, rotating flows envelop the vertical tails. Wind tunnel tests and full-scale flight experiments conducted by McDonnell Douglas and the Navy (ref. 3) indicate that the vertical tail buffet is a maximum at angles of attack of approximately  $25^\circ$  to  $30^\circ$ . The corresponding vortex burst positions are contained within a band, centered about the LEX-wing-leading-edge junction, of approximately 25 percent of the wing centerline chord. Early flights of the F-18 HARV featured forward-looking video cameras mounted to the vertical tails to observe the LEX vortex flows (ref. 13). The camera vibration was severe at angles of attack of about  $25^\circ$  and greater, which was an indicator of the tail excitation. More recent results obtained in flight on the F-18 HARV (ref. 4), which included vertical tail accelerometer data, LEX vortex core visualizations, and observations of the vertical tail buffet from a chase aircraft, demonstrated the severe tail excitation induced by the burst LEX vortices. The excitation was greatest when the core breakdown had advanced to positions similar to those observed in the wind tunnel. It is interesting to note that, although clearly visible, the vertical tail dynamics could not be felt by the pilot.

The flow visualization results in figures 28 through 33 also reveal the development of numerous vortices along the length of the LEX leading edge. They appear in the photographs as distinct irregularities about the outer edge of the LEX vortical flows, and have been referred to as shear layer instabilities. These vortices are discussed in references 14 through 16 and are characteristic of the vortex development about slender lifting surfaces. They have been observed at low Reynolds number and low subsonic speeds (ref. 14), transonic and supersonic speeds (ref. 15), and high Reynolds number (ref. 16). At low angles of attack, the vortices are separate and distinct, whereas at higher angles of attack they merge to form a central, dominant vortical flow. There was no discernible movement of the multiple vortices at a given model station and angle of attack. The vortex structure illuminated by the laser light sheet in the present experiment on the 0.06-scale model is very similar to the in-flight (natural condensation) photograph in figure 34 (ref. 16) corresponding to the full-scale F/A-18 aircraft.

Figure 35 presents the progression of vortex breakdown with the angle of attack at free-stream Mach numbers of 0.20, 0.40, and 0.60 determined from the laser vapor screen observations. At  $M_\infty = 0.20$ , the vortex core and core bursting were first visible at an angle of attack of approximately  $27.5^\circ$ . At the higher Mach numbers, the cores were visible at much lower angles of attack. The results in figure 35 indicate that the vortex breakdown characteristics are insensitive to the Mach number from  $M_\infty = 0.20$  to 0.60. In contrast, the Navier-Stokes computations performed in reference 17 on an F/A-18 forward fuselage component (forebody, canopy, and LEX's) at  $\alpha = 20^\circ$  and  $M_\infty = 0.60$  revealed a high level of compressibility associated with the core of the LEX vortex system. The condensation patterns also change, as noted previously in reference to figure 27. However, the compressibility effect within the core region is dominated by the adverse pressure gradient in the external potential flow field. The presence of the twin vertical tails may also help to "mask" a Mach number effect, particularly at angles of attack where vortex bursting occurs in the vicinity of the tails.

Increasing the free-stream Mach number to 0.80 promotes noticeable changes in the LEX vortex cross-flow pattern. It has been documented in reference 6 that the cross section of a wing leading-edge vortex is flatter, or lobe-shaped, and the vortex core moves inboard and closer to the surface at transonic speeds. However, another factor affecting the vortex cross flow on the F/A-18 is the fuselage, which limits

the inboard movement of the vortical flow along the LEX. The constraint on the lateral movement causes an upward displacement of the vortical flow from the surface. The overall effects of the boundary constraint and the increasing Mach number are a slight flattening and inboard movement of the vortex and an upward rotation of the vortex cross section about the LEX leading edge. As a result of the altered shape and position of the LEX vortex, the primary flow reattachment induced by the vortex typically occurs along the side or top of the fuselage, depending on the angle of attack. At the lower Mach numbers, the flow reattaches to the LEX upper surface. Downstream of the LEX, where the vortex is no longer fed by the boundary-layer separation from the leading edge, the flow cross section becomes approximately circular.

The vapor screen results at  $M_\infty = 0.60$  and 0.80 from the model sting-mounted camera are shown in figure 36. The cross-flow patterns at the vertical tail apex (FS 525 (31.50)) are presented at  $\alpha = 15^\circ$ ,  $17.5^\circ$ , and  $20^\circ$ . At each angle of attack, the condensation pattern enlarges, and the vortex core moves inboard and upward, at the higher Mach number. At  $\alpha = 20^\circ$  and  $M_\infty = 0.80$ , there was no evidence of the vortex core bursting near the tail that occurred at  $M_\infty = 0.60$ . At  $\alpha = 22.5^\circ$  (flow visualizations not shown), however, the vortex core exhibited a pulsation, and condensed water vapor would intermittently enter the core region beginning at FS 450 (27.00). This effect could be traced downstream to the vertical tails. Concurrently, the vortex cross-flow patterns were very unsteady. The onset of the vortex core pulsing advanced to FS 410 (24.60) (near the juncture of the LEX and the wing leading edge) at  $\alpha = 25^\circ$  and the magnitude of the flow unsteadiness increased. These trends coincided with the development of strong shock waves that interacted with the vortices. Unpublished surface oil flow visualizations conducted by NASA in previous testing of the 0.06-scale F/A-18 model in the DTRC 7- by 10-Foot Transonic Tunnel revealed a normal shock wave situated over the wing and just upstream of the trailing edge. This shock wave could not be discerned directly from the vapor screen flow visualizations, however.

The laser light sheet did reveal a shock wave situated above the aft fuselage section between the LEX vortices beginning at  $M_\infty = 0.80$ . An intense downflow is induced between the vortices, and the locally supersonic flow recompresses through a shock wave situated above the fuselage. At  $\alpha = 27.5^\circ$  and  $30^\circ$ , the cross sections of the burst vortices expanded sufficiently over the aft fuselage that they intersected

along their inboard edges. Under these conditions, the cross-flow shock wave was no longer apparent.

The flow visualizations at  $M_\infty = 0.80$  were not of sufficient detail to accurately determine the vortex breakdown location at any angle of attack. This was rendered more difficult by the intermittent nature of the core flow over the wing. The loss of definition of the vortex cross flow is typical of laser vapor screen flow visualizations at the transonic speeds.

The effect of sideslip on the vortex cross-flow structure near the twin vertical tails is shown in figure 37 at  $M_\infty = 0.60$ ,  $\alpha = 20^\circ$ , and  $\beta = 0^\circ$  and  $4^\circ$ . The asymmetries in the leeward and windward LEX vortex core paths and breakdown positions due to sideslip are apparent. Sideslip promotes a forward advance of the windward LEX vortex breakdown position and a more extensive wake that envelops the windward vertical tail. In contrast, the leeward vortex is stabilized and the core passes outboard of the vertical tail.

The strengths of the forebody vortical flows on the baseline F/A-18 model are less than those of the LEX vortices. The cross-sectional shape and fineness ratio of the F/A-18 forebody are not conducive to the development of strong vortex flows. As a consequence, visualization of the baseline model forebody vortices was limited to angles of attack near and beyond maximum lift ( $35^\circ$  and greater), where the vortex strengths were sufficient to create a condensation pattern visible with the aid of the laser light sheet. Figure 38 presents a result obtained at an angle of attack of  $50^\circ$  and  $M_\infty = 0.60$ , which shows a pair of distinct, donut-shaped vortices at FS 163 (9.78), which is midway between the second and third pressure rings on the forebody. Farther aft, the forebody vortices were rapidly entrained into the burst LEX vortices and could not be tracked beyond the canopy.

At Mach numbers below 0.60, the forebody vortices were not visible, even at angles of attack up to  $50^\circ$ . This is a shortcoming of the vapor screen technique, since the condensation of water vapor is insufficient in the weaker vortices to yield good flow definition. However, alternative particle seeding methods can yield vivid visualizations of the forebody vortices. In recent flight experiments on the F-18 HARV (ref. 12), for example, the forebody vortices have been clearly seen at  $M_\infty = 0.20$  to  $0.30$  and  $\alpha = 30^\circ$  to  $50^\circ$ . The smoke seeding particles were injected from the nose region of the aircraft. This provided sufficient particle density in the region of the vortex cores to make them visible.

At Mach numbers of 0.80 and 0.90, the forebody vortices were visible beginning at an angle of attack

of approximately  $35^\circ$ . The vortical flows appeared larger and stronger at a given angle of attack in comparison with the result at  $M_\infty = 0.60$ , and they penetrated farther into the LEX flow field before being entrained by the LEX vortices. The LEX vortices were weaker at the higher Mach numbers, which would allow the body vortices to persist farther downstream. However, the clarity of the forebody vortices at the transonic speeds is greater than the flow-field visualizations on wings at the same conditions. A plausible explanation for the apparent increase in the forebody vortex strength is the development of a cross-flow shock wave along the forebody side that causes an early separation of the primary boundary layer. This is discussed in more detail later.

**LEX upper surface static pressure distributions.** The effect of the angle of attack on the LEX upper surface static pressure distributions at FS 253 (15.18), 296 (17.76), and 357 (21.42) is illustrated in figures 39, 40, 41, and 42 corresponding to free-stream Mach numbers of 0.40, 0.60, 0.80, and 0.90, respectively. The LEX vortex breakdown characteristics that were derived from the vapor screen flow visualizations at  $M_\infty = 0.40$  and  $0.60$  in figure 24 and figures 28 through 33, and the more limited flow-field information at  $M_\infty = 0.80$  and  $0.90$ , will augment the analysis of the pressure distribution trends.

The pressure distributions at  $M_\infty = 0.40$  and  $0.60$  in figures 39 and 40, respectively, display a consistent increase in the vortex-induced suction peaks at  $\alpha = 10^\circ$  to  $25^\circ$ . This is consistent with the vapor screen flow visualizations which revealed a stable vortical flow over the LEX surface through this range of angle of attack. The inboard movement of the suction peak as the angle of attack increases reflects the growth of the LEX vortex. This migration is less apparent at angles of attack greater than  $20^\circ$  due to the barrier imposed by the fuselage which impedes the lateral translation. At  $\alpha = 30^\circ$ , vortex breakdown is between the aft pressure row (FS 357 (21.42)) and the LEX-wing-leading-edge junction (FS 404 (24.24)). The approach of core breakdown and the upward movement of the vortex promote a decrease in the vortex suction peaks at FS 357 (21.42). At  $\alpha = 35^\circ$ , vortex breakdown has passed this measurement station. The pressure distributions are flatter, and the maximum suction pressure levels underneath the vortex exhibit a marked decrease. Similar trends are observed at FS 296 (17.76) and 253 (15.18) as vortex breakdown reaches these measurement stations at  $\alpha = 40^\circ$  and  $45^\circ$ , respectively. The signatures of the LEX vortices are weaker at  $M_\infty = 0.60$ . This is consistent with the compressibility effect on the vortex pressure signatures noted in reference 18. It



is noted that the port and starboard LEX surface pressure distributions are asymmetric at  $M_\infty = 0.40$  and  $\alpha = 50^\circ$ . This may be due to asymmetric flow development from the forebody, which is discussed in the next section.

The compressibility effect on the LEX surface pressures is even more apparent at  $M_\infty = 0.80$  and  $0.90$  in figures 41 and 42, respectively. The reduced vortex strength, flatter vortex cross section, and upward displacement of the vortex are manifested in figures 41 and 42 as diminished suction levels and flatter pressure distributions underneath the vortical flows. The vortex pressure signature is also more conical in character at the transonic speeds. This is due to the diminished upstream influence of the trailing-edge pressure recovery at the higher Mach numbers. As a result, the maximum suction pressures are comparable at a given angle of attack at all three measurement stations on the LEX. At FS 357 (21.42), the increased suction pressures near the LEX-fuselage junction beginning at  $\alpha = 25^\circ$  coincide with the onset of the vortex-induced primary flow reattachment to the fuselage instead of the LEX surface.

In contrast to the results at the lower Mach numbers, it is difficult to infer the position of vortex breakdown from the LEX pressure distributions at  $M_\infty = 0.80$  and  $0.90$ . The laser vapor screen visualizations suggested that core bursting occurred near the LEX-wing-leading-edge junction (FS 404 (24.24)) at  $\alpha = 27.5^\circ$  and approached the aft pressure row on the LEX at  $\alpha = 30^\circ$ . This would account for the loss of the suction peak underneath the vortex at FS 357 (21.42) as the angle of attack increases from  $25^\circ$  to  $30^\circ$  in figures 41 and 42. This progression of the burst position with  $\alpha$  is similar to the results at the lower subsonic Mach numbers. At higher angles of attack, the vapor screen flow visualizations were inconclusive. The flat pressure distributions along the forward portion of the LEX provide no indication of the approach, or passage, of vortex breakdown.

Figures 43, 44, 45, 46, and 47 illustrate the effect of the Mach number on the LEX upper surface static pressure distributions at angles of attack of  $10^\circ$ ,  $20^\circ$ ,  $30^\circ$ ,  $40^\circ$ , and  $50^\circ$ , respectively. At  $\alpha = 50^\circ$ , the data were obtained at  $M_\infty = 0.20$  to  $0.60$  only. The DTRC roll sting normal-force limit precluded testing to higher Mach numbers at this angle of attack. The test results reveal a high level of compressibility of the LEX vortex system. A significant decrease in the vortex-induced suction pressures occurs as the Mach number increases. The effect of compressibility is apparent at Mach numbers as low as  $0.20$  to  $0.30$ . The flattening of the pressure distributions at the higher Mach numbers is also apparent at angles of

attack of  $20^\circ$  and greater. At  $\alpha = 40^\circ$  and  $50^\circ$  (figs. 46 and 47), where vortex breakdown dominates the flow about the LEX's, the signature of the burst vortex system displays a similar sensitivity to the Mach number.

CFD results have also revealed the compressible nature of the LEX vortex. The density contours derived from Navier-Stokes computations on an F/A-18 forward fuselage component in reference 17 corresponding to  $M_\infty = 0.60$  and  $\alpha = 20^\circ$  revealed a 40- to 50-percent expansion in the vortex core region compared with that of the free-stream condition. In addition, the majority of the core flow achieved a local Mach number of  $0.90$  or greater, with a small supersonic zone occurring near the apex.

*Forebody surface static pressure distributions.* Simplified sketches, taken from reference 2, of three basic flow patterns in cross section about a body at a high angle of attack are shown in figure 48. An understanding of these basic flows will assist in the interpretation of the 0.06-scale F/A-18 model forebody pressure distributions. It is conjectured that the flow about the wind tunnel model features elements of all three cross-flow patterns. Figures 49 through 56 present the effect of the angle of attack on the forebody surface static pressure distributions at  $M_\infty = 0.40$ ,  $0.60$ ,  $0.80$ , and  $0.90$ , corresponding to FS 107 (6.42), 142 (8.52), and 184 (11.04). To assist in the discussion of the forebody flow characteristics, the pressure distributions at selected angles of attack are isolated in separate plots. It is noted that the forebody cross section is circular at FS 107 (6.42). At FS 142 (8.52) and 184 (11.04), the cross sections are rounded on the top and bottom but relatively flat along the sides.

The first pattern in figure 48 corresponds to the case of laminar cross-flow separation (LP), followed by flow reattachment (R) and subsequent secondary separation (SS). This flow situation may exist along the nose region of the F/A-18 model. In fact, in-flight surface flow visualizations on the F-18 HARV (ref. 19) suggest the existence of a laminar separation zone near the nose tip.

The second sketch in figure 48 depicts a transitional pattern (TRP). Of the three cross-flow patterns, this is the most complicated. Primary laminar separation (LS) occurs but the separated shear layer becomes turbulent and reattaches to the body forming a confined bubble region (B). The flow reattaches at the leeside of the bubble and subsequently separates as a turbulent boundary layer (TS). This pattern is considered representative of the flow downstream of the nose region of the F/A-18 model.



Farther aft along the forebody, where the local body width is greatest, the effective Reynolds number is high enough for boundary-layer transition to occur before laminar separation. Thus, no separation bubble forms and the flow separates in a turbulent manner (TS).

At  $M_\infty = 0.40$  (figs. 49 and 50), the footprint of the forebody primary vortex pair is first apparent at all three pressure rings at an angle of attack of  $35^\circ$ . For reference, the stagnation point at zero sideslip corresponds to an angular position  $\theta$  of  $0^\circ$ . Examination of the pressure distribution at  $\alpha = 40^\circ$  and FS 107 (6.42) in figure 50 indicates that the flow accelerates around the circular cross section and induces a maximum suction pressure at an angular position  $6^\circ$  above the maximum half-breadth (MHB at  $\theta = 90^\circ$  and  $270^\circ$ ). A steep pressure recovery, which is indicative of a turbulent boundary layer, occurs on the leeward side of the body, followed by primary separation about  $30^\circ$  from the top centerline ( $\theta = 180^\circ$ ). The forebody primary vortex footprints are indicated by a pair of suction pressure peaks situated approximately  $12^\circ$  on either side of the top centerline.

The character of the pressure distribution at FS 142 (8.52) is similar. Because of the flatter sides at this fuselage station, the attached flow suction pressure maximum is achieved at a lower angular position (approximately  $18^\circ$  below the MHB). The ensuing pressure recovery region is terminated by primary boundary-layer separation about  $30^\circ$  on either side of the top centerline. The forebody vortices induce suction peaks at an estimated angular position  $15^\circ$  from the top centerline.

At FS 184 (11.04), an attached flow suction pressure maximum occurs at  $\theta = 60^\circ$ . This is followed by a narrow band of uniform surface pressures along the flat sides of the forebody and then a second region of local flow acceleration. This pressure ring is in proximity to the apex of the wing leading-edge extension, and the locally accelerated flow is attributed to the LEX upwash. Similar to the results at FS 107 (6.42) and 142 (8.52), primary separation at FS 184 (11.04) occurs at approximately  $30^\circ$  from the top centerline and the resultant vortex pair induces suction peaks situated about  $9^\circ$  from the leeward-side centerline.

At higher angles of attack, the pressure distributions are asymmetric. There was no indication during the testing that the asymmetry was time dependent. At  $\alpha = 50^\circ$  (fig. 50), a mild asymmetry is apparent at FS 107 (6.42). Reference 2 has suggested a number of parameters that may cause this asymmetric flow development, including Reynolds num-

ber, slenderness of the nose, geometric irregularities at the nose apex, surface roughness, free-stream turbulence, and model support and vibration. The asymmetry is amplified at FS 142 (8.52) and 184 (11.04). At FS 184 (11.04), a single vortex suction peak is evident. This pressure distribution is consistent with the movement of one primary vortex toward the forebody surface, accentuating its suction peak, and an upward displacement of the second vortex, with a corresponding loss of its signature in the pressure distribution. The asymmetric flow development on the forebody was the apparent triggering mechanism for the LEX vortex asymmetries that were manifested in the pressure distributions in figure 39.

It is not possible to provide a complete description of the surface flow characteristics on the basis of the pressure distributions. However, a plausible surface flow situation on the F/A-18 model is that the initial flow separation along the forebody is laminar (LP cross flow sketched in fig. 48) due to the low local Reynolds number. The laminar region is succeeded by a transitional pattern (TRP) and finally a fully turbulent region (TP). (See fig. 48.)

The character of the forebody pressure distributions at  $M_\infty = 0.60$  (figs. 51 and 52) is similar to that at  $M_\infty = 0.40$ . It is noted that favorable comparisons have been presented in reference 17 of the current experimental results at  $\alpha = 20^\circ$  and  $M_\infty = 0.60$  to the turbulent flow Navier-Stokes solutions on an F-18 forward fuselage component. At  $\alpha = 40^\circ$  (fig. 52), the footprint of the forebody primary vortices is apparent at all three pressure rings. The flow asymmetry that was evident at  $M_\infty = 0.40$  and  $\alpha = 50^\circ$  in figure 50 is reduced at the higher Mach number. A laser vapor screen result corresponding to  $M_\infty = 0.60$  and  $\alpha = 50^\circ$  was shown previously in figure 38, which revealed a pair of donut-shaped vortices above the forebody. A flow-field asymmetry was not apparent in figure 38, which was at a longitudinal station between FS 142 (8.52) and 184 (11.04).

Transonic flow mechanisms are manifested in the forebody pressure distributions at  $M_\infty = 0.80$  and  $0.90$  (figs. 53 through 56). The principal differences from the results at the lower Mach numbers are earlier separation of the primary boundary layer and stronger forebody vortex footprints. At  $\alpha = 40^\circ$  and FS 142 (8.52) (figs. 54 and 56), for example, the pressure recovery region beginning at  $30^\circ$  below the MHB is terminated by boundary-layer separation at an angular position approximately  $30^\circ$  above the MHB. A supersonic expansion occurs along the sides of the forebody. This can be seen by comparing the experimental surface pressures with the critical

pressure coefficient  $C_p^*$  at  $M_\infty = 0.8$  and  $0.9$ . It is hypothesized that the flow recompresses to subsonic conditions through a cross-flow shock wave that is strong enough to separate the boundary layer. This flow situation is sketched in figure 57. The shock-induced primary flow separation promotes stronger vortices in comparison with the subsonic results. The pressure distribution trends are consistent with the laser vapor screen flow-field observations at the transonic speeds, where the vortices became visible at lower angles of attack and appeared stronger and larger relative to their counterparts at the subsonic speeds.

**Longitudinal and lateral-directional characteristics.** Figure 58 presents the lift, drag, and pitching-moment characteristics of the baseline model at free-stream Mach numbers from  $0.20$  to  $0.90$ . In contrast to the sensitivity of the LEX and forebody surface pressures, the character of the lift and drag curves is similar through the range of the Mach number. Maximum lift is obtained at  $\alpha = 40^\circ$  for all Mach numbers. The principal influence of the Mach number is reflected in the pitching-moment curves. Increasing the Mach number promotes a stable pitching-moment increment at a given lift coefficient, and the pitch stability at low lift levels is increased at the transonic speeds ( $M_\infty = 0.80$  and  $0.90$ ).

Figures 59 through 61 show the variations of the rolling-moment, yawing-moment, and side-force coefficients with the sideslip angle at selected angles of attack and free-stream Mach numbers of  $0.60$ ,  $0.80$ , and  $0.90$ . At  $M_\infty = 0.60$  (fig. 59), the model exhibits a stable variation of the rolling moment with the sideslip angle at all angles of attack from  $20^\circ$  to  $40^\circ$ . This trend is similar to the results obtained in previous testing by NASA, the Navy, and McDonnell Douglas with the  $0.06$ -scale model, which has consistently displayed lateral stability at subsonic speeds through the range of angle of attack. This result differs from the data obtained at low speed on a  $0.16$ -scale F/A-18 (ref. 9), which show a reduction in lateral stability at angles of attack near maximum lift.

The laser vapor screen flow visualizations presented previously in figure 37 revealed asymmetries in the LEX vortex core paths and breakdown positions due to sideslip. The qualitative information can be misleading, however, when compared with the total forces and moments. The LEX vortex on the windward side is stronger and closer to the LEX and wing surfaces relative to the leeward vortical flow (ref. 20). Despite the early bursting of the wind-

ward vortex over the wing surface, the lift remains higher on the windward side, creating a stable rolling moment. The correlation of the vapor screen results with the yawing-moment characteristics is more straightforward, however. The burst windward vortex blankets the windward vertical tail, which promotes the directional instability at small sideslip angles at  $\alpha = 20^\circ$ . At higher angles of attack where bursting of both LEX vortices occurs, the yawing-moment variation with sideslip becomes increasingly unstable.

The  $0.06$ -scale model exhibits a reduction in lateral stability at small sideslip angles at  $\alpha = 20^\circ$  and  $M_\infty = 0.80$  and at  $\alpha = 20^\circ$  and  $25^\circ$  and  $M_\infty = 0.90$  (figs. 60 and 61). This is caused by the interaction of the LEX vortex with a rear shock wave over the wing, which promotes a rapid forward advance of core bursting on the windward side. It is not known whether this interaction persists to higher angles of attack, since the vapor screen flow visualizations were not of sufficient detail to identify the flow mechanisms. It was apparent, however, that the flow-field asymmetries were significantly reduced at the higher model attitudes, which compares favorably with the recovery in lateral stability indicated in figures 60 and 61 at the higher angles of attack.

#### 0.06-Scale F/A-18 With LEX Fences

**Laser vapor screen flow visualizations.** The laser vapor screen results at the subsonic and transonic speeds indicate that the LEX vortex is situated outboard of the fence at  $\alpha = 10^\circ$  (flow visualization not shown). A single, primary vortex from each LEX is apparent over the wings and outboard of the vertical tails. The inboard and upward movement of the vortex at  $\alpha = 12.5^\circ$  (vapor screen result not presented) places the fence in the path of the core. This marks the onset of major changes to the cross-flow structure about the wings and vertical tails. The solid boundary introduced into the flow changes the pressure field about the LEX's and wings. The fence also disrupts the secondary boundary-layer separation on the LEX upper surface. The vortex-induced reattached flow impinges on the inboard surface of the fence and is diverted upward; this creates a local upwash. A modified mechanism of vortex development from the LEX is established in response to these effects.

Figure 62 presents representative off-body flow visualizations obtained on the  $0.06$ -scale F/A-18 model with and without the LEX fences at an angle of attack of  $20^\circ$  and a free-stream Mach number of  $0.40$ . The flow field is viewed from a three-quarter, right rear position. The LEX vortex is displaced inboard

and upward as it passes over the fence. The fence impedes the development of the primary vortical flow from the leading-edge extension and effectively reduces the vortex generating length. The termination of the vortex feeding mechanism weakens the LEX vortex in comparison with the baseline case. In addition, the vortex shears away from the leading edge and becomes a "free vortex" system upstream of the LEX-wing junction. The vortex cross section is distorted downstream of the fence. Concurrent with the compression and stretching of the LEX vortex is a downward and outboard movement of the vortical flow as it passes over the wing surface.

The distortion and displacement of the LEX primary vortex downstream of the fence are due to its interaction with another vortical flow. A second corotating vortex (vortex rotating in the same sense) develops from the LEX leading edge. This is illustrated in the close-up photographs of the LEX and wing regions in figure 63 at  $M_\infty = 0.60$  and  $\alpha = 20^\circ$  and  $25^\circ$ . The flow phenomena at this higher Mach number were similar to those at  $M_\infty = 0.40$  but were revealed in greater detail. The origin of the second vortex is near the point at which the main LEX vortical flow shears away from the edge. The effective generating length of the second vortex extends from this point aft to the intersection of the LEX with the leading-edge flap hingeline. In practice, this generating length is not constant, since the leading-edge flap deflection angle is scheduled with the angle of attack and the Mach number. In the present experiment, the leading-edge flap is deflected to its maximum angle of  $34^\circ$ , which exposes the longest possible run length for the second vortex. The corotating vortex induces downward velocities at the LEX primary vortex, which compresses and stretches the LEX vortex and draws it downward toward the wing surface. This effect is seen from the perspective of the sting camera in figures 64 and 65, which present the cross-flow patterns on the LEX fence and baseline configurations at  $M_\infty = 0.60$  and  $\alpha = 20^\circ$  and  $25^\circ$ , respectively. As the LEX vortex path moves downward, it also bends outward slightly. Tracking the respective vortex trajectories along the wings and near the tails reveals a slight rotation of the vortical flows about each other, although the interaction at zero sideslip angle is not strong enough to promote a coiling, or wrapping around, of the vortices. The results in figures 64 and 65 demonstrate the significant change in the cross-flow structure at the vertical tails due to the LEX fences.

The velocities induced by the corotating vortices on each other are in opposition. In combination with the reduced vortex strengths, the expected net

result is a reduction in the normal, lateral, and axial velocity components in the vicinity of the vertical tails. In the range of angle of attack from  $25^\circ$  to  $30^\circ$ , where the vortex-induced tail excitation is maximum on the baseline configuration, the LEX fences promote a flow at the tails consisting of two corotating vortices of reduced strength that induce lower mean velocities and flow angularity. This effect was quantified in low-speed wind tunnel testing by McDonnell Douglas of an earlier version of the LEX fence. As shown in figure 66, the mean velocities and flow angularity in the vicinity of the vertical tail of a 0.083-scale F/A-18 model are reduced with the fences on.

The laser vapor screen flow visualizations provided further qualitative evidence of the effectiveness of the LEX fences in improving the vertical tail buffet environment. The LEX vortex burst phenomenon observed on the baseline configuration at angles of attack of approximately  $20^\circ$  and greater was characterized by a sudden flaring of the vortex core, the appearance of condensate along the core axis, and a marked flow unsteadiness within the region of bursting. The breakdown locations from the vapor screen flow visualizations were clearly defined. In contrast, a burst location at  $\alpha = 20^\circ$  on the model with the LEX fences could not be identified. Repeated sweeps of the laser light sheet failed to pinpoint the telltale signs of vortex breakdown. At higher angles of attack,  $\alpha = 25^\circ$ , for example, the breakdown was identified as a very mild, gradual process, and the level of turbulence within the expanded, rotating flows was visibly reduced in comparison with the baseline flow field. At angles of attack of about  $30^\circ$  and greater, where the breakdown position advanced forward to a position at, or ahead of, the fence, the burst phenomenon was very similar to the baseline case.

An early concern with the fence was the possibility of prematurely bursting the LEX vortices due to the physical obstacle present in the flow. The fence that was tested on the 0.06-scale model was selected from hundreds of configuration modifications tested by McDonnell Douglas (ref. 3). The fact that the fence did not significantly impact the longitudinal or lateral-directional characteristics obtained in the earlier testing is an indicator of the benign nature of the device. Nonetheless, special attention was given in the laser vapor screen flow visualizations to the primary LEX vortex core stability in the presence of the fence. At  $M_\infty = 0.60$ , the results show a delay of vortex core breakdown due to the fence at angles of attack up to approximately  $27.5^\circ$ . The delayed bursting is apparent in the sting camera results shown previously in figure 65 at  $\alpha = 25^\circ$ . At FS 450 (27.00),

the vortex core on the baseline model is burst. The core is filled with condensate as a result of the reverse flow along its axis. With the fences on, the LEX vortex at this station exhibits a stable, hollow core. A plot of the progression of vortex bursting with the angle of attack for the baseline and fence configurations is shown in figure 67. The more stable behavior of the LEX vortex in the presence of the fence is due to the favorable flow gradients induced by the second corotating vortex from the rear portion of the LEX. Once vortex breakdown reaches the fence, however, the vortex breakdown progression with the angle of attack is similar on both configurations.

The favorable interference of two suitably spaced, corotating vortices has been documented in references 6 and 7 on a generalized  $55^\circ$  cropped delta wing fighter model with chine-like forebody strakes. Under certain conditions, it was found that the corotating vortex system delayed vortex breakdown and reduced the undesirable effects of bursting once it occurred. In addition, the altered cross-sectional shape of interacting vortices has been reported in reference 7 on the  $55^\circ$  cropped delta wing model and in reference 21 on a  $65^\circ$  cropped delta wing-LEX configuration.

The interpretation of the off-body flow visualization warrants special note. The initial wind tunnel results on the model with the LEX fences were obtained at free-stream Mach numbers of 0.30 and 0.40. Good definition of the LEX primary vortex core was provided by condensation within the vortex, in combination with the lighting of the wind tunnel test section only. The second corotating vortex could not be seen under these conditions, however. Upstream of the fence, the LEX primary vortex was visible as a donut-shaped structure, void of condensed water vapor along its axis, with an accumulation of condensate along the outer edge. Slightly downstream of the fence, the vortex appeared to expand and the definition of the core region deteriorated, or was lost altogether. A similar flow pattern would be obtained in a smoke flow visualization experiment if the seeding particles were injected near the LEX apex into the vicinity of the vortex core, as is the case on the F-18 HARV in flight. A likely interpretation of results obtained in this manner is that the fence promotes vortex breakdown. Illuminating the model cross flow with an intense sheet of laser light yields an entirely different interpretation, however. A distinct LEX primary vortex core could be discerned downstream of the fence and the second vortex from the rear portion of the LEX was visible. The fence promotes a system of two weaker vortices and, consequently, the condensation patterns will be less vivid

in comparison to the single, stronger vortex on the baseline model.

Prior comparisons of the baseline model LEX vortex breakdown behavior obtained with the laser vapor screen method with the flight results obtained on the NASA F-18 HARV using smoke have been straightforward. The structure of vortex breakdown has been of the classical sense in both cases, namely, a sudden expansion of a well-defined vortex core, followed by a large, turbulent rotating flow downstream. However, differing interpretations of the F/A-18 flow field with the fences installed have arisen as a result of recent flight tests of the F-18 HARV (ref. 4). A representative result from flight at a Mach number of 0.27 and an angle of attack of approximately  $20^\circ$  is shown in figure 68. The smoke particles were introduced into the vortex from a port located near the apex of each LEX. The vortex core in flight is well-defined along the LEX, and it moves upward and inboard in the vicinity of the fence. Aft of the fence, however, the smoke particles define a larger, diffused flow that moves downward and outboard over the wings. Videotape results from a wingtip-mounted camera revealed a rotating mass downstream of the fence that was less turbulent than the clearly defined vortex breakdown on the aircraft without the fences. This result is similar to the wind tunnel model condensation pattern at  $M_\infty = 0.4$  illuminated by the test section lights only, as shown in figure 68. These results indicate that the traditional interpretation of vortex breakdown as a rapid expansion of the vortical region does not apply in flow situations such as this. The smoke traces in the flight visualization yield a subset of the overall vortical flow field. Other flow visualization techniques are necessary to extract additional information contained within the flow field.

**LEX upper surface static pressure distributions.** Figures 69, 70, and 71 show the effect of the fences on the LEX upper surface static pressures at selected angles of attack and free-stream Mach numbers of 0.30, 0.60, and 0.80, respectively. The last pressure row on the LEX's is approximately 1.27 in. (0.06 scale) ahead of the fence leading edge.

At  $M_\infty = 0.30$  (fig. 69) and angles of attack of  $20^\circ$ ,  $25^\circ$ , and  $30^\circ$ , the fence promotes a reduction in the LEX primary vortex-induced suction peak at the aft pressure row (FS 357 (21.42)). This is consistent with the upward displacement of the vortex core that was observed in the laser vapor screen flow visualizations. There is no effect of the fence at these angles of attack on the surface pressures at the two upstream measurement stations (FS 253 (15.18) and 296 (17.76)). This trend is maintained

at  $\alpha = 35^\circ$ , where vortex bursting has advanced upstream of FS 357 (21.42). The fence causes an upward displacement of the burst vortex at higher angles of attack, and the reduced signature of the burst vortex propagates forward to FS 296 (17.76) at  $\alpha = 40^\circ$ . There is no indication from the surface pressures that the fence promotes early bursting of the vortical flow.

The upstream influence of the fence diminishes at  $M_\infty = 0.60$  and  $0.80$  (figs. 70 and 71). This is attributed to the weakening of the vortical flows at the higher Mach numbers and the development of regions of supersonic flow that limit the upstream "communication" of the LEX fence.

**Longitudinal and lateral-directional characteristics.** The effect of the LEX fences on the lift, drag, and pitching-moment characteristics is shown in figures 72, 73, and 74 for Mach numbers of 0.30, 0.60, and 0.80, respectively. At  $M_\infty = 0.30$  (fig. 72), the fences promote a slight increase in the lift at angles of attack of approximately  $20^\circ$  to  $27.5^\circ$  and a drag decrease at the corresponding lift coefficients. The favorable interference of the two corotating vortices with the fences promotes the lift and drag improvements. At  $\alpha = 30^\circ$  and greater, the slight lift decrease and drag increase are due to the upward displacement of the burst vortices, which was discussed in the previous section. This reduces the vortex-induced suction pressures on the LEX's and wings.

The effects of the fence on the lift and drag characteristics at the high angles of attack diminish with increasing values of the Mach number (figs. 73 and 74). At  $M_\infty = 0.80$  (fig. 74), for example, there is no change in the lift and drag at angles of attack greater than about  $25^\circ$ .

The fences promote nose-down pitching-moment increments up to maximum lift at  $M_\infty = 0.30$  (fig. 72). The reduced suction pressures on the LEX's, which act ahead of the moment reference center, contribute to the nose-down pitching moments. The downward displacement of the LEX vortex toward the wing surface, resulting from its interaction with the second corotating vortex, may also promote higher suction pressures along the rear portion of the wing. The increased loading aft of the moment reference center is a probable source of the larger nose-down pitching-moment increments at lift coefficients up to approximately 1.2. The effect of the fences on the pitching moment diminishes at  $M_\infty = 0.60$  (fig. 73) and is negligible at  $M_\infty = 0.80$  (fig. 74).

The variations of the rolling-moment, yawing-moment, and side-force coefficients with the sideslip

angle at selected angles of attack and  $M_\infty = 0.60$  are shown in figure 75. The data show relatively minor effects of the LEX fences on the lateral-directional stability through the range of angle of attack.

#### 0.06-Scale F/A-18 With Flight Test Nose Boom (LEX Fences on)

**Laser vapor screen flow visualizations.** Figure 76 shows the effect of the flight test nose boom on the forebody cross-flow pattern at an angle of attack of  $50^\circ$  and a free-stream Mach number of 0.60. The light sheet is positioned at FS 184 (11.04). The result at  $\alpha = 50^\circ$  was selected because it illustrates to a larger scale the trends that were observed at angles of attack near and beyond maximum lift. The flow visualization photograph reveals the boom wake and the forebody primary vortex envelope. The boom wake consists of multiple, asymmetric vortices shed from each step increase in the boom local diameter. The boom wake may induce a downwash on the forebody, which could reduce the size and strength of the forebody primary vortices. The boom may also reduce, or eliminate, the laminar separation region near the nose. The more turbulent nature of the boundary layer along the forebody would also be consistent with the smaller and weaker vortices.

The influence of the asymmetric boom wake is also manifested in the LEX vortex structure. With the nose boom installed, the LEX vortices exhibit asymmetric breakdown at zero sideslip at angles of attack from approximately  $30^\circ$  to  $40^\circ$ . Reversals of the asymmetry occur as the angle of attack increases through this range. Typical results from the vapor screen flow visualizations are shown in figure 77, which illustrate the asymmetric LEX vortex breakdown of opposite sense at  $\alpha = 30^\circ$  and  $32.5^\circ$  and  $M_\infty = 0.60$ . These trends are indicative of a switching of the asymmetric boom wake as the angle of attack increases. In contrast, the model without the boom exhibits symmetric LEX vortex bursting at the same angles of attack.

The model with LEX fences may be more susceptible to the effects of the boom wake, since the LEX primary vortex is displaced upward toward the wake generated from the forward fuselage, and is weakened as a result of its reduced generating length. During the LEX fence flight validation program conducted by McDonnell Douglas and the Navy (ref. 3), the nose boom degraded the handling qualities of the F/A-18 aircraft at angles of attack near maximum lift. Removal of the nose boom eliminated the degraded handling qualities.

This result is a further example of the sensitivity of interactive, or coupled, vortices to the flow

development near the nose. This is of importance to future fighter aircraft that may feature increased forebody-wing vortex interactions at high angles of attack.

**Forebody surface static pressure distributions.** Figures 78 and 79 present the forebody surface static pressure distributions with and without the flight test nose boom at  $M_\infty = 0.6$  and  $0.8$  and  $\alpha = 50^\circ$  and  $40^\circ$ , respectively. The presence of the nose boom delays primary boundary-layer separation and reduces the pressure signature of the forebody vortices. This is indicated most clearly in the surface pressures at FS 142 (6.42), which show a marked decrease in the primary vortex-induced suction peaks with the boom on. This result is consistent with the reduced size of the forebody vortices that was shown previously in the vapor screen photograph in figure 76.

**Longitudinal and lateral-directional characteristics.** The nose boom has essentially no effect on the lift, drag, and pitching-moment characteristics at subsonic through transonic speeds. Data corresponding to the model with and without the boom are shown in figures 80 and 81 at  $M_\infty = 0.60$  and  $0.80$ , respectively.

The principal effect of the flight test nose boom is manifested in the lateral-directional characteristics at sideslip angles ranging from approximately  $-4^\circ$  to  $+4^\circ$  (ref. 9). Figure 82 presents the variation of the rolling-moment, yawing-moment, and side-force coefficients with angle of attack at  $\beta = 0^\circ$  and  $M_\infty = 0.60$ . The nose boom promotes asymmetric rolling- and yawing-moment coefficients that repeatedly change sign as the angle of attack increases.

## Summarization of Results

The laser vapor screen flow surveys revealed a complex vortex structure generated from the LEX's of the baseline 0.06-scale F/A-18 model. Multiple, smaller scale vortices were generated along the length of the wing leading-edge extension. These shear layer instabilities rolled up to form the central, dominant vortex that is typically observed in water tunnel and wind tunnel testing and in full-scale flight. Evidence has surfaced recently from smoke flow and condensation patterns on the F-18 airplane that similar vortex flow structures exist in flight.

The global characteristics of the F/A-18 LEX vortex were insensitive to the Reynolds number at subsonic speeds. The location of LEX vortex breakdown and its progression with the angle of attack that were determined from the wind tunnel vapor screen flow

visualizations agreed well with similar measurements obtained in flight on the F-18 HARV. These results should be interpreted with caution, however, since the twin vertical tails or leading-edge flaps may mask the Reynolds number effect at angles of attack where vortex bursting occurs near the tails.

The LEX vortices were flatter and higher off the surface at the transonic speeds. The shear layer instabilities that comprised the LEX vortex at the subsonic speeds were also evident at the higher Mach numbers. The onset of core breakdown near the twin vertical tails was slightly delayed due to a diminished adverse, longitudinal pressure gradient. The vortex bursting phenomenon at the transonic speeds was unsteady and exhibited a fore-and-aft movement of the breakdown position over the wing. This was due to an interaction with a normal, or rear, shock wave. The locally supersonic flow induced between the LEX vortices recompressed to subsonic speeds through a shock wave situated above the aft fuselage and between the vertical tails. The flow details provided by the vapor screen method deteriorated at the higher Mach numbers, which may be the result of decreased values of the local relative humidity within the vortical flow regions.

The forebody vortices were weak in comparison with the LEX vortical flows. For this reason, they were not visible with the laser vapor screen technique until angles of attack near maximum lift and only at Mach numbers of  $0.60$  and greater. These results are in contrast to recent flow visualization results obtained on the F-18 HARV with a sufficient quantity of seeding particles injected from the nose region of the airplane, which yielded good definition of the forebody vortices at  $M_\infty = 0.2$  to  $0.3$  and  $\alpha = 30^\circ$  to  $50^\circ$ . The forebody vortices visualized in the wind tunnel and in flight were rapidly entrained into the dominant LEX vortical flows. At the transonic speeds, the forebody vortex size and strength increased due to cross-flow shock-induced boundary-layer separation. In contrast, the LEX vortex strength diminished at the higher Mach numbers. This allowed the forebody vortices to persist farther into the LEX flow field prior to their entrainment.

The footprints of the LEX vortices were easily discerned in the surface static pressures at the subsonic speeds. The progression of vortex bursting over the LEX correlated well with the pressure distribution trends. In contrast to the vapor screen results, the surface pressures revealed a high level of compressibility of the leading-edge vortex, beginning at free-stream Mach numbers as low as  $M_\infty = 0.20$  to  $0.30$ . The pressure distributions were flatter at the transonic speeds, which made it difficult to identify

the LEX vortex footprint or the passage of vortex breakdown at the higher angles of attack.

The forebody vortex signatures were well-defined in the model pressure distributions at the subsonic and transonic speeds at angles of attack of approximately  $30^\circ$  and greater. The surface pressures along most of the forebody were insensitive to the Mach number from  $M_\infty = 0.20$  to  $0.60$ . At  $M_\infty = 0.80$  and  $0.90$ , however, primary separation occurred at a lower position on the body, and the forebody vortex suction peaks exhibited a significant increase. The cross-flow Mach number at angles of attack near maximum lift was sufficiently high to promote the development of a shock wave along the side of the body, which was strong enough to separate the boundary layer.

A fence mounted to the upper surface of the LEX's in a streamwise orientation and near the wing-LEX junction altered the development of the primary vortex. The LEX vortex sheared away from the leading edge and moved upward and inboard as it passed over the fence. The migration of the LEX vortex allowed the formation of a second corotating vortical flow (rotating in the same sense) from the leading edge. The cross-flow structure over the wings and near the vertical tails was significantly changed as a result of an interaction of the corotating vortices. The flow induced by the vortices on each other was in opposition, which reduced the mean flow velocities and flow angularity at the vertical tails. This effect was observed within the angle-of-attack range ( $\alpha = 25^\circ$  to  $30^\circ$ ) where the tail excitation due to LEX vortex bursting was greatest on the baseline F/A-18. The fences did not adversely affect the LEX vortex breakdown characteristics. The core breakdown was more gradual and the level of turbulence within the burst vortical flow was less with the fences installed. The maximum lift was reduced slightly as a result of a vortex displacement effect. Otherwise, the fences were benign and had minimal impact on the configuration aerodynamic and stability characteristics at the subsonic through transonic speeds.

The effectiveness of the fences in improving the vertical tail buffet environment has been quantified by McDonnell Douglas, the U.S. Navy, and NASA in full-scale flight tests. Recent flow visualization experiments conducted by NASA on the F-18 HARV with LEX fences have shown effects of the fence on the vortex location and structure similar to those observed in the wind tunnel.

The flight test nose boom generated a multiple, asymmetric vortex wake at the high angles of attack. The presence of the boom reduced the strength of the forebody primary vortices at subsonic and transonic

speeds. At angles of attack beginning at approximately  $30^\circ$ , the wake from the nose boom promoted an asymmetry in the LEX vortex breakdown positions. Reversals of the asymmetry occurred as the angle of attack increased toward maximum lift. The LEX vortices in the presence of the fences were sensitive to the asymmetric flow development near the nose caused by the nose boom, due to their reduced strength and upward displacement toward the boom wake. The ensuing asymmetric rolling moments and yawing moments measured on the wind tunnel model were consistent with the degraded handling qualities experienced in the Navy/McDonnell Douglas flight tests of the F/A-18 with both LEX fences and nose boom. Removal of the nose boom eliminated the adverse flow interaction. It is noted that the production F/A-18 radome does not incorporate a nose boom.

The forebody and LEX surface pressures obtained on the baseline 0.06-scale model in the DTRC 7- by 10-Foot Transonic Tunnel and the Langley 14- by 22-Foot Subsonic Tunnel at the same free-stream Mach number ( $M_\infty = 0.20$ ) and Reynolds number ( $Re_z = 0.96 \times 10^6$ ) were in reasonable agreement up through poststall angles of attack. The differences in the tunnel blockage, free-stream turbulence, model support system, and the proximity of the model nose to the DTRC ceiling at the extreme angles of attack were not sufficient to affect the data repeatability at the low subsonic speeds. Comparison of the 0.06-scale model forebody and LEX pressures with data obtained on a 0.16-scale model tested in the Langley 14- by 22-foot facility at  $Re_z = 0.96 \times 10^6$  and  $M_\infty = 0.08$  revealed large differences. The primary separation occurred earlier on the forebody of the larger scale model, with a consequent increase in the vortex strengths. The signatures of the LEX vortices were also more pronounced on the 0.16-scale F/A-18 model. The differences in the strength of the forebody vortices and their subsequent interaction with the LEX vortical flows may account for the different lateral stability characteristics that the two models have consistently exhibited at angles of attack near maximum lift.

The interpretation of flow visualization results obtained with different illumination and/or particle seeding techniques requires care. The vortical flows on the 0.06-scale model were illuminated by the wind tunnel test section lights, which provided a three-dimensional perspective of the condensation patterns, and by the laser light sheet, which yielded flow-field cross sections. On the baseline F/A-18 model, the two illumination techniques provided similar information. For example, the shear layer instabilities and vortex breakdown that were visible with



the tunnel lighting only were also seen, in greater detail, with the light sheet. The results obtained with the two lighting schemes compared well and, in a straightforward fashion, with the in-flight smoke flow visualizations obtained on the F-18 HARV.

Independent analysis of the flow patterns obtained with the tunnel lighting and the laser light sheet on the model with the LEX fences could lead to conflicting conclusions, however. The vortex flows, made visible by the tunnel lights, expanded downstream of the LEX fences and exhibited what appeared to be a classical vortex breakdown phenomenon. The second corotating vortex was not visible. The laser light sheet revealed two stable vortices that interacted with each other to form a unique cross-flow structure downstream of the LEX fence with the vortex cores defined. This cross flow could easily have been misinterpreted as an expanded burst vortex without the aid of the laser-illuminated cross flows. The smoke injection method employed on the F-18 HARV with LEX fences yielded vortex patterns similar to the wind tunnel observations with the test section lights only. A more detailed description of the in-flight flow field was possible when analyzed along with the laser light-sheet results from the ground-based facility.

The injection of water into the tunnel circuit in sufficient quantity to conduct the laser vapor screen flow visualizations did not affect the forebody and LEX surface pressures or the total forces and moments. This result is of importance to high-angle-of-attack testing, since it supports the simultaneous acquisition of the vapor screen off-body flow-field information and quantitative model measurements.

### Concluding Remarks

A wind tunnel experiment was conducted in the David Taylor Research Center (DTRC) 7- by 10-Foot Transonic Tunnel to improve the understanding and control of the vortical flows about a 0.06-scale model of the F/A-18 at high angles of attack and at subsonic through transonic speeds. Laser vapor screen flow visualizations, model surface static pressures, and six-component forces and moments were obtained at angles of attack from  $10^\circ$  to  $50^\circ$ , free-stream Mach numbers of 0.20 to 0.90, and Reynolds numbers based on the wing mean aerodynamic chord of  $0.96 \times 10^6$  to  $1.75 \times 10^6$ . The model was tested in a baseline configuration and with wing-leading-edge-extension (LEX) upper surface fences and flight test nose boom.

The high Reynolds number behavior of the LEX vortex flows on the F/A-18 aircraft can be simulated at lower Reynolds numbers in the wind tunnel.

The LEX vortices are highly compressible, even at the very low subsonic Mach numbers. The core breakdown location is insensitive to the Mach number, however, until shock waves appear over the wings that interact with the vortex flows.

The F/A-18 forebody vortices are comparatively weak and are dominated by the LEX vortical flows at all Mach numbers. Compressibility effects are not manifested to a significant degree on the forebody until the transonic speeds, where shock-induced boundary-layer separation promotes larger and stronger vortices.

The 0.06-scale model exhibits high levels of lateral stability up to maximum lift at subsonic speeds. A reduction in lateral stability is apparent at the transonic speeds, however, due to a vortex-shock interaction. The high-angle-of-attack directional stability is nonlinear due to the interaction of the burst LEX vortices with the vertical tails.

The LEX fence effectively reduces the vertical tail excitation at high angles of attack by restructuring the LEX vortex. The fence promotes a system of two weaker vortices from the LEX, and their mutual interaction reduces the mean flow velocities and flow angularity at the tails.

The LEX fence does not adversely affect the vortex breakdown behavior and has a minimal impact on the aerodynamic and stability characteristics. Flight experiments of the F-18 airplane corroborate the wind tunnel observations.

A flight test nose boom alters the development of the forebody vortices at the subsonic and transonic speeds. Transition to turbulent flow may occur earlier on the forebody, which promotes smaller and weaker vortices.

The F-18 with LEX fences is susceptible to LEX vortex burst asymmetries at zero sideslip with the nose boom installed. Wind tunnel and flight experiments show that the adverse forebody-LEX flow interaction and the resultant handling qualities degradation are eliminated when the boom is removed.

The analysis of the off-body flow visualizations obtained in the wind tunnel and in flight requires care. The traditional interpretation of vortex core breakdown as a rapid expansion of the vortical region does not apply to the F-18 with LEX fences. The diffused nature of the interacting vortices near the fence resembles a classical breakdown of a single vortex system.

A model scale effect exists in wind tunnel testing of the F/A-18 even when the models are tested in



the same facility at the same nominal value of the Reynolds number. The boundary-layer development on the forebody may be sensitive to the surface finish, trip arrangements, and scale of the free-stream turbulence. These effects could promote significantly different forebody and LEX vortex signatures and corresponding differences in the high-angle-of-attack stability characteristics.

Injection of water into the tunnel circuit in sufficient quantity to promote local condensation in the vortex flow regions about the F/A-18 model

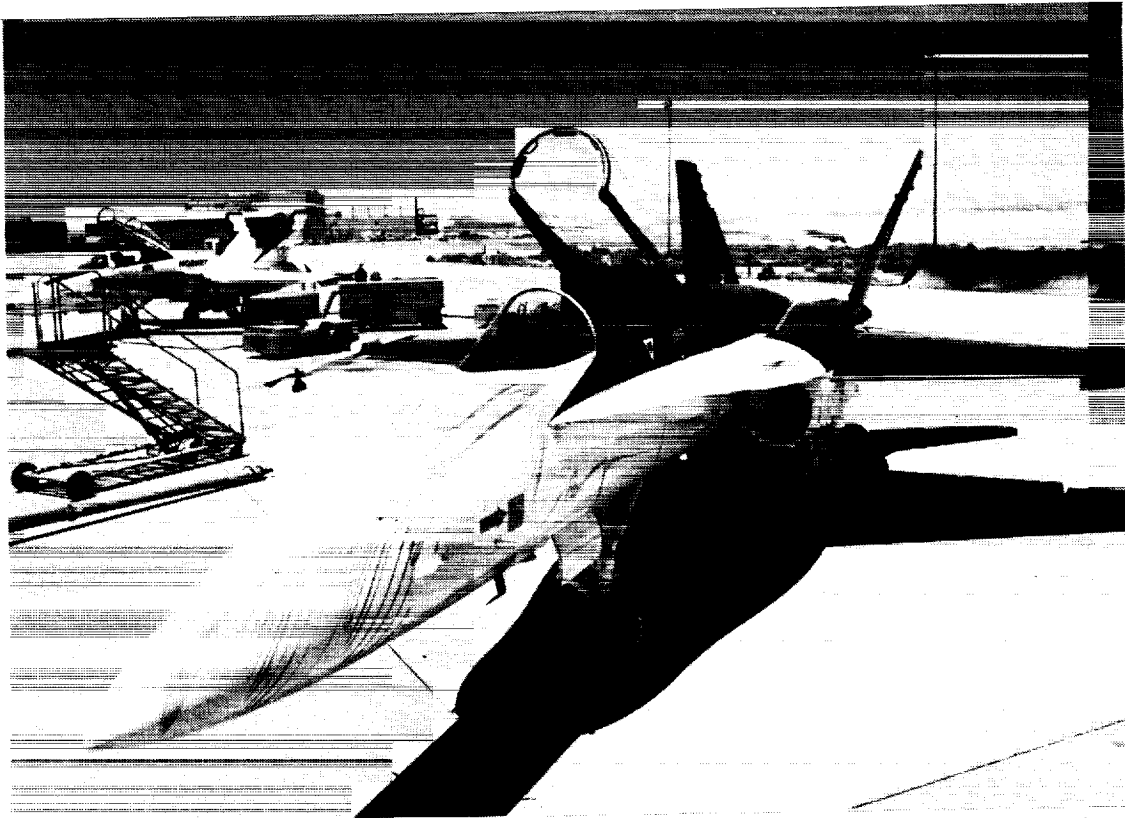
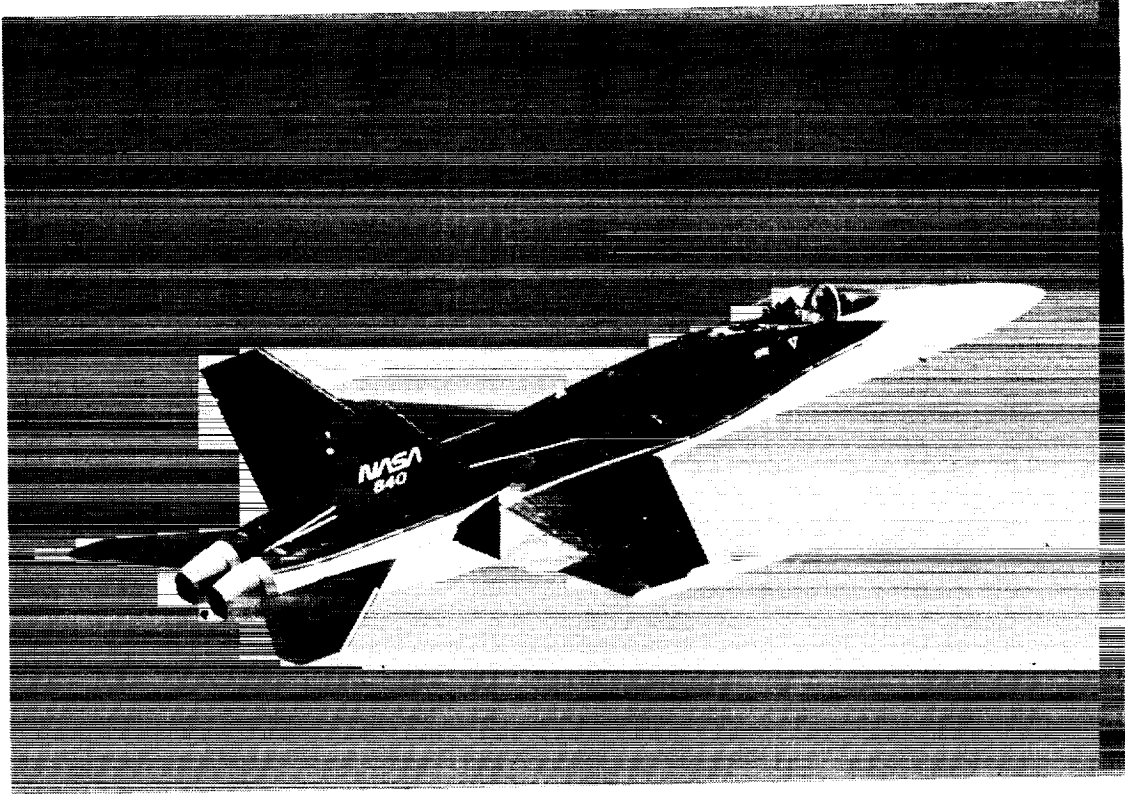
does not adversely affect the quantitative model measurements.

The details that are extracted from the off-body flow visualizations are dependent on the illumination and particle seeding techniques employed. A combination of flow visualization methods can help to ensure the correct interpretation of the vortex-dominated flow fields.

NASA Langley Research Center  
Hampton, VA 23665-5225  
September 30, 1991

## References

1. Fisher, David F.; Richwine, David M.; and Banks, Daniel W.: *Surface Flow Visualization of Separated Flows on the Forebody of an F-18 Aircraft and Wind-Tunnel Model*. NASA TM-100436, 1988.
2. Hall, Robert M.: Influence of Reynolds Number on Forebody Side Forces for 3.5-Diameter Tangent-Ogive Bodies. *A Collection of Technical Papers—AIAA 5th Applied Aerodynamics Conference*, Aug. 1987, pp. 63–73. (Available as AIAA-87-2274.)
3. Frazier, F. Alan: F/A-18 Hornet–LEX Fence Flight Test Results. *1988 Report to the Aerospace Profession – Thirty-Second Symposium Proceedings*, Soc. of Experimental Test Pilots, 1988, pp. 72–89.
4. Schneider, Edward T.; and Meyer, Robert R., Jr.: F-18 High Alpha Research Vehicle Description, Results, and Plans. *1989 Report to the Aerospace Profession – Thirty-Third Symposium Proceedings*, Soc. of Experimental Test Pilots, 1989, pp. 135–162.
5. McGregor, I.: The Vapour-Screen Method of Flow Visualization. *J. Fluid Mech*, vol. 11, pt. 4, Dec. 1961, pp. 481–511.
6. Erickson, Gary E.; Rogers, Lawrence W.; Schreiner, John A.; and Lee, David G.: Subsonic and Transonic Vortex Aerodynamics of a Generic Forebody Strake-Cropped Delta Wing Fighter. AIAA-88-2596, June 1988.
7. Erickson, Gary E.; Rogers, Lawrence W.; Schreiner, John A.; and Lee, David G.: Further Studies of the Subsonic and Transonic Vortex Flow Aerodynamics of a Close-Coupled Forebody-Slender Wing Fighter. AIAA-88-4369, Aug. 1988.
8. ASED Staff: *Transonic Wind-Tunnel Facility at the Naval Ship Research and Development Center*. ASED Rep. 332, David W. Taylor Naval Ship Research and Development Center, June 1975. (Available from DTIC as AD A014 927.)
9. Banks, Daniel W.: Wind-Tunnel Investigation of the Forebody Aerodynamics of a Vortex-Lift Fighter Configuration at High Angles of Attack. *Advanced Aerospace Aerodynamics*, SP-757, Soc. of Automotive Engineers, Inc., Oct. 1988, pp. 101–123. (Available as SAE 881419.)
10. Erickson, Gary E.: *Water Tunnel Flow Visualization and Wind Tunnel Data Analysis of the F/A-18*. NASA CR-165859, 1982.
11. Headley, Jack W.: *Analysis of Wind Tunnel Data Pertaining to High Angle of Attack Aerodynamics*. U.S. Air Force, July 1978.
- Volume I. *Technical Discussion and Analysis of Results*. AFFDL-TR-78-94, Vol. I. (Available from DTIC as AD A069 646.)
- Volume II. *Data Base*. AFFDL-TR-78-94, Vol. II. (Available from DTIC as AD A069 647.)
12. Del Frate, John H.; and Zuniga, Fanny A.: In-Flight Flow Field Analysis on the NASA F-18 High Alpha Research Vehicle With Comparisons to Ground Facility Data. AIAA-90-0231, Jan. 1990.
13. Fisher, David F.; and Meyer, Robert R., Jr.: *Flow Visualization Techniques for Flight Research*. NASA TM-100455, 1988.
14. Payne, F. M.; Ng, T. T.; Nelson, R. C.; and Schiff, L. B.: Visualization and Flow Surveys of the Leading Edge Vortex Structure on Delta Wing Planforms. AIAA-86-0330, Jan. 1986.
15. Squire, L. C.; Jones, J. G.; and Stanbrook, A.: *An Experimental Investigation of the Characteristics of Some Plane and Cambered 65° Delta Wings at Mach Numbers From 0.7 to 2.0*. R. & M. No. 3305, British Aeronautical Research Council, 1963.
16. Campbell, James F.; Chambers, Joseph R.; and Rumsey, Christopher L.: Observation of Airplane Flow Fields by Natural Condensation Effects. AIAA-88-0191, Jan. 1988.
17. Ghaffari, Farhad; Luckring, James M.; Thomas, James L.; and Bates, Brent L.: Navier-Stokes Solutions About the F/A-18 Forebody-LEX Configuration. AIAA-89-0338, Jan. 1989.
18. Küchemann, D.: *The Aerodynamic Design of Aircraft*. Pergamon Press Inc., c.1978.
19. Fisher, David F.; Banks, Daniel W.; and Richwine, David M.: F-18 High Alpha Research Vehicle Surface Pressures: Initial In-Flight Results and Correlation With Flow Visualization and Wind-Tunnel Data. *A Collection of Technical Papers, Part 1—AIAA 8th Applied Aerodynamics Conference*, Aug. 1990, pp. 421–451. (Available as AIAA-90-3018-CP.)
20. Lorincz, Dale J.: *A Water Tunnel Flow Visualization Study of the F-15*. NASA CR-144878, 1978.
21. Erickson, Gary E.; Schreiner, John A.; and Rogers, Lawrence W.: On the Structure, Interaction, and Breakdown Characteristics of Slender Wing Vortices at Subsonic, Transonic, and Supersonic Speeds. AIAA-89-3345, Aug. 1989.



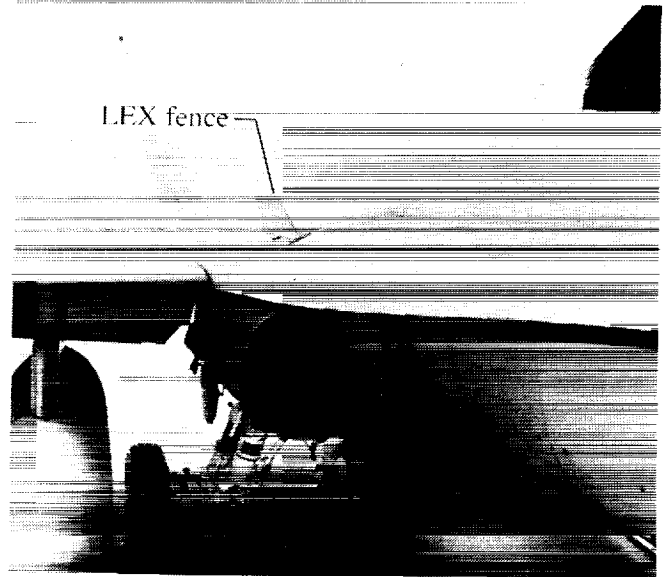
L-91-65

Figure 1. NASA F-18 High-Alpha Research Vehicle.

ORIGINAL PAGE  
BLACK AND WHITE PHOTOGRAPH



(a) Top view of F-18.



(b) Close-up of LEX.



(c) Carrier landing of F/A-18.

Figure 2. Navy fleet airplanes with LEX fences.

L-91-66

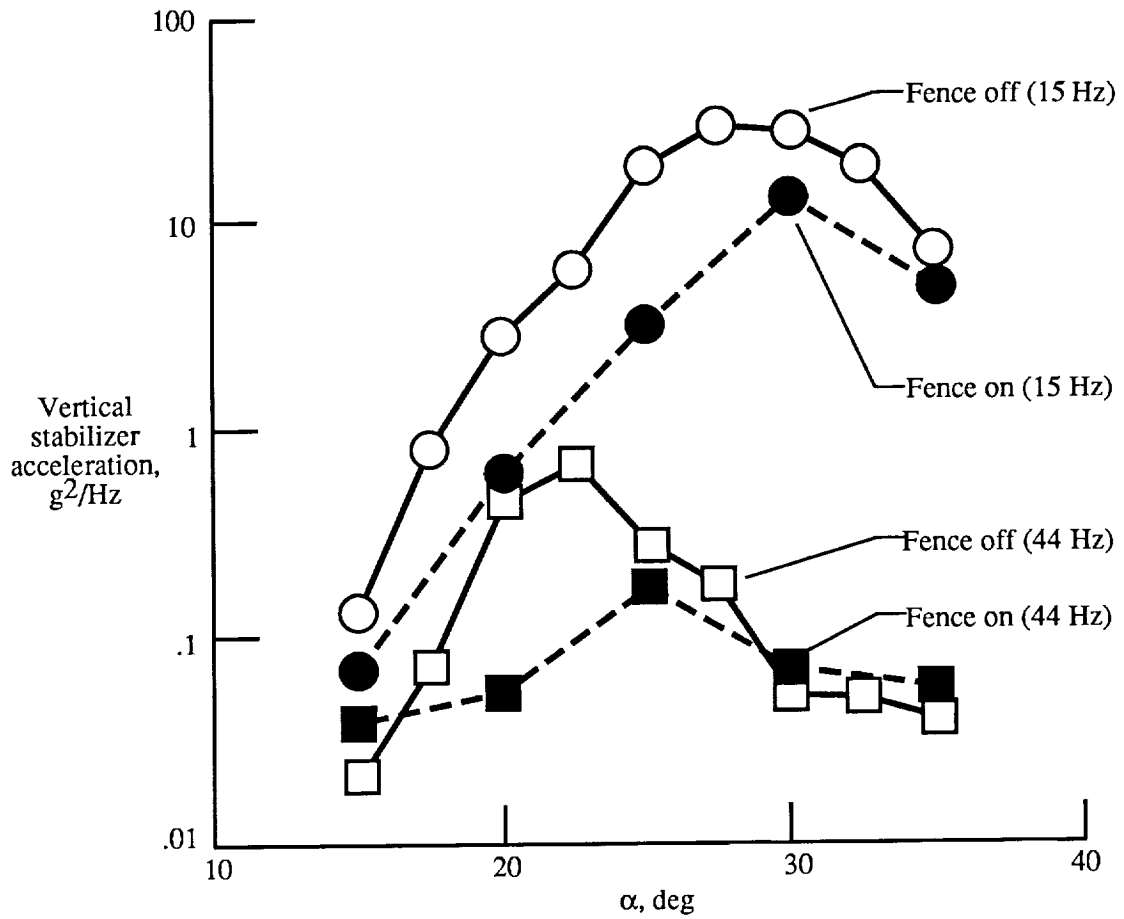


Figure 3. Effect of LEX fence on vertical tail buffet (from ref. 4).

Reference dimensions
$S = 400 \text{ ft}^2$ (1.440 $\text{ft}^2$ )
$b = 37.417 \text{ ft}$ (2.245 $\text{ft}$ )
$\bar{c} = 11.517 \text{ ft}$ (0.691 $\text{ft}$ )
c.g. = 25% $\bar{c}$

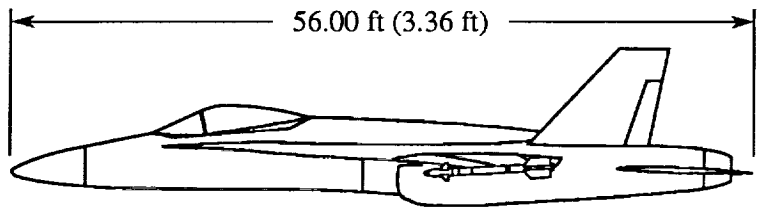
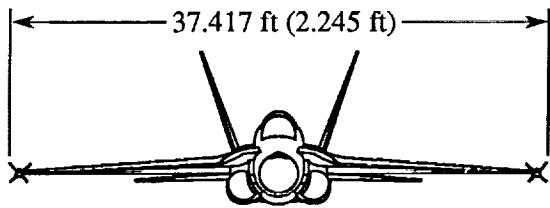
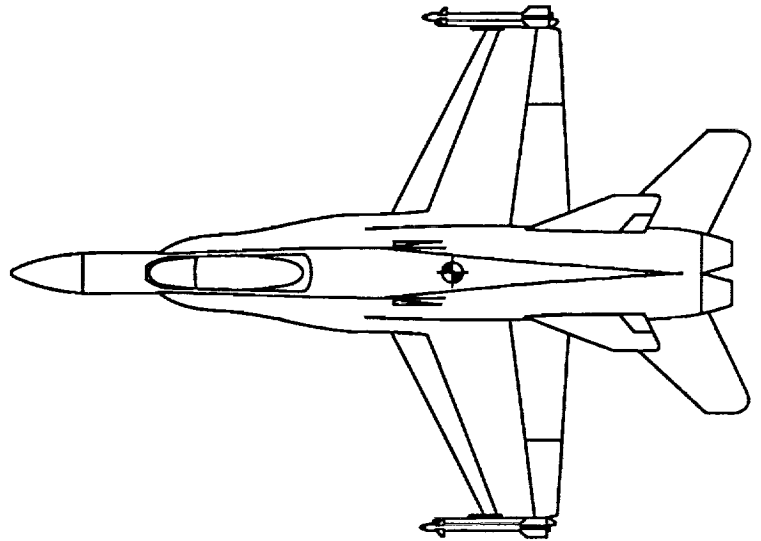


Figure 4. F/A-18 geometry details. Dimensions are in feet full scale (0.06 scale).

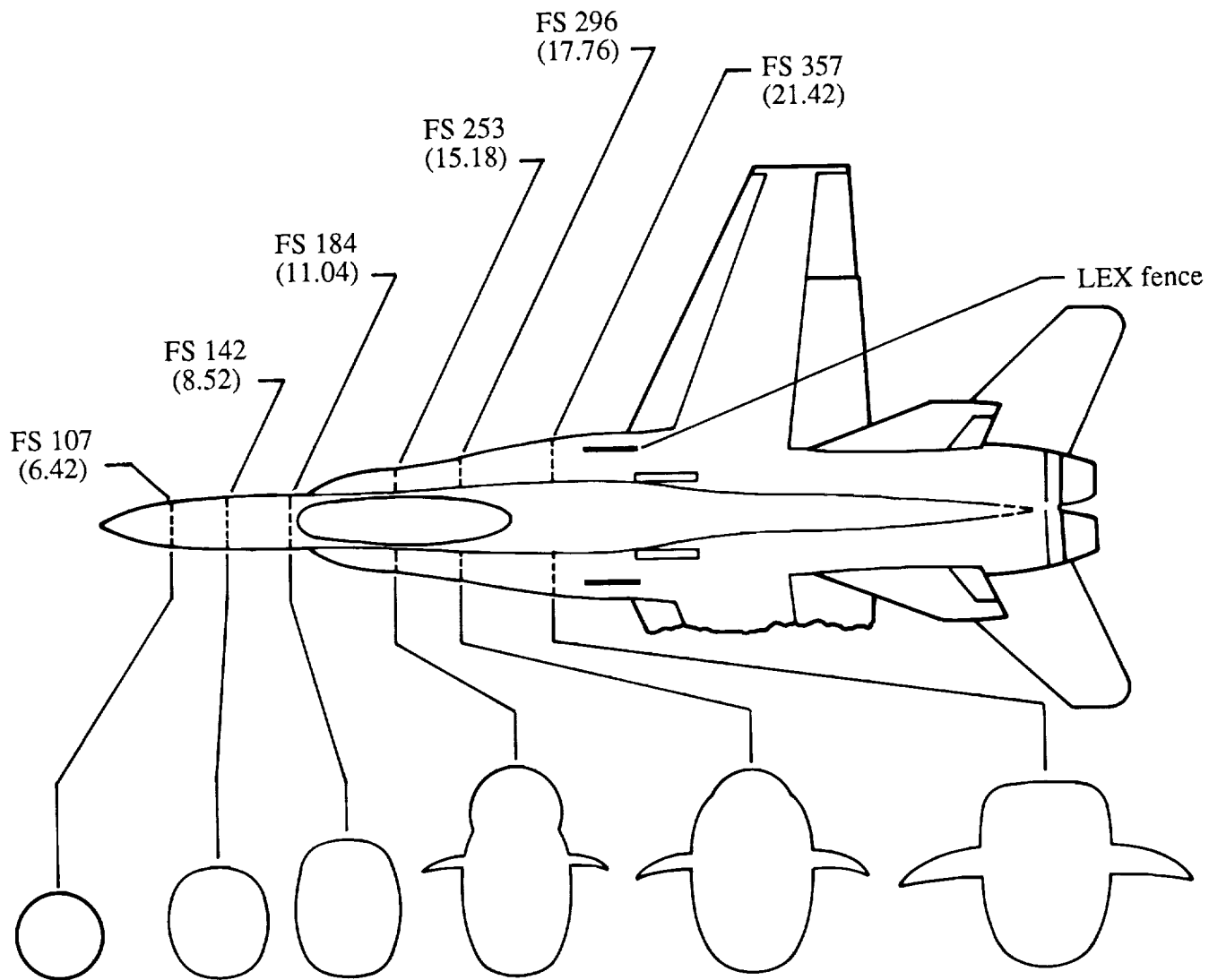
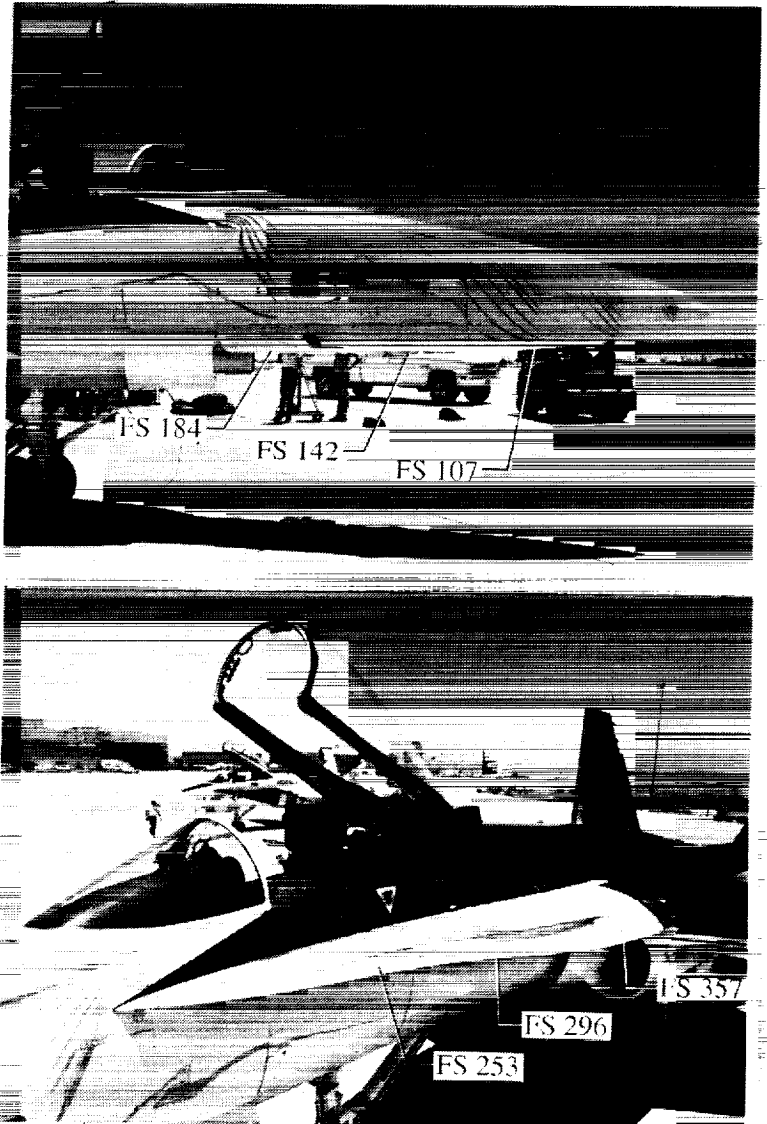
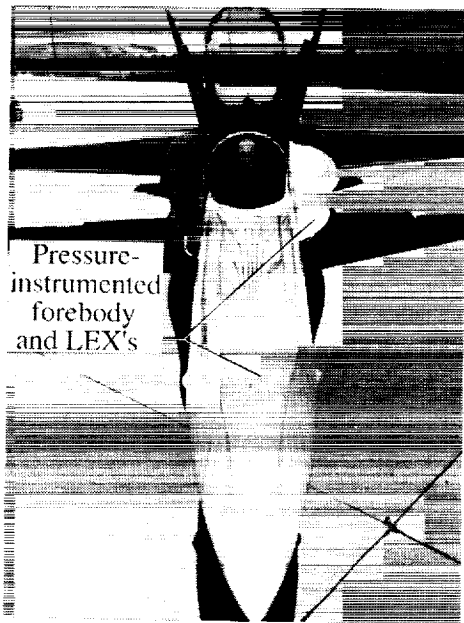


Figure 5. Wind tunnel model forebody and LEX pressure measurement stations. Dimensions are in inches full scale (0.06 scale).

ORIGINAL PAGE  
BLACK AND WHITE PHOTOGRAPH



L-91-67

Figure 6. Forebody and LEX pressure measurement stations on F-18 HARV. Dimensions are in inches full scale.



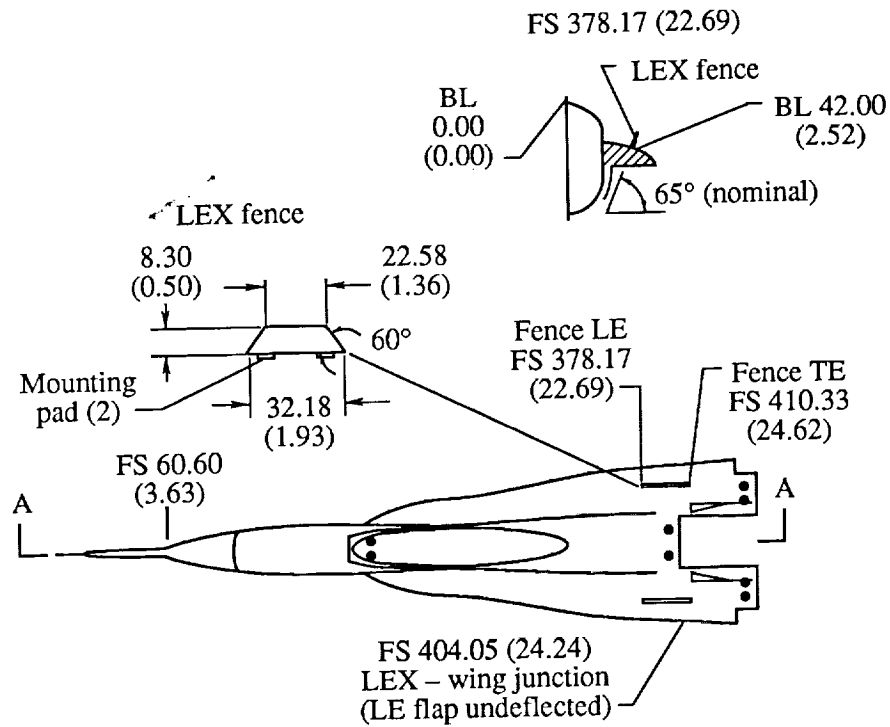


Figure 7. Details of LEX fences on forward fuselage component. Dimensions are in inches full scale (0.06 scale).

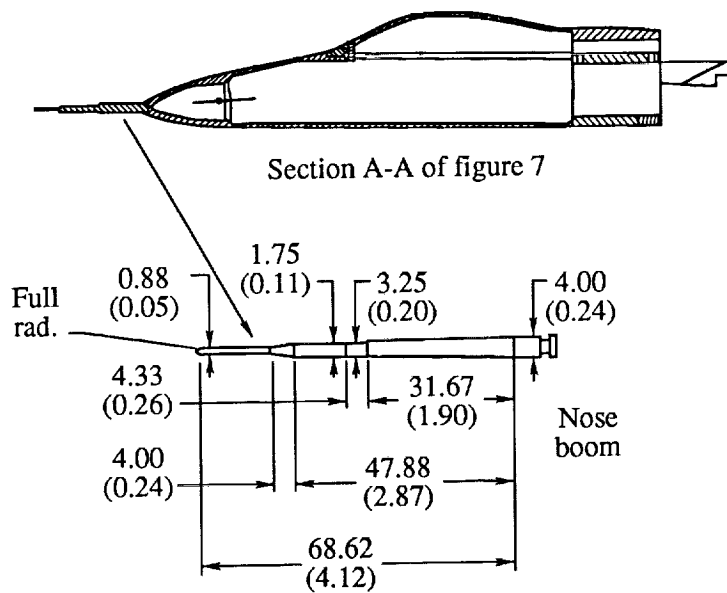
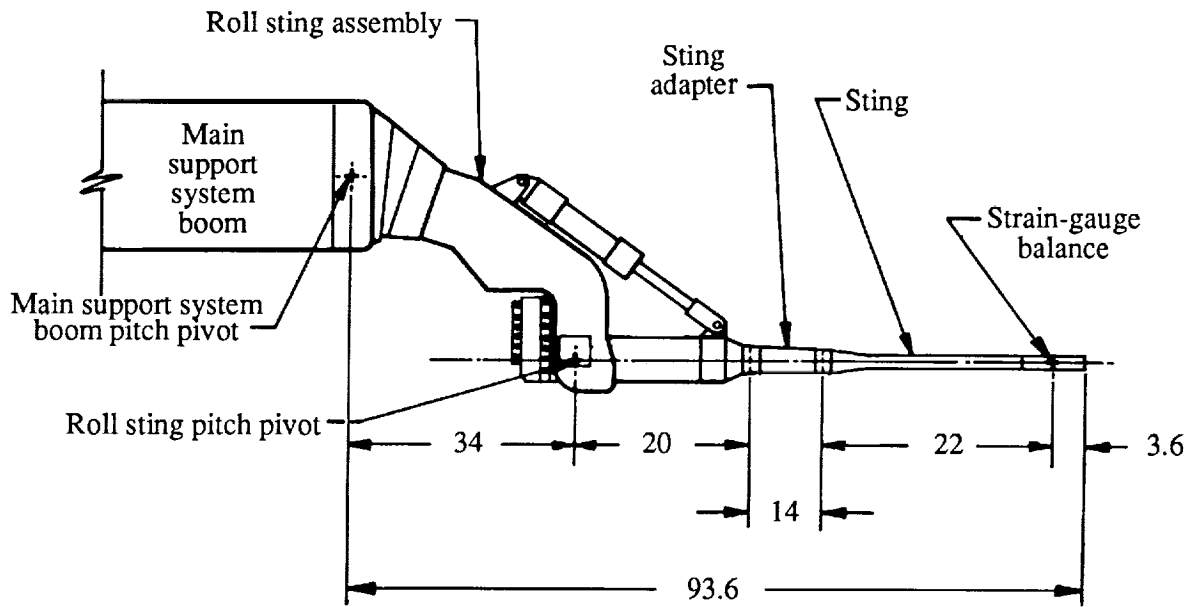


Figure 8. Flight test nose boom geometry details. Dimensions are in inches full scale (0.06 scale).



ORIGINAL PAGE  
BLACK AND WHITE PHOTOGRAPH



Figure 9. DTRC roll sting arrangement used for high-angle-of-attack testing. Dimensions are in inches.

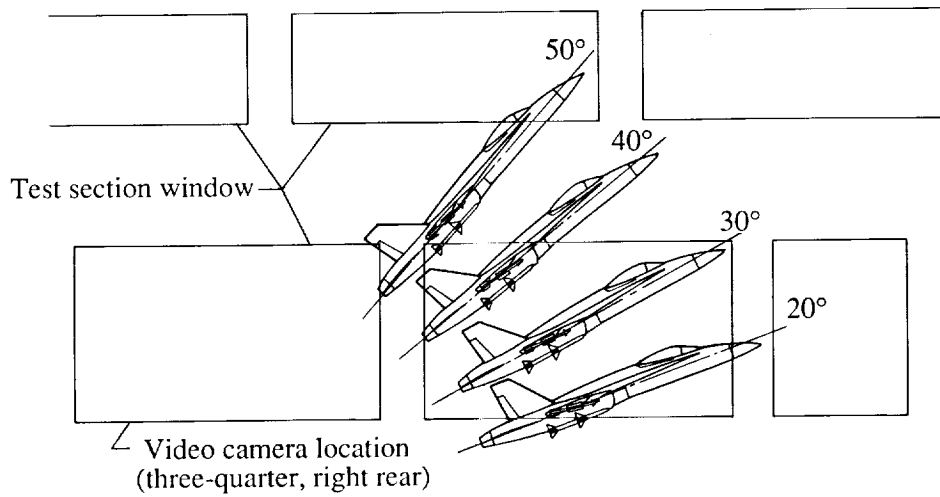


Figure 10. Model movement through test section at selected angles of attack.

ORIGINAL PAGE  
BLACK AND WHITE PHOTOGRAPH

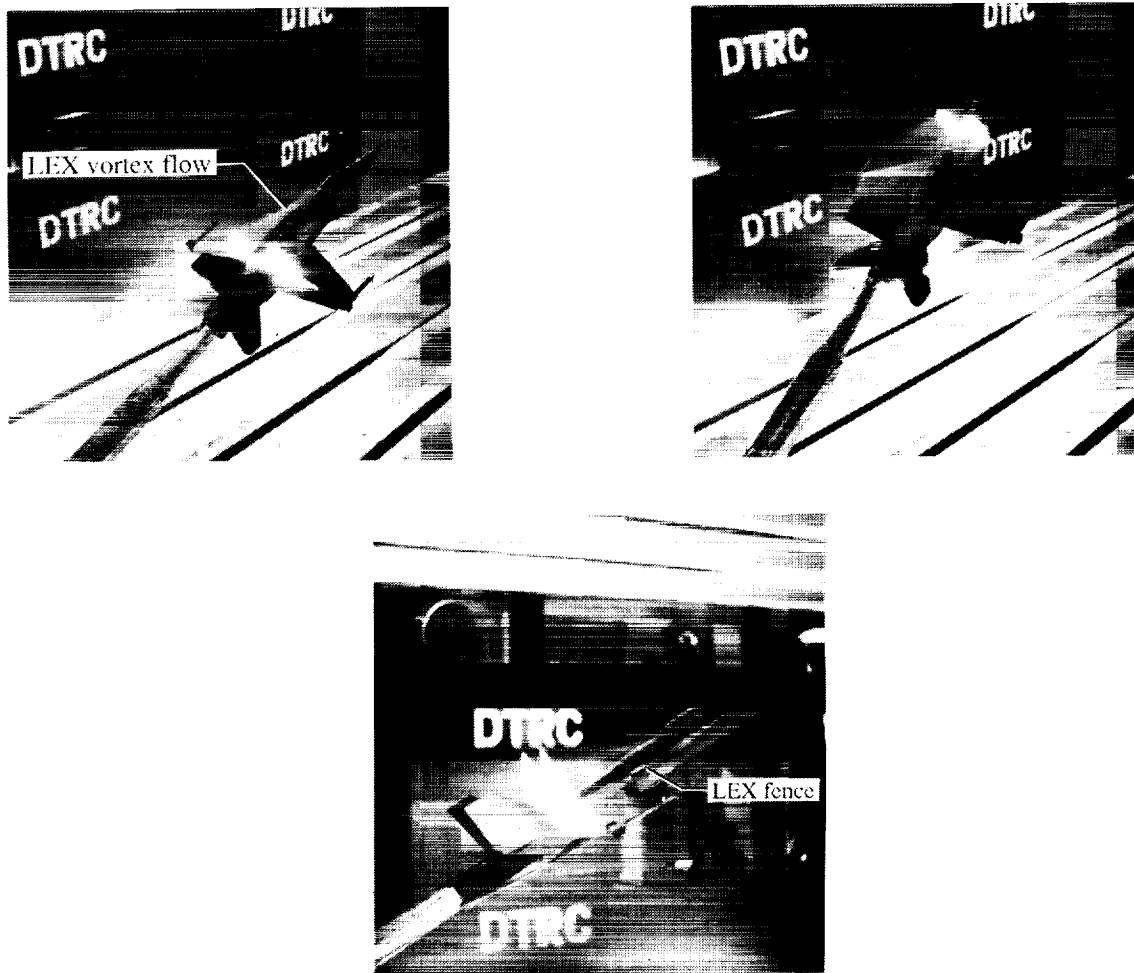
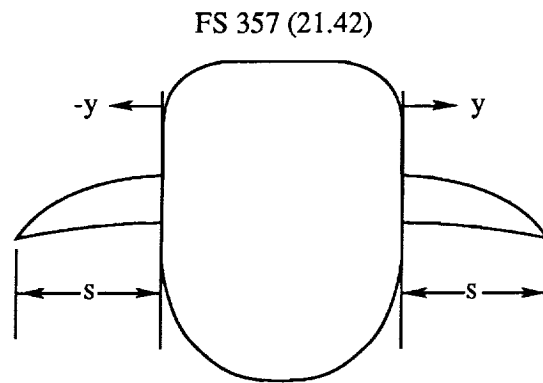
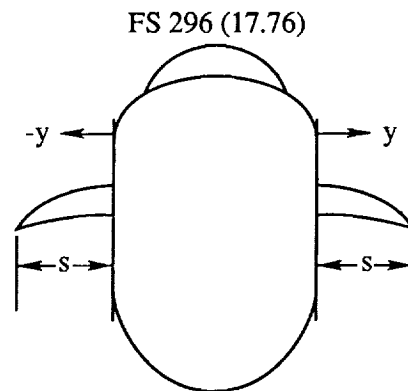
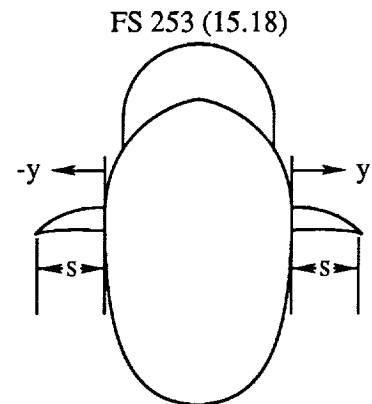
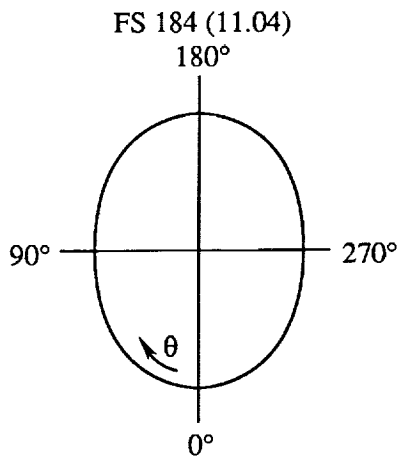
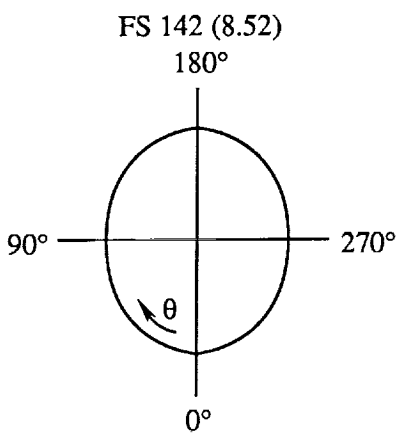
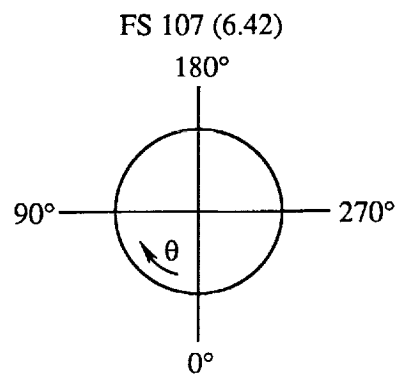


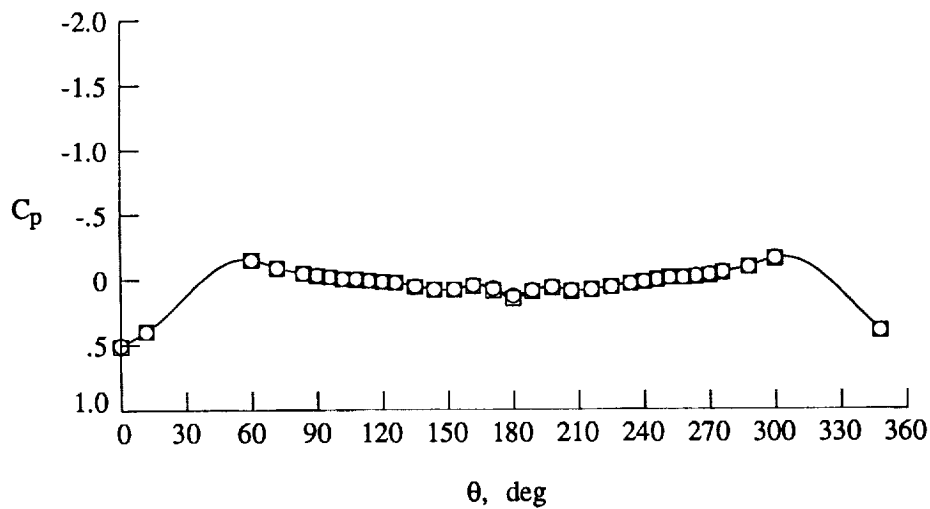
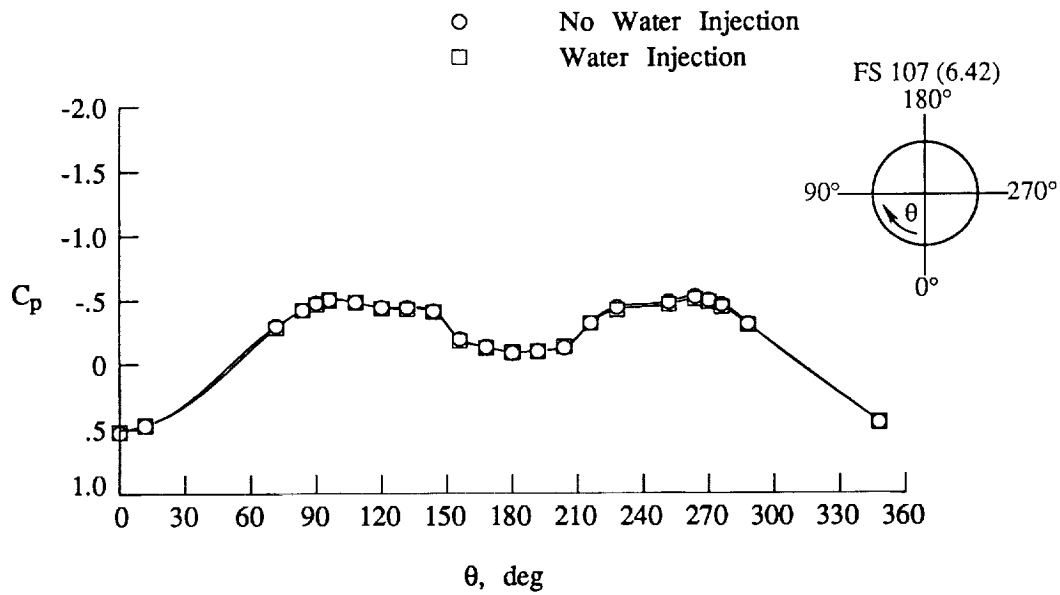
Figure 11. Sting-mounted 0.06-scale F/A-18 model in the DTRC 7- by 10-Foot Transonic Tunnel.



(a) Forebody angular position.

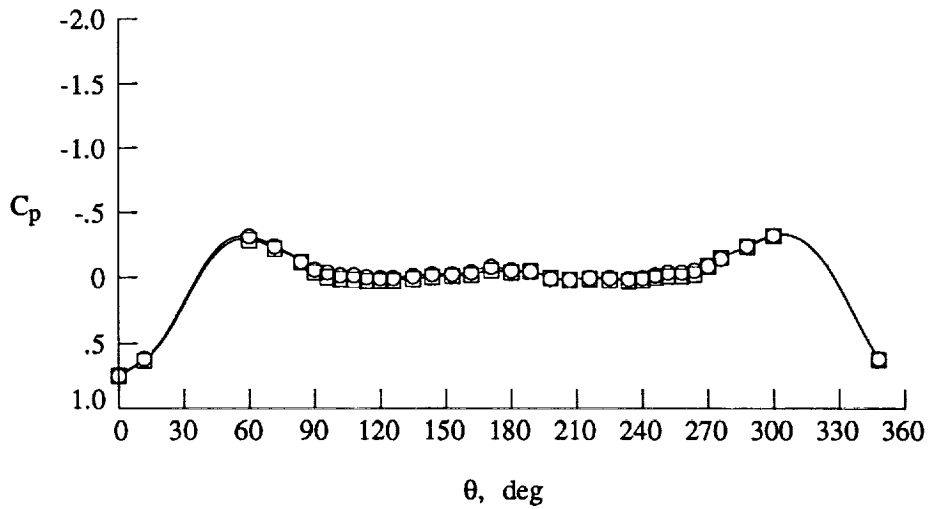
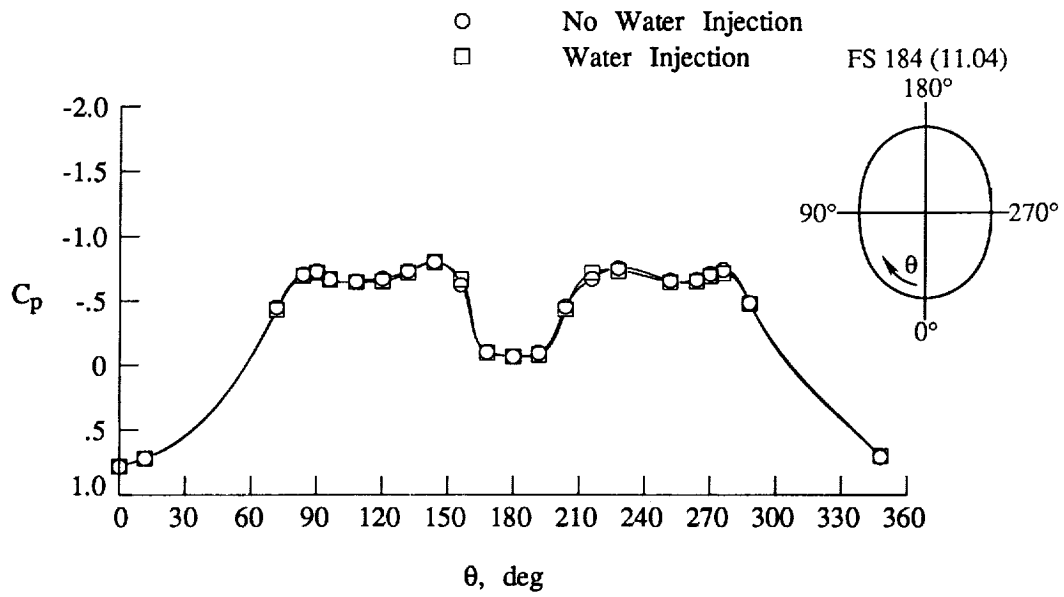
(b) LEX spanwise position.

Figure 12. Forebody and LEX surface static pressure orifice orientations. Dimensions are in inches full scale (0.06 scale).



(a) FS 107 (6.42);  $\alpha = 30^\circ$ .

Figure 13. Forebody surface pressures with and without water injection at  $M_\infty = 0.90$  and  $Re_c = 1.02 \times 10^6$ . Dimensions are in inches full scale (0.06 scale).



(b) FS 184 (11.04);  $\alpha = 40^\circ$ .

Figure 13. Concluded.

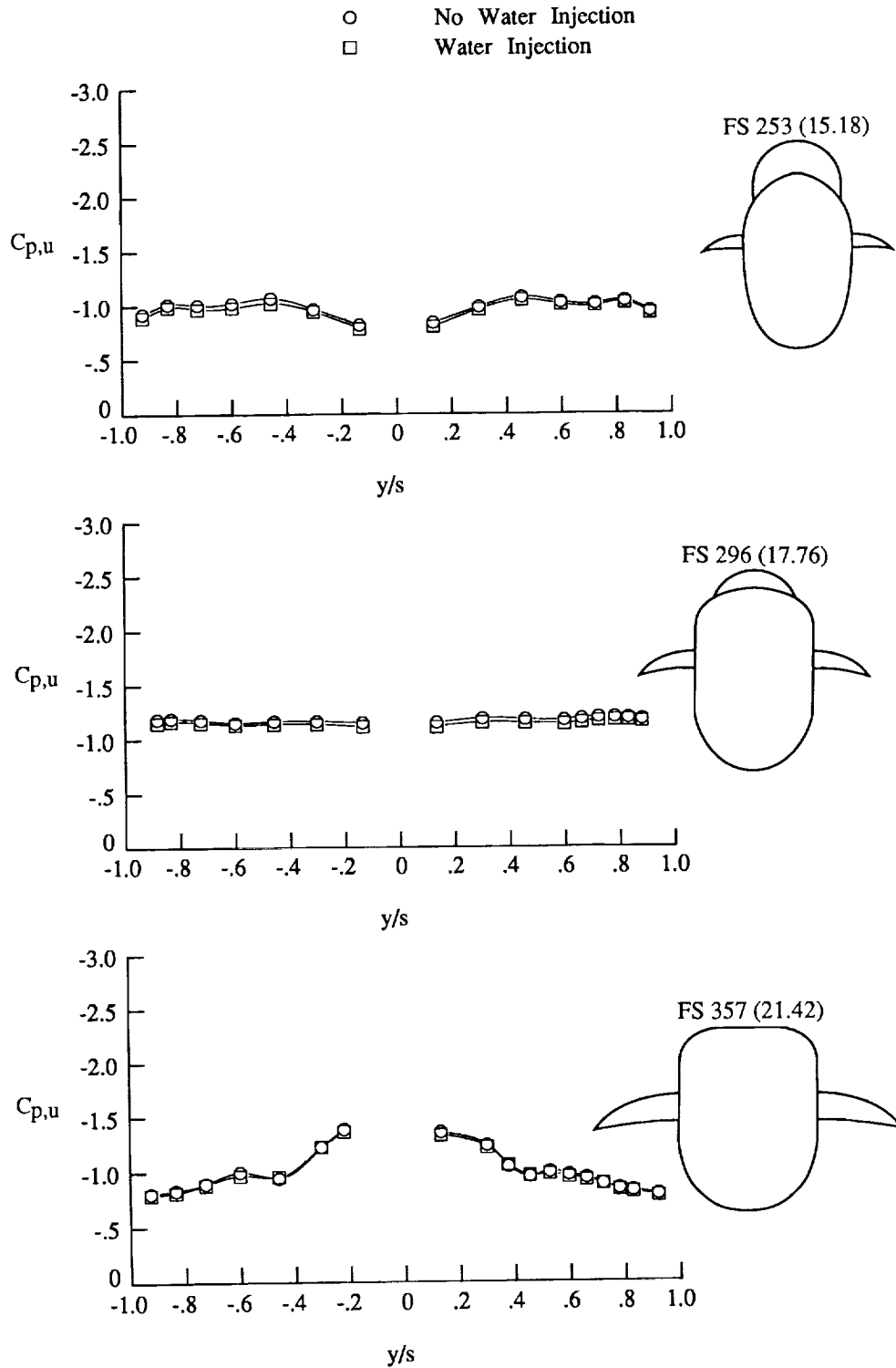
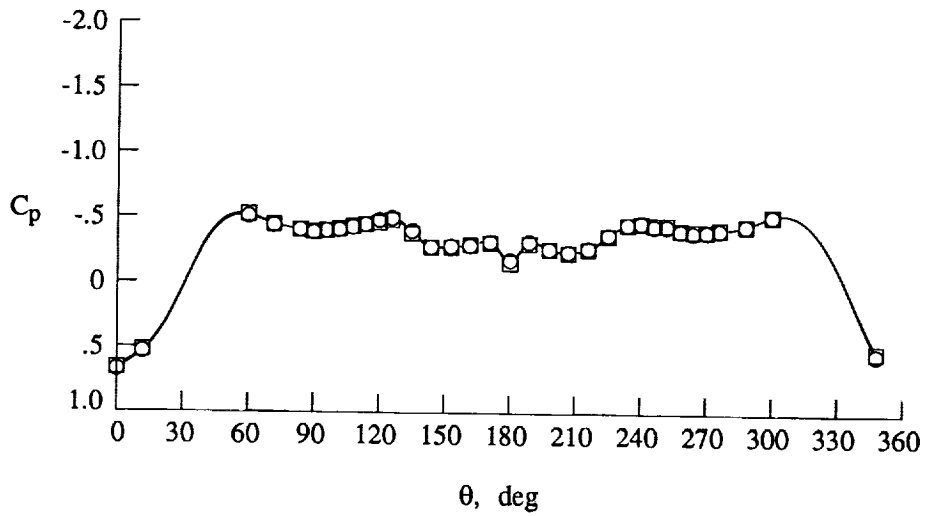
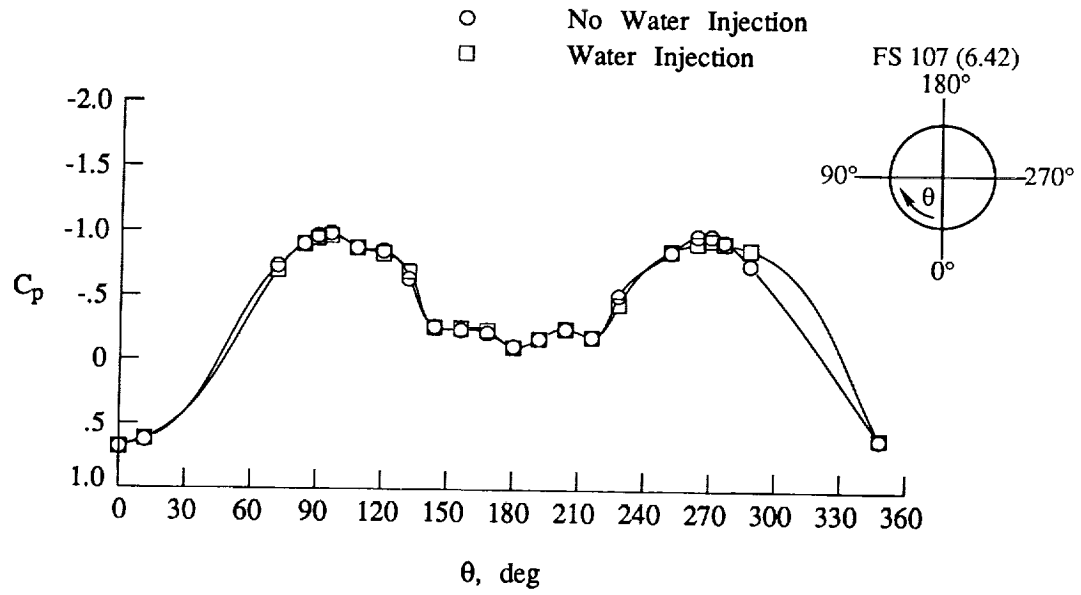


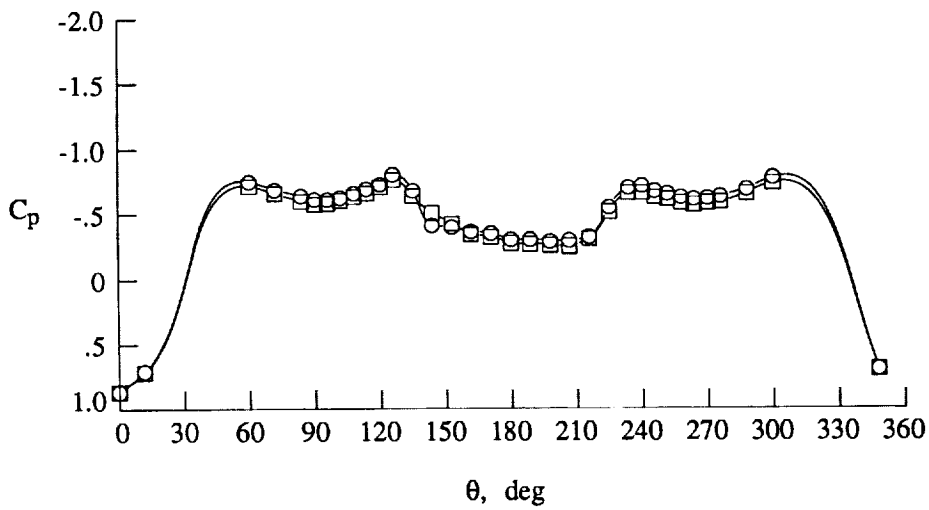
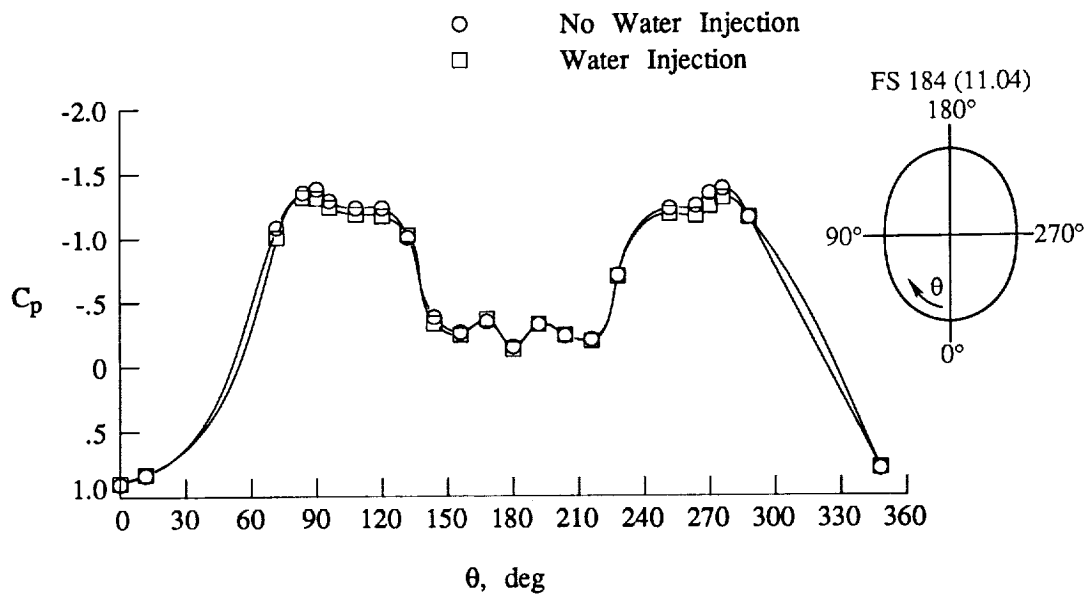
Figure 14. LEX surface pressures with and without water injection at  $M_\infty = 0.90$ ,  $Re_c = 1.02 \times 10^6$ , and  $\alpha = 30^\circ$ . Dimensions are in inches full scale (0.06 scale).



(a) FS 107 (6.42);  $\alpha = 40^\circ$ .

Figure 15. Forebody surface pressures with and without water injection at  $M_\infty = 0.60$  and  $Re_\xi = 1.32 \times 10^6$ . Dimensions are in inches full scale (0.06 scale).





(b) FS 184 (11.04);  $\alpha = 50^\circ$ .

Figure 15. Concluded.

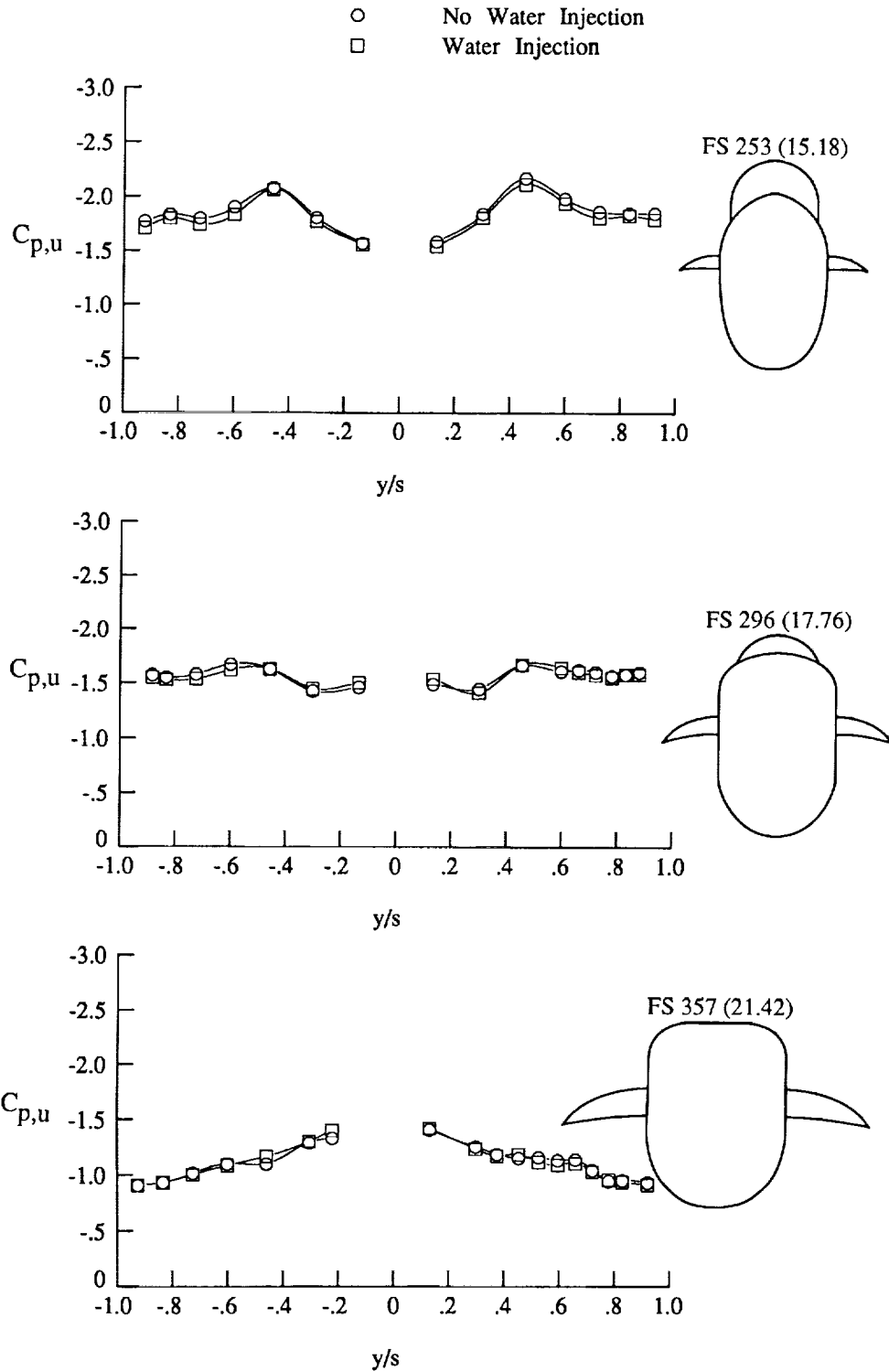


Figure 16. LEX surface pressures with and without water injection at  $M_\infty = 0.60$ ,  $Re_c = 1.32 \times 10^6$ , and  $\alpha = 40^\circ$ . Dimensions are in inches full scale (0.06 scale).

	$M_\infty$	Tunnel	Configuration
○	0.20	DTRC 7 × 10	0.06-scale F/A-18
□	0.20	LaRC 14 × 22	0.06-scale F/A-18

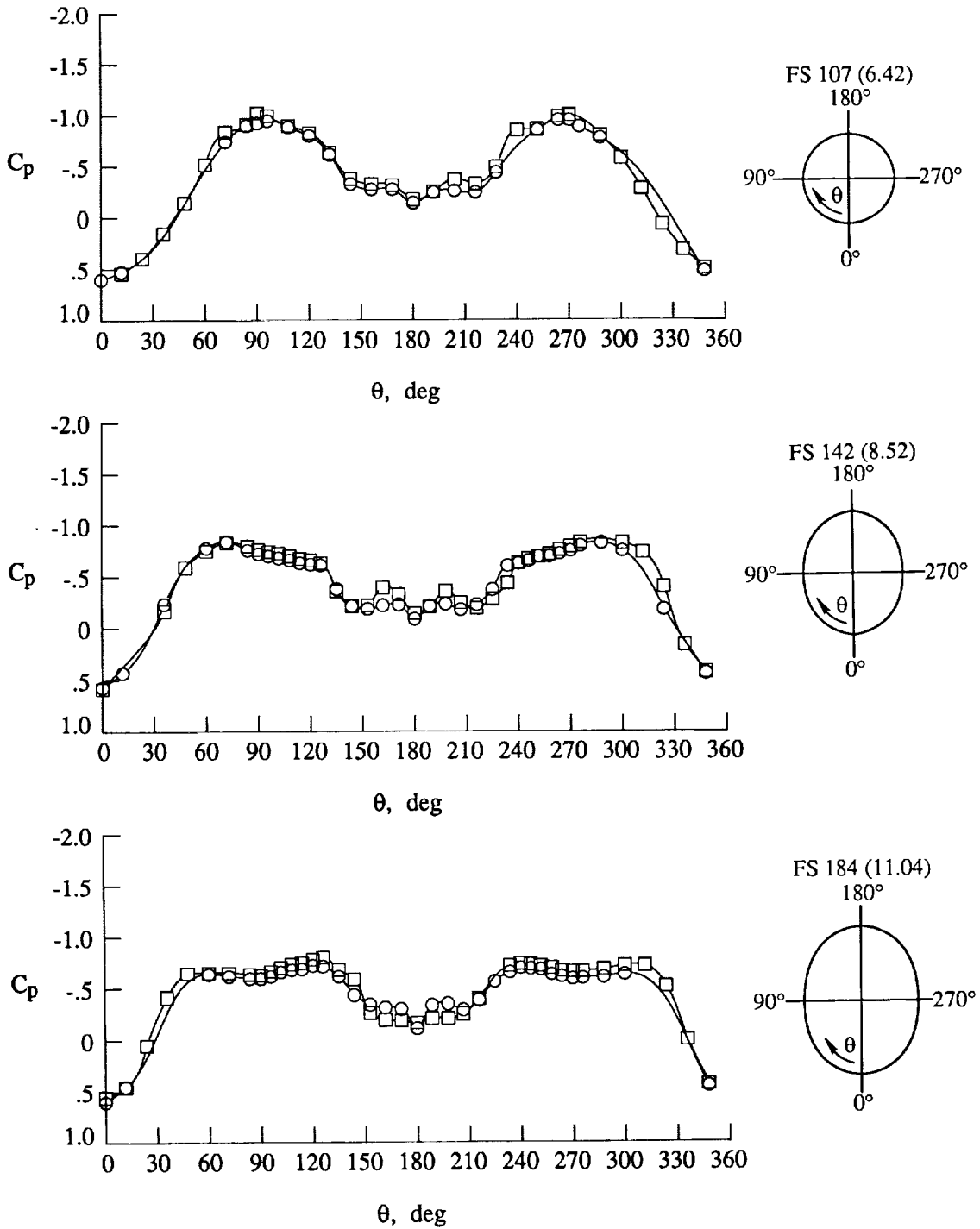


Figure 17. Forebody surface static pressures on 0.06-scale F/A-18 model at  $M_\infty = 0.20$ ,  $Re_z = 0.96 \times 10^6$ , and  $\alpha = 40^\circ$ . Dimensions are in inches full scale (0.06 scale).

	$M_\infty$	Tunnel	Configuration
○	0.20	DTRC 7 × 10	0.06-scale F/A-18
□	0.20	LaRC 14 × 22	0.06-scale F/A-18

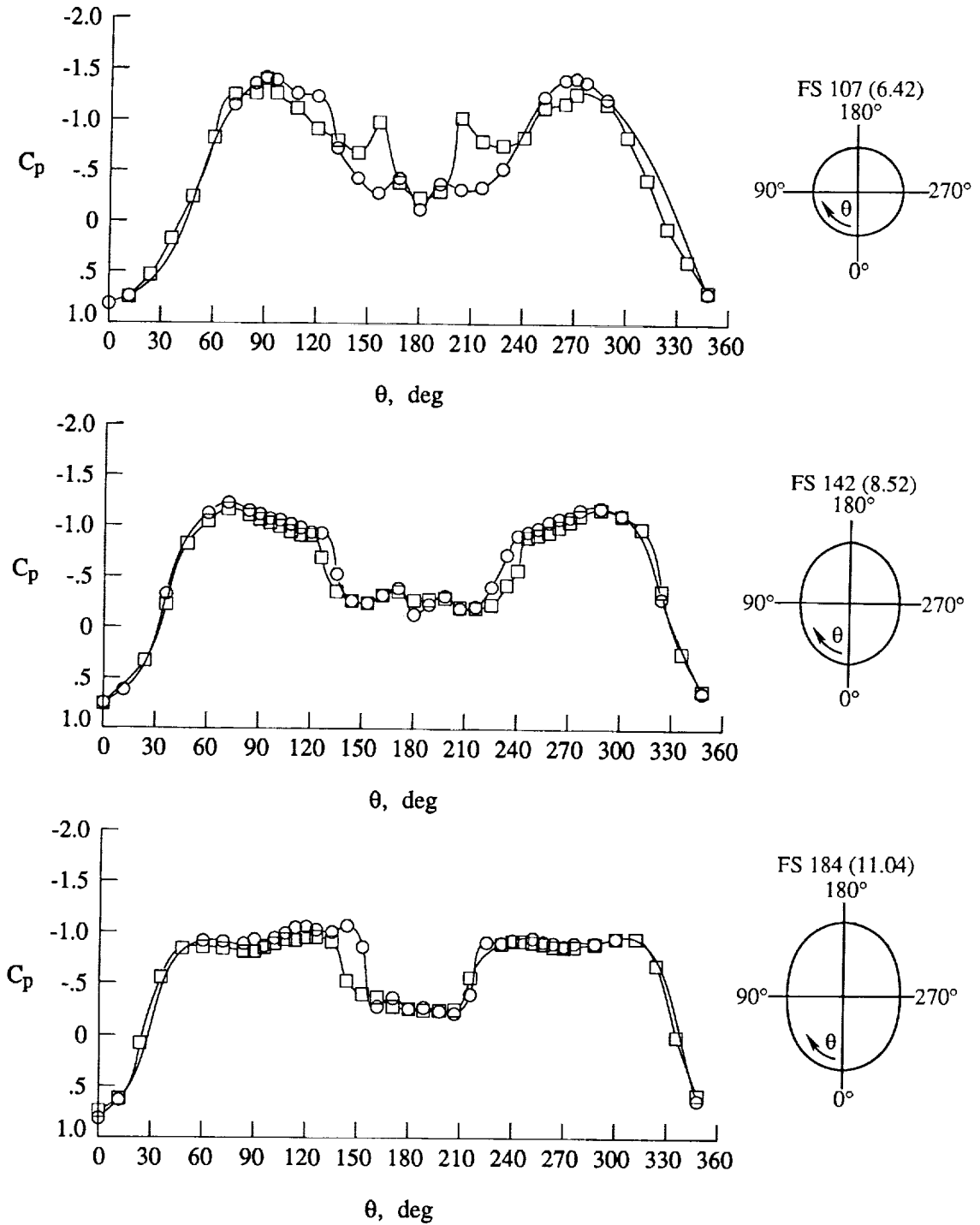


Figure 18. Forebody surface static pressures on 0.06-scale F/A-18 model at  $M_\infty = 0.20$ ,  $Re_c = 0.96 \times 10^6$ , and  $\alpha = 50^\circ$ . Dimensions are in inches full scale (0.06 scale).

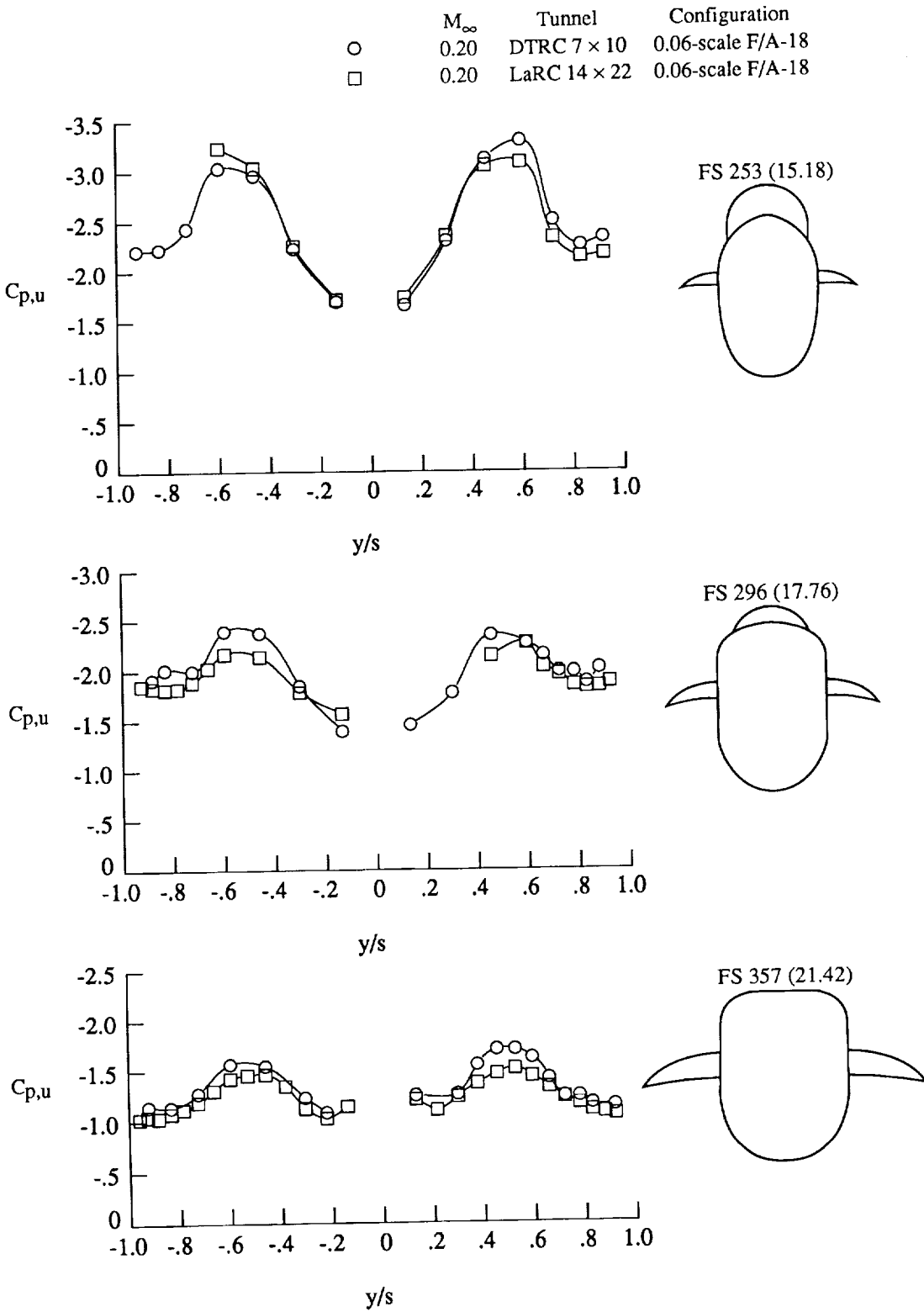


Figure 19. LEX surface pressures on 0.06-scale F/A-18 model at  $M_\infty = 0.20$ ,  $Re_c = 0.96 \times 10^6$ , and  $\alpha = 40^\circ$ . Dimensions are in inches full scale (0.06 scale).

	$M_\infty$	Tunnel	Configuration
○	0.20	DTRC 7 × 10	0.06-scale F/A-18
□	0.08	LaRC 14 × 22	0.16-scale F/A-18

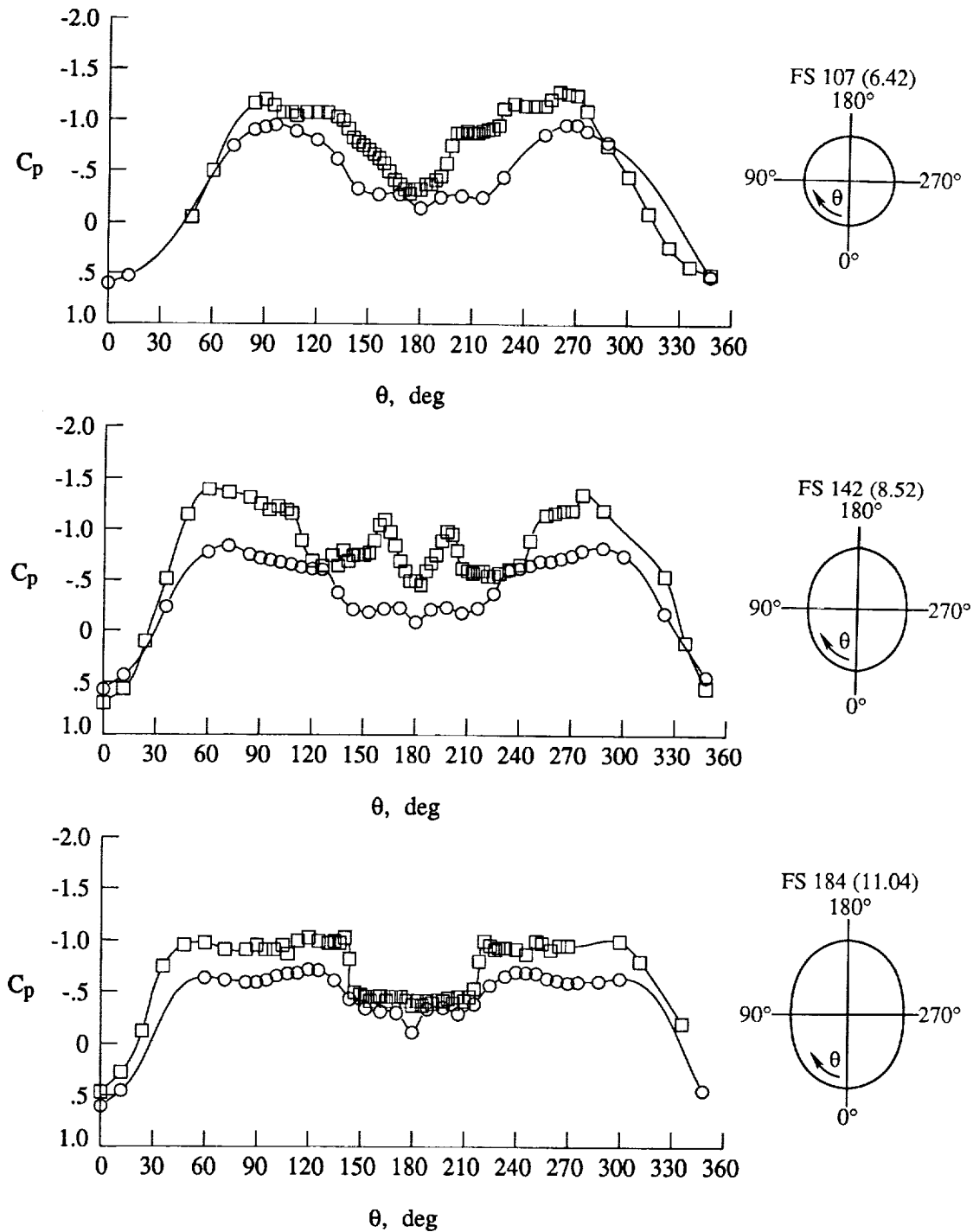


Figure 20. Forebody surface pressures on 0.06- and 0.16-scale F/A-18 models at  $\alpha = 40^\circ$  and  $Re_c = 0.96 \times 10^6$ . Dimensions are in inches full scale (0.06 scale).

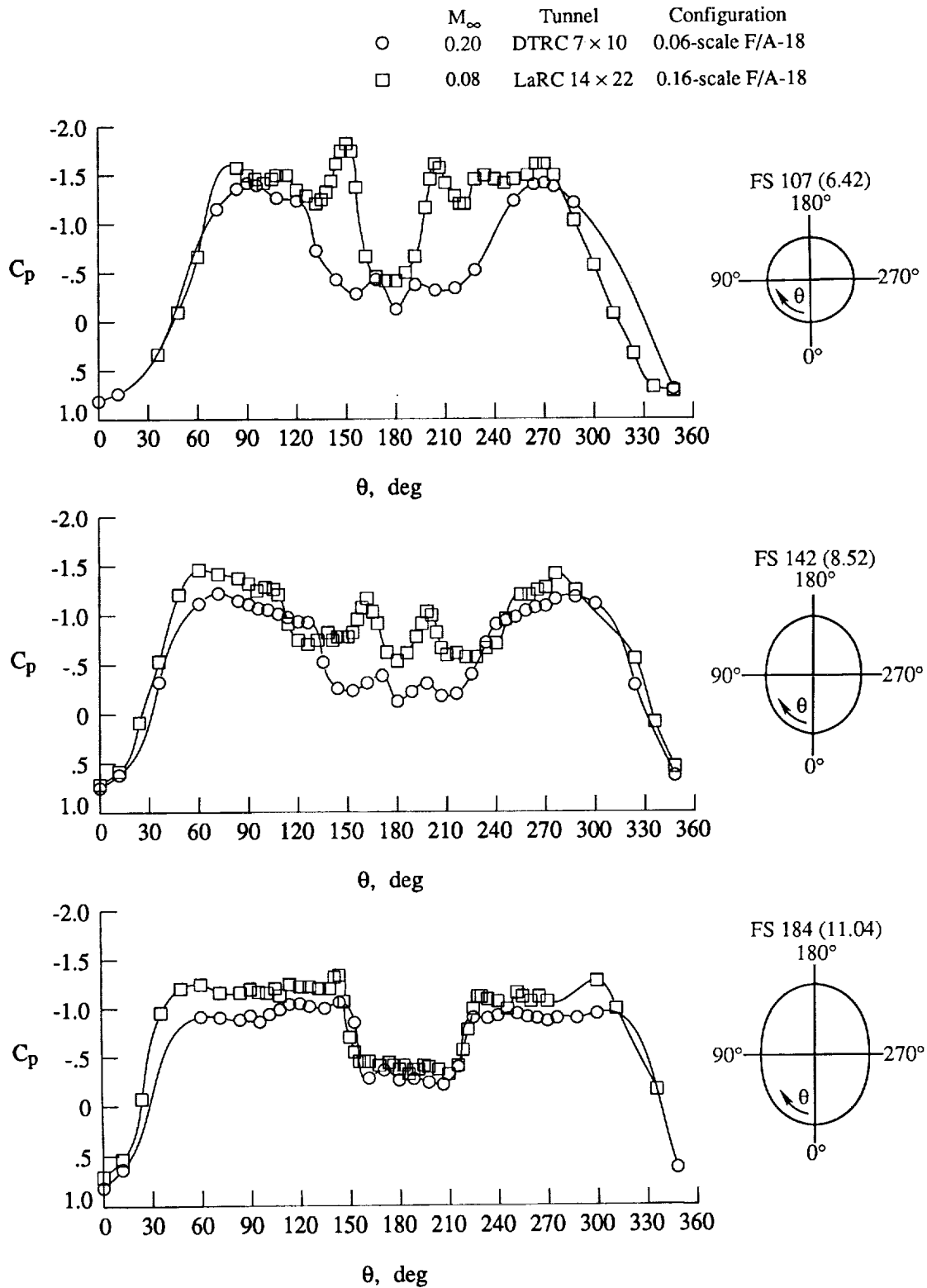


Figure 21. Forebody surface pressures on 0.06- and 0.16-scale F/A-18 models at  $\alpha = 50^\circ$  and  $Re_{\bar{c}} = 0.96 \times 10^6$ . Dimensions are in inches full scale (0.06 scale).

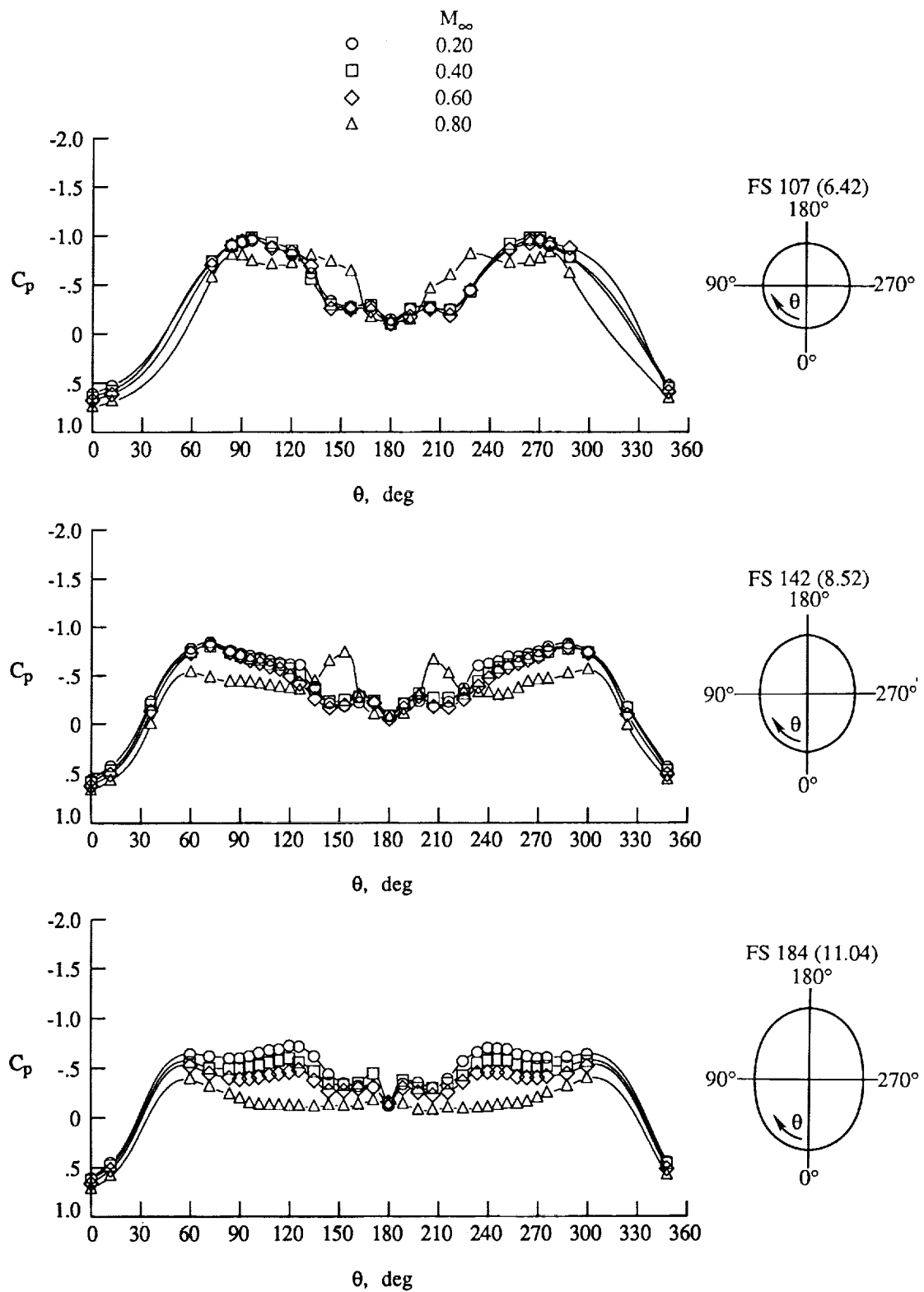


Figure 22. Effect of Mach number on 0.06-scale F/A-18 model forebody surface pressures at  $\alpha = 40^\circ$ . Dimensions are in inches full scale (0.06 scale).



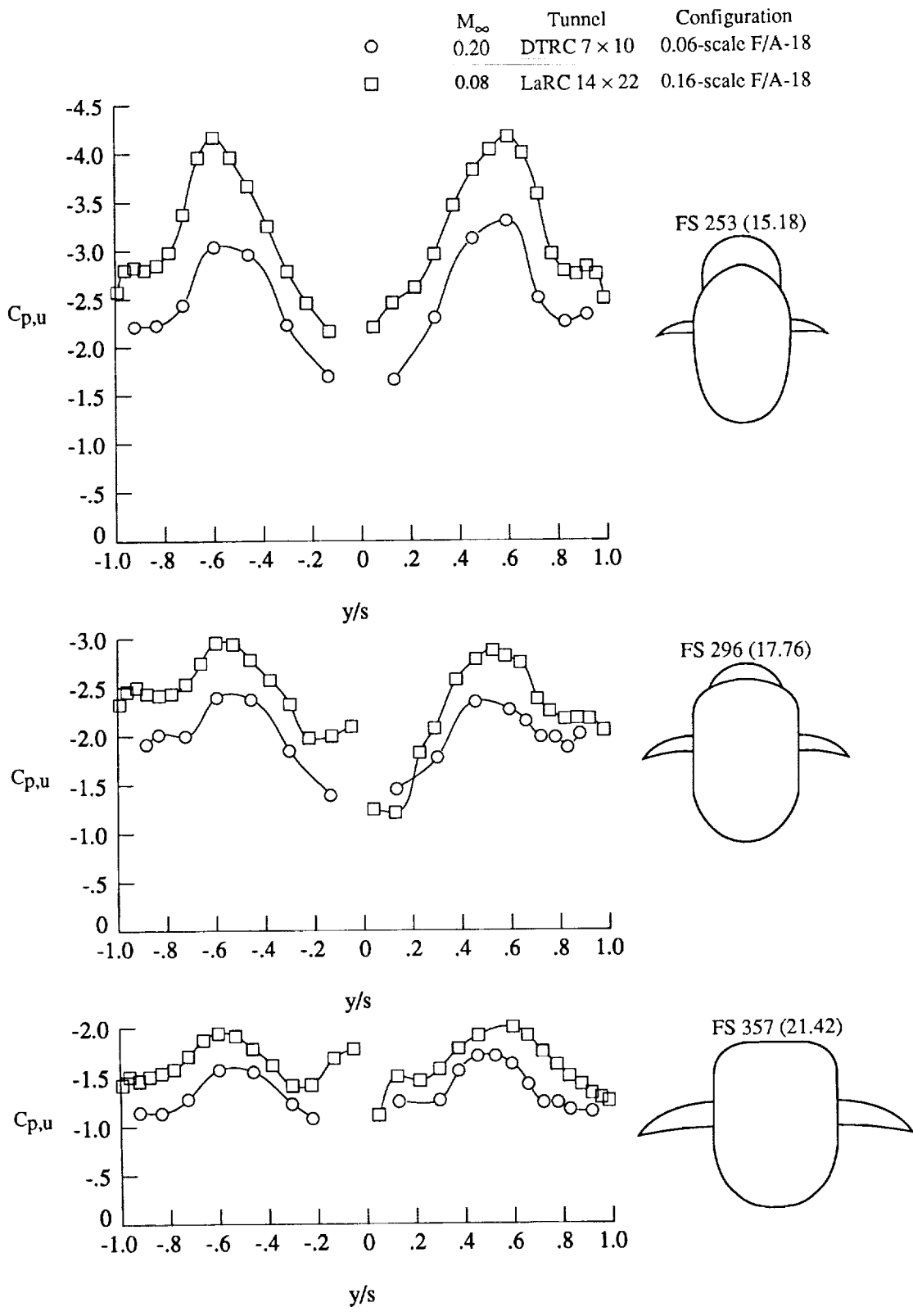
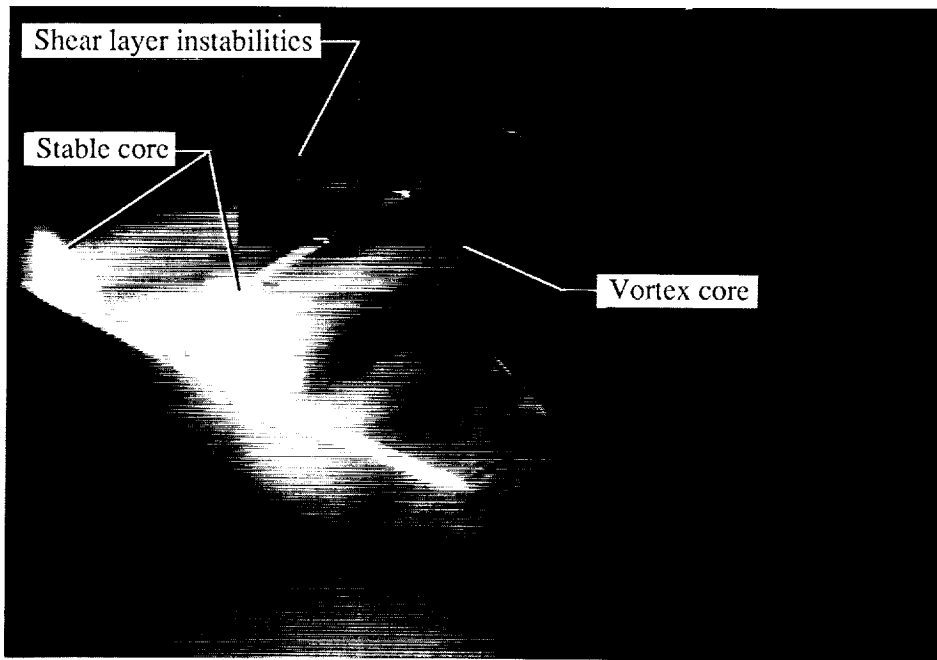
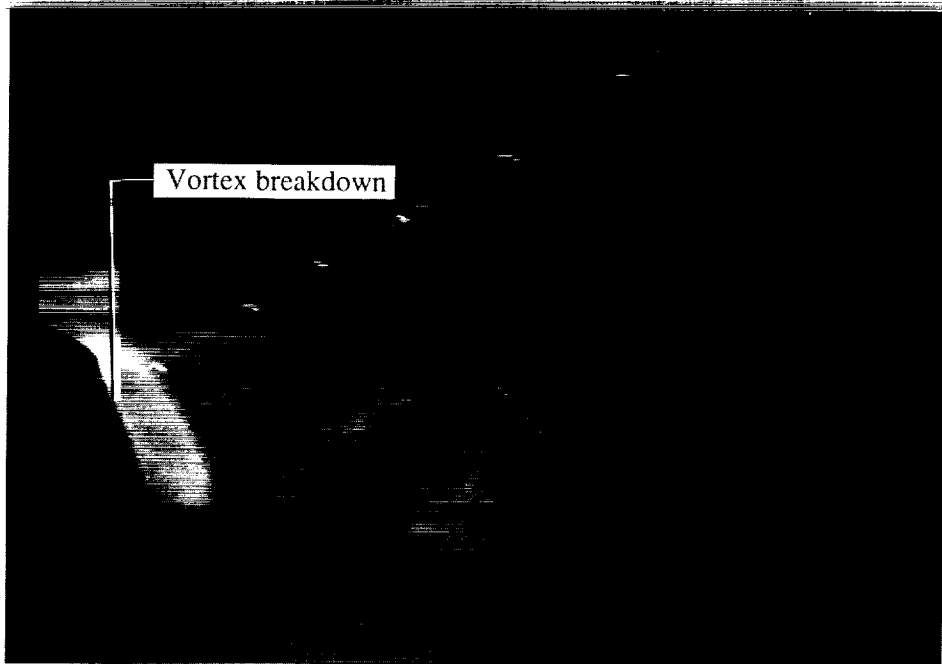


Figure 23. LEX surface pressures on 0.06- and 0.16-scale F/A-18 models at  $\alpha = 40^\circ$  and  $Re_z = 0.96 \times 10^6$ . Dimensions are in inches full scale (0.06 scale).

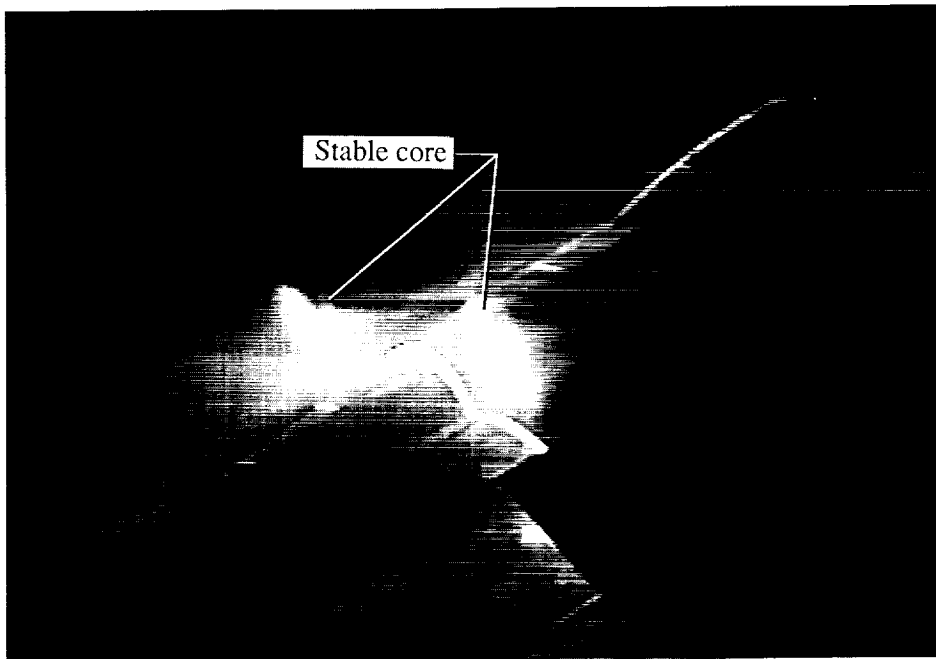


(a)  $\alpha = 20^\circ$ ; FS 525 (31.51).

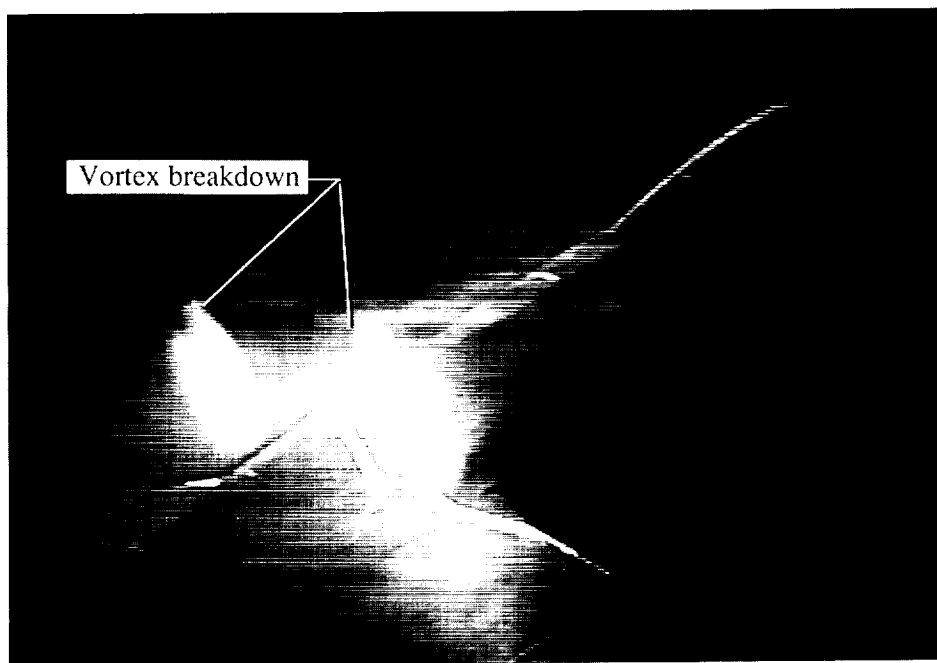


(b)  $\alpha = 20^\circ$ ; FS 567 (34.02).

Figure 24. Laser vapor screen flow visualizations on baseline F/A-18 model at  $M_\infty = 0.40$  and  $Re_c = 1.75 \times 10^6$ . Camera is in three-quarter, right rear position; dimensions are in inches full scale (0.06 scale).

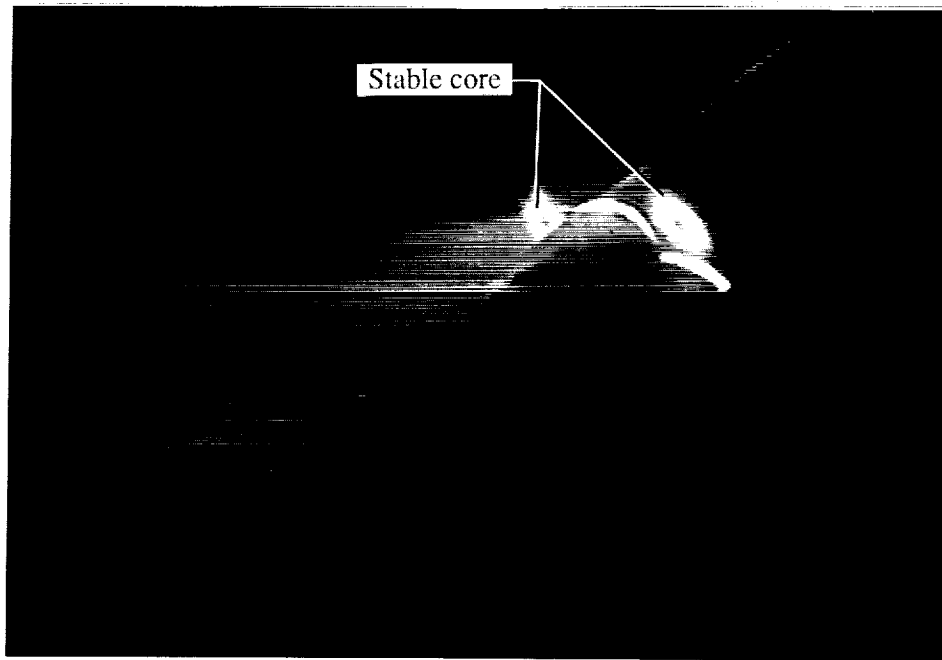


(c)  $\alpha = 25^\circ$ ; FS 411 (24.67).

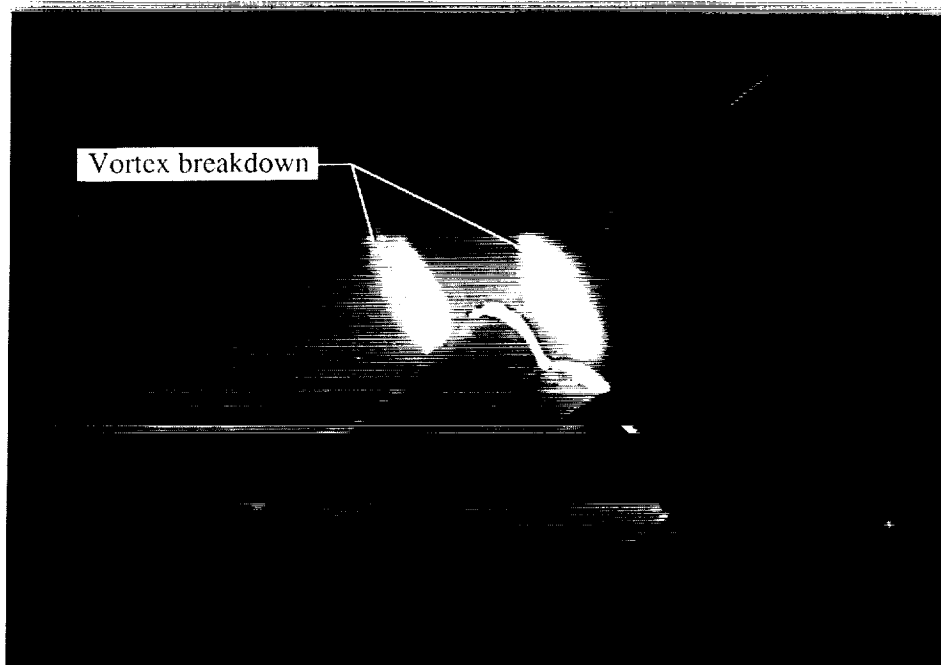


(d)  $\alpha = 25^\circ$ ; FS 450 (31.51).

Figure 24. Continued.



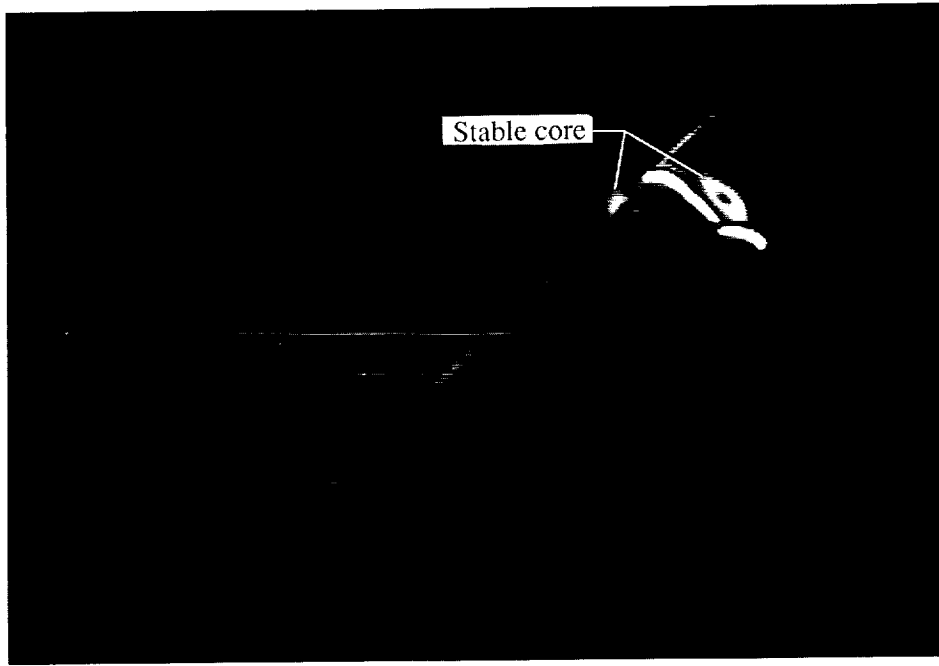
(e)  $\alpha = 30^\circ$ ; FS 357 (21.42).



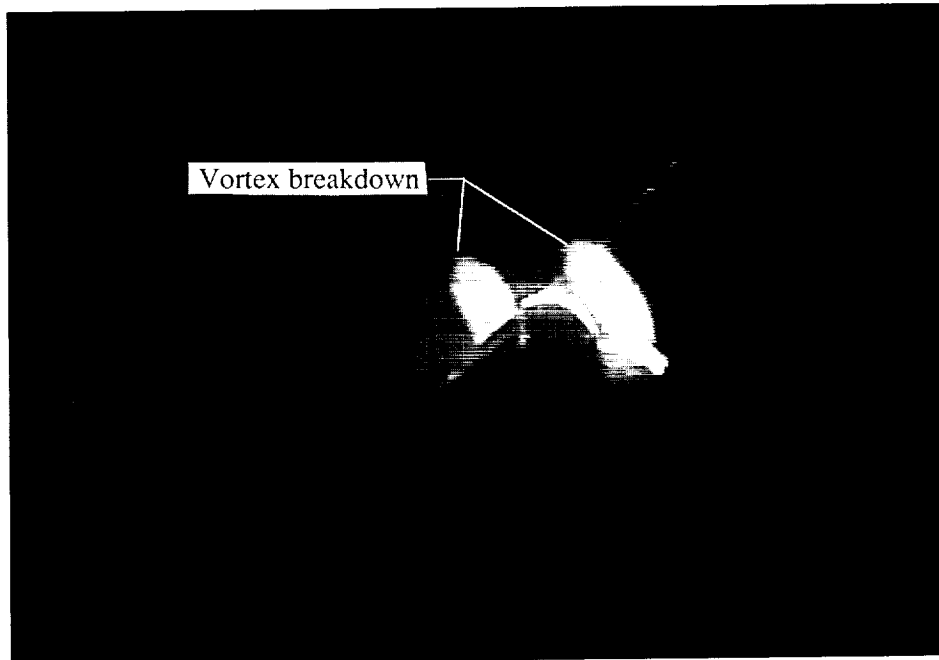
(f)  $\alpha = 30^\circ$ ; FS 411 (24.67).

Figure 24. Continued.

ORIGINAL PAGE  
BLACK AND WHITE PHOTOGRAPH

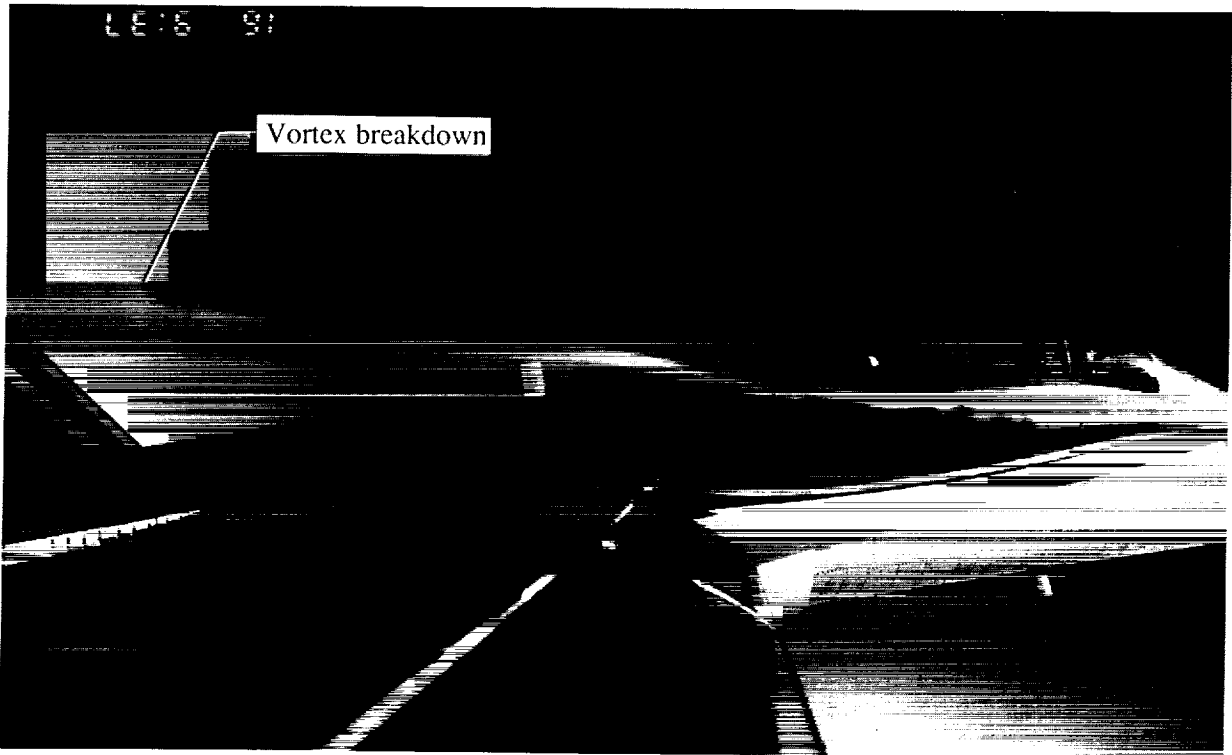


(g)  $\alpha = 35^\circ$ ; FS 296 (17.76).



(h)  $\alpha = 35^\circ$ ; FS 357 (21.42).

Figure 24. Concluded.



(a)  $\alpha = 19.65^\circ$ ;  $\beta = 0.35^\circ$ .

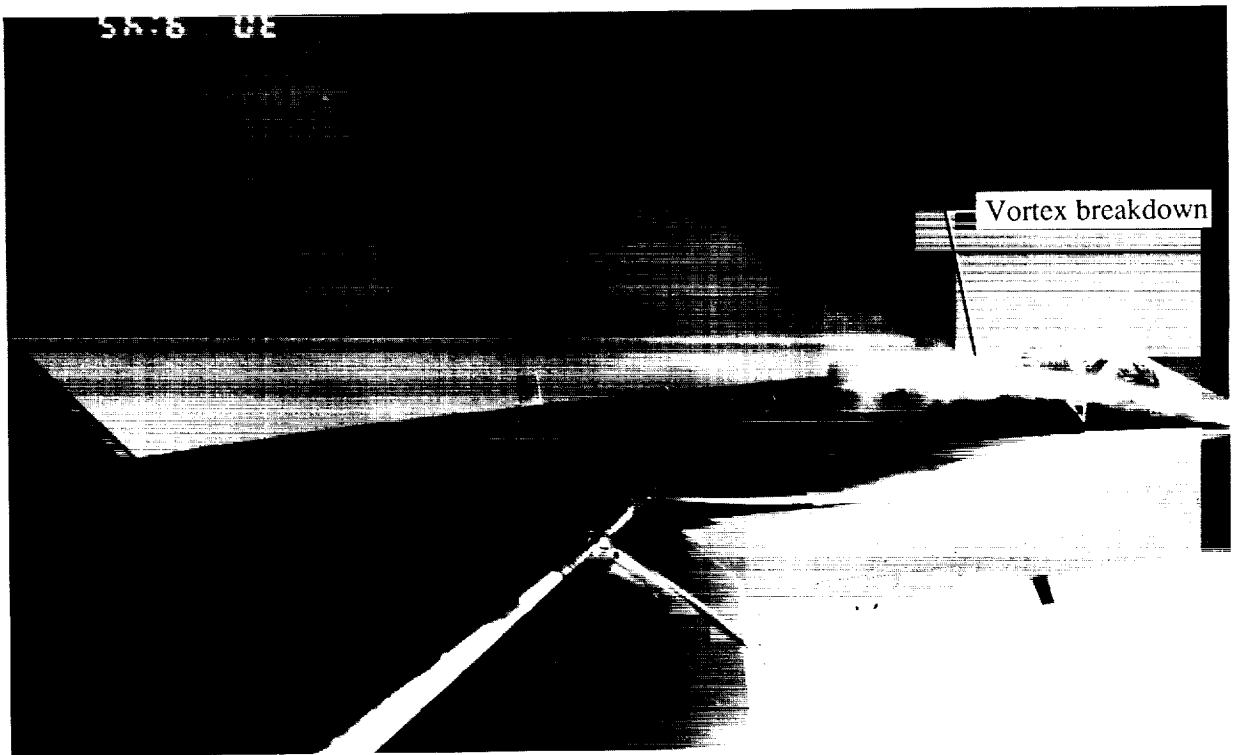


(b)  $\alpha = 25.28^\circ$ ;  $\beta = 0.65^\circ$ .

Figure 25. In-flight smoke flow visualizations of LEX vortex breakdown on F-18 HARV at  $M_\infty \approx 0.3$  and  $Re_{\bar{c}} \approx 13.5 \times 10^6$  (ref. 12).



(c)  $\alpha = 29.85^\circ$ ;  $\beta = 0.25^\circ$ .



(d)  $\alpha = 33.50^\circ$ ;  $\beta = 0.60^\circ$ .

Figure 25. Concluded.

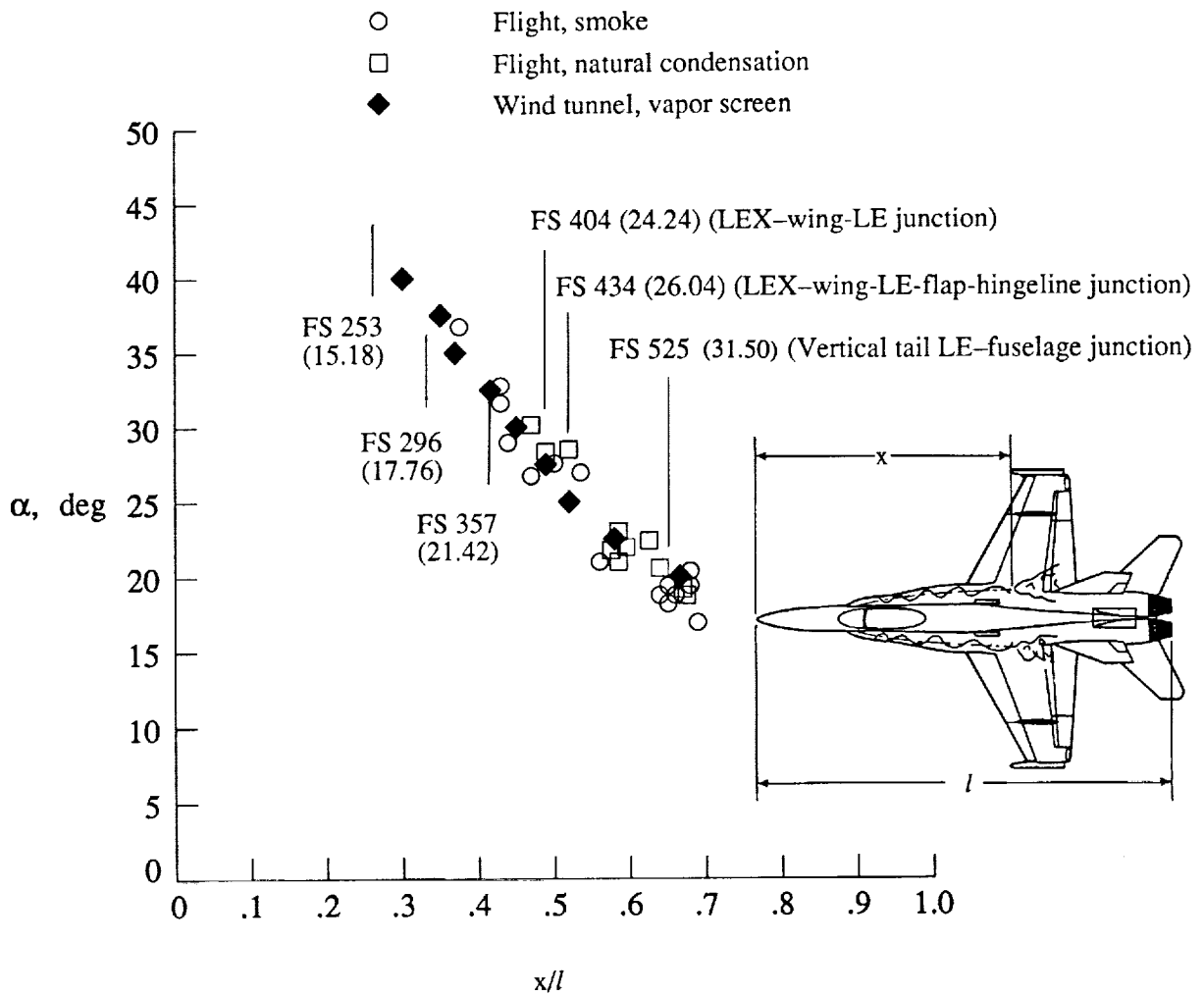
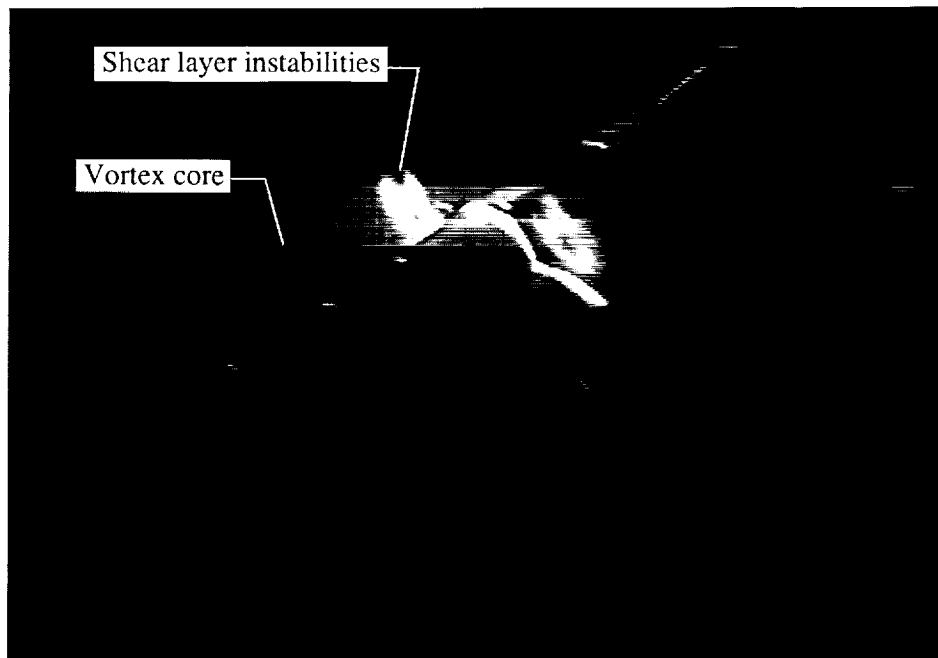


Figure 26. LEX vortex breakdown progression with angle of attack on baseline 0.06-scale F/A-18 model ( $M_\infty = 0.40$ ,  $Re_{\bar{c}} = 1.75 \times 10^6$ ) and F-18 HARV ( $M_\infty \approx 0.3$ ;  $Re_{\bar{c}} \approx 13.5 \times 10^6$ ). (Flight results are from ref. 13.)



ORIGINAL PAGE  
BLACK AND WHITE PHOTOGRAPH



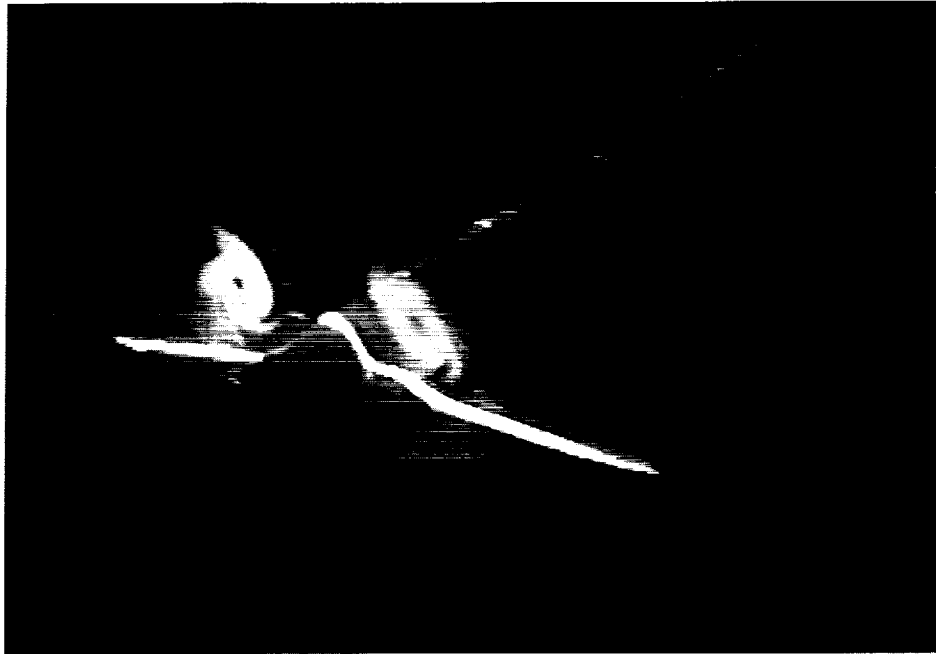
(a) FS 411 (24.66).



(b) FS 450 (27.00).

Figure 27. Laser vapor screen flow visualizations on baseline F/A-18 model at  $M_\infty = 0.60$ ,  $Re_c = 1.32 \times 10^6$ , and  $\alpha = 20^\circ$ . Dimensions are in inches full scale (0.06 scale).

ORIGINAL PAGE  
BLACK AND WHITE PHOTOGRAPH

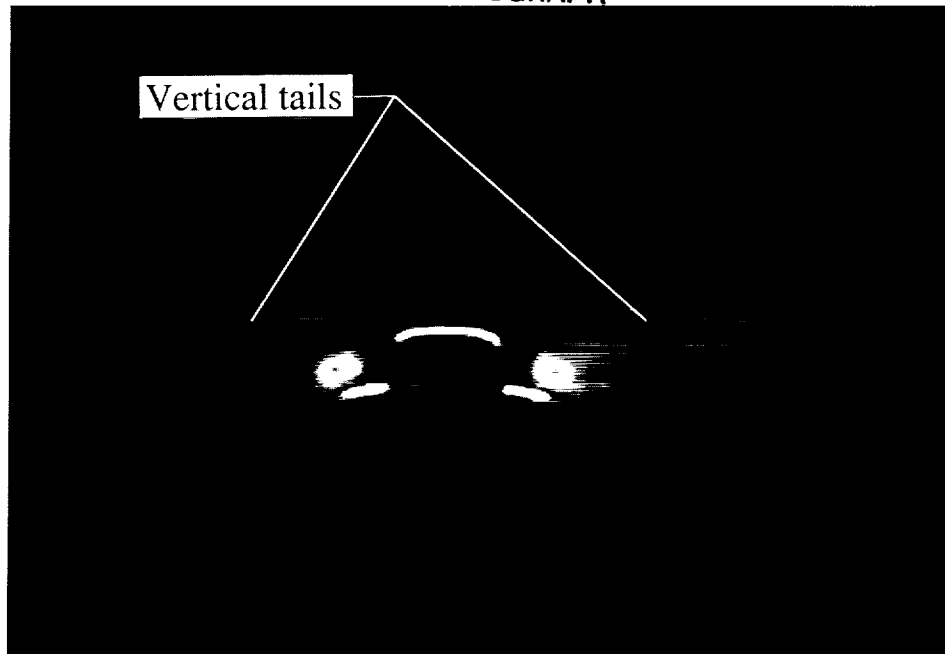
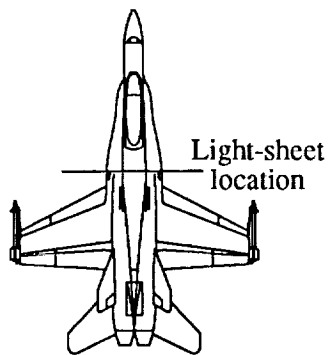


(c) FS 483 (28.98).

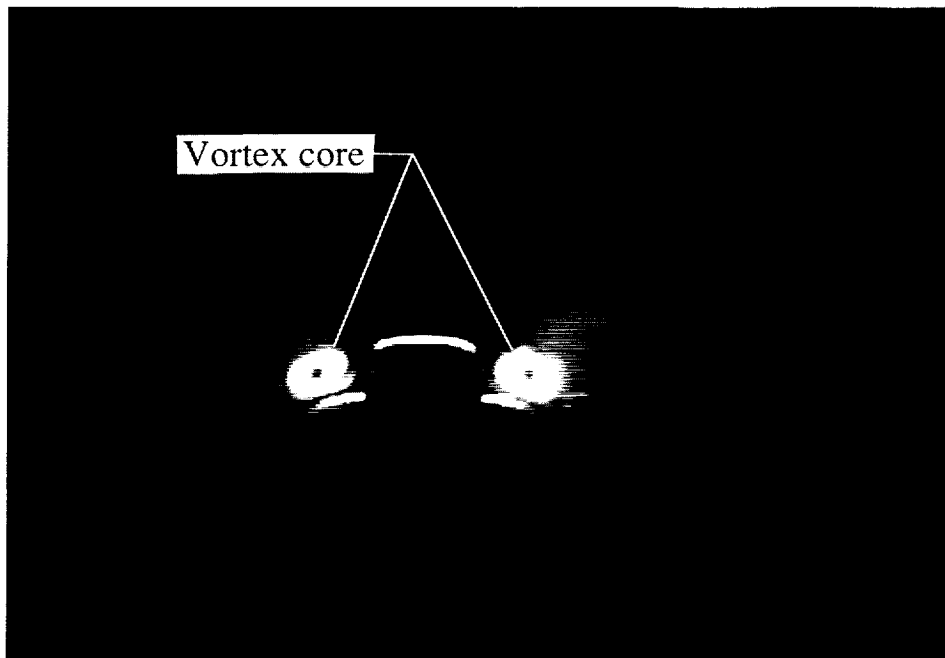
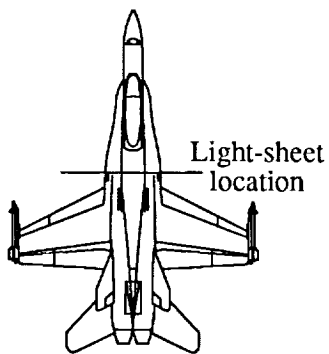


(d) FS 525 (31.50) (just prior to breakdown).

Figure 27. Concluded.

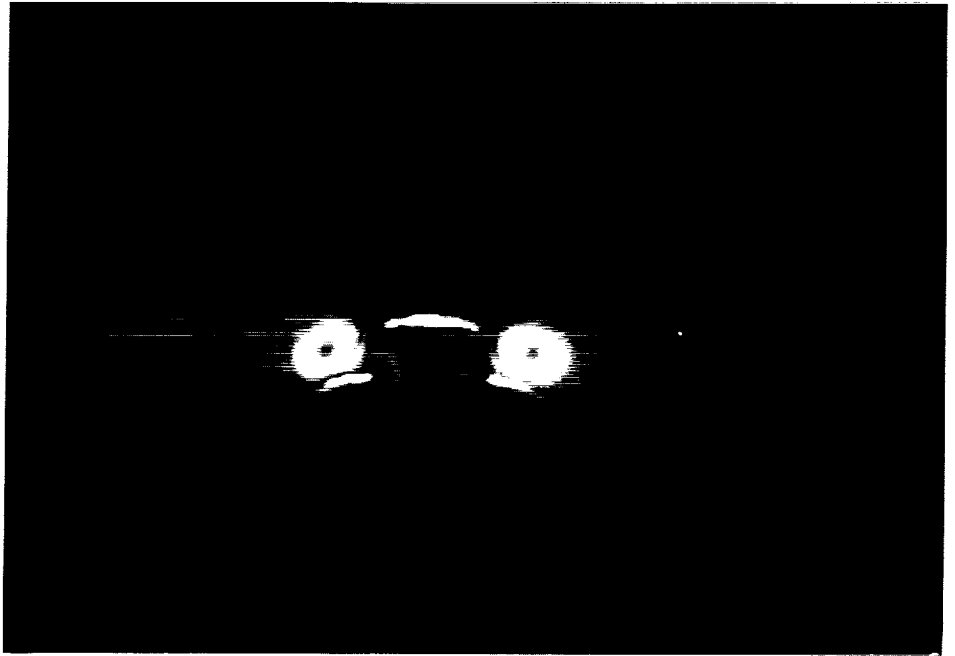
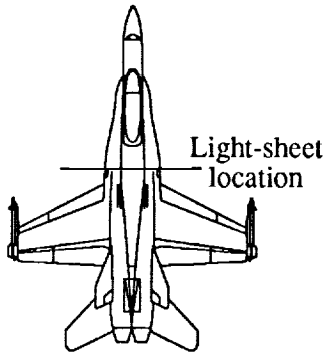


(a)  $\alpha = 15^\circ$ .

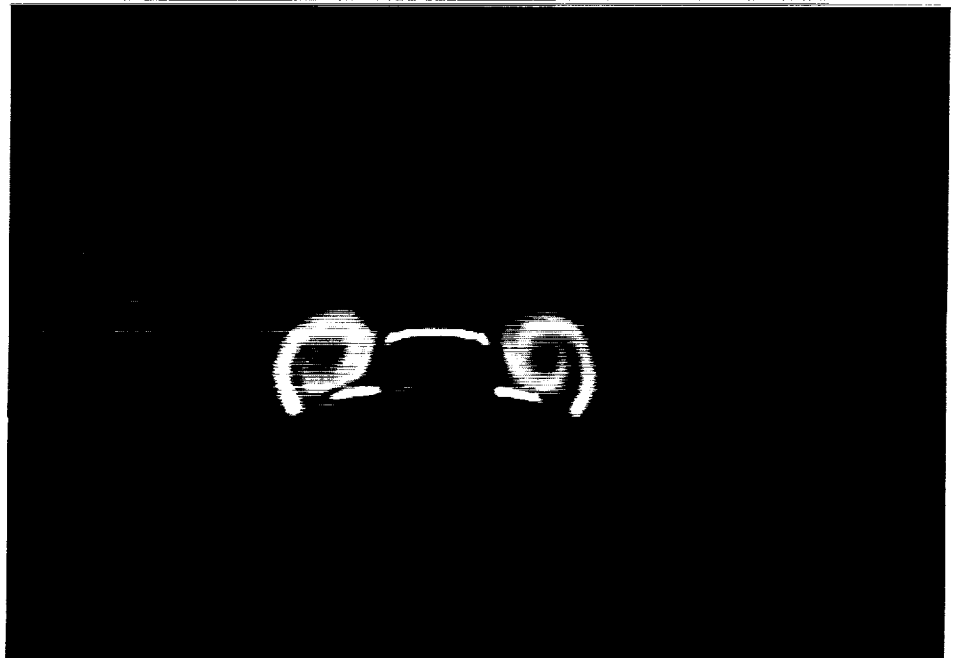
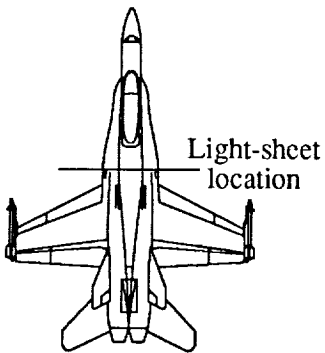


(b)  $\alpha = 17.5^\circ$ .

Figure 28. Effect of angle of attack on cross flow about baseline F/A-18 model at  $M_\infty = 0.60$ ,  $Re_{\bar{c}} = 1.32 \times 10^6$ , and FS 357 (21.42). Dimensions are in inches full scale (0.06 scale).

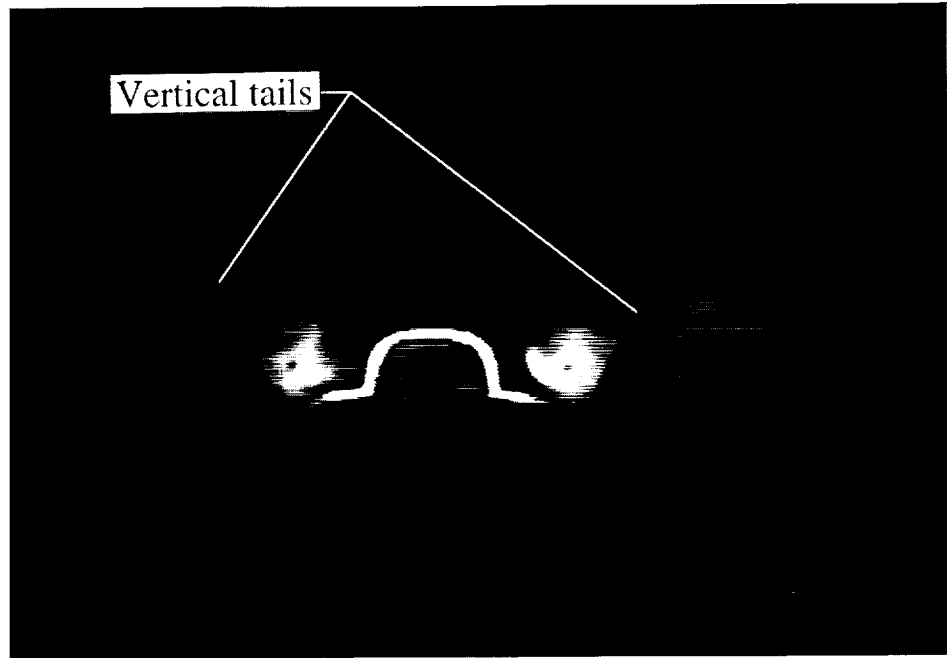
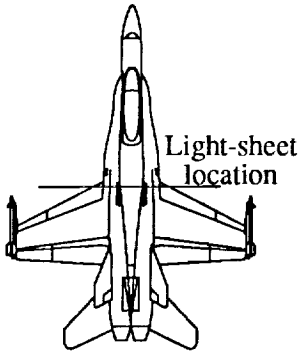


(c)  $\alpha = 20^\circ$ .

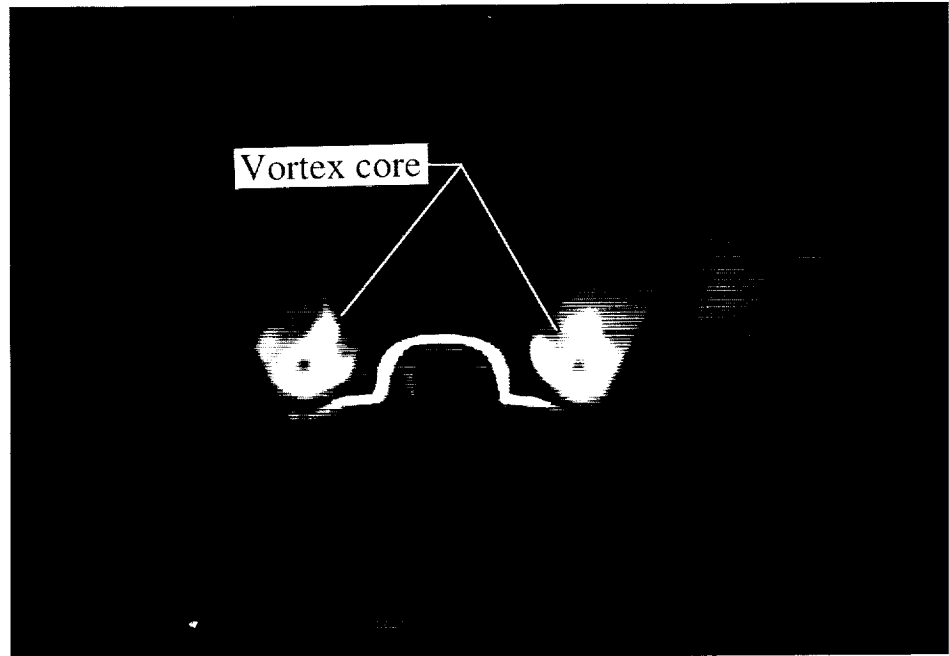
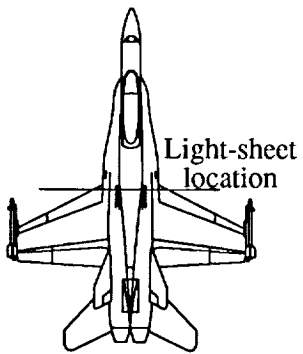


(d)  $\alpha = 25^\circ$ .

Figure 28. Concluded.

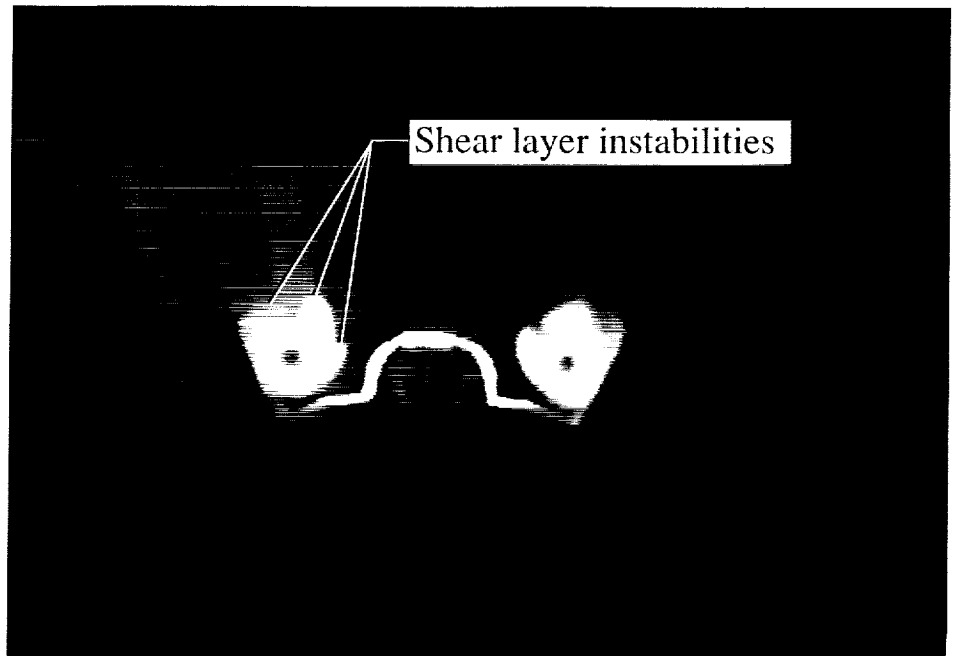
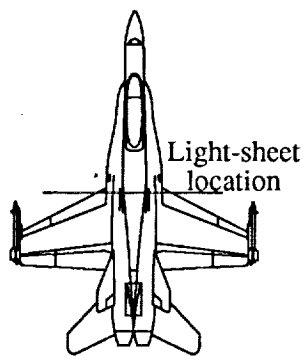


(a)  $\alpha = 15^\circ$ .

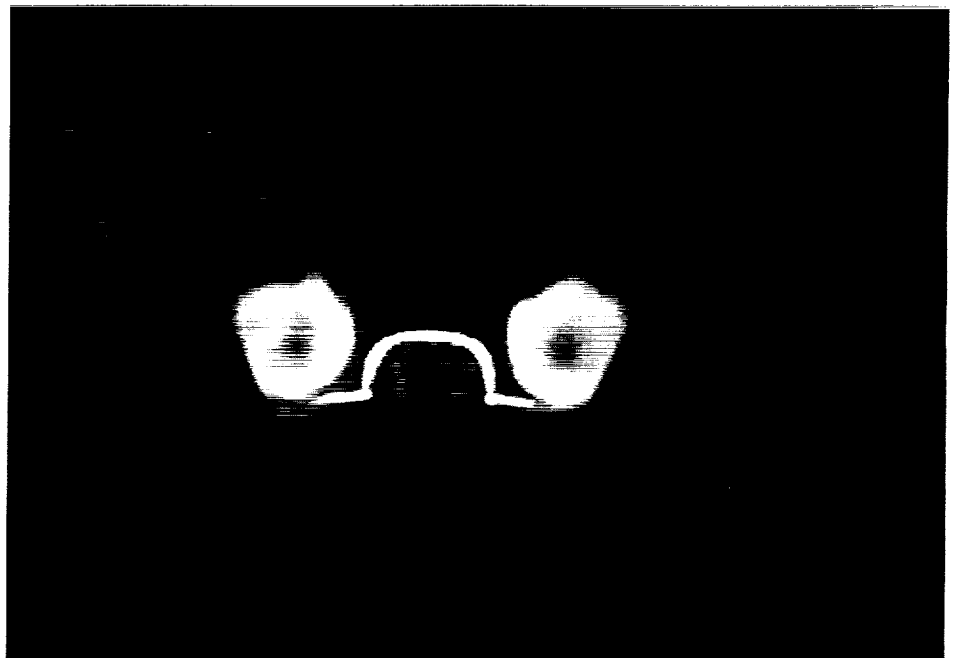
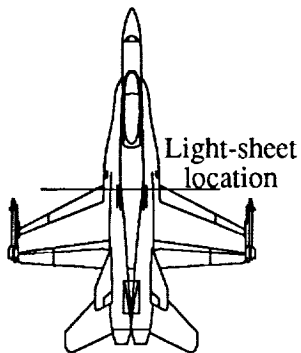


(b)  $\alpha = 17.5^\circ$ .

Figure 29. Effect of angle of attack on cross flow about baseline F/A-18 model at  $M_\infty = 0.60$ ,  $Re_c = 1.32 \times 10^6$ , and FS 411 (24.66). Dimensions are in inches full scale (0.06 scale).



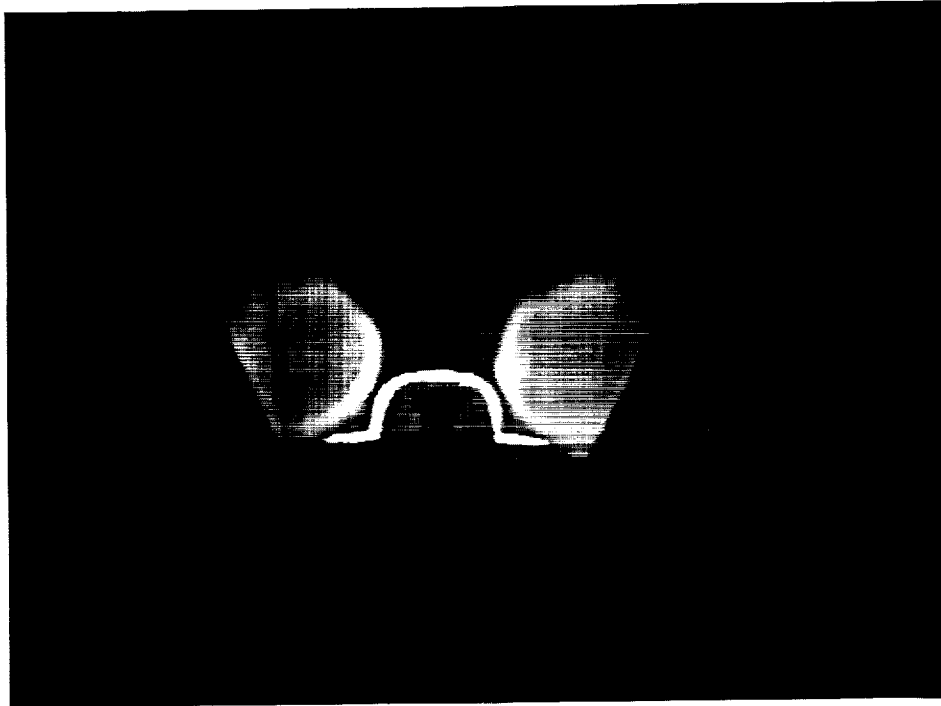
(c)  $\alpha = 20^\circ$ .



(d)  $\alpha = 25^\circ$ .

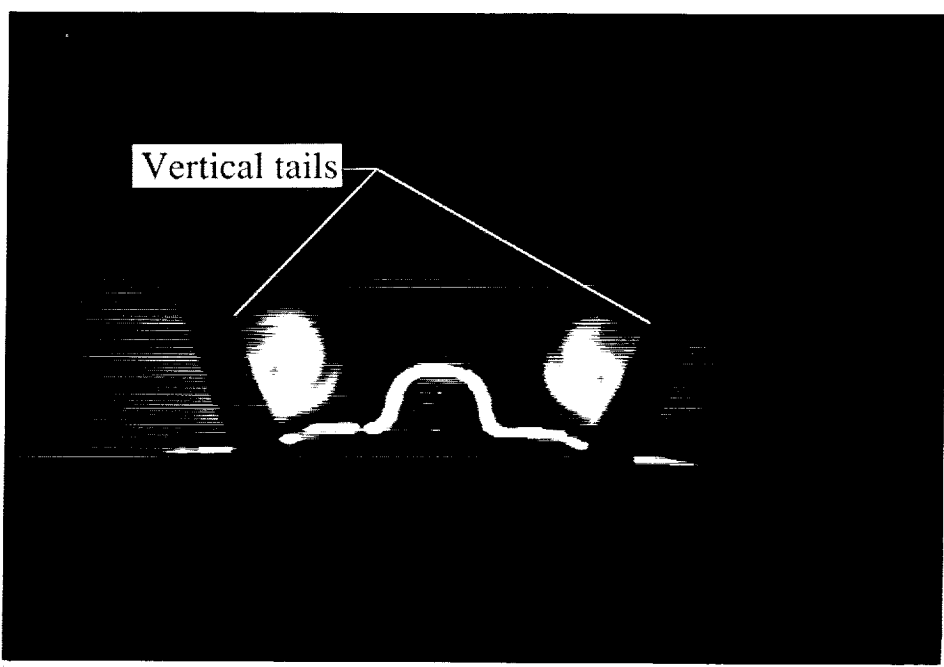
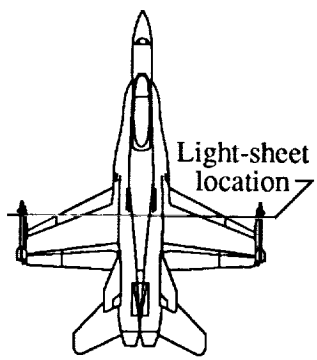
Figure 29. Continued.

ORIGINAL PAGE  
BLACK AND WHITE PHOTOGRAPH

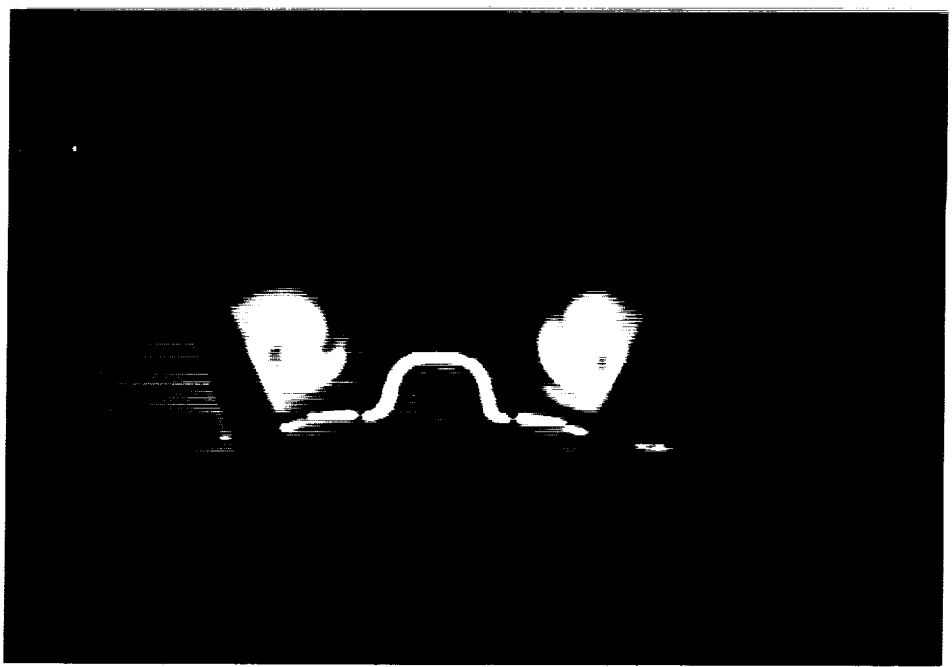
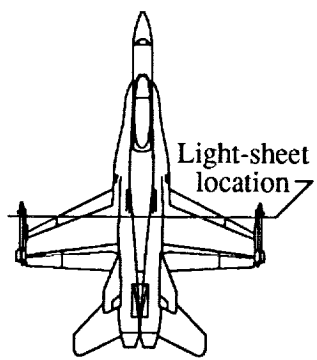


(e)  $\alpha = 30^\circ$ .

Figure 29. Concluded.



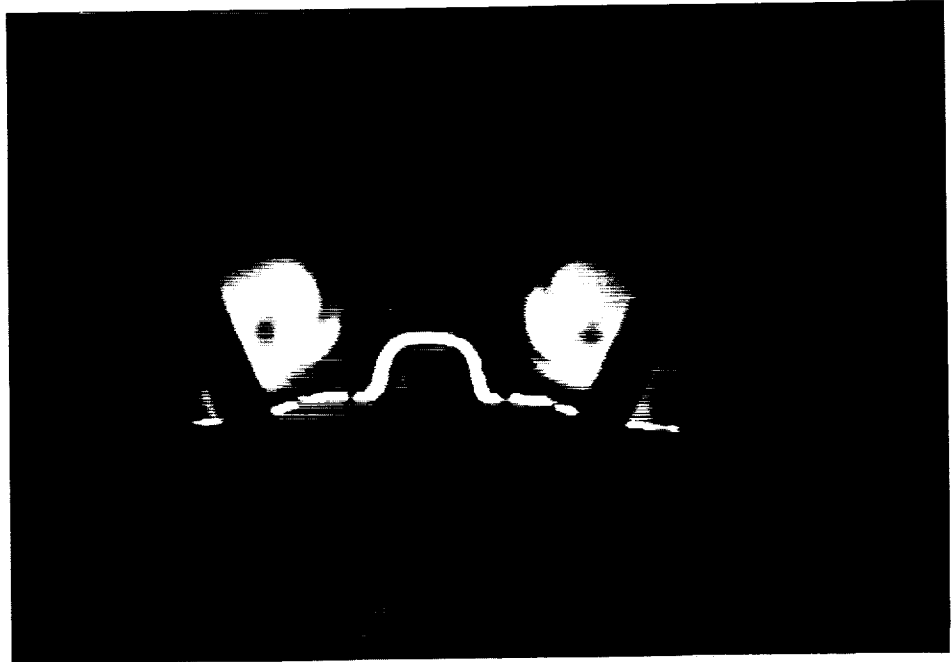
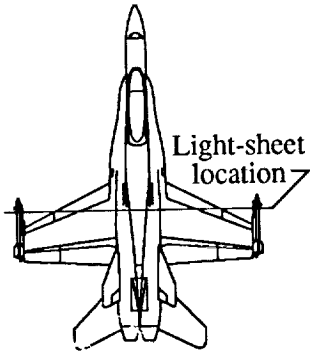
(a)  $\alpha = 15^\circ$ .



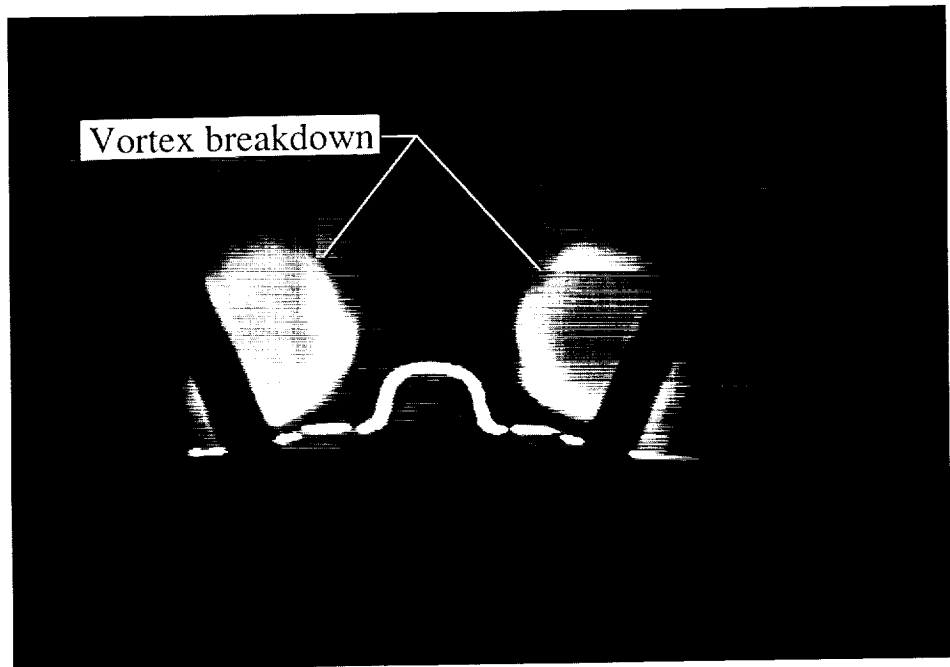
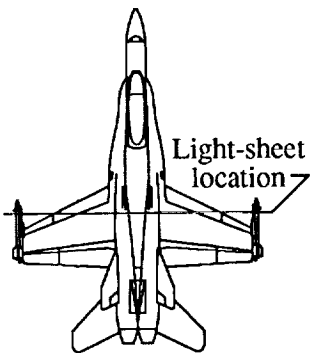
(b)  $\alpha = 17.5^\circ$ .

Figure 30. Effect of angle of attack on cross flow about baseline F/A-18 model at  $M_\infty = 0.60$ ,  $Re_z = 1.32 \times 10^6$ , and FS 450 (27.00). Dimensions are in inches full scale (0.06 scale).





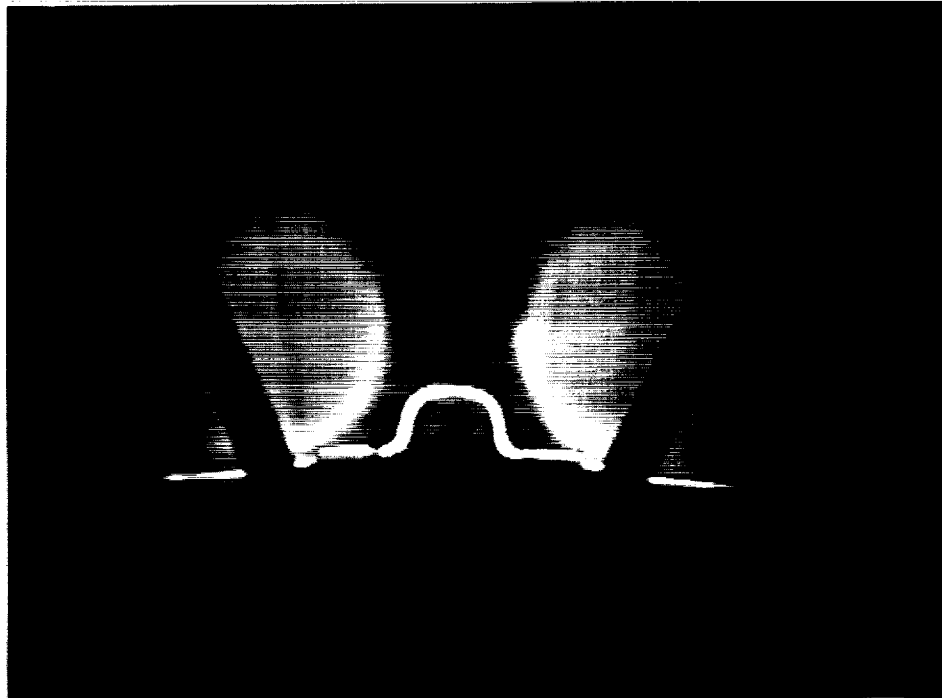
(c)  $\alpha = 20^\circ$ .



(d)  $\alpha = 25^\circ$ .

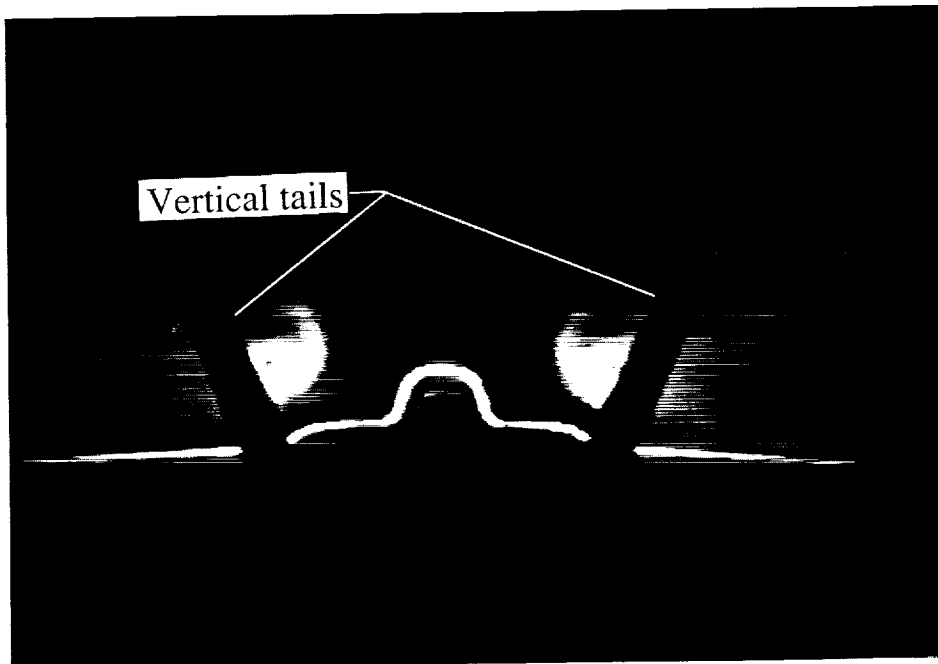
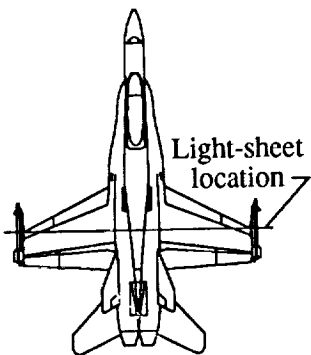
Figure 30. Continued.

ORIGINAL PAGE  
BLACK AND WHITE PHOTOGRAPH

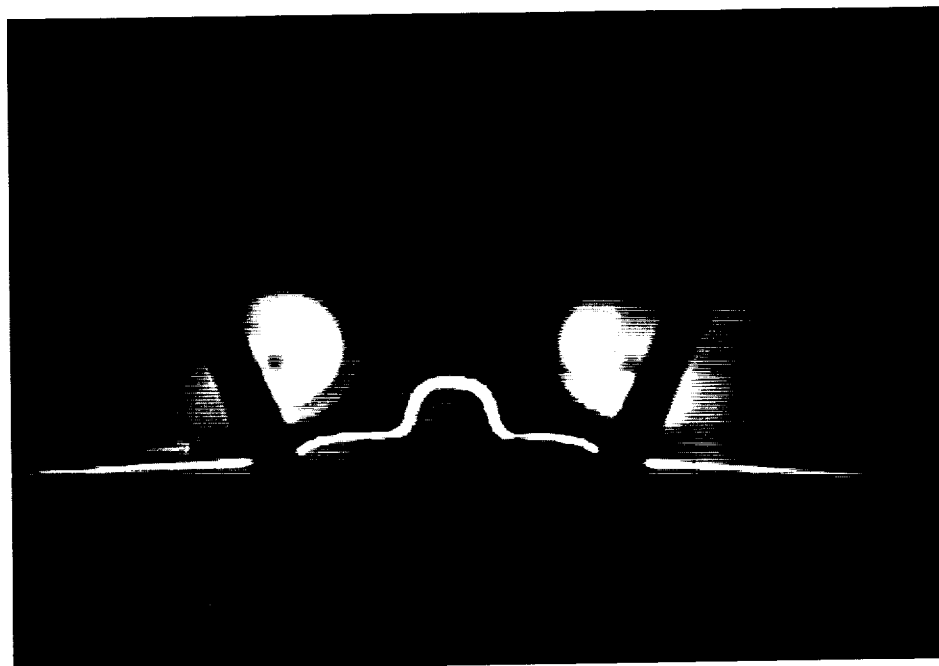
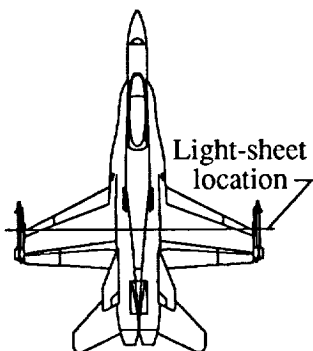


(e)  $\alpha = 30^\circ$ .

Figure 30. Concluded.

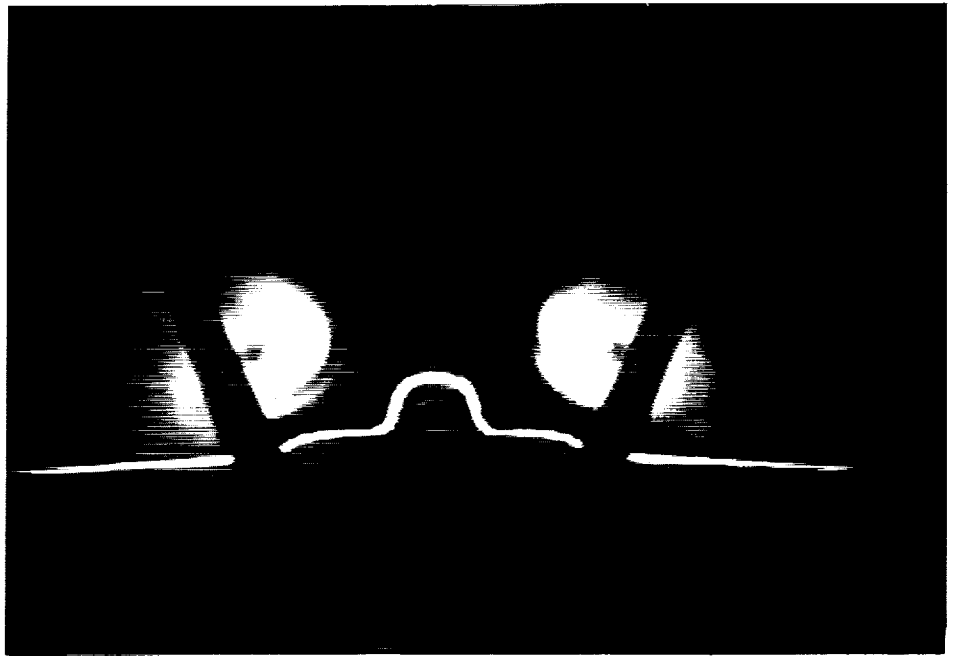
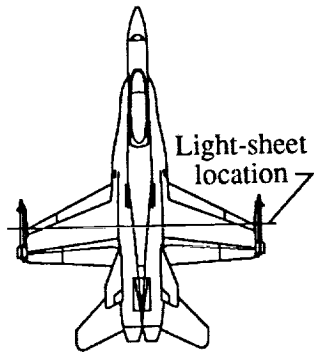


(a)  $\alpha = 15^\circ$ .

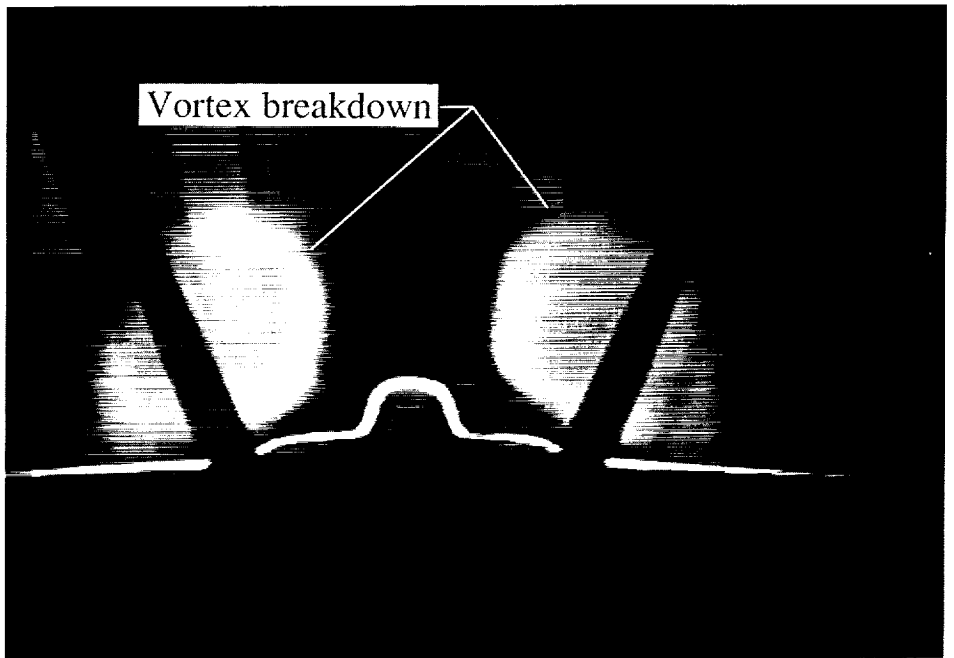
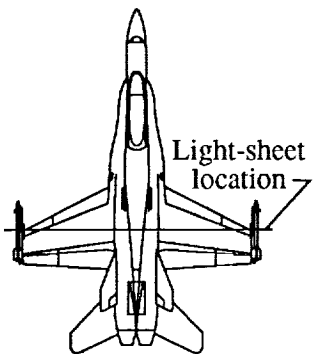


(b)  $\alpha = 17.5^\circ$ .

Figure 31. Effect of angle of attack on cross flow about baseline F/A-18 model at  $M_\infty = 0.60$ ,  $Re_z = 1.32 \times 10^6$ , and FS 483 (28.98). Dimensions are in inches full scale (0.06 scale).



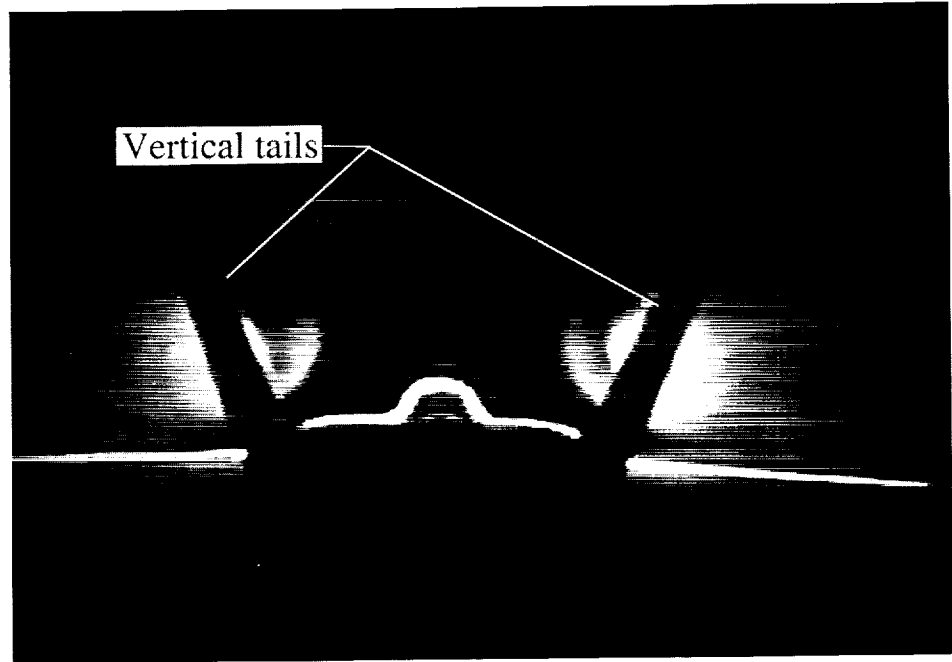
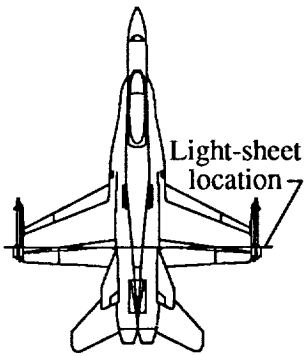
(c)  $\alpha = 20^\circ$ .



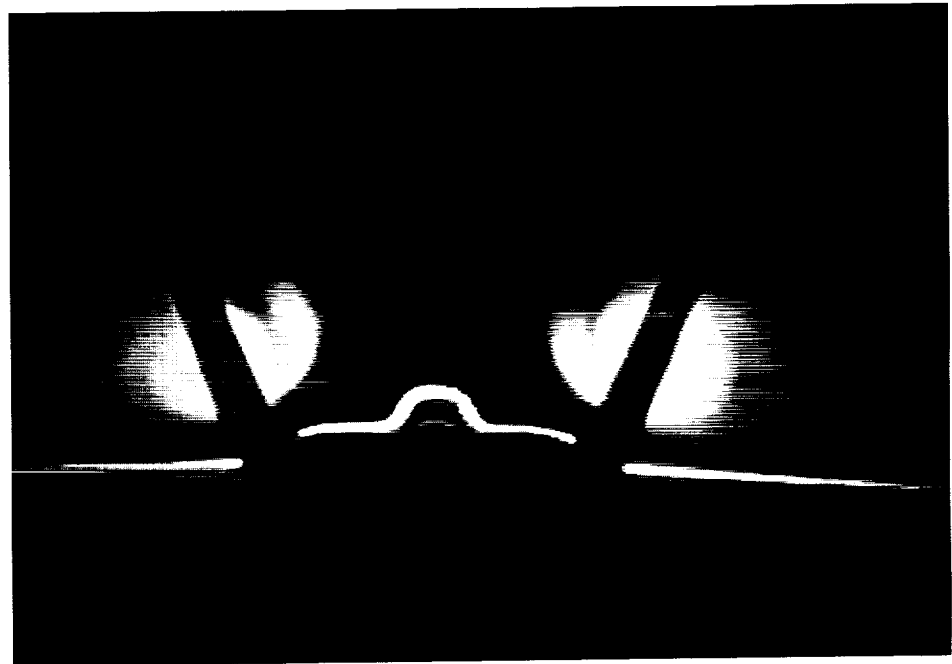
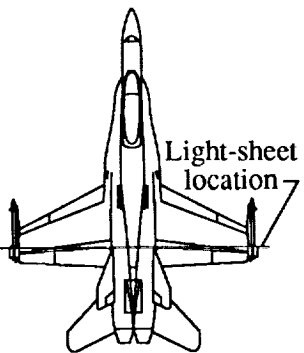
(d)  $\alpha = 25^\circ$ .

Figure 31. Concluded.

ORIGINAL PAGE  
BLACK AND WHITE PHOTOGRAPH

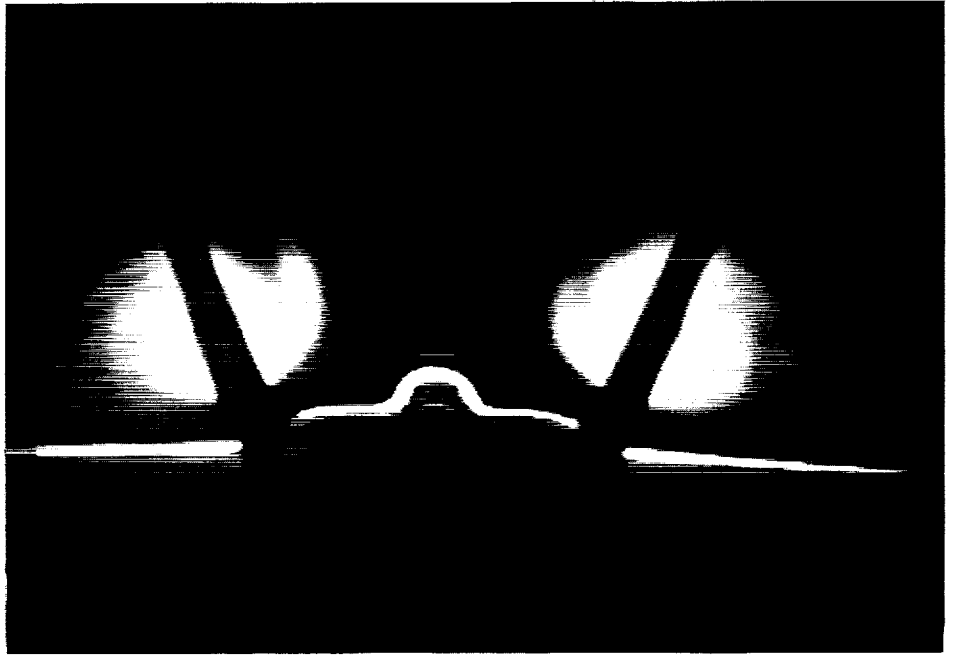
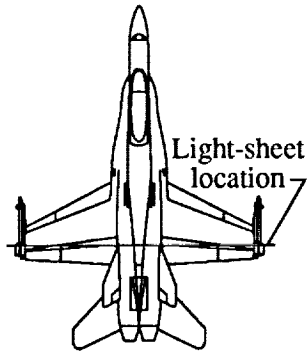


(a)  $\alpha = 15^\circ$ .

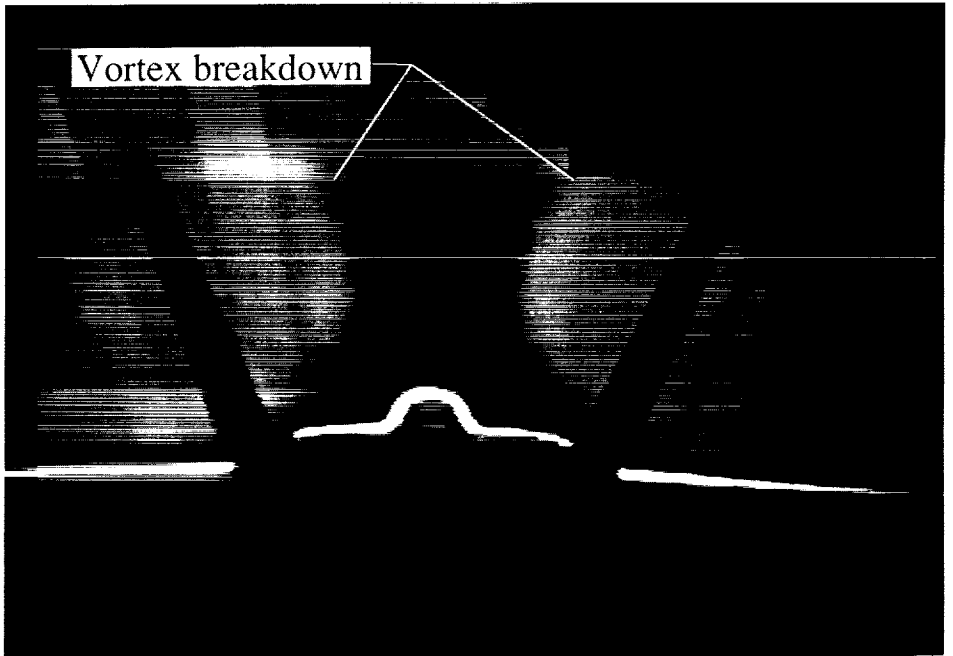
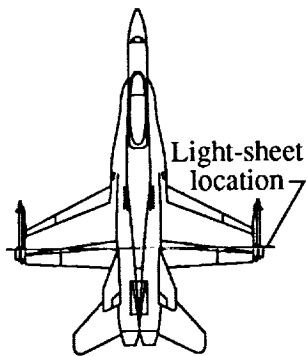


(b)  $\alpha = 17.5^\circ$ .

Figure 32. Effect of angle of attack on cross flow about baseline F/A-18 model at  $M_\infty = 0.60$ ,  $Re_c = 1.32 \times 10^6$ , and FS 525 (31.50). Dimensions are in inches full scale (0.06 scale).

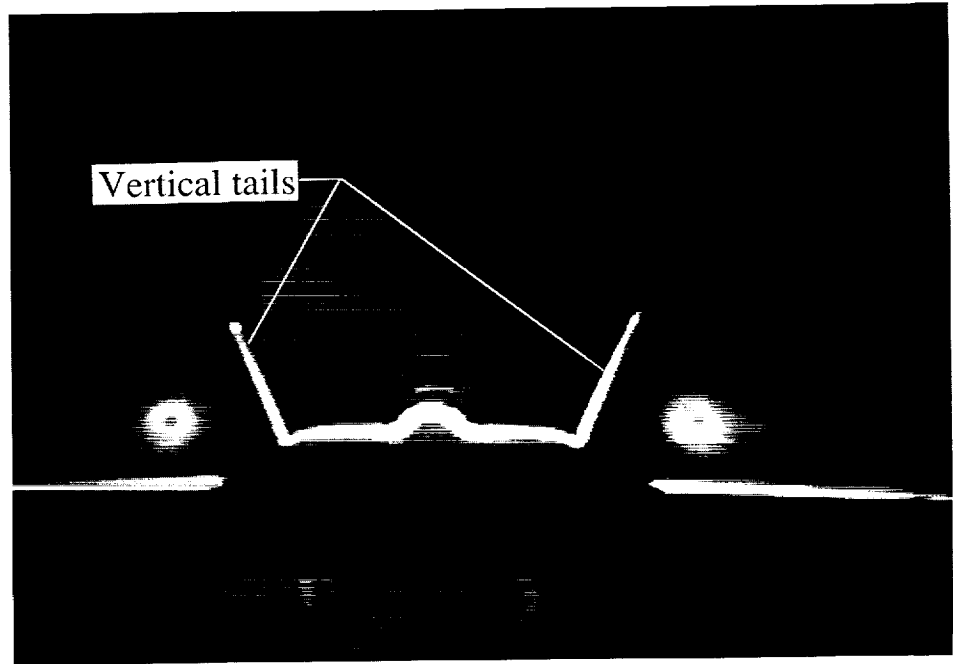
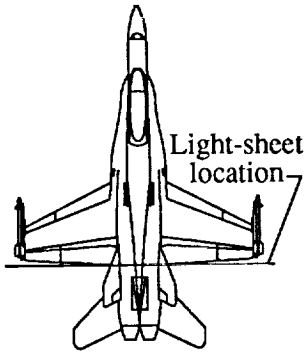


(c)  $\alpha = 20^\circ$ .

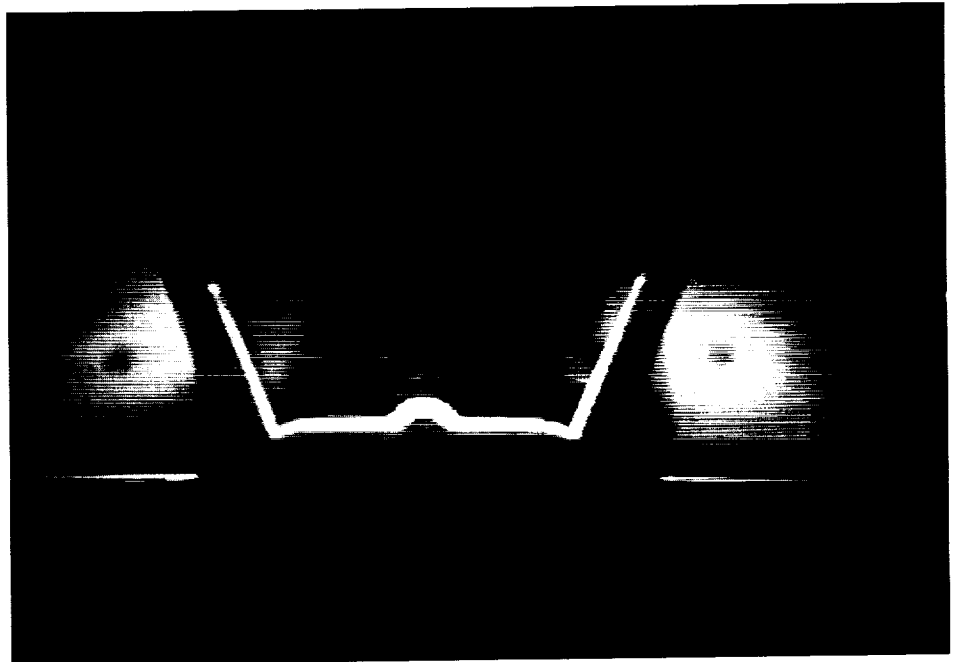
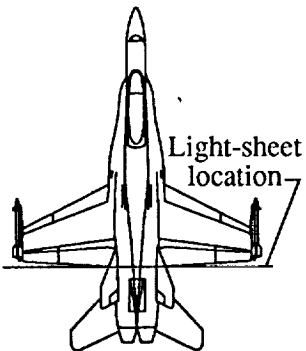


(d)  $\alpha = 25^\circ$ .

Figure 32. Concluded.

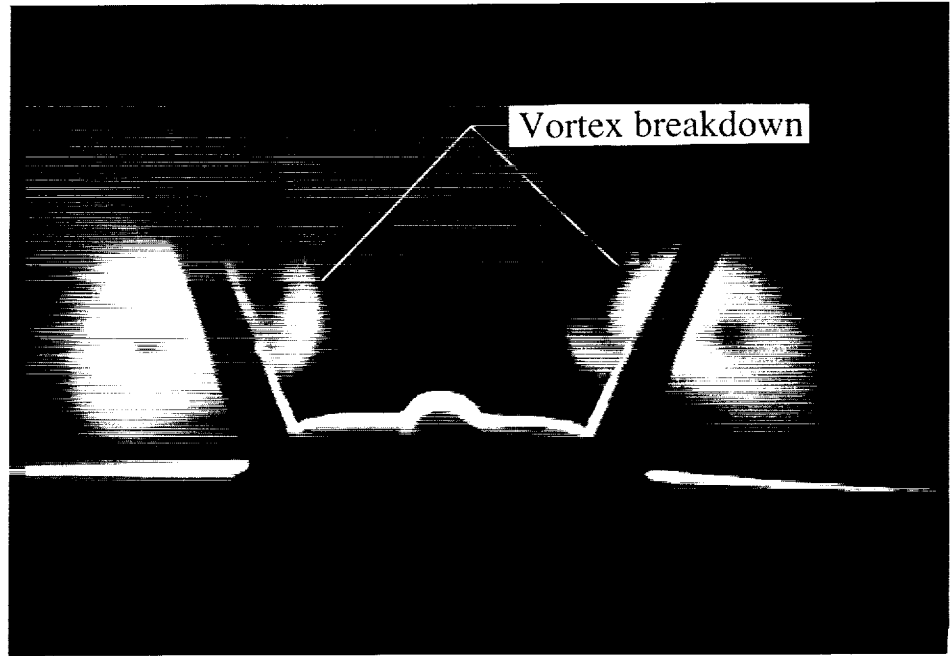
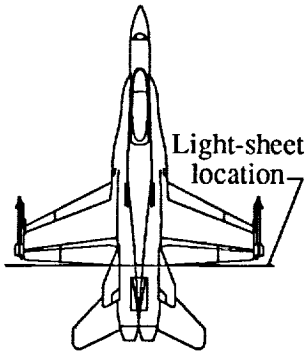


(a)  $\alpha = 15^\circ$ .

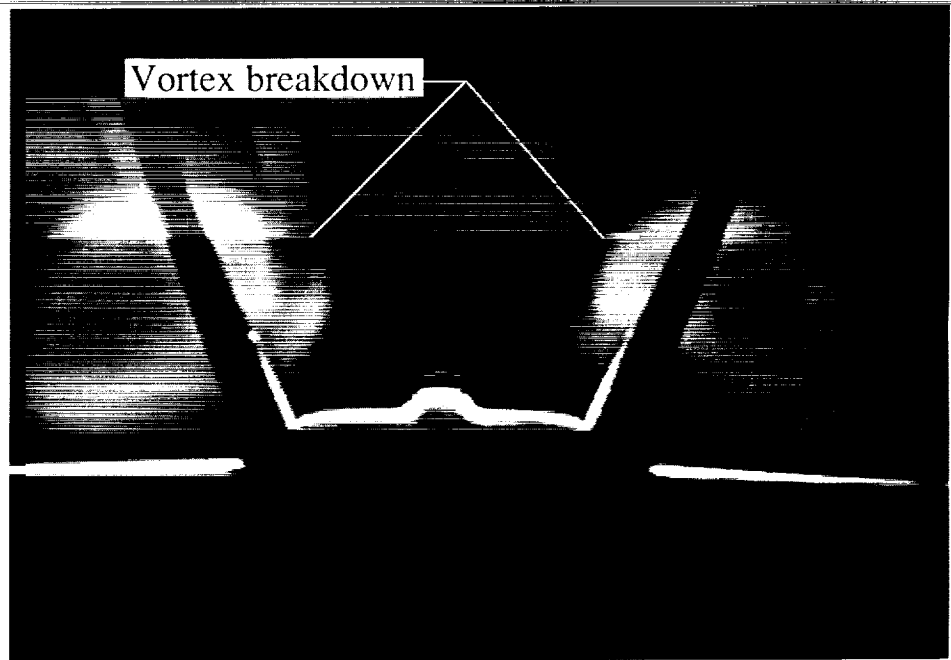
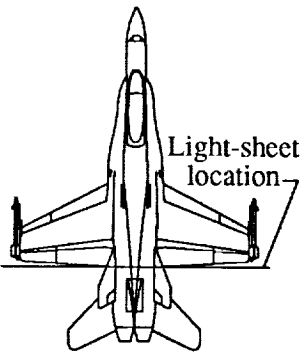


(b)  $\alpha = 17.5^\circ$ .

Figure 33. Effect of angle of attack on cross flow about baseline F/A-18 model at  $M_\infty = 0.60$ ,  $Re_c = 1.32 \times 10^6$ , and FS 567 (34.02). Dimensions are in inches full scale (0.06 scale).



(c)  $\alpha = 20^\circ$ .

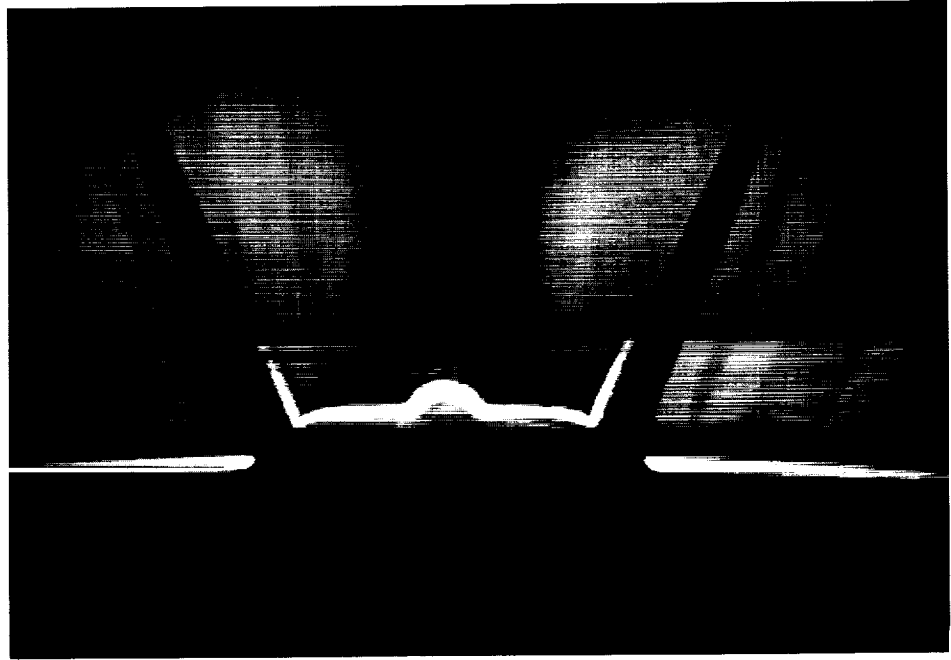
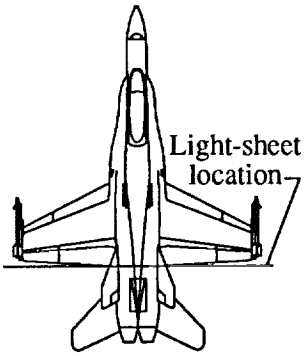


(d)  $\alpha = 25^\circ$ .

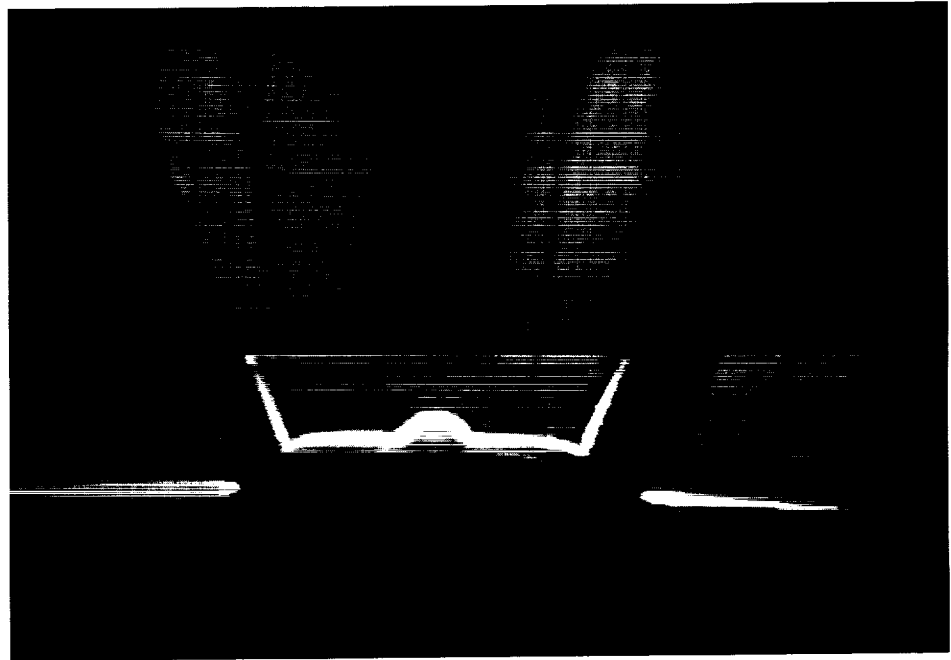
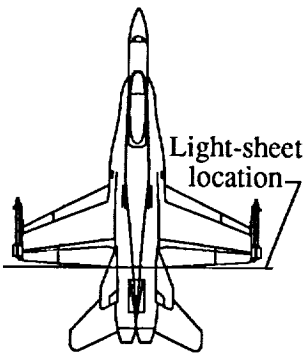
Figure 33. Continued.



ORIGINAL PAGE  
BLACK AND WHITE PHOTOGRAPH



(e)  $\alpha = 30^\circ$ .



(f)  $\alpha = 35^\circ$ .

Figure 33. Concluded.

ORIGINAL PAGE  
BLACK AND WHITE PHOTOGRAPH

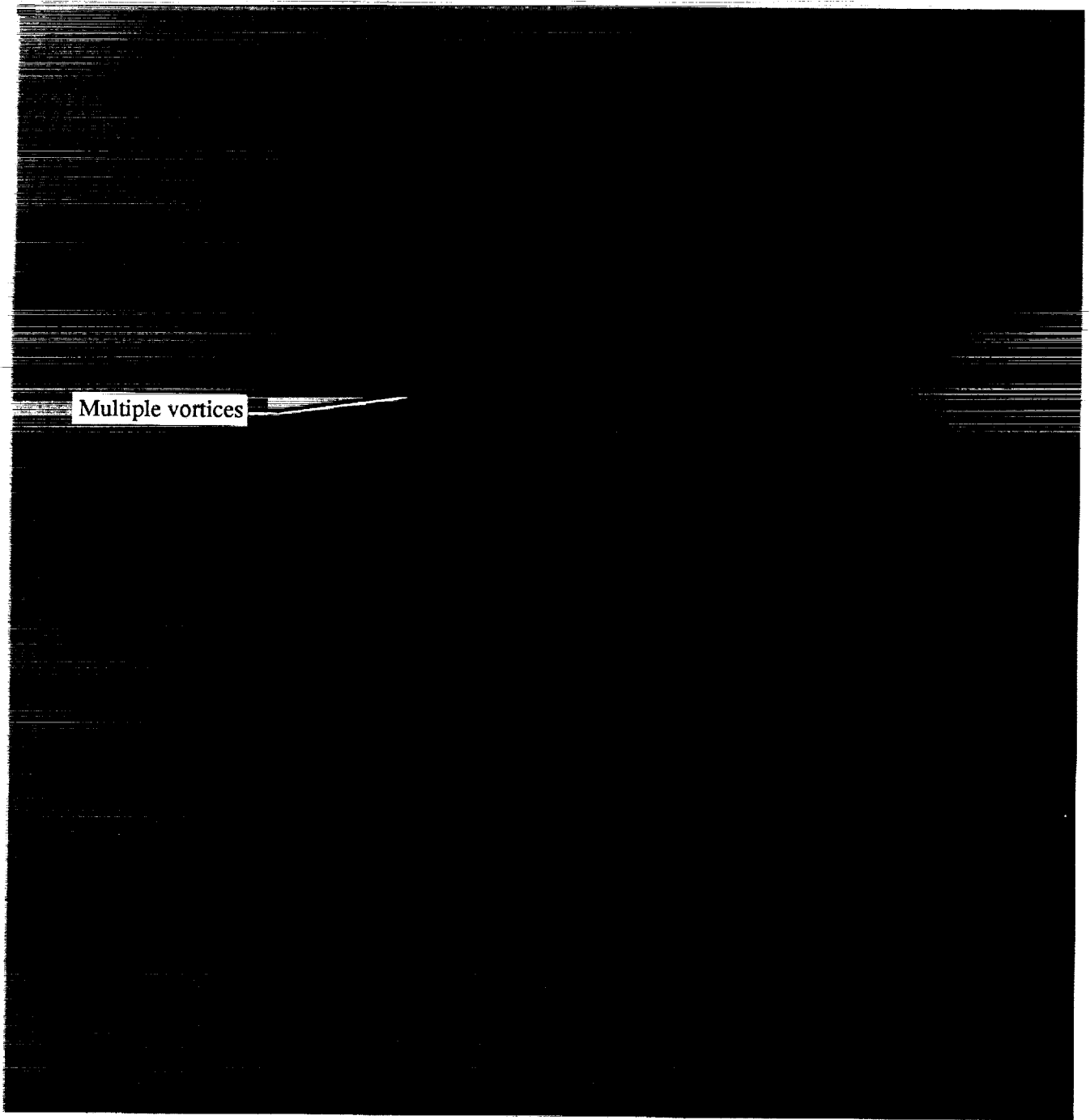


Figure 34. In-flight flow visualization (natural condensation) of the F/A-18 LEX vortices (ref. 16).

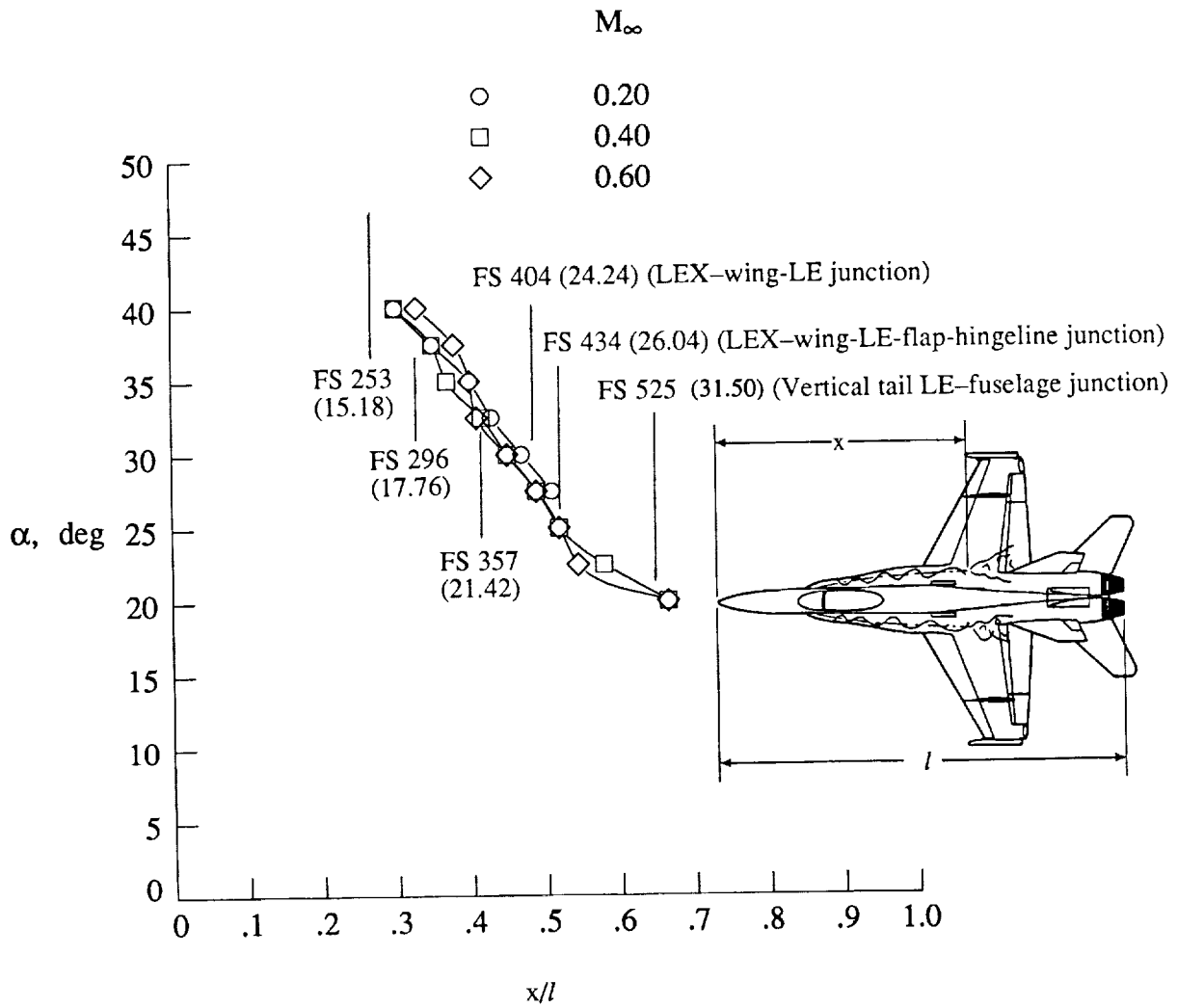
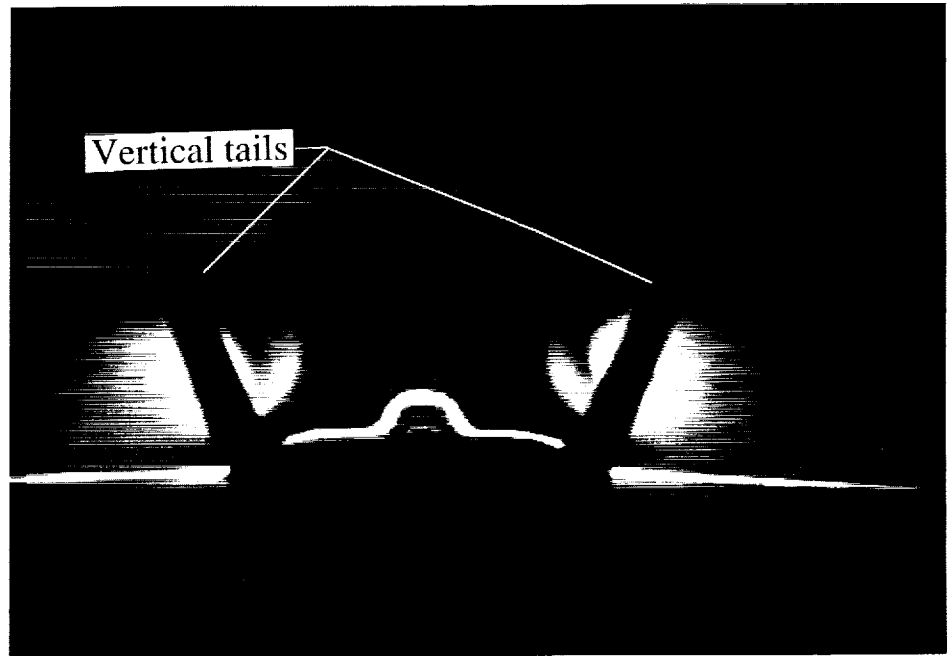
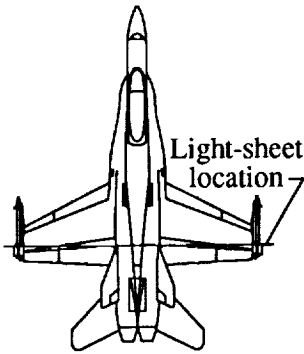
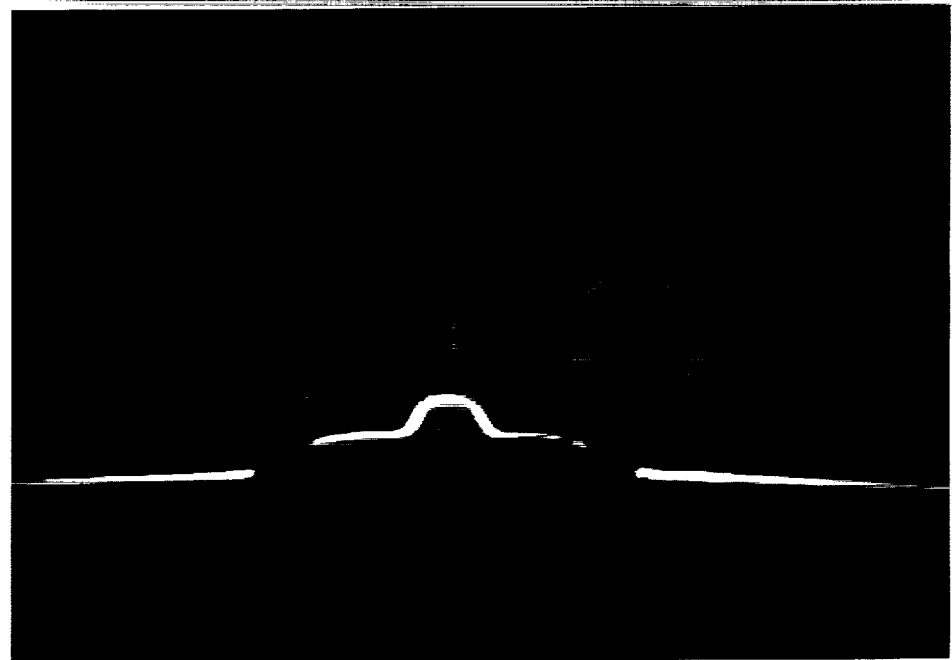
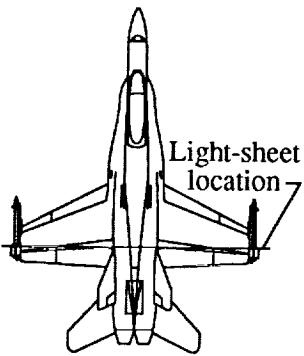


Figure 35. Effect of Mach number on LEX vortex breakdown characterizations of baseline F/A-18 model. Dimensions are in inches full scale (0.06 scale).

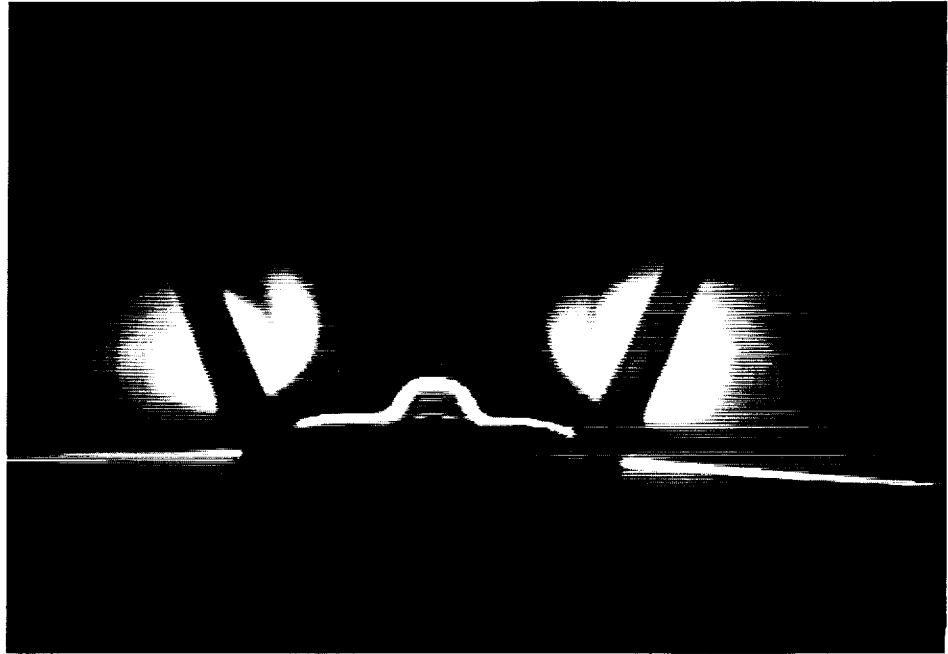
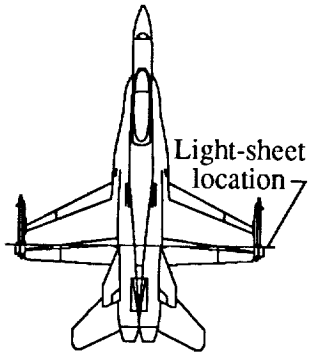


(a)  $M_\infty = 0.60$ ,  $\alpha = 15^\circ$ .

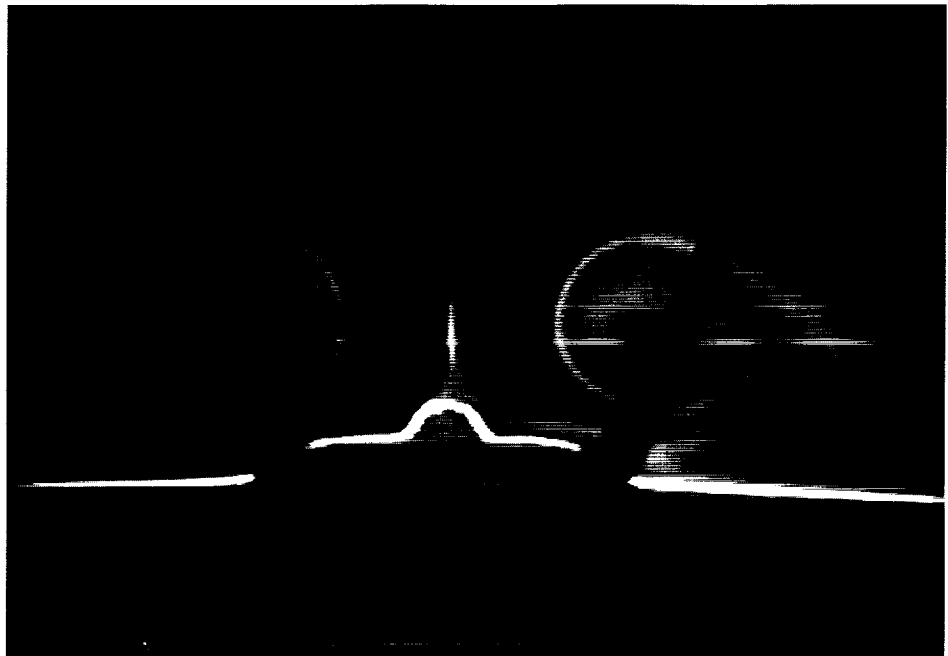
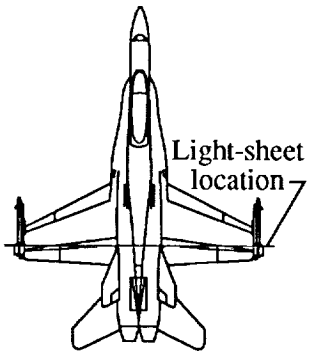


(b)  $M_\infty = 0.80$ ,  $\alpha = 15^\circ$ .

Figure 36. Cross-flow patterns about baseline F/A-18 model at  $M_\infty = 0.60$  ( $Re_{\bar{c}} = 1.32 \times 10^6$ ) and  $M_\infty = 0.80$  ( $Re_{\bar{c}} = 1.02 \times 10^6$ ) at FS 525 (31.50). Dimensions are in inches full scale (0.06 scale).

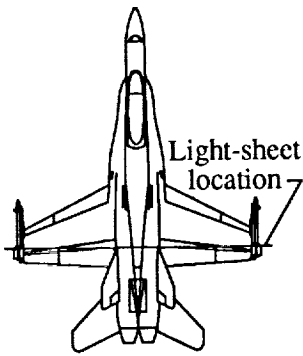


(c)  $M_\infty = 0.60$ ,  $\alpha = 17.5^\circ$ .

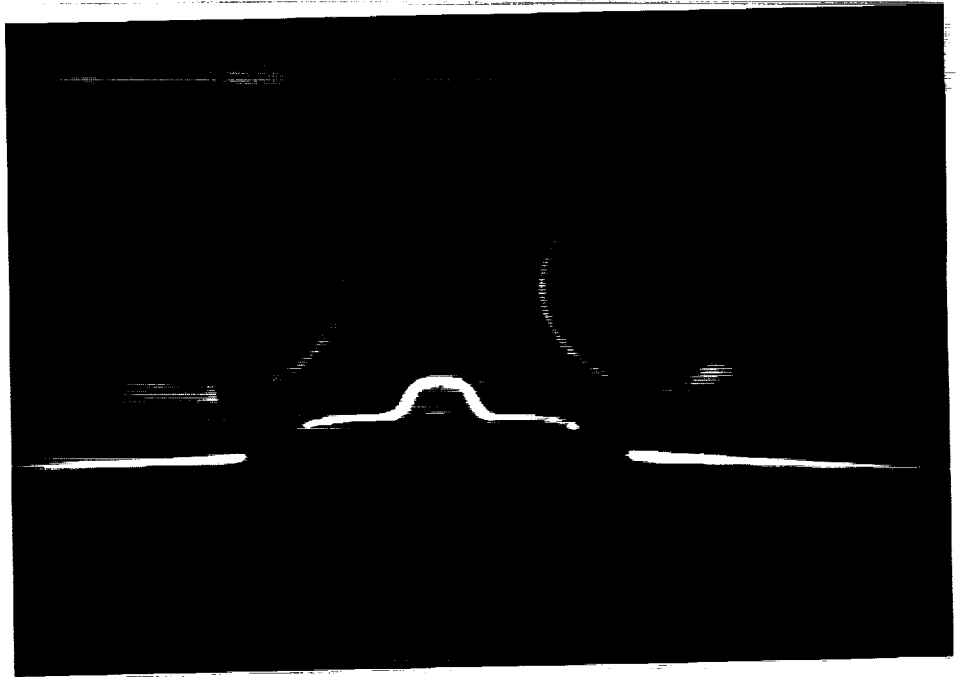
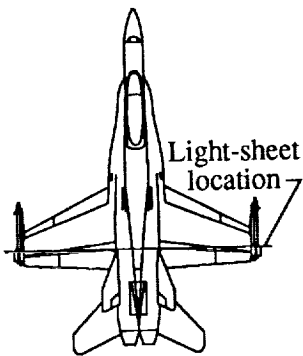


(d)  $M_\infty = 0.80$ ,  $\alpha = 17.5^\circ$ .

Figure 36. Continued.

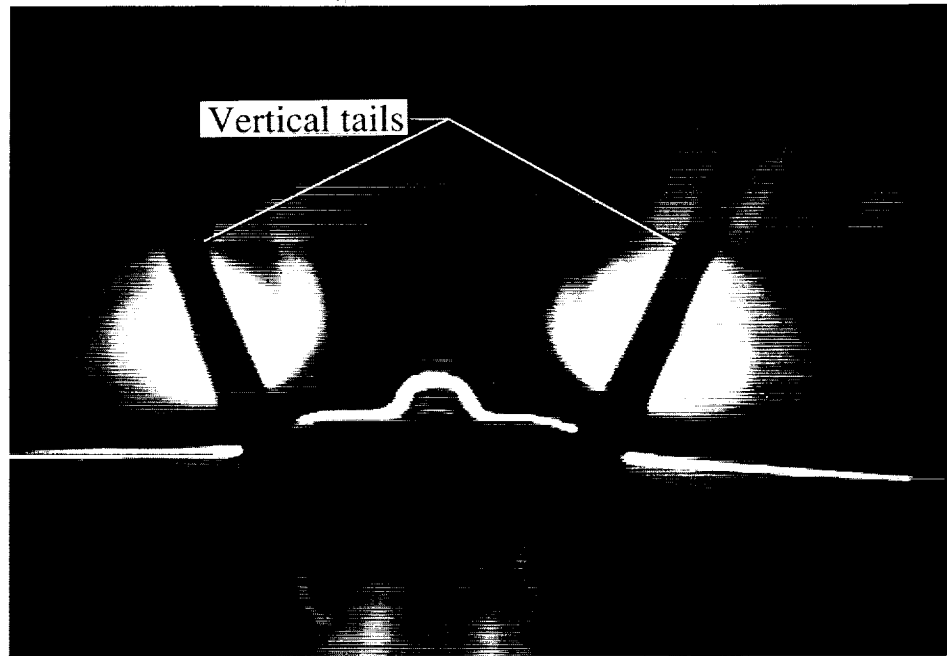
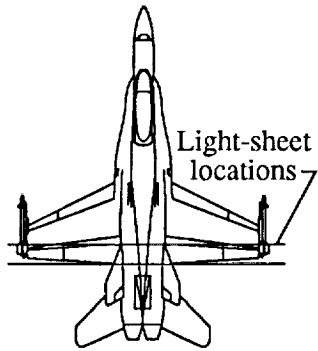


(e)  $M_\infty = 0.60, \alpha = 20^\circ$ .

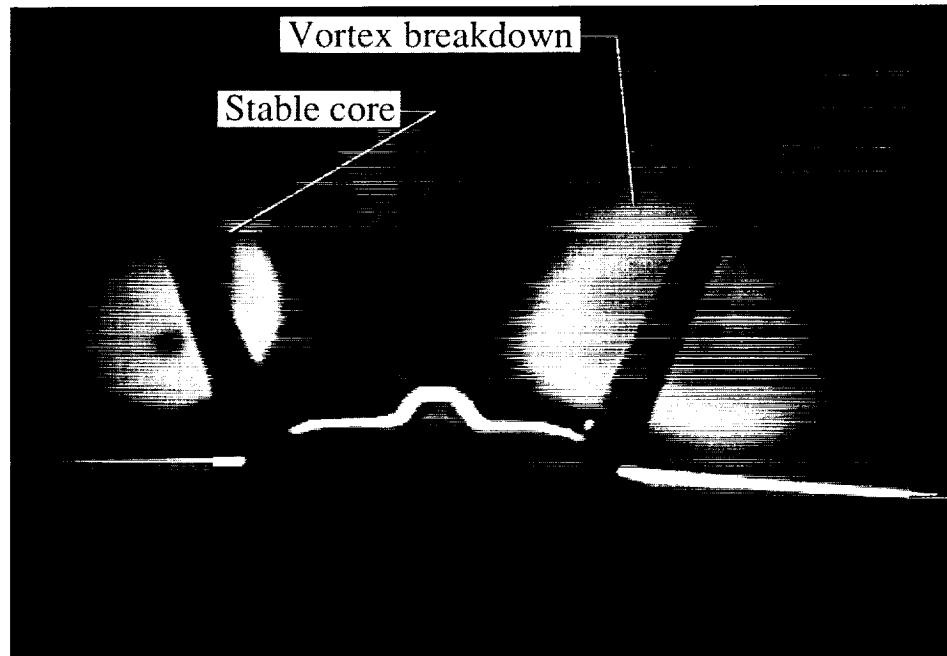
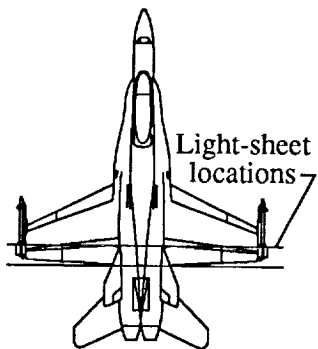


(f)  $M_\infty = 0.80, \alpha = 20^\circ$ .

Figure 36. Concluded.

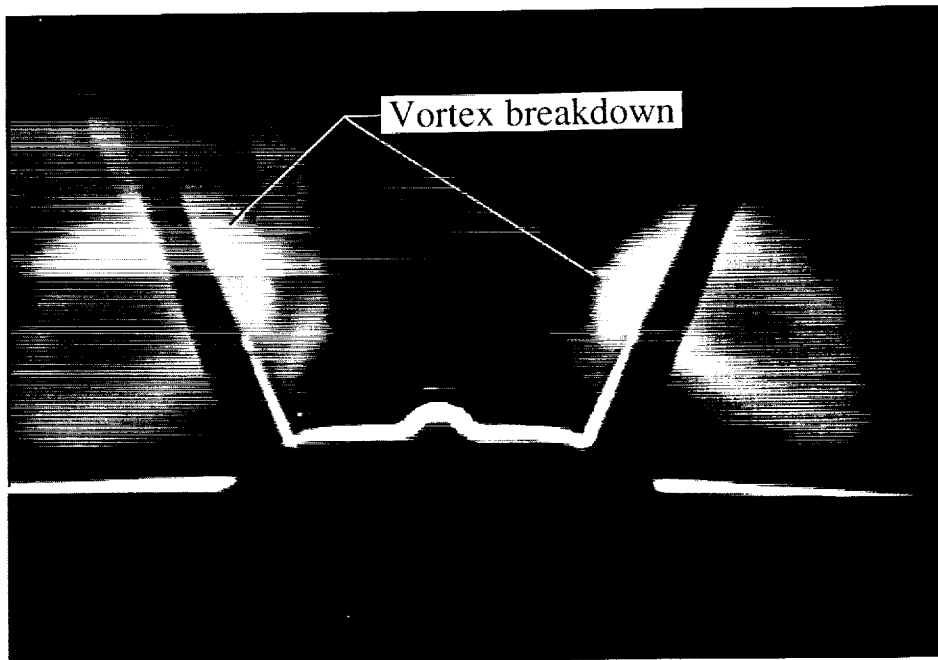
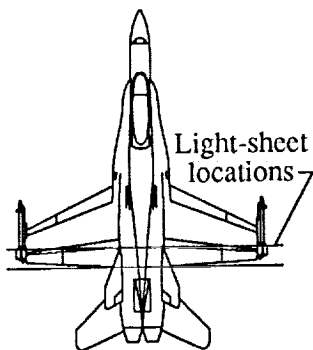


(a)  $\beta = 0^\circ$ , FS 525 (31.50).

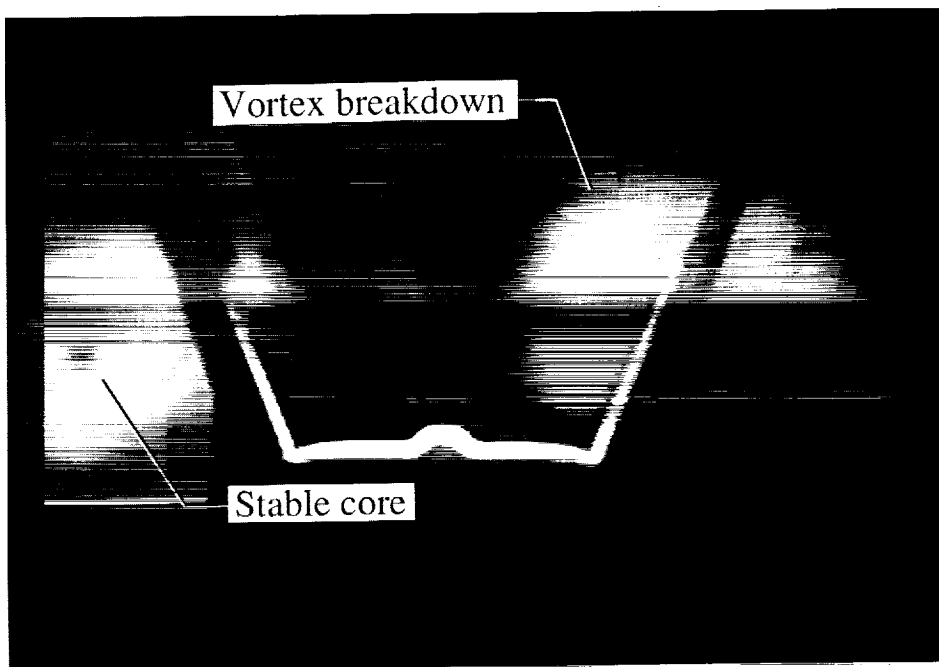
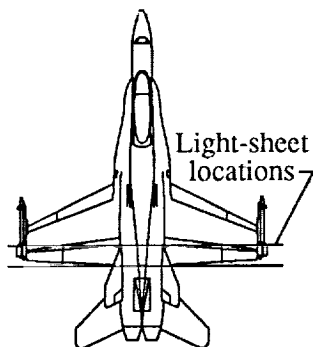


(b)  $\beta = 4^\circ$ , FS 525 (31.50).

Figure 37. Effect of sideslip on cross-flow patterns about baseline F/A-18 model at  $M_\infty = 0.6$ ;  $Re_c = 1.32 \times 10^6$ ; and  $\alpha = 20^\circ$ . Dimensions are in inches full scale (0.06 scale).



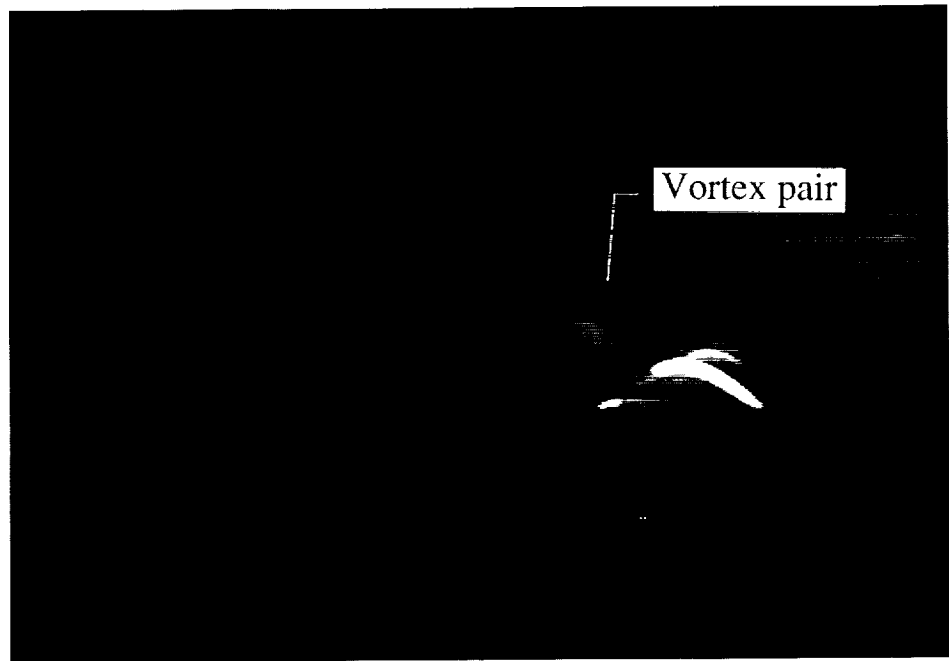
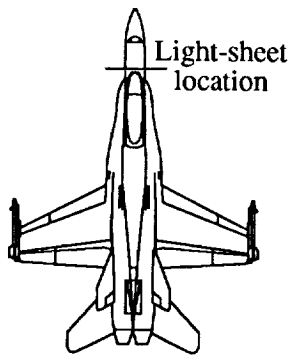
(c)  $\beta = 0^\circ$ , FS 567 (34.02).



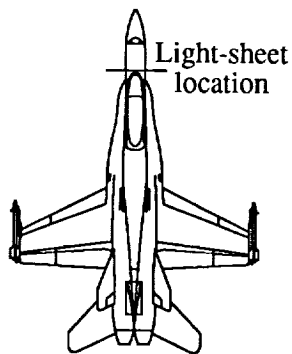
(d)  $\beta = 4^\circ$ , FS 567 (34.02).

Figure 37. Concluded.



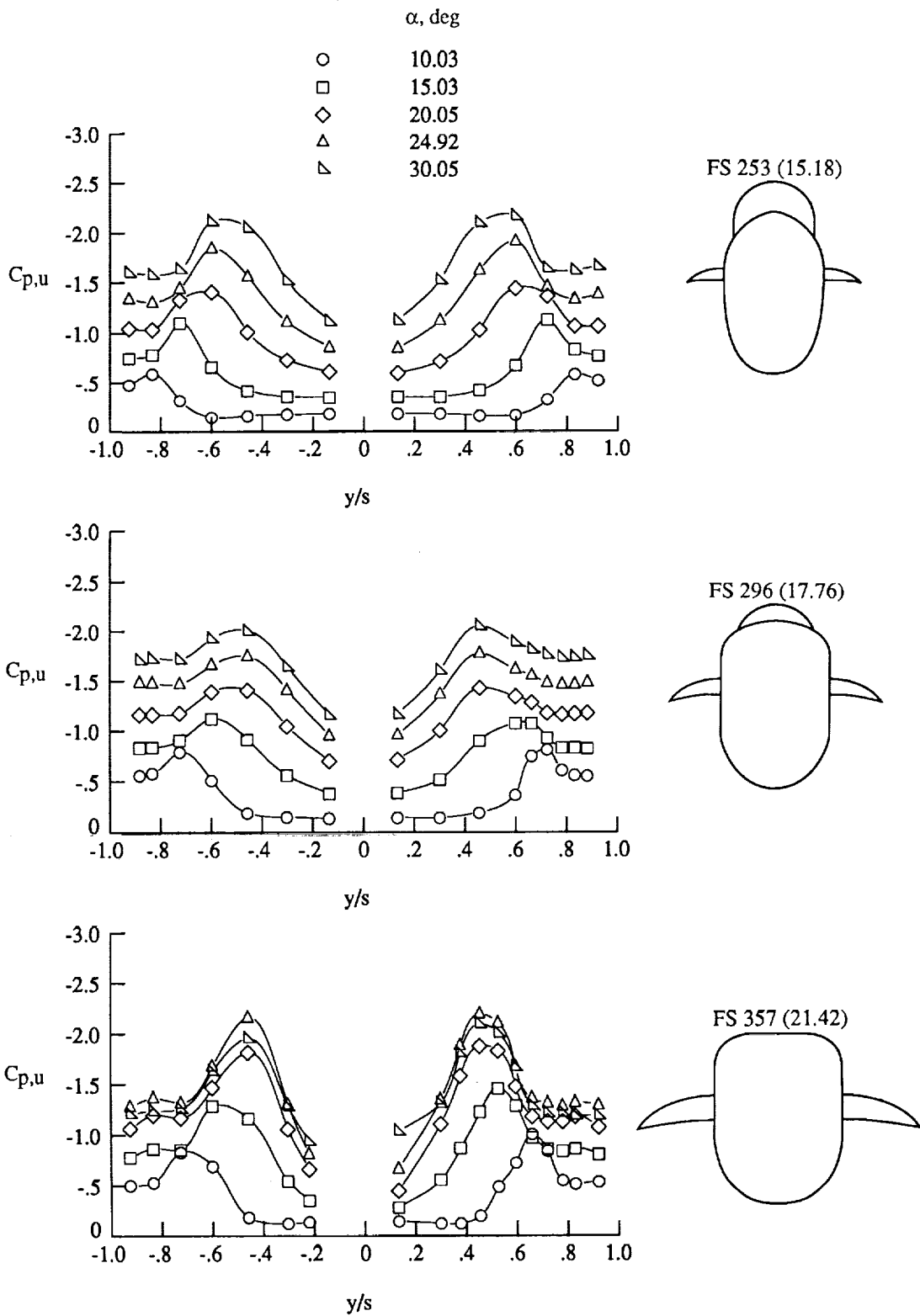


(a) FS 163 (9.78).



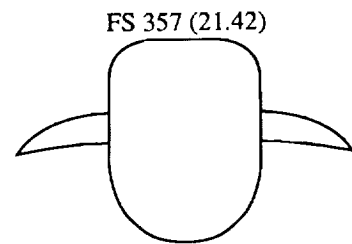
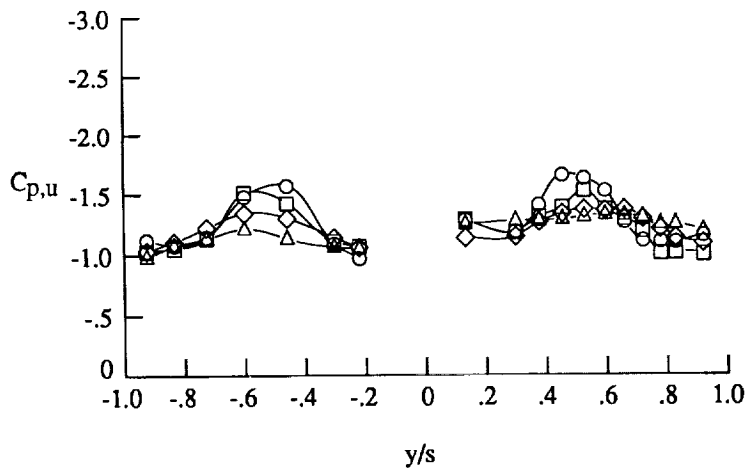
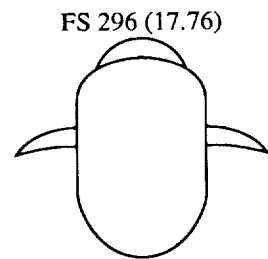
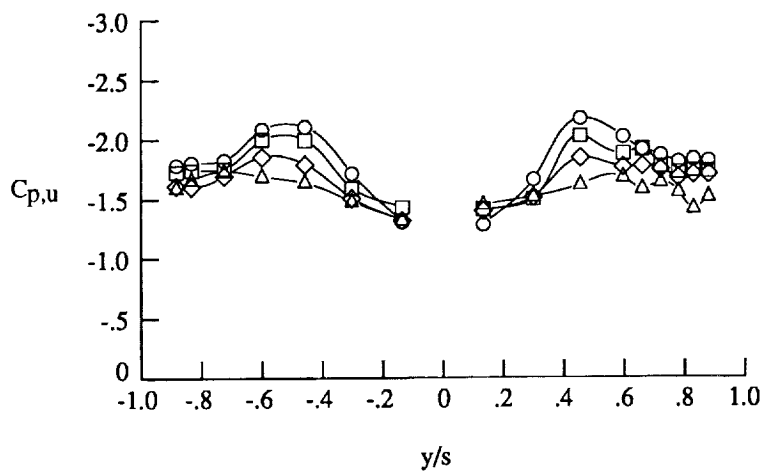
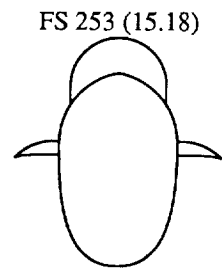
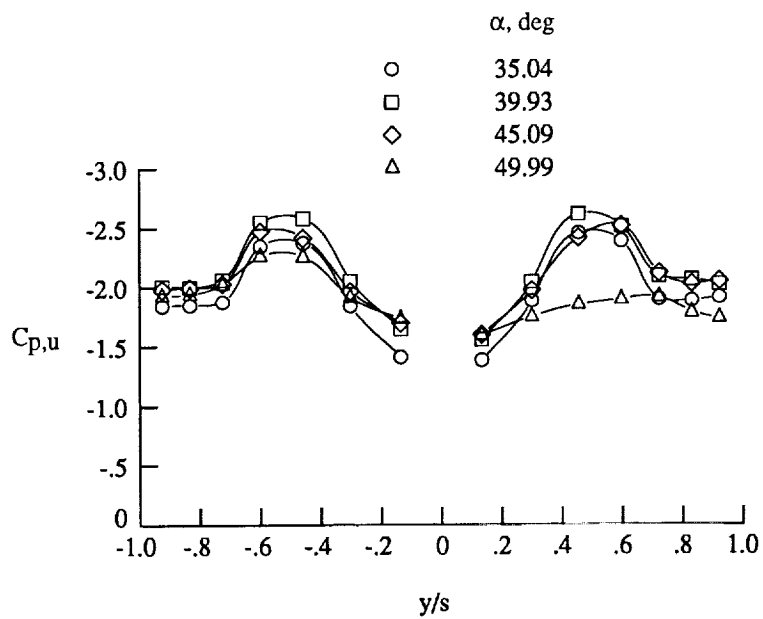
(b) Close-up of vortex pair.

Figure 38. Forebody cross flow about baseline F/A-18 model at  $M_\infty = 0.60$ ,  $Re_z = 1.32 \times 10^6$ , and  $\alpha = 50^\circ$ . Dimensions are in inches full scale (0.06 scale).



(a)  $\alpha = 10^\circ$  to  $30^\circ$ .

Figure 39. Effect of angle of attack on baseline F/A-18 model LEX surface static pressures at  $M_\infty = 0.40$  and  $Re_c = 1.75 \times 10^6$ . Dimensions are in inches full scale (0.06 scale).



(b)  $\alpha = 35^\circ$  to  $50^\circ$ .

Figure 39. Concluded.

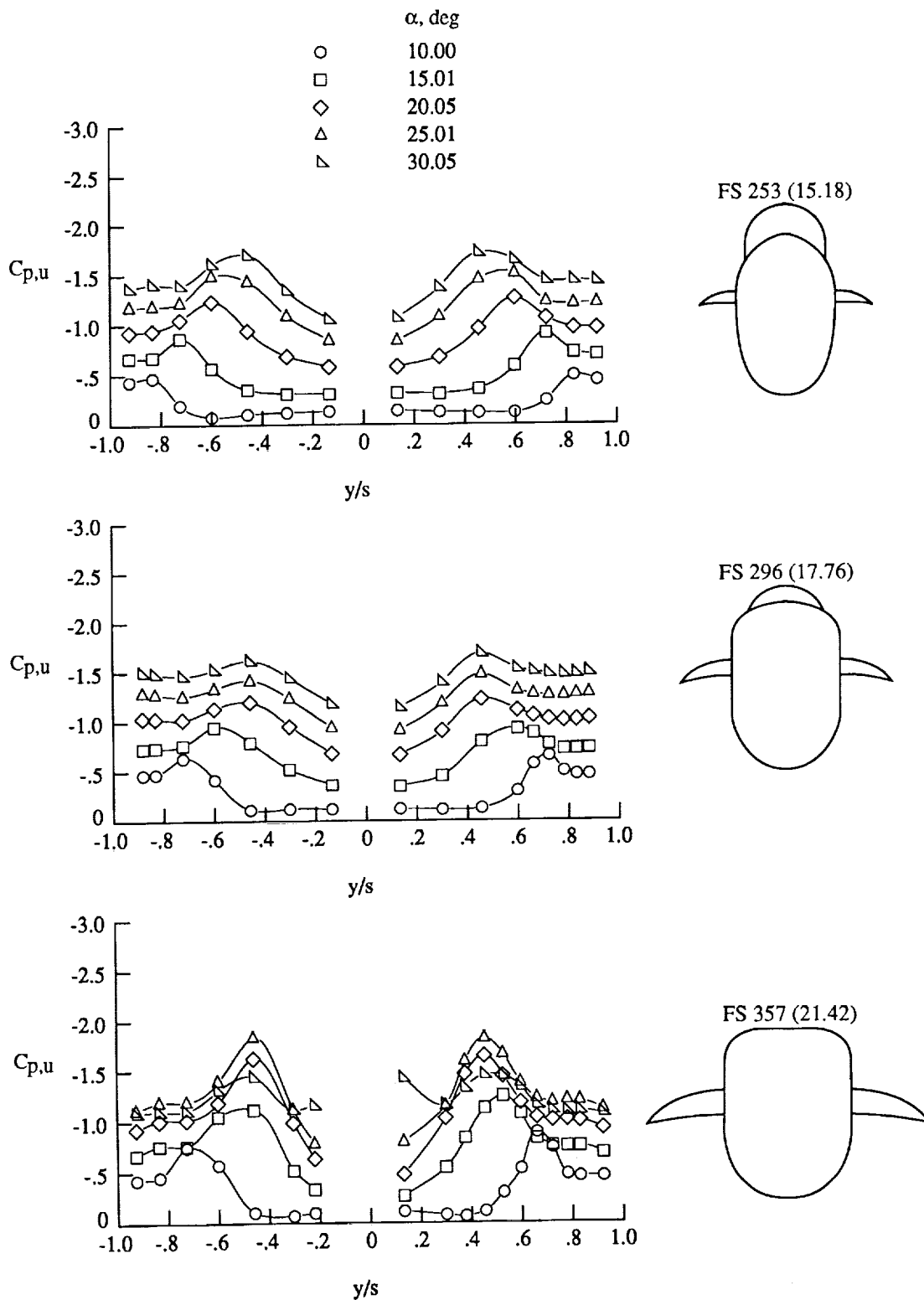
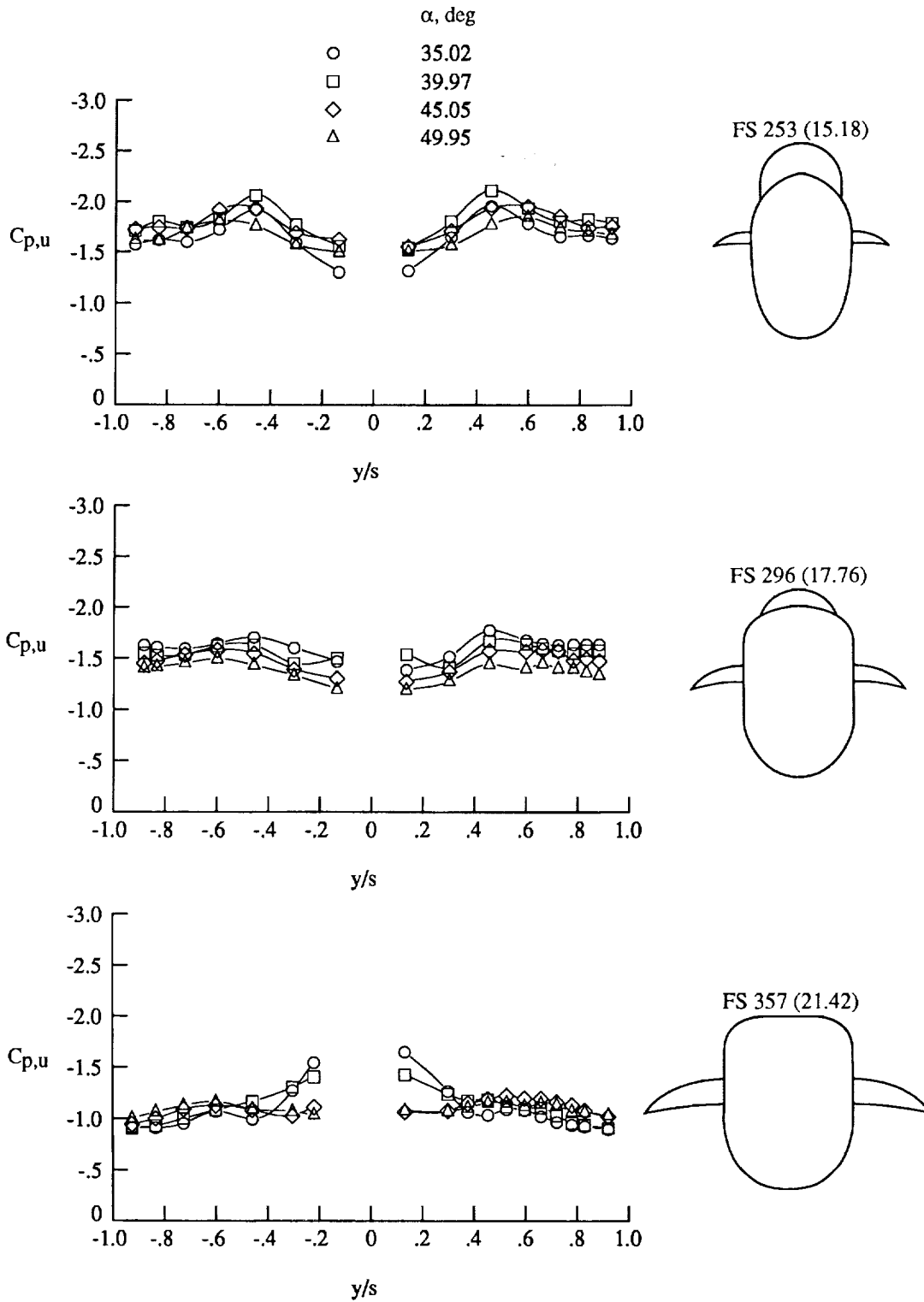


Figure 40. Effect of angle of attack on baseline F/A-18 model LEX surface static pressures at  $M_\infty = 0.60$  and  $Re_{\bar{c}} = 1.32 \times 10^6$ . Dimensions are in inches full scale (0.06 scale).



(b)  $\alpha = 35^\circ$  to  $50^\circ$ .

Figure 40. Concluded.

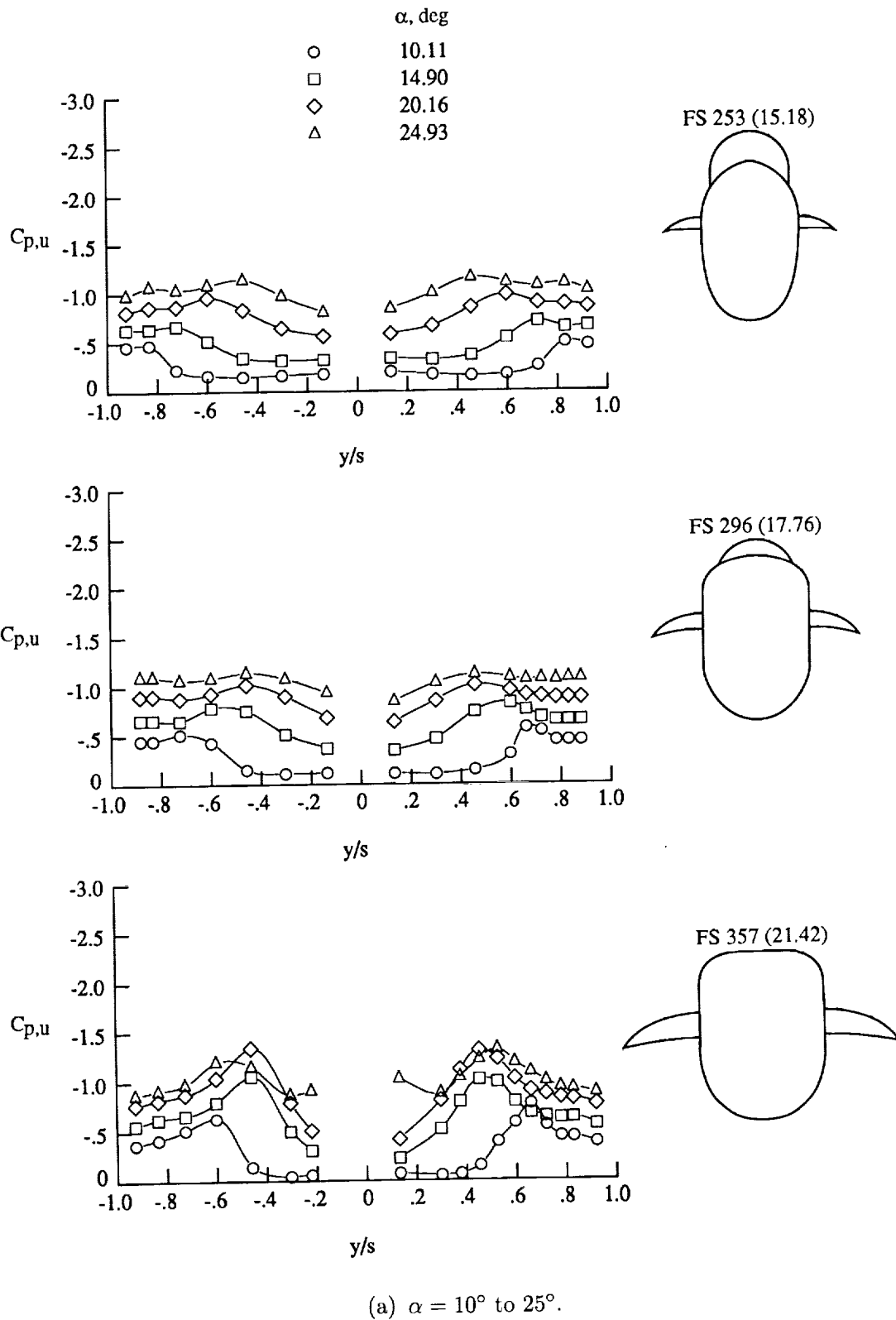
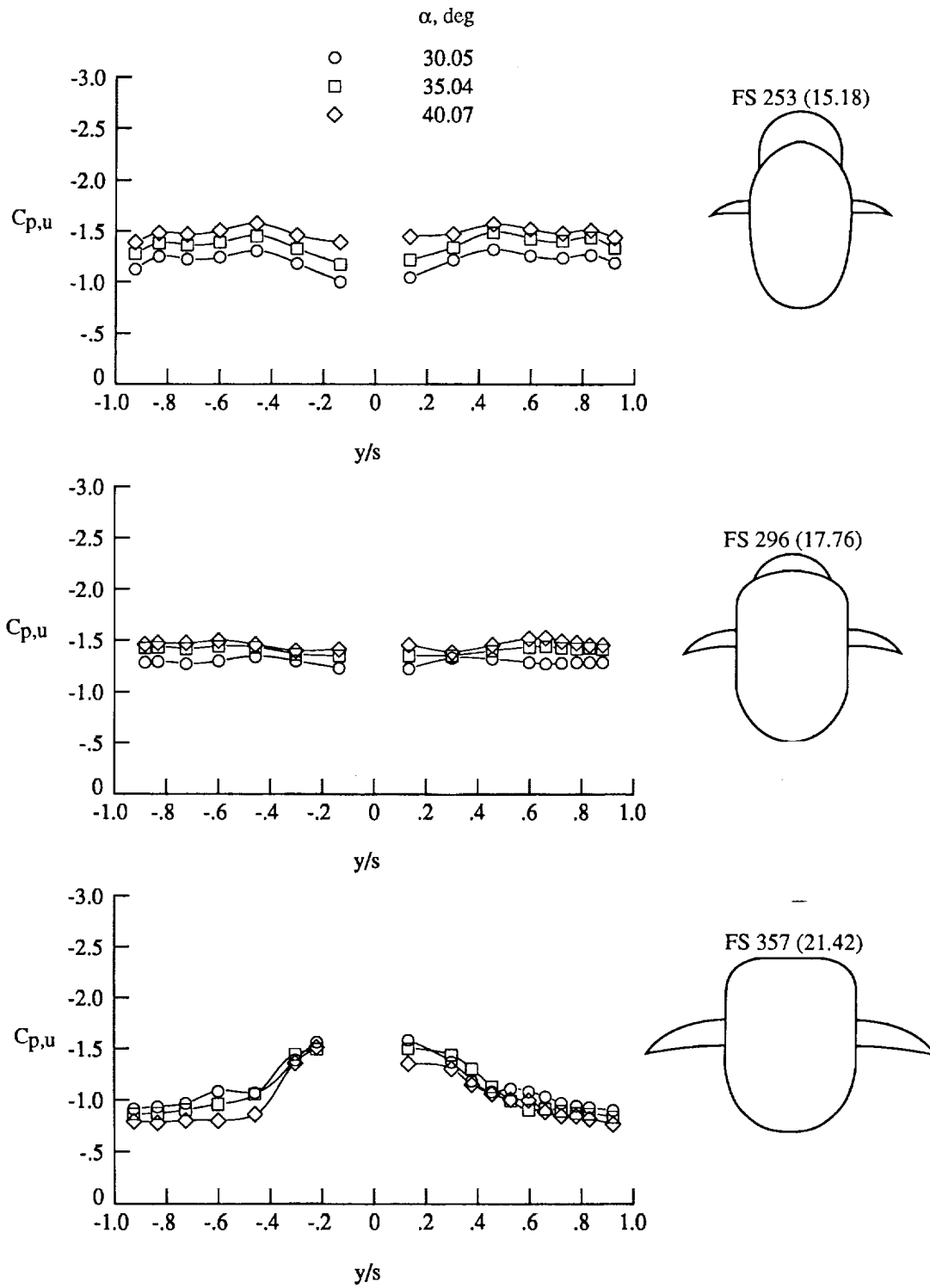
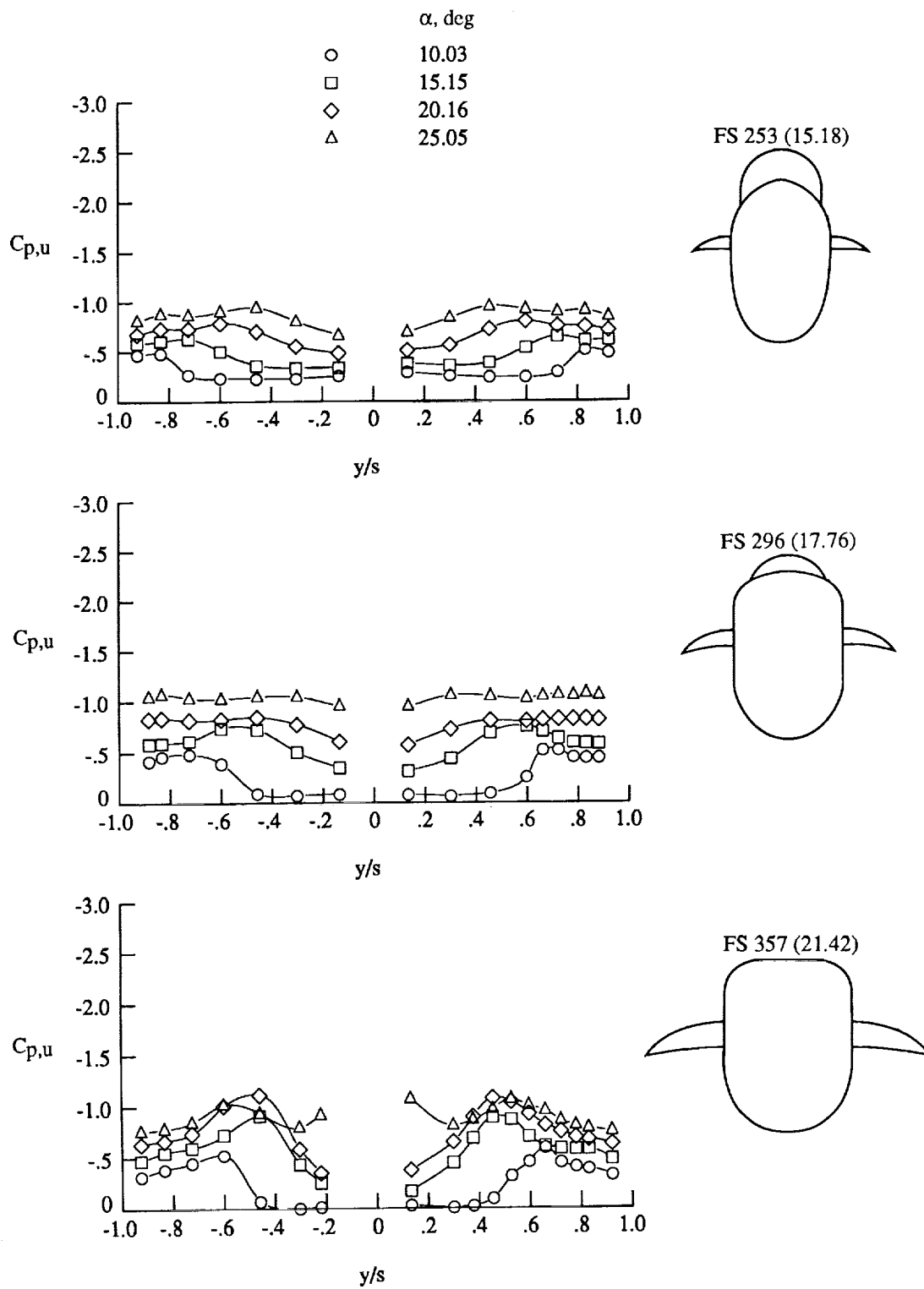


Figure 41. Effect of angle of attack on baseline F/A-18 model LEX surface static pressures at  $M_\infty = 0.80$  and  $Re_{\bar{c}} = 1.02 \times 10^6$ . Dimensions are in inches full scale (0.06 scale).



(b)  $\alpha = 30^\circ$  to  $40^\circ$ .

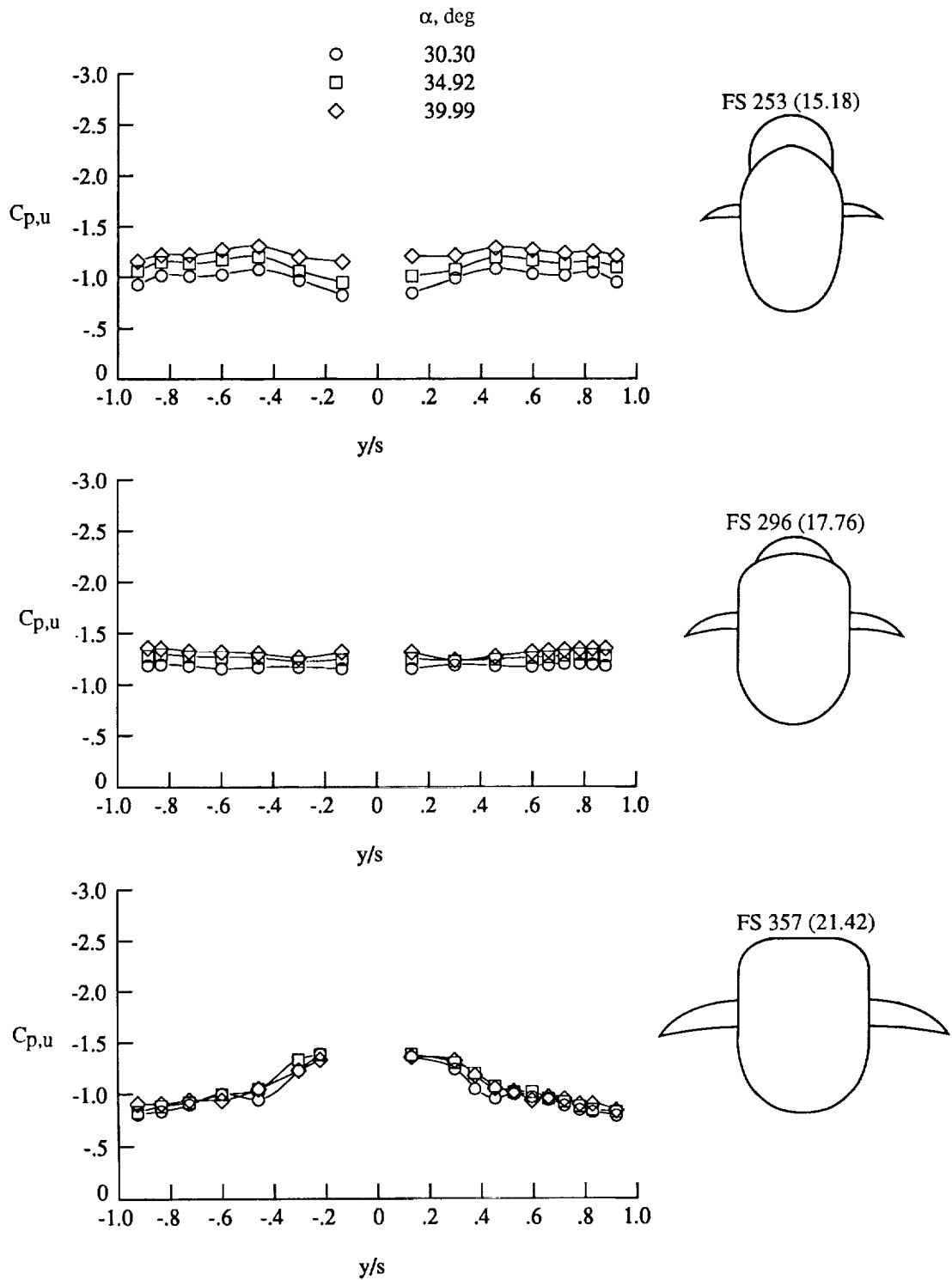
Figure 41. Concluded.



(a)  $\alpha = 10^\circ$  to  $25^\circ$ .

Figure 42. Effect of angle of attack on baseline F/A-18 model LEX surface static pressures at  $M_\infty = 0.90$  and  $Re_c = 1.02 \times 10^6$ . Dimensions are in inches full scale (0.06 scale).





(b)  $\alpha = 30^\circ$  to  $40^\circ$ .

Figure 42. Concluded.

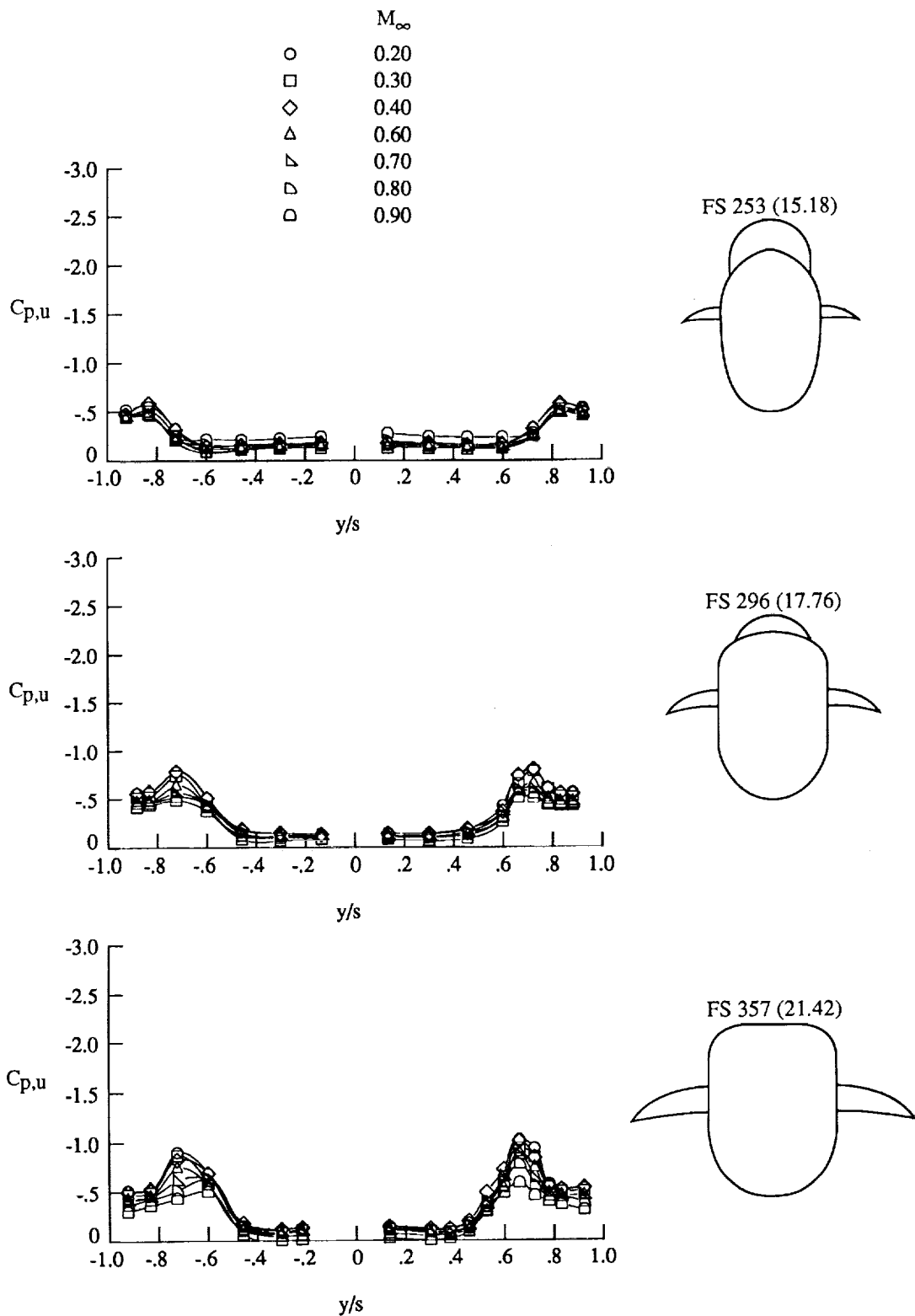


Figure 43. Effect of Mach number on baseline F/A-18 model LEX surface static pressures at  $\alpha = 10^\circ$ . Dimensions are in inches full scale (0.06 scale).

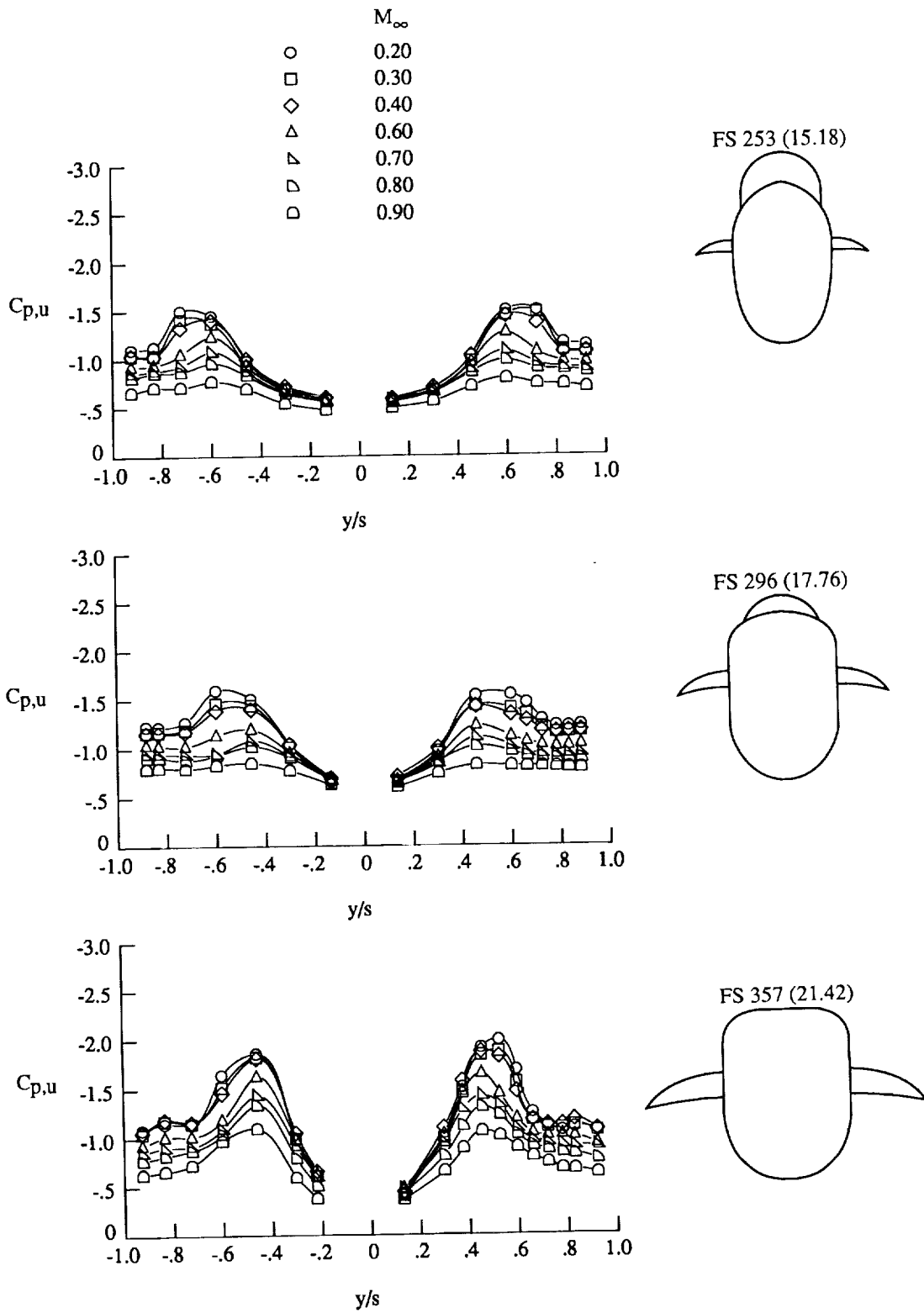


Figure 44. Effect of Mach number on baseline F/A-18 model LEX surface static pressures at  $\alpha = 20^\circ$ . Dimensions are in inches full scale (0.06 scale).

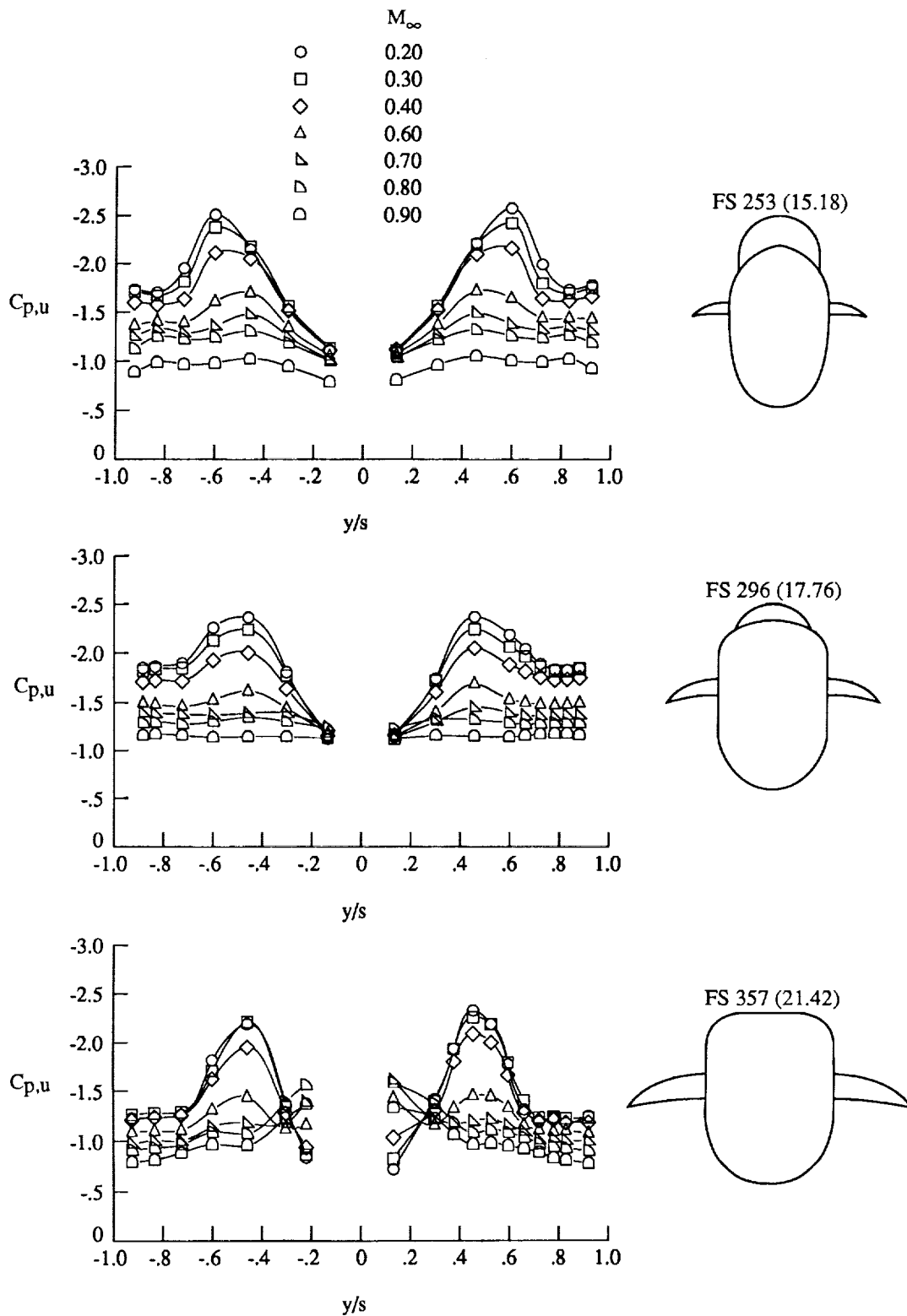


Figure 45. Effect of Mach number on baseline F/A-18 model LEX surface static pressures at  $\alpha = 30^\circ$ . Dimensions are in inches full scale (0.06 scale).

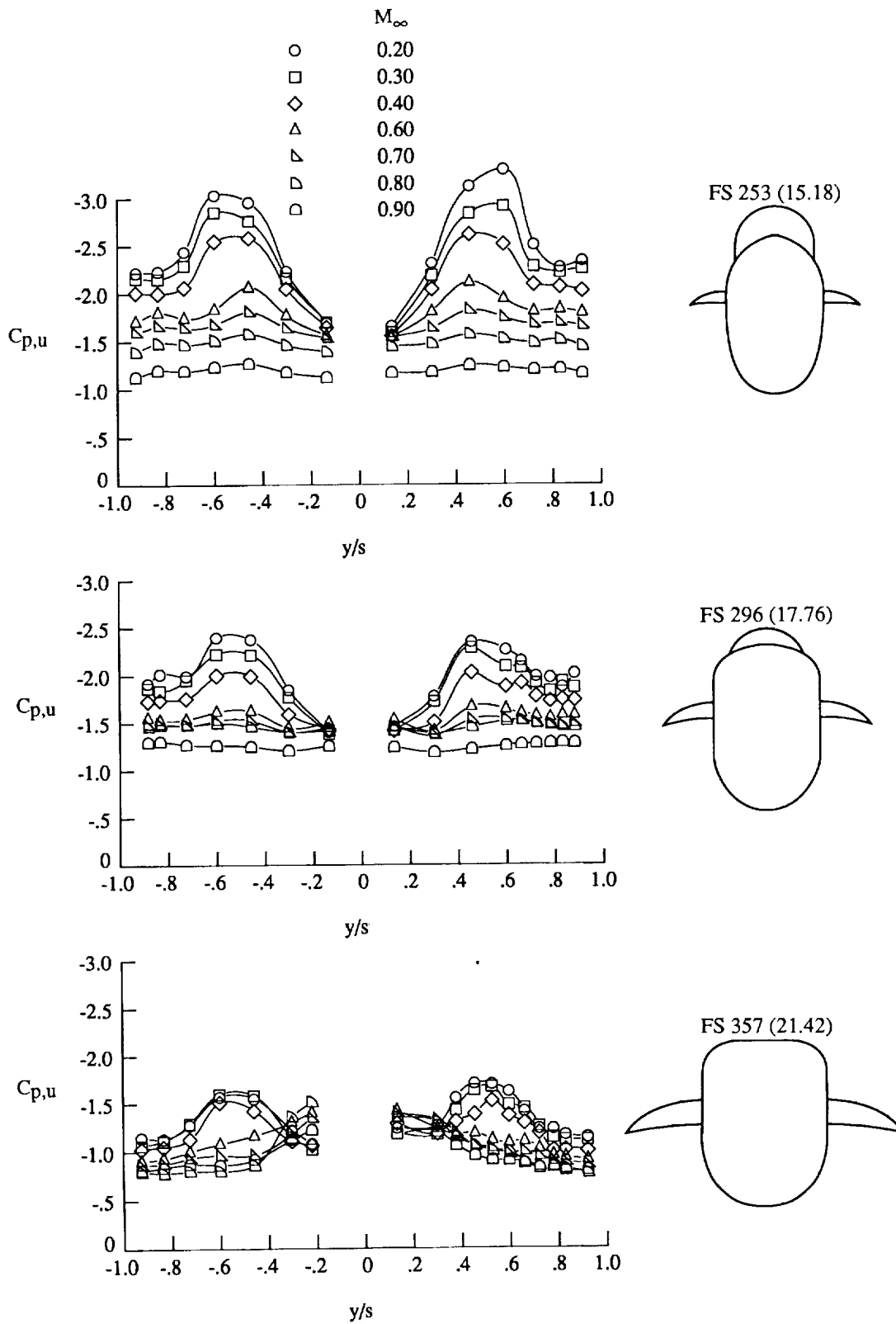


Figure 46. Effect of Mach number on baseline F/A-18 model LEX surface static pressures at  $\alpha = 40^\circ$ . Dimensions are in inches full scale (0.06 scale).

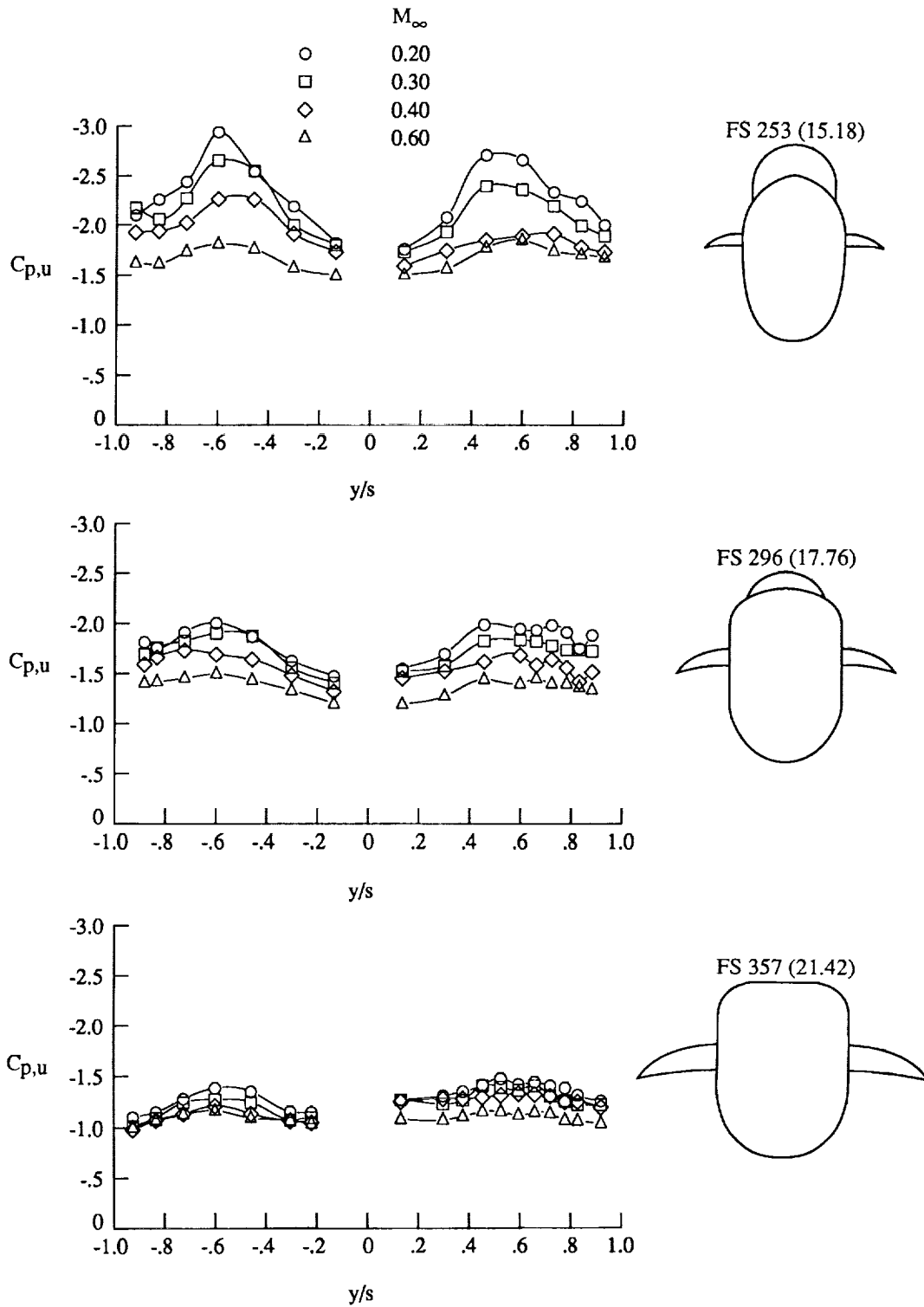


Figure 47. Effect of Mach number on baseline F/A-18 model LEX surface static pressures at  $\alpha = 50^\circ$ . Dimensions are in inches full scale (0.06 scale).

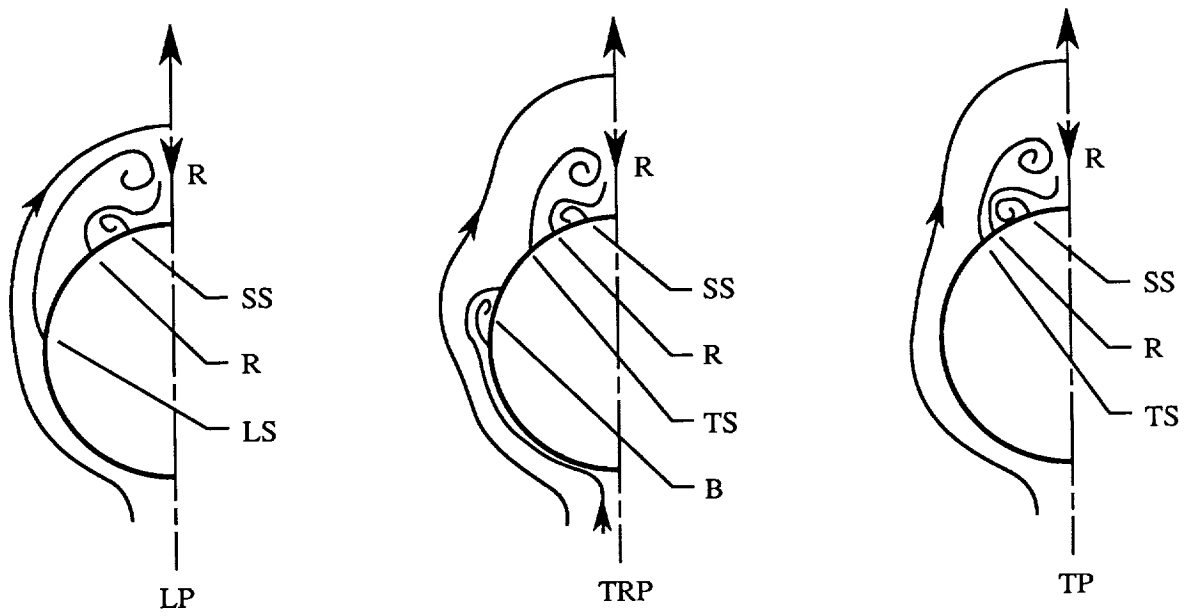
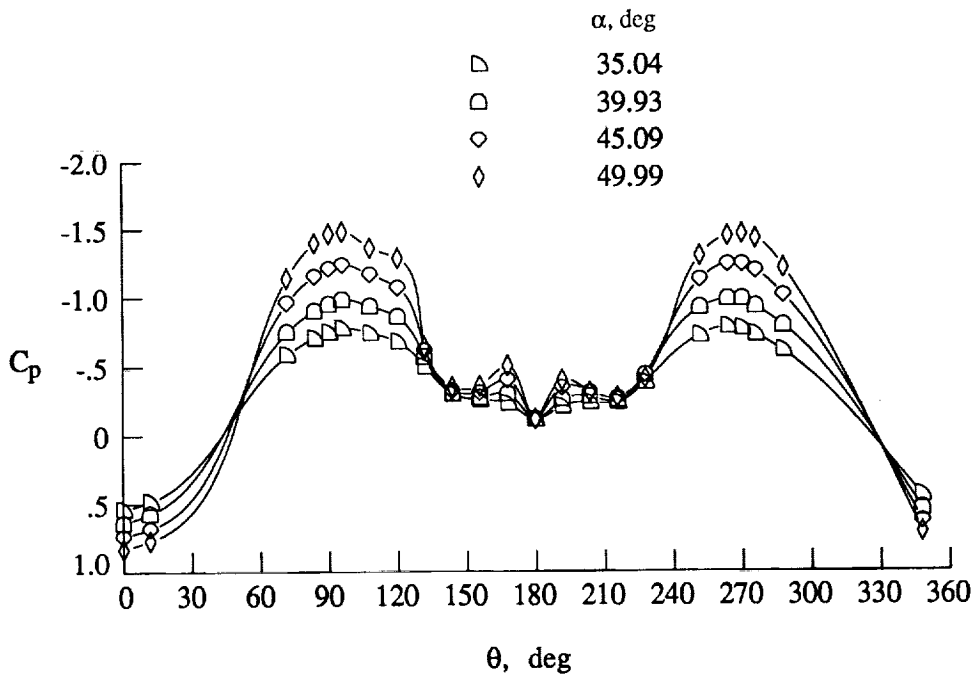
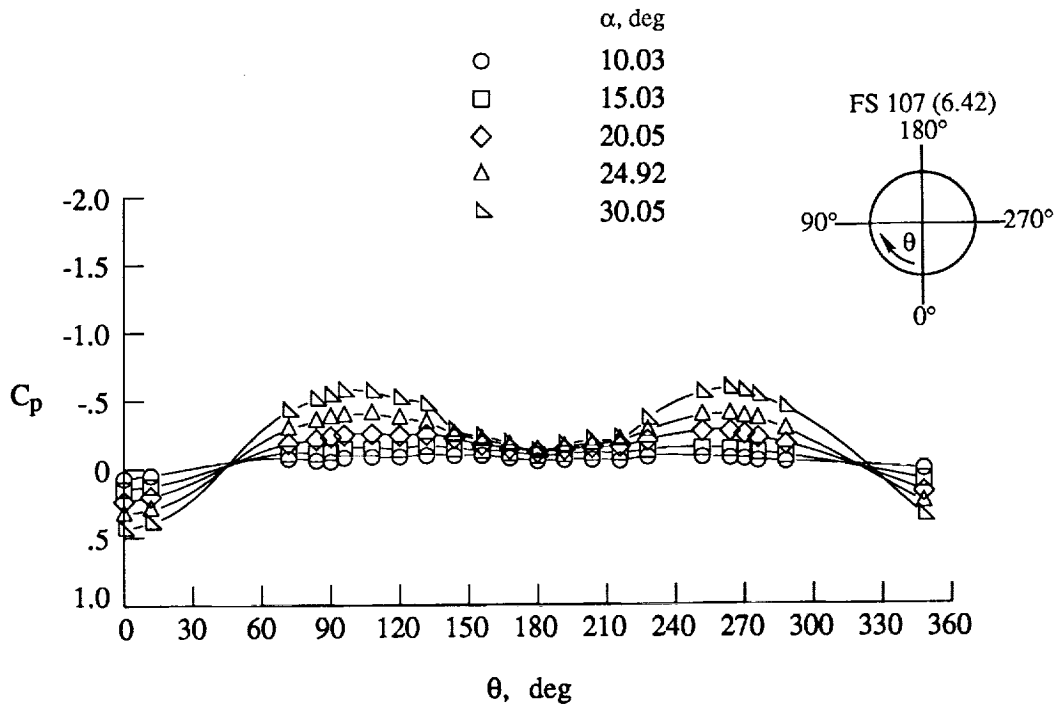


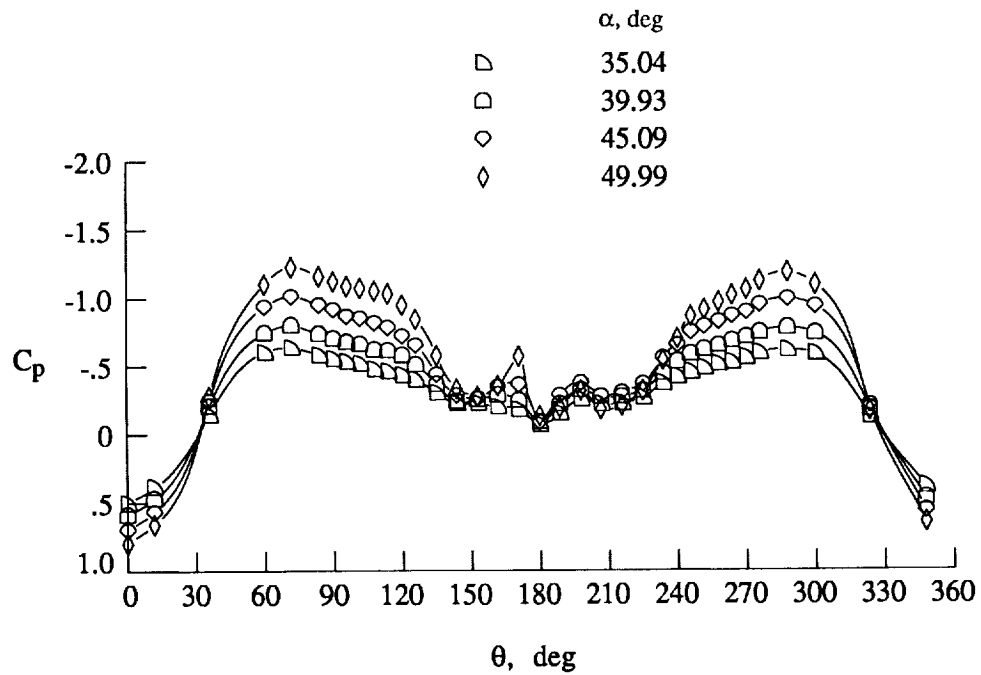
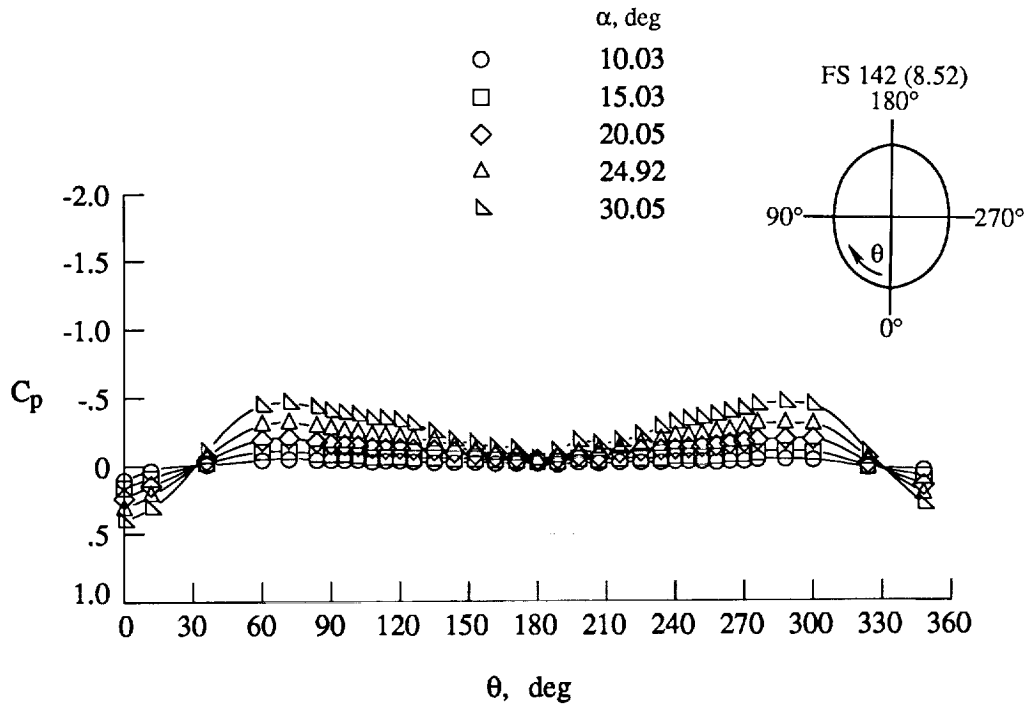
Figure 48. Sketches of cross-flow patterns about a body at a high angle of attack (from ref. 2).



(a) FS 107 (6.42).

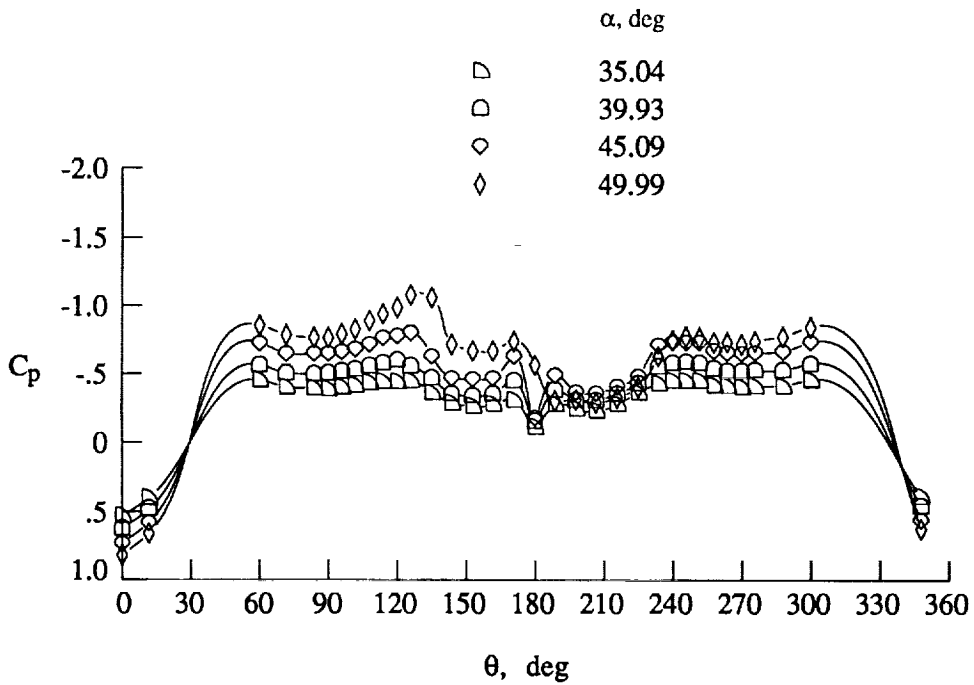
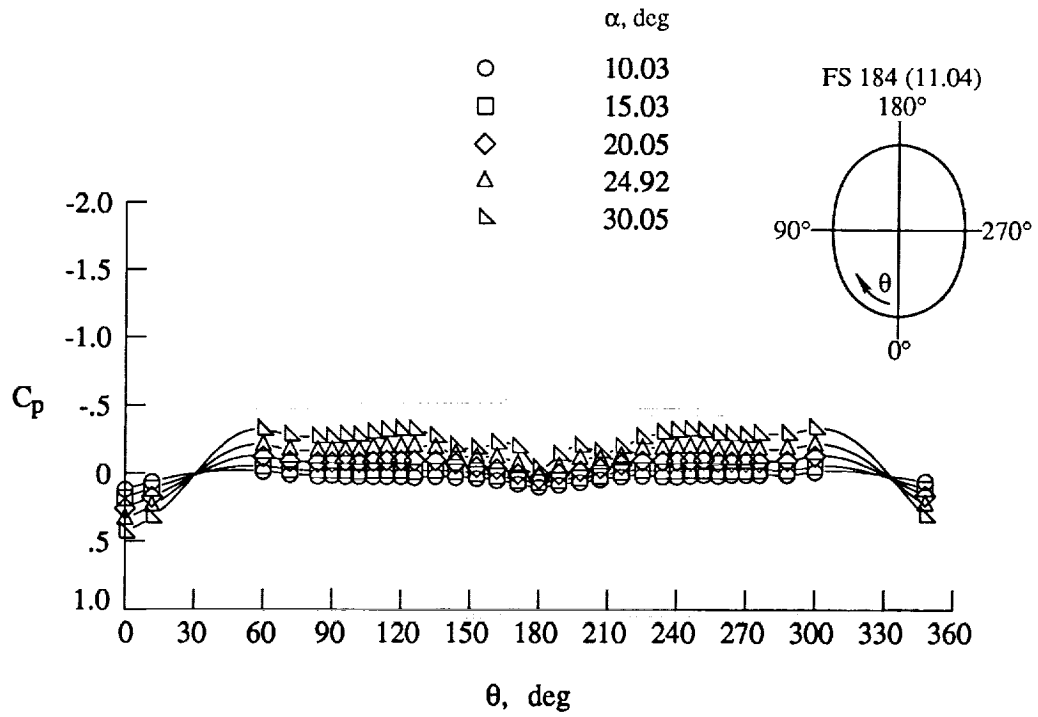
Figure 49. Effect of angle of attack on forebody surface static pressures at  $M_\infty = 0.40$  and  $Re_{\bar{c}} = 1.75 \times 10^6$ . Dimensions are in inches full scale (0.06 scale).





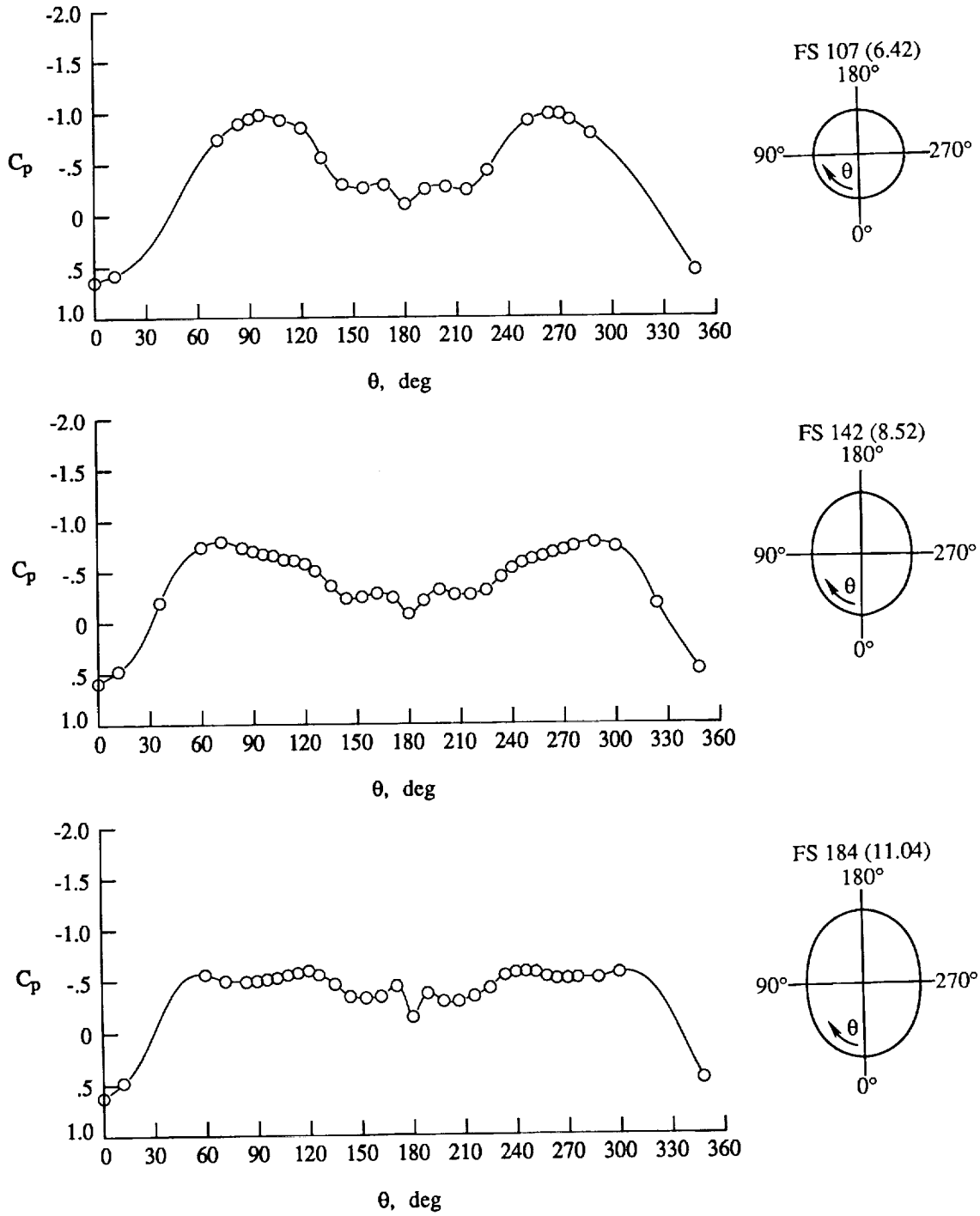
(b) FS 142 (8.52).

Figure 49. Continued.



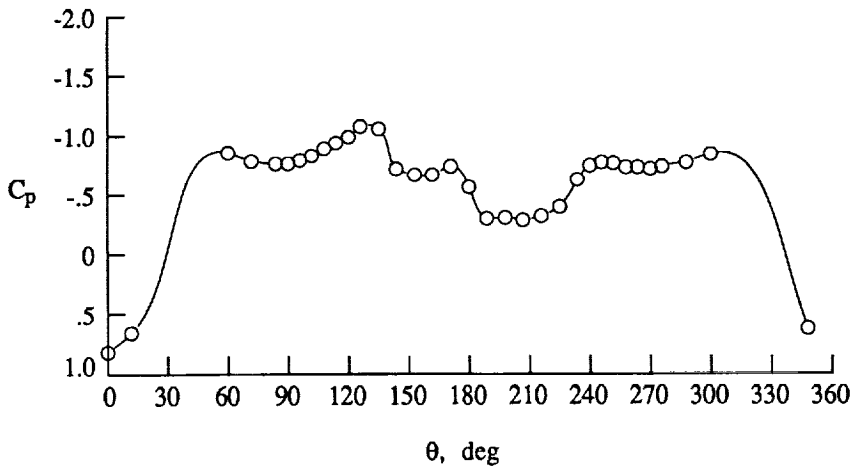
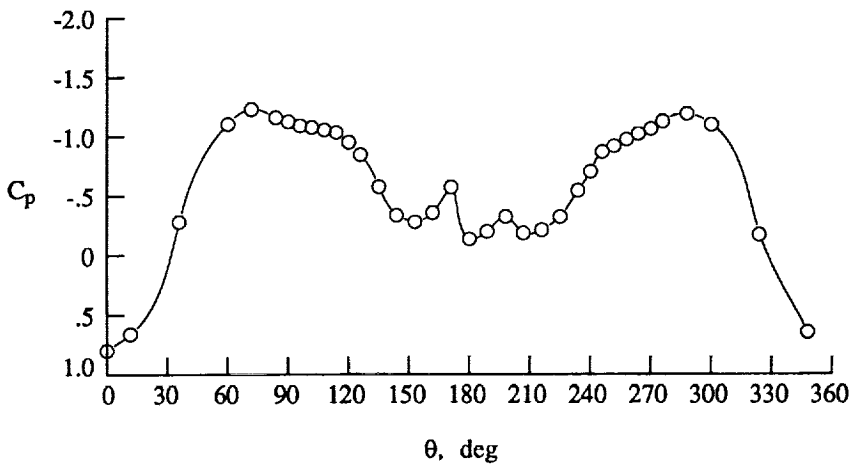
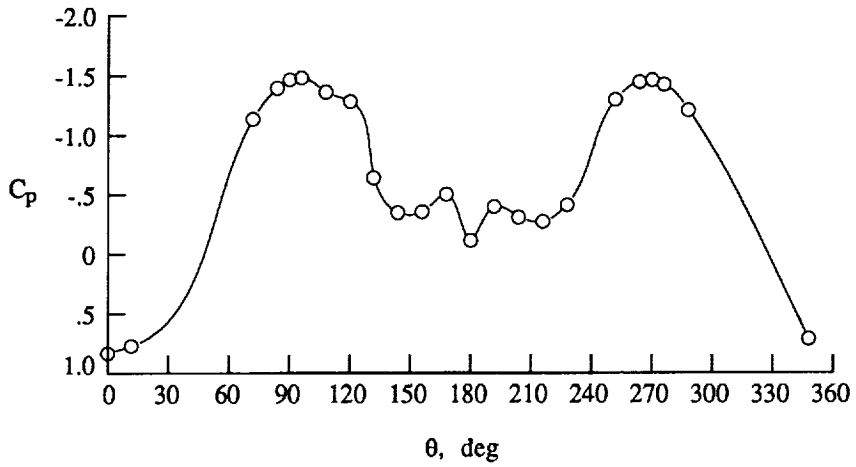
(c) FS 184 (11.04).

Figure 49. Concluded.



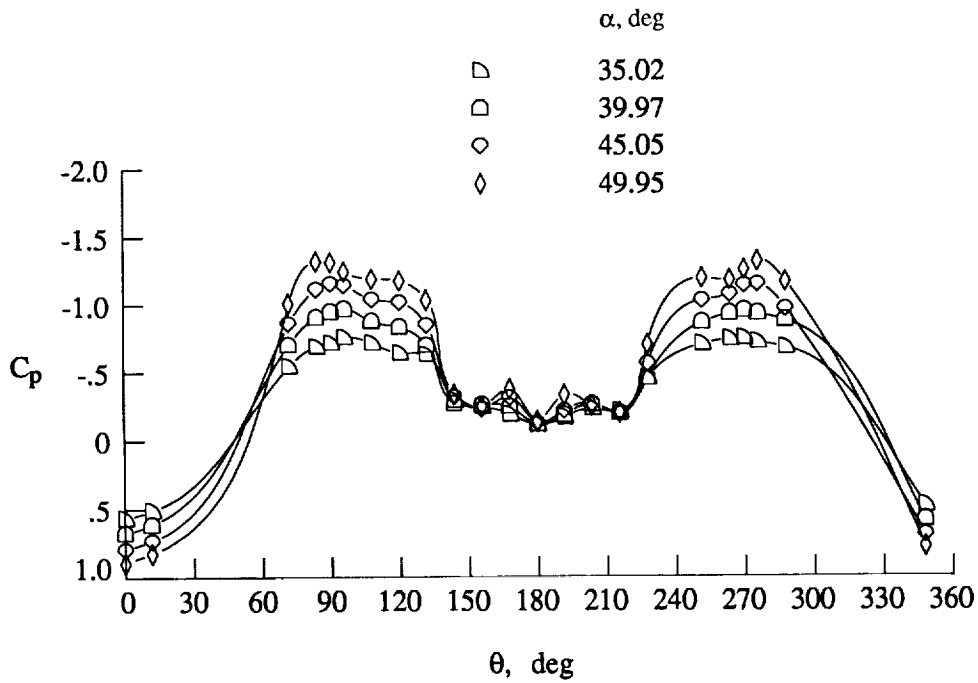
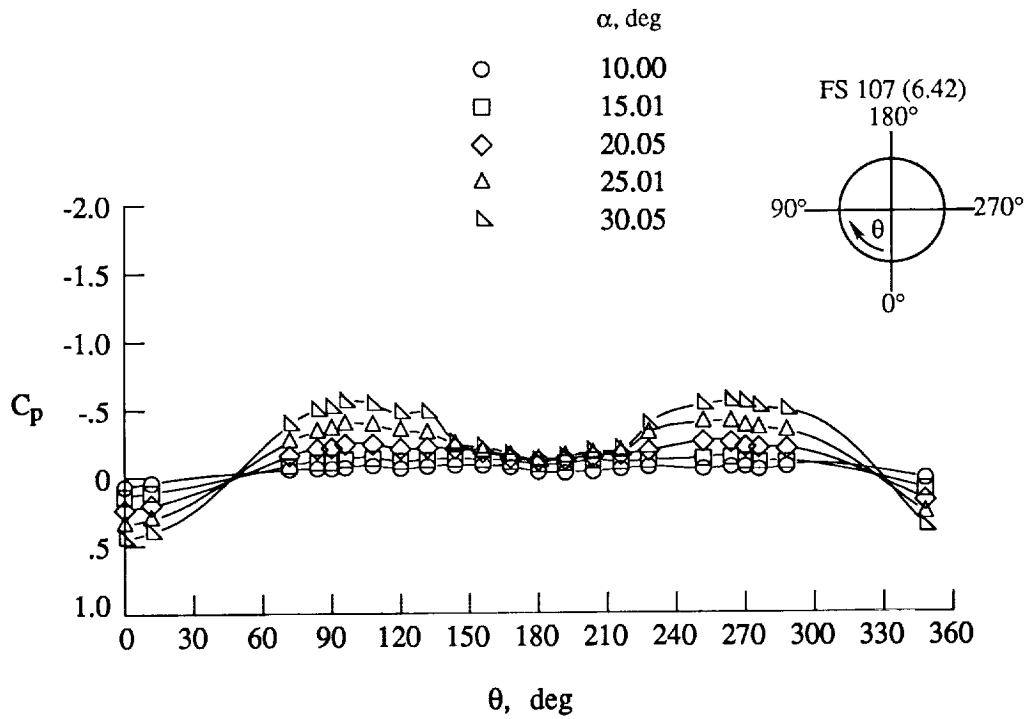
(a)  $\alpha = 40^\circ$ .

Figure 50. Forebody surface static pressures on baseline F/A-18 model at  $M_\infty = 0.40$  and  $Re_c = 1.75 \times 10^6$ . Dimensions are in inches full scale (0.06 scale).



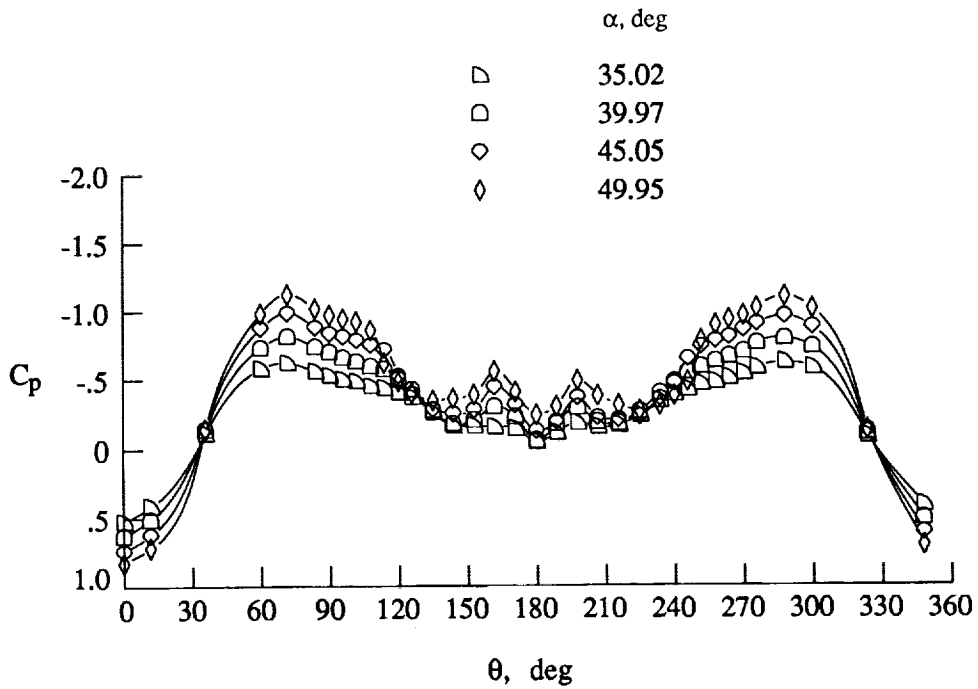
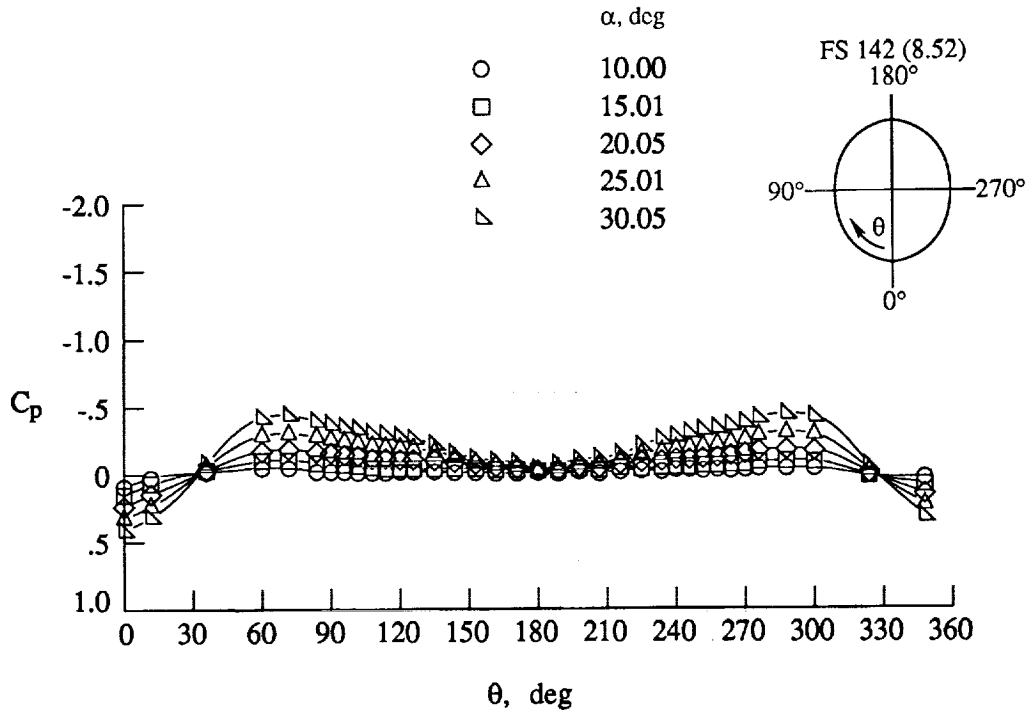
(b)  $\alpha = 50^\circ$ .

Figure 50. Concluded.



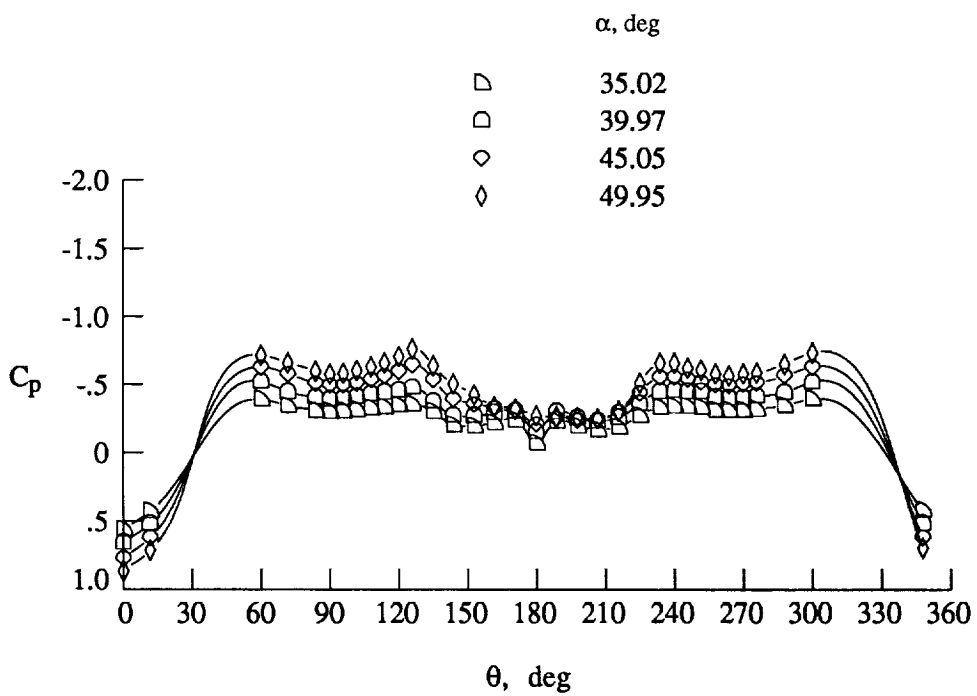
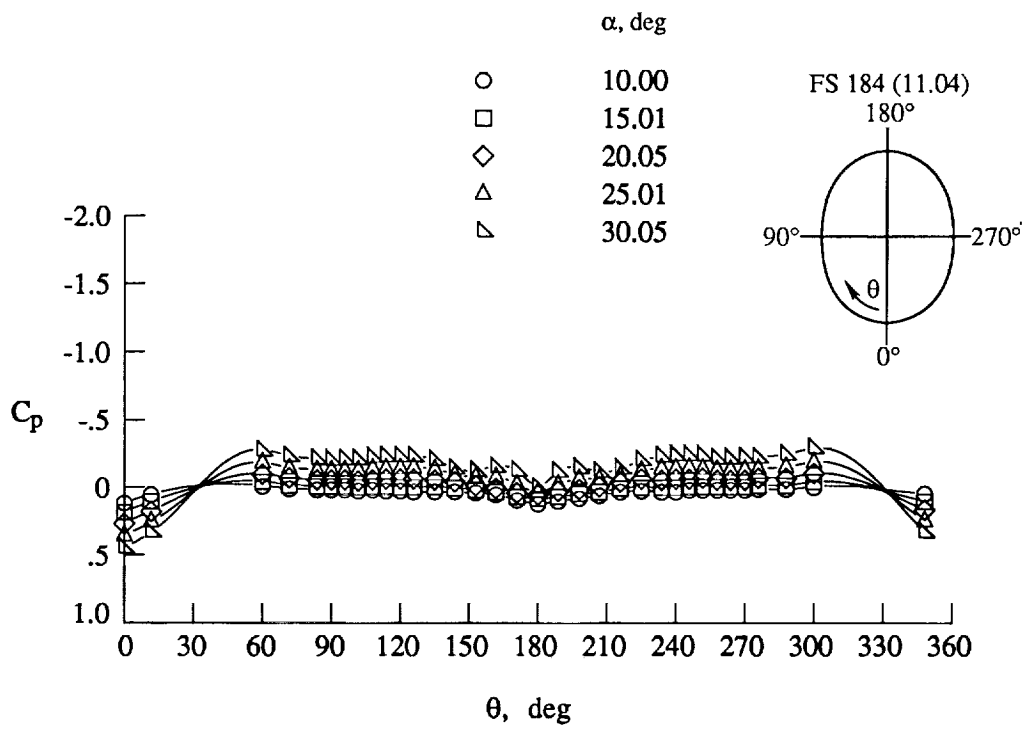
(a) FS 107 (6.42).

Figure 51. Effect of angle of attack on baseline F/A-18 model forebody surface static pressures at  $M_\infty = 0.60$  and  $Re_{\bar{c}} = 1.32 \times 10^6$ . Dimensions are in inches full scale (0.06 scale).



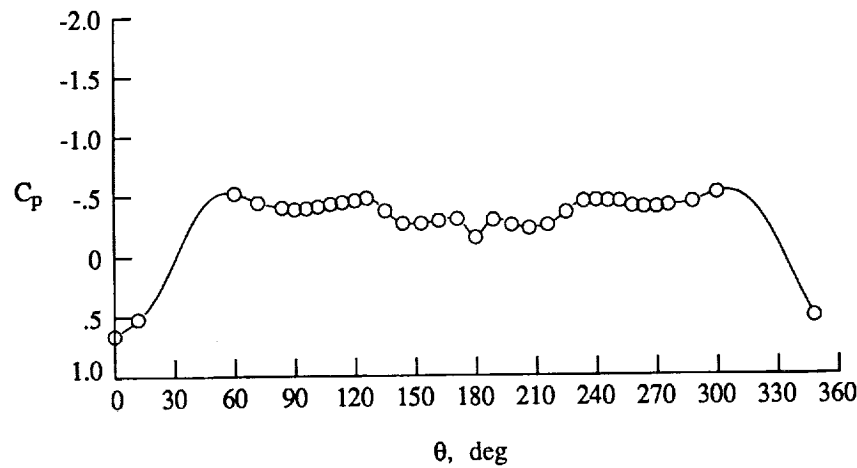
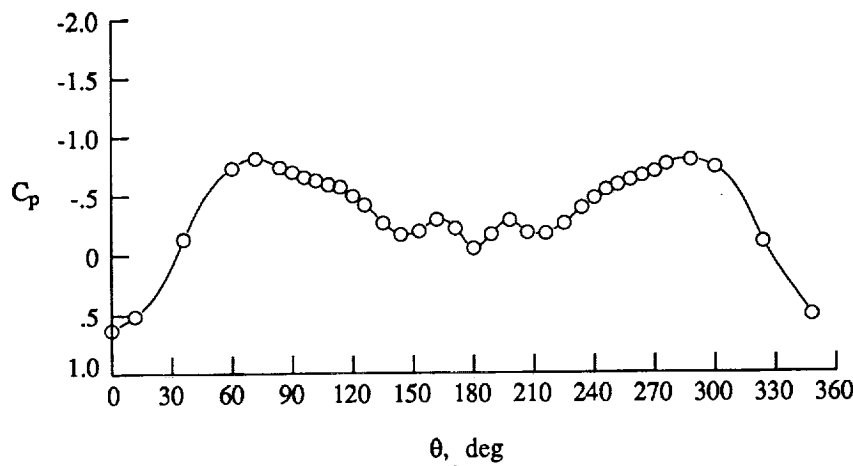
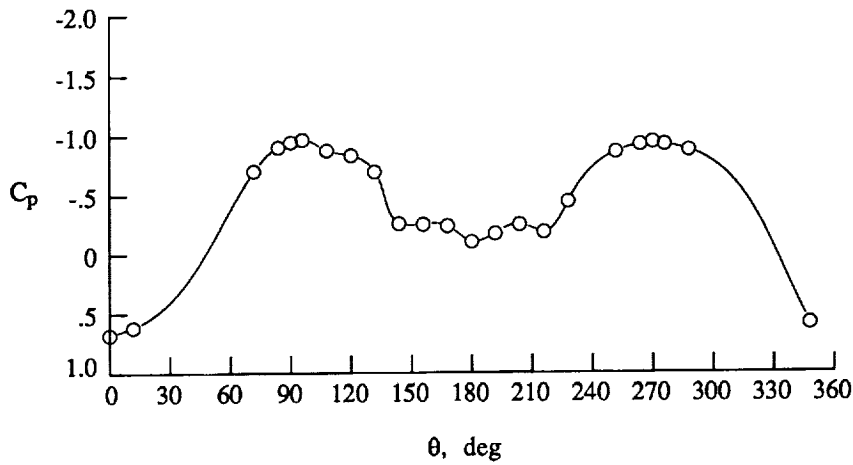
(b) FS 142 (8.52).

Figure 51. Continued.



(c) FS 184 (11.04).

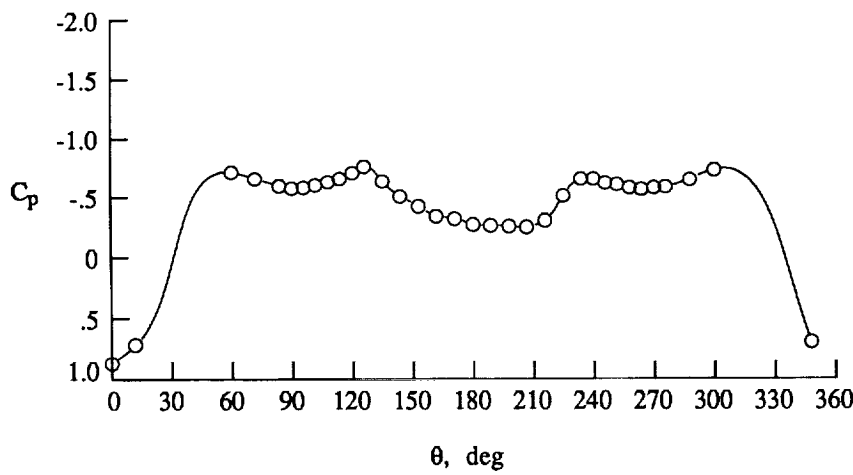
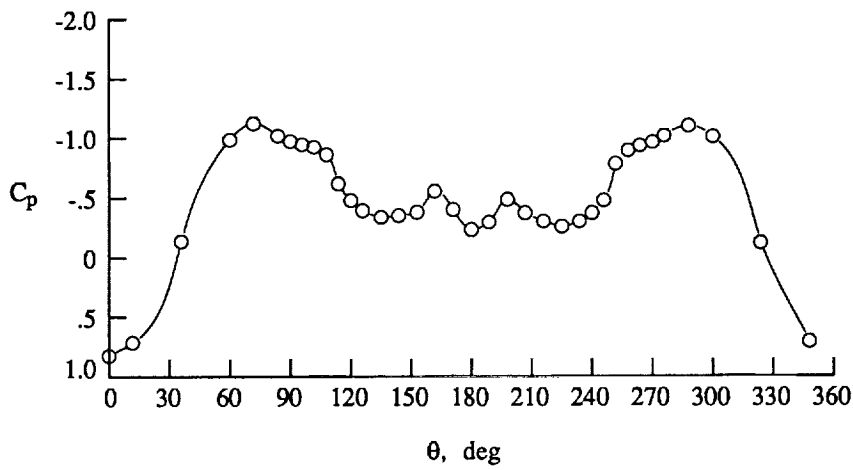
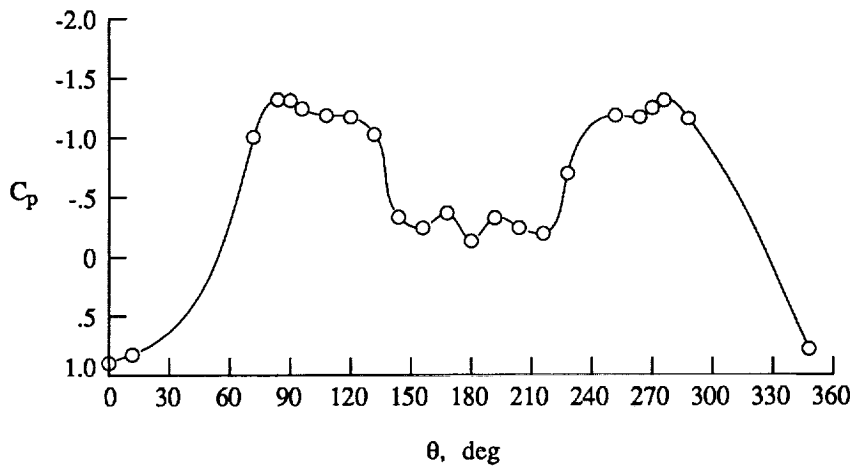
Figure 51. Concluded.



(a)  $\alpha = 40^\circ$ .

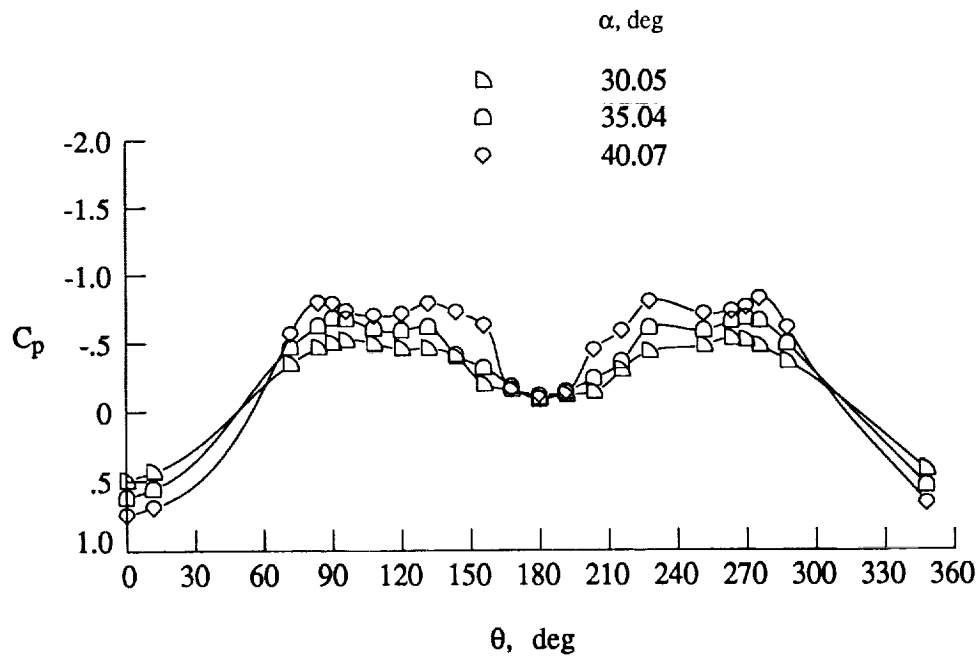
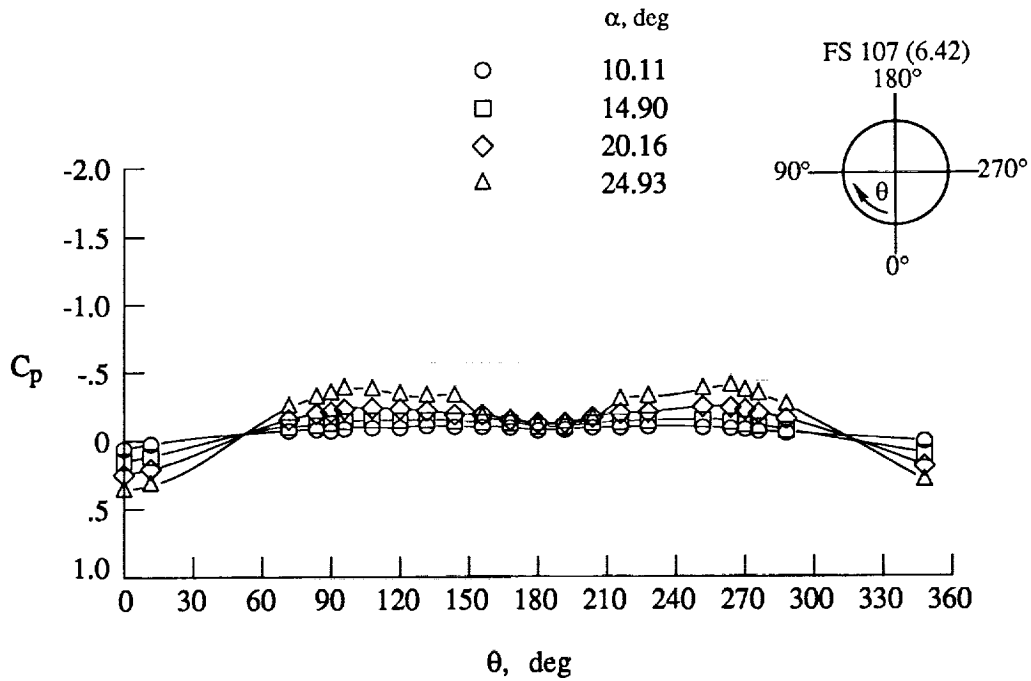
Figure 52. Forebody surface static pressure on baseline F/A-18 model at  $M_\infty = 0.60$  and  $Re_c = 1.32 \times 10^6$ . Dimensions are in inches full scale (0.06 scale).





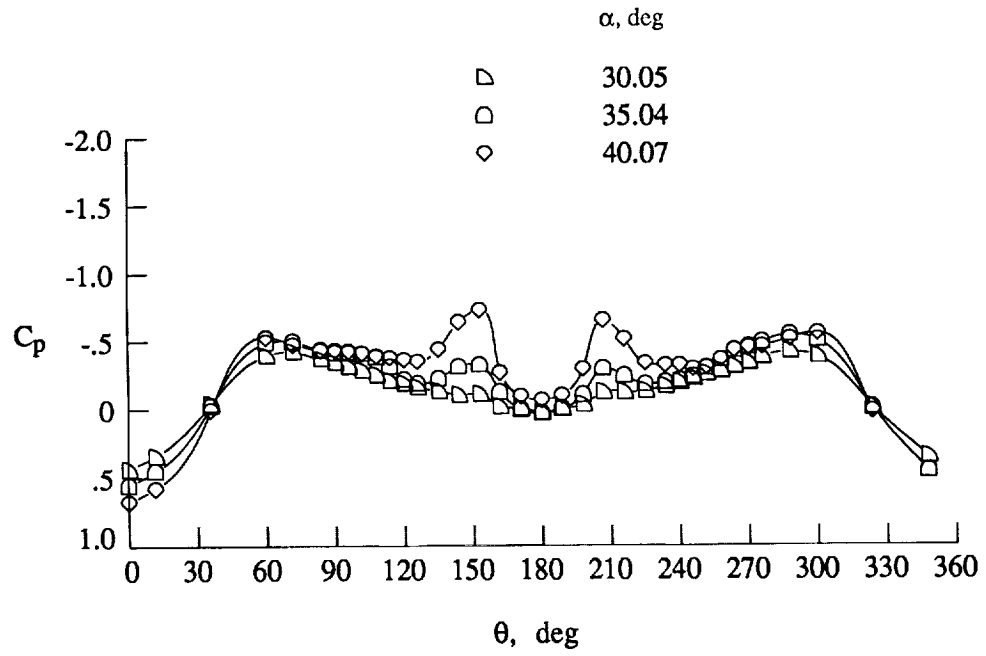
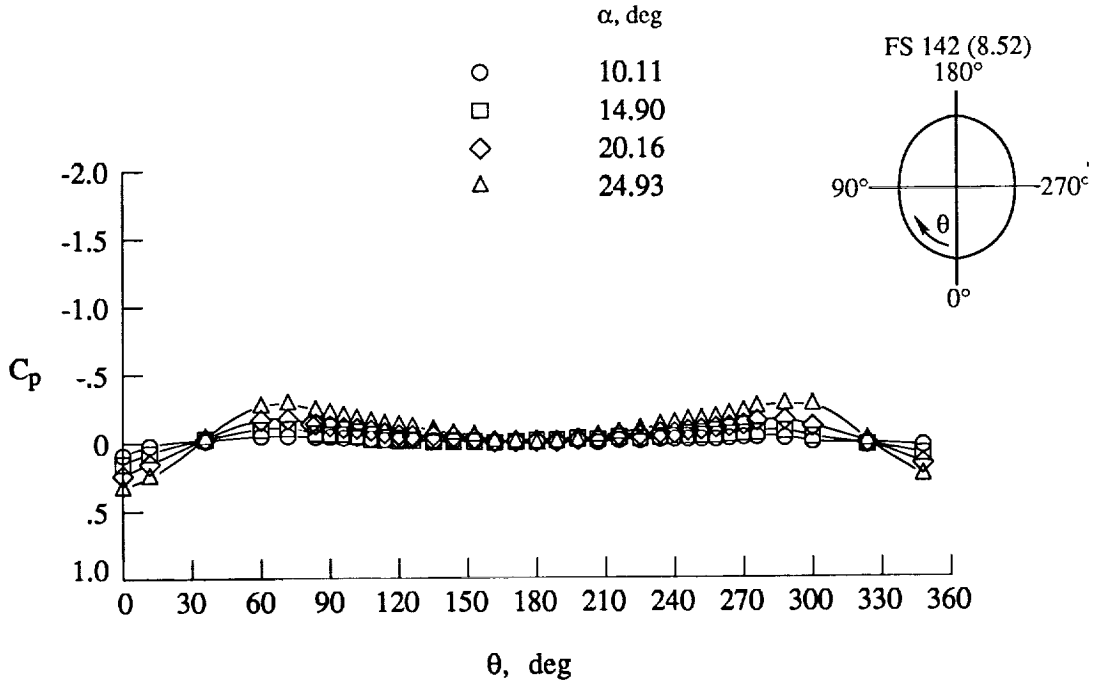
(b)  $\alpha = 50^\circ$ .

Figure 52. Concluded.



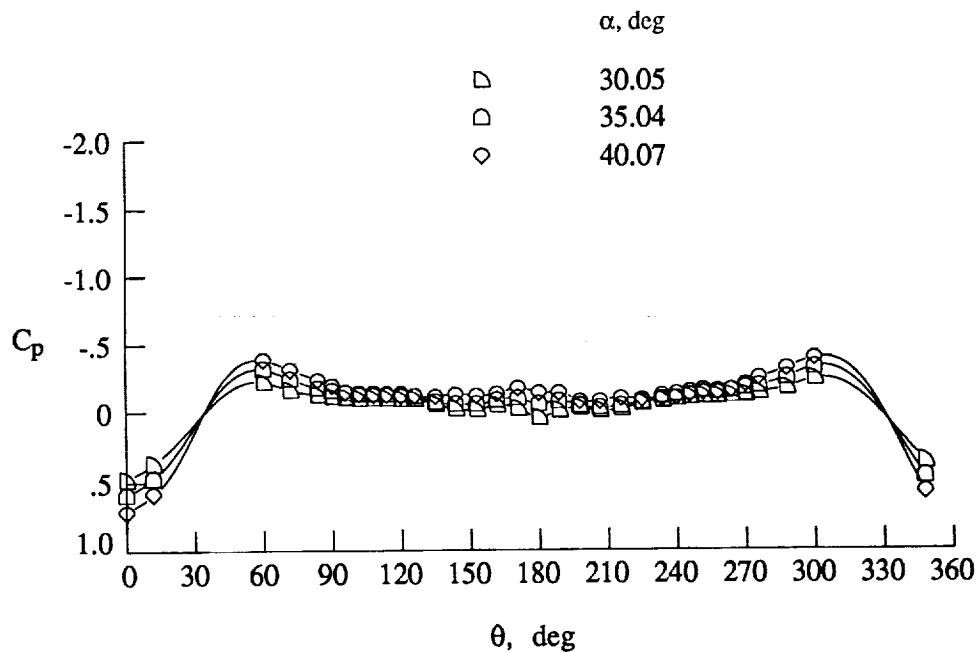
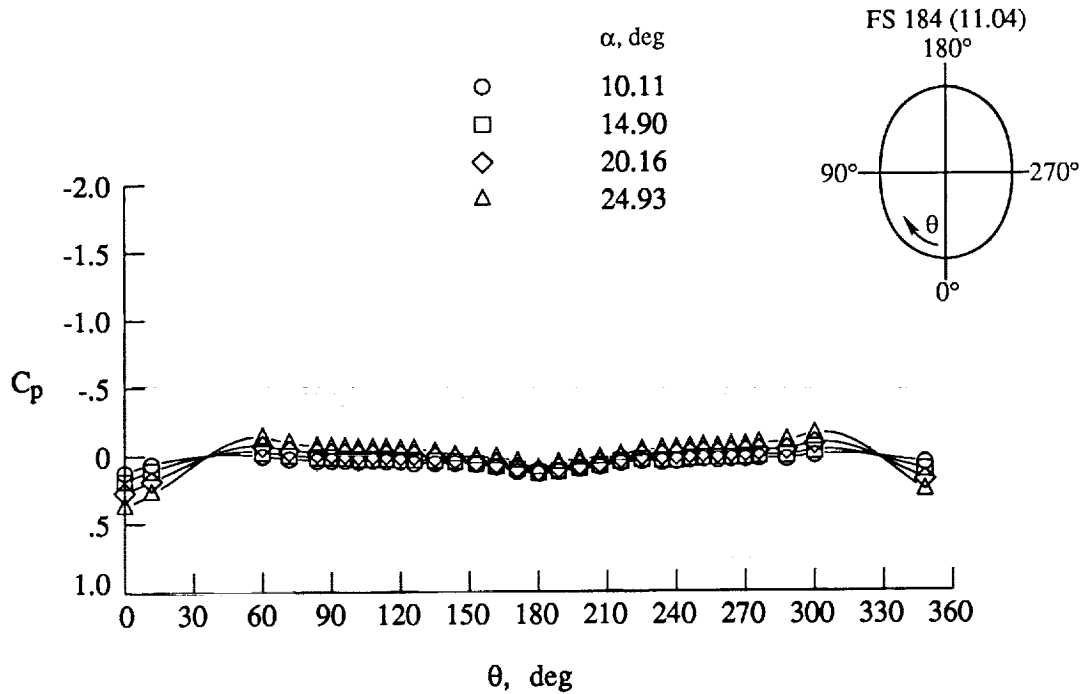
(a) FS 107 (6.42).

Figure 53. Effect of angle of attack on baseline F/A-18 model forebody surface static pressures at  $M_\infty = 0.80$  and  $Re_{\bar{c}} = 1.02 \times 10^6$ . Dimensions are in inches full scale (0.06 scale).



(b) FS 142 (8.52).

Figure 53. Continued.



(c) FS 184 (11.04).

Figure 53. Concluded.

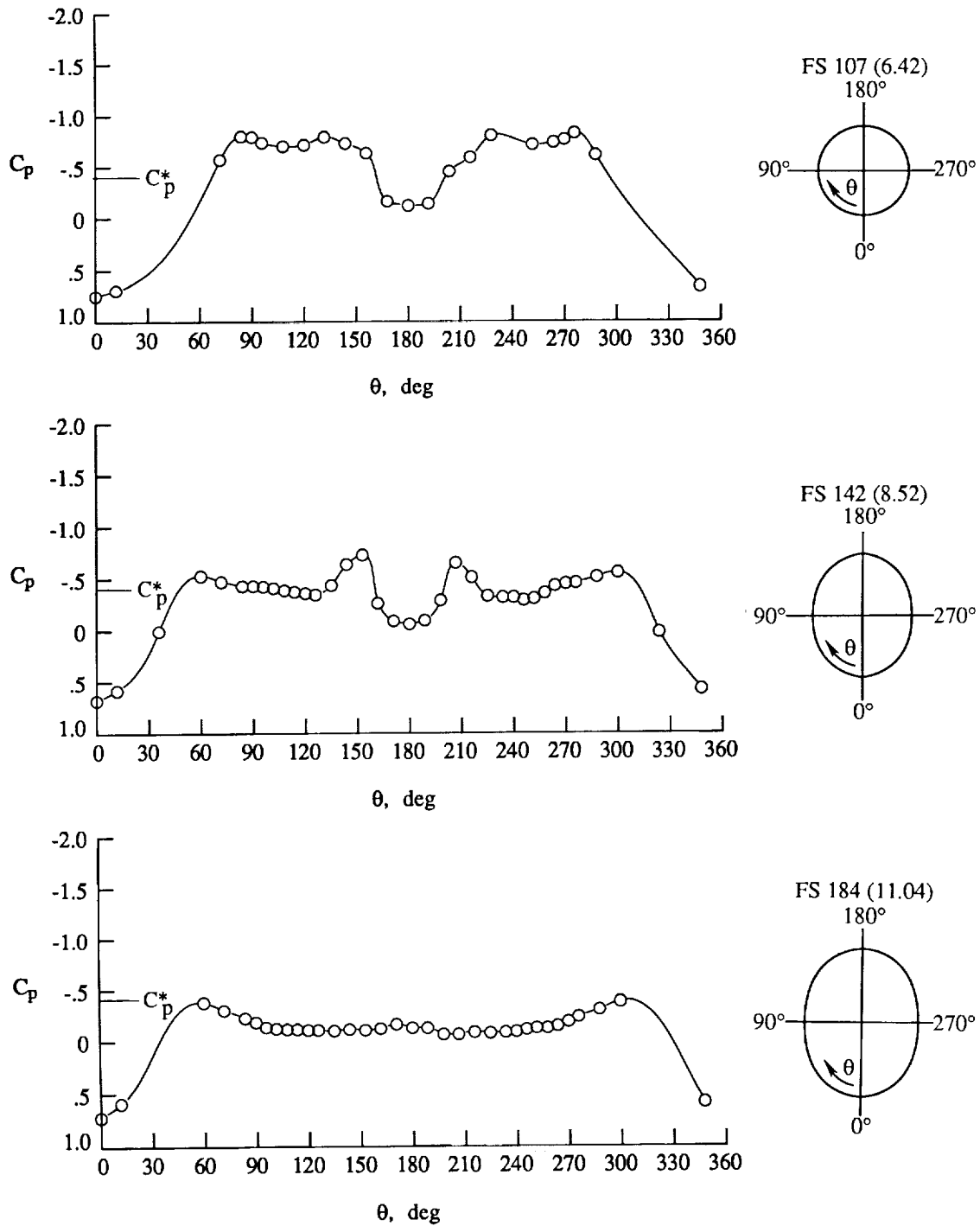
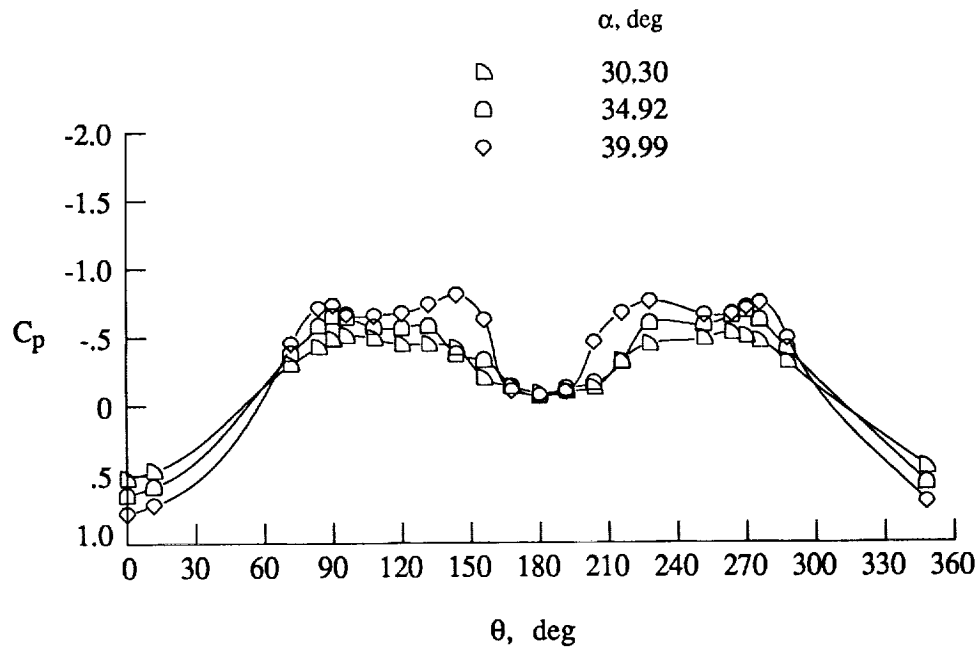
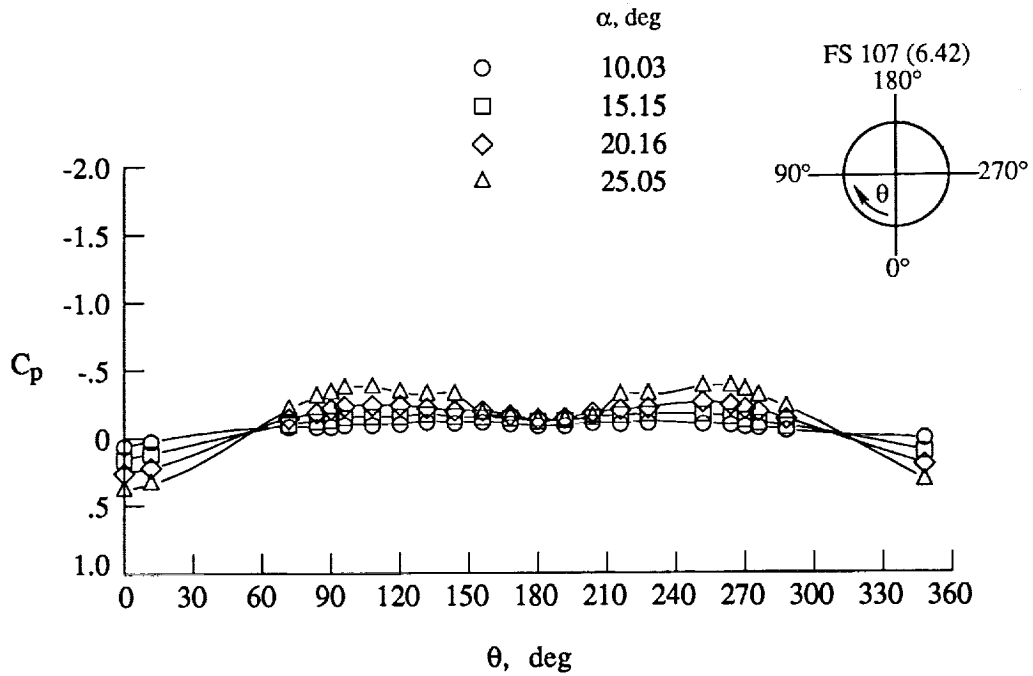
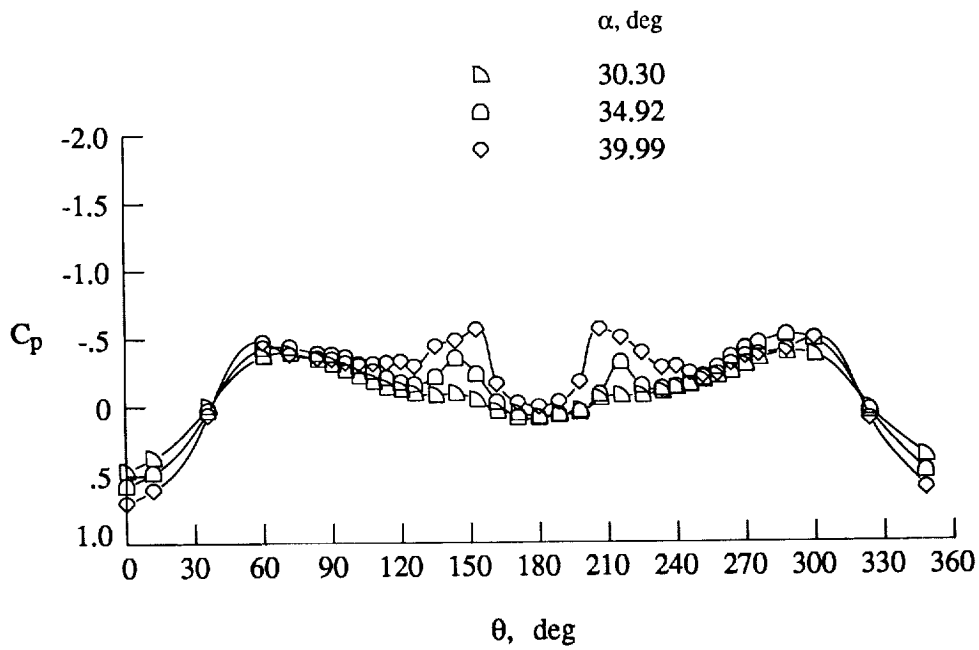
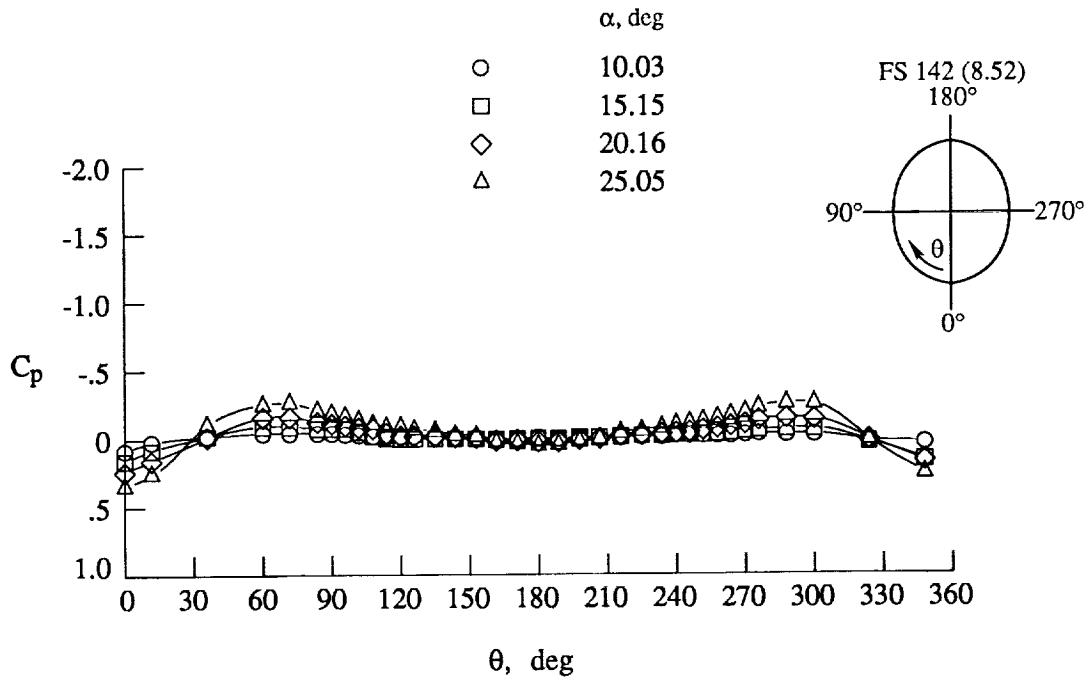


Figure 54. Forebody surface static pressures on baseline F/A-18 model at  $M_\infty = 0.80$ ,  $Re_c = 1.02 \times 10^6$ , and  $\alpha = 40^\circ$ . Dimensions are in inches full scale (0.06 scale).



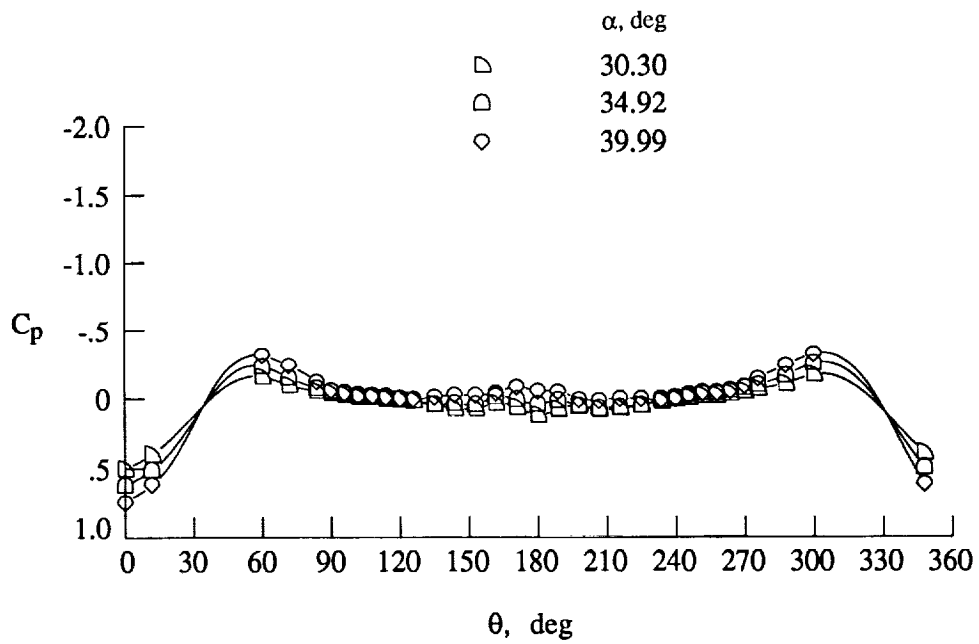
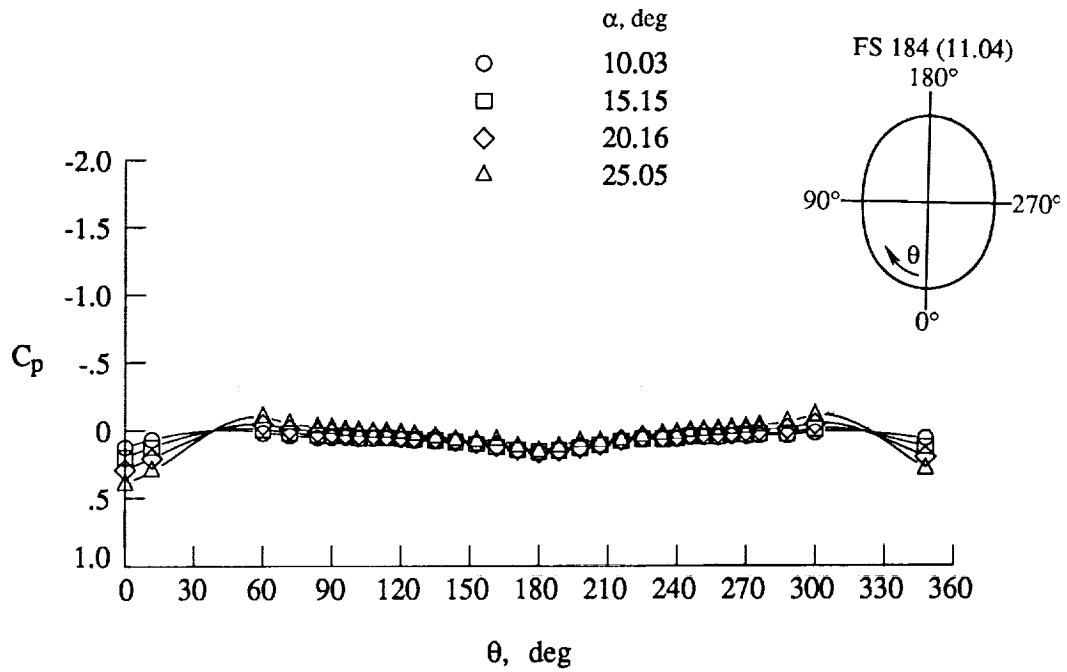
(a) FS 107 (6.42).

Figure 55. Effect of angle of attack on baseline F/A-18 model forebody surface static pressures at  $M_\infty = 0.90$  and  $Re_{\bar{c}} = 1.02 \times 10^6$ . Dimensions are in inches full scale (0.06 scale).



(b) FS 142 (8.52).

Figure 55. Continued.



(c) FS 184 (11.04).

Figure 55. Concluded.



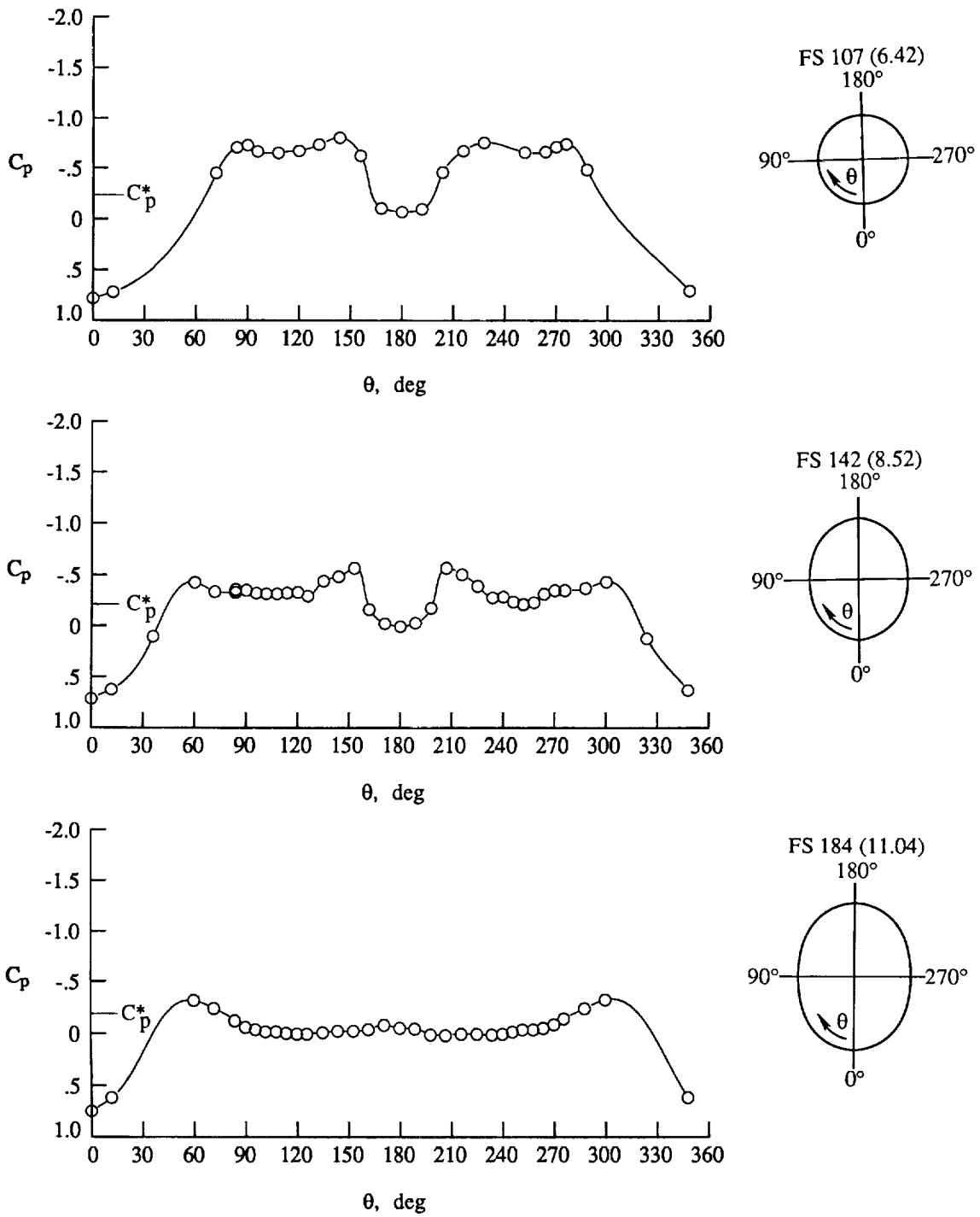


Figure 56. Forebody surface static pressures on baseline F/A-18 model at  $M_\infty = 0.90$ ,  $Re_{\bar{c}} = 1.02 \times 10^6$ , and  $\alpha = 40^\circ$ . Dimensions are in inches full scale (0.06 scale).

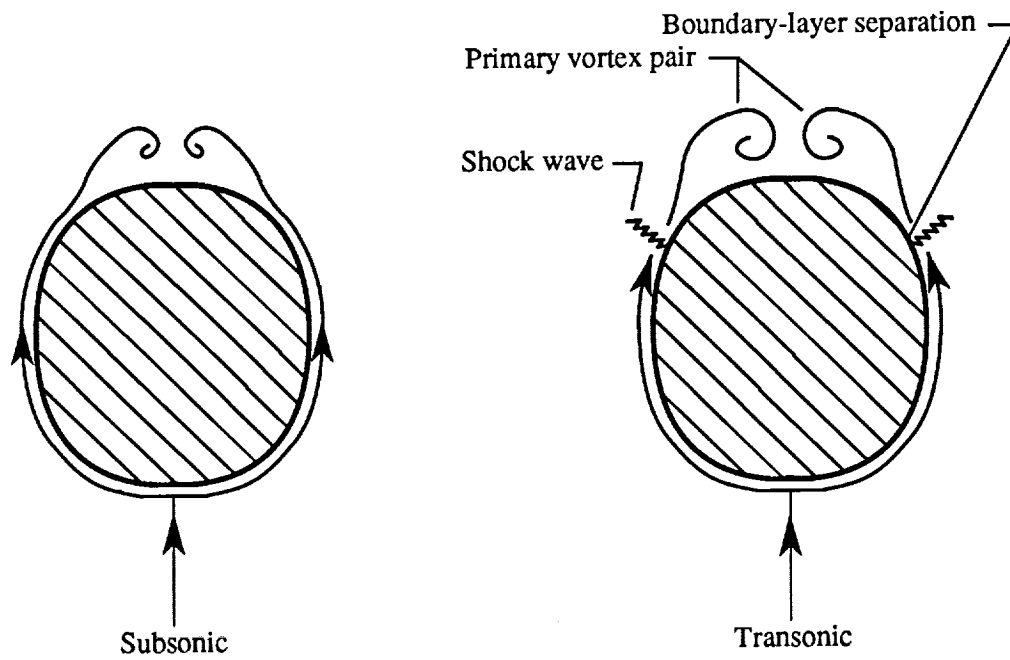


Figure 57. Hypothesized cross-flow shock-induced boundary-layer separation on forebody of 0.06-scale F/A-18 model.

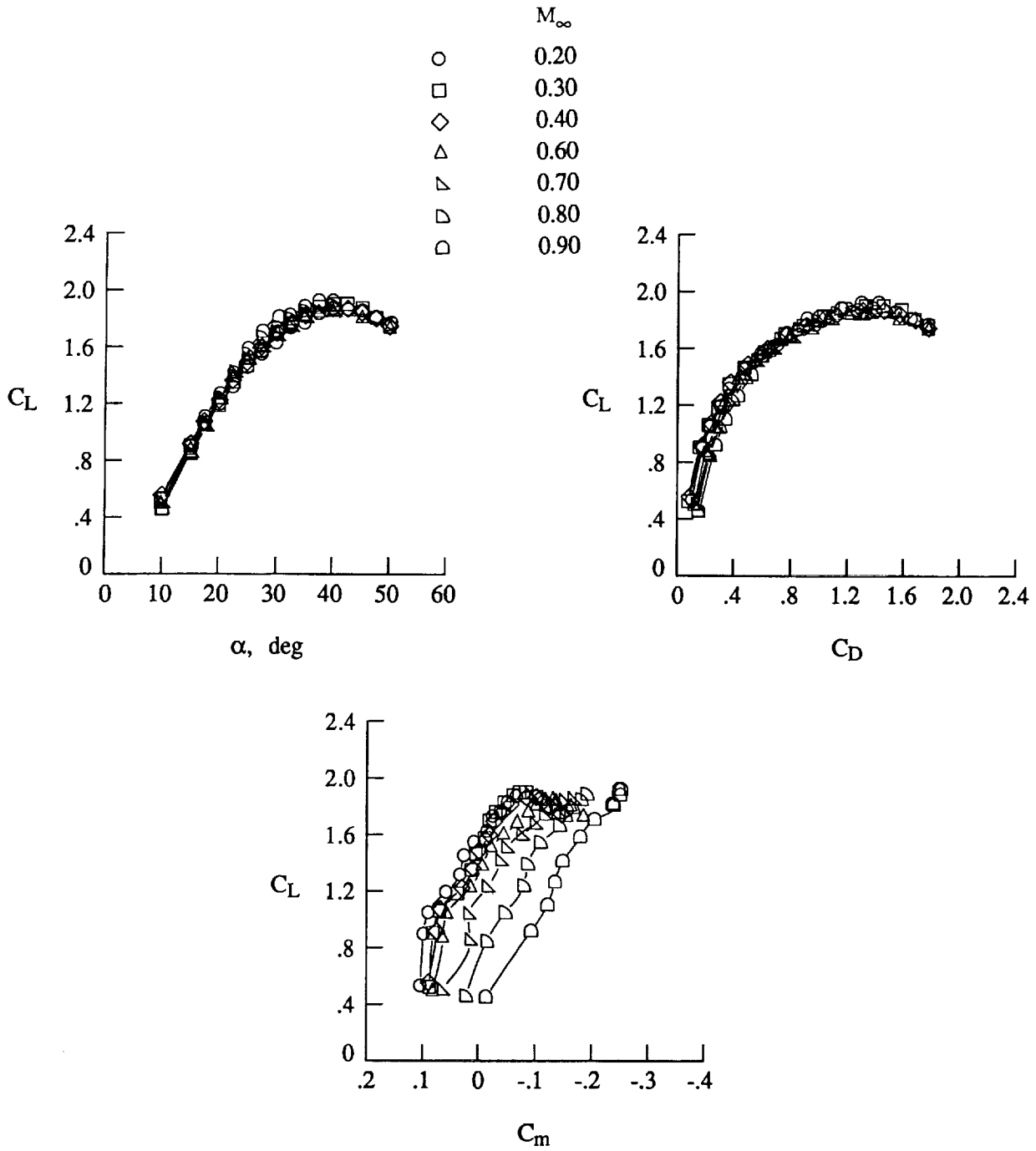
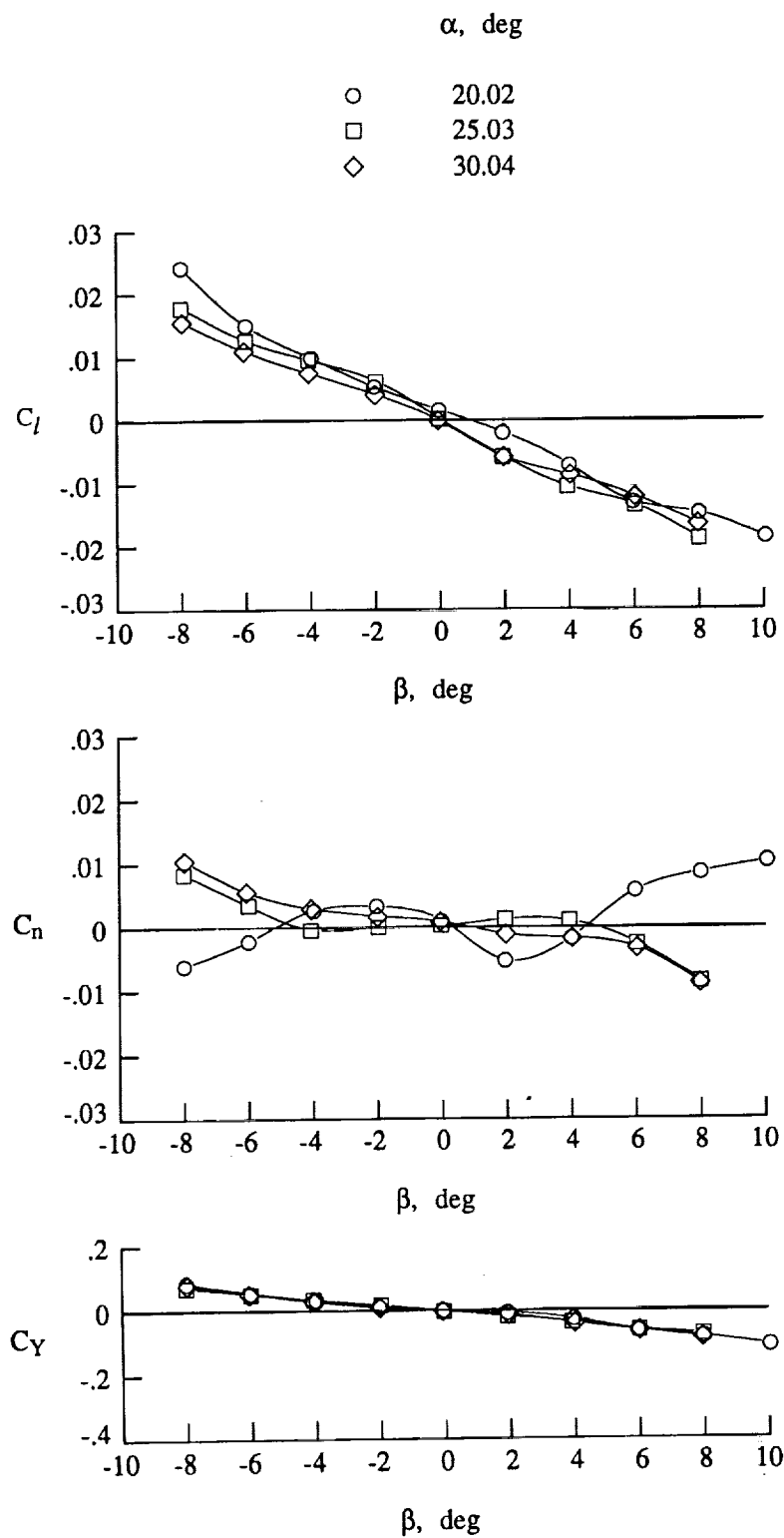
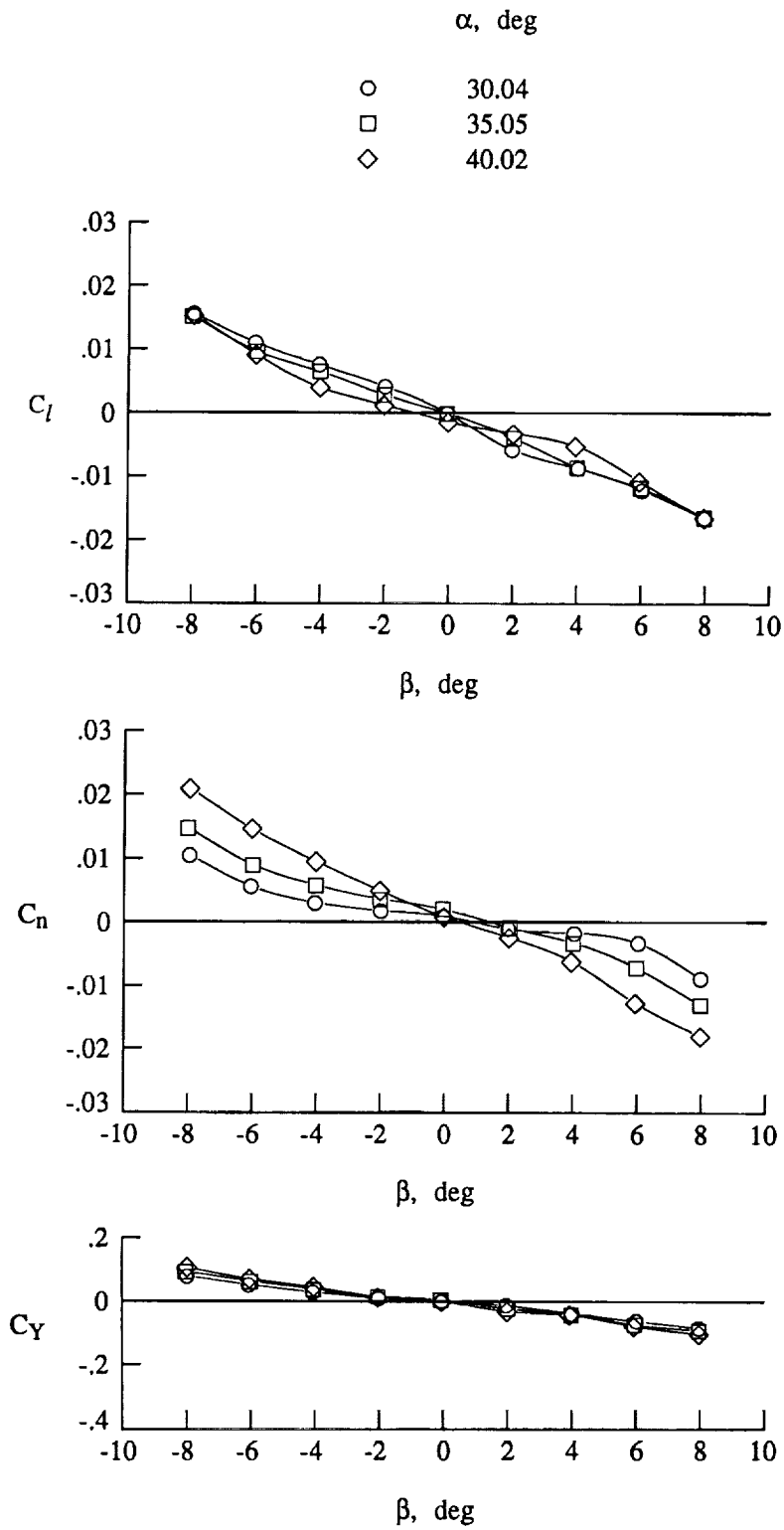


Figure 58. Effect of Mach number on lift, drag, and pitching-moment characteristics of baseline F/A-18 model.



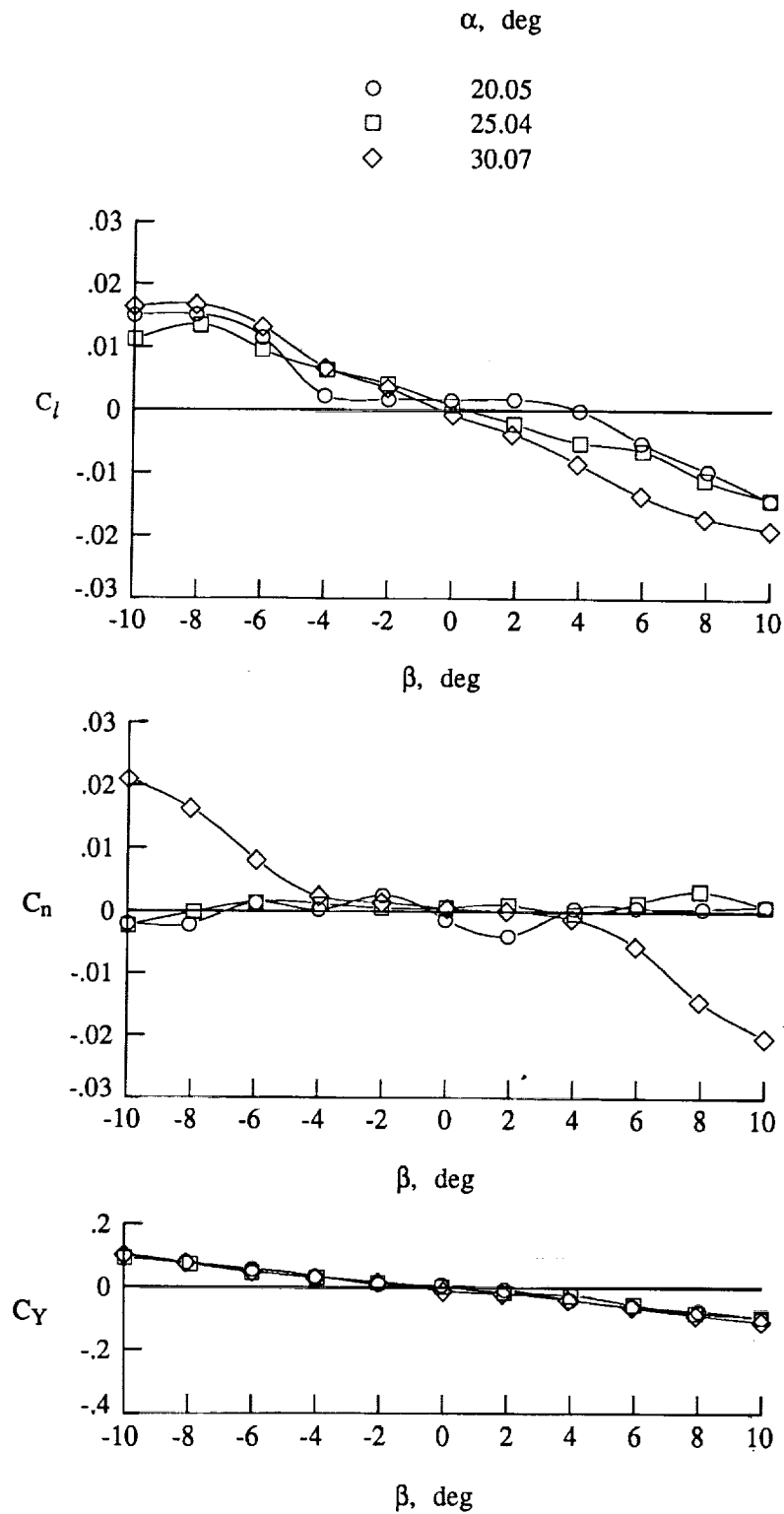
(a)  $\alpha = 20^\circ$  to  $30^\circ$ .

Figure 59. Variations of rolling-moment, yawing-moment, and side-force coefficients with sideslip at  $M_\infty = 0.60$  and  $Re_{\bar{c}} = 1.32 \times 10^6$ .



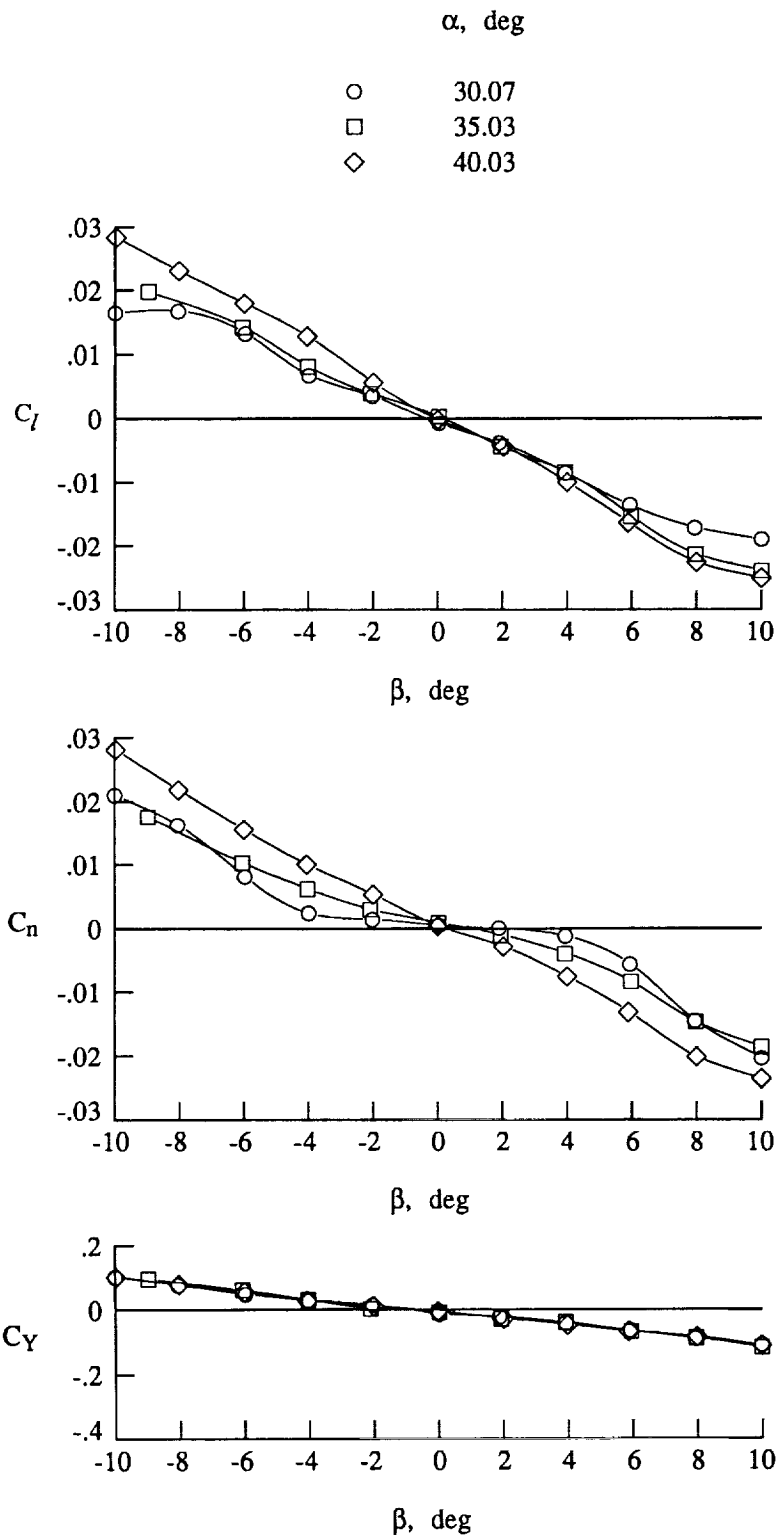
(b)  $\alpha = 30^\circ$  to  $40^\circ$ .

Figure 59. Concluded.



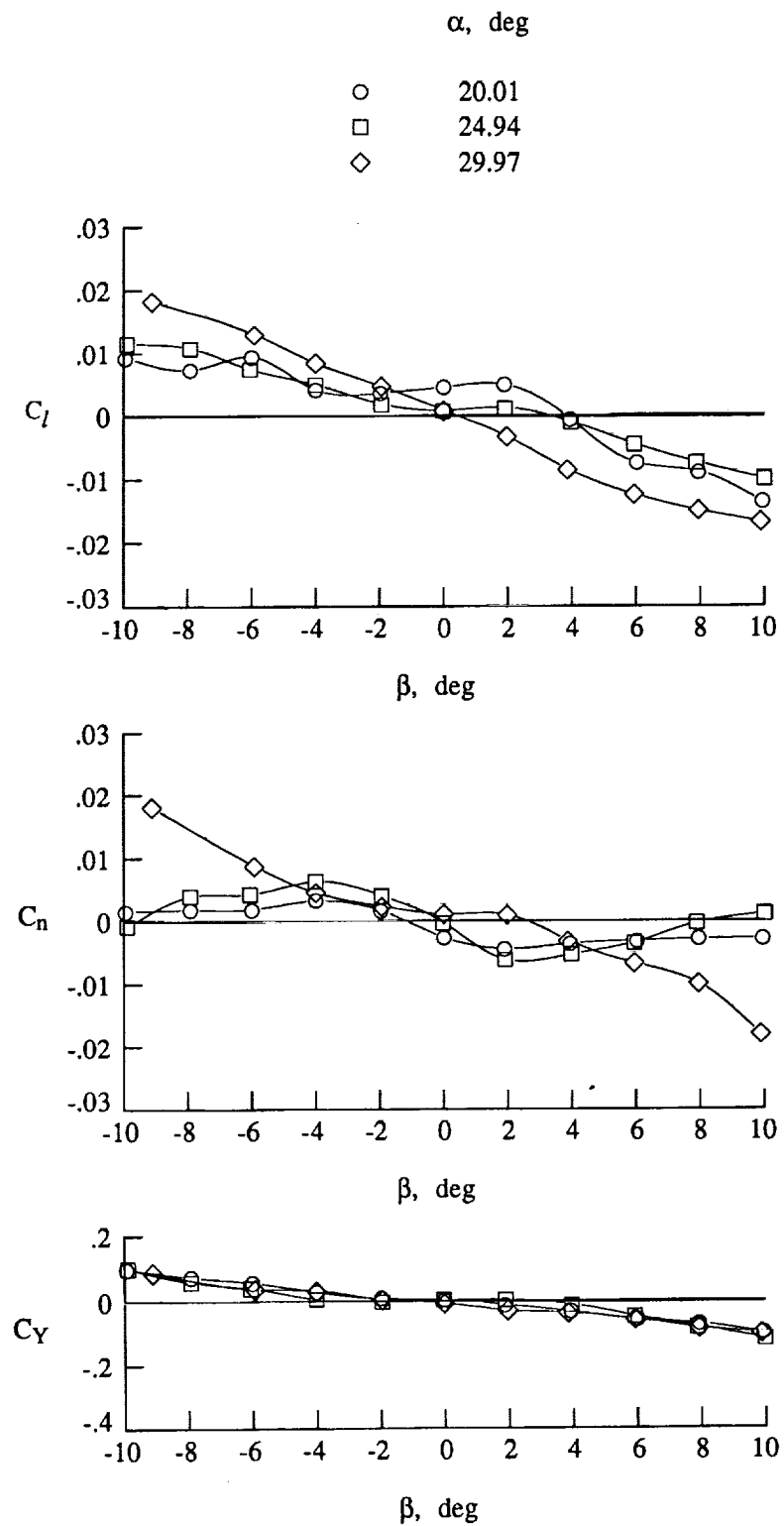
(a)  $\alpha = 20^\circ$  to  $30^\circ$ .

Figure 60. Variations of rolling-moment, yawing-moment, and side-force coefficients with sideslip at  $M_\infty = 0.80$  and  $Re_{\bar{c}} = 1.02 \times 10^6$ .



(b)  $\alpha = 30^\circ$  to  $40^\circ$ .

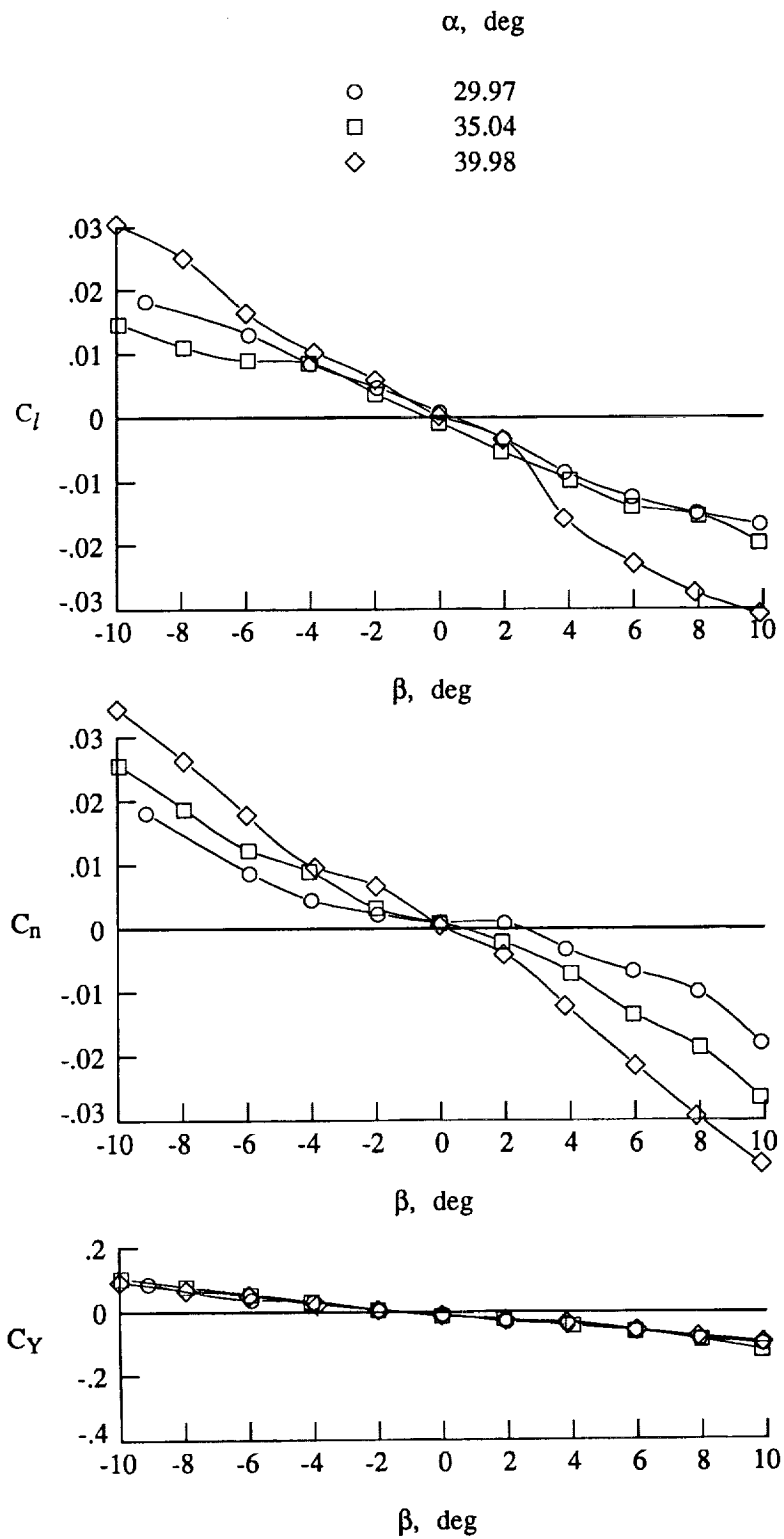
Figure 60. Concluded.



(a)  $\alpha = 20^\circ$  to  $30^\circ$ .

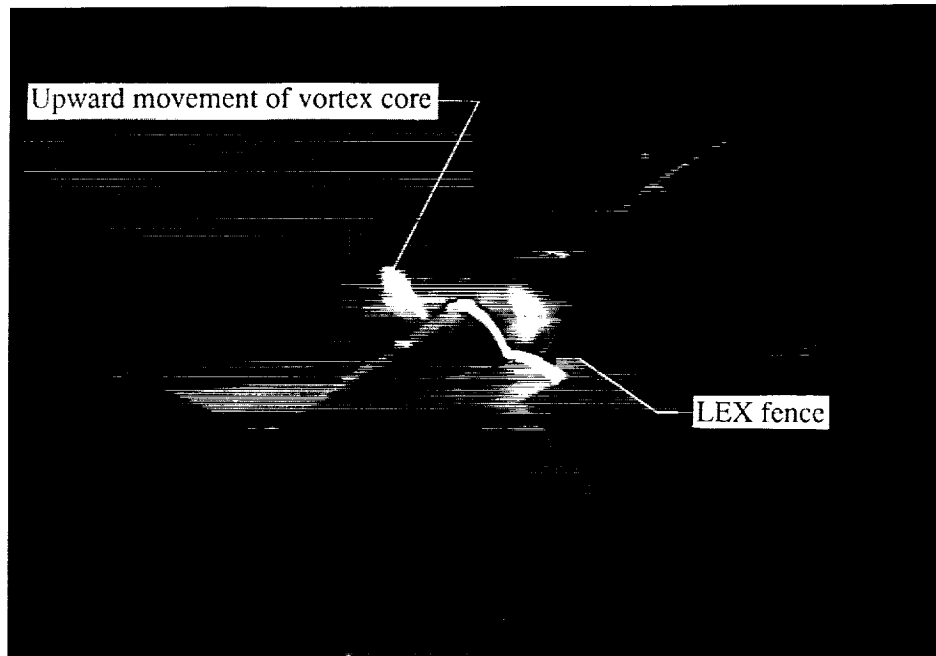
Figure 61. Variations of rolling-moment, yawing-moment, and side-force coefficients with sideslip at  $M_\infty = 0.90$  and  $Re_{\bar{c}} = 1.02 \times 10^6$ .





(b)  $\alpha = 30^\circ$  to  $40^\circ$ .

Figure 61. Concluded.

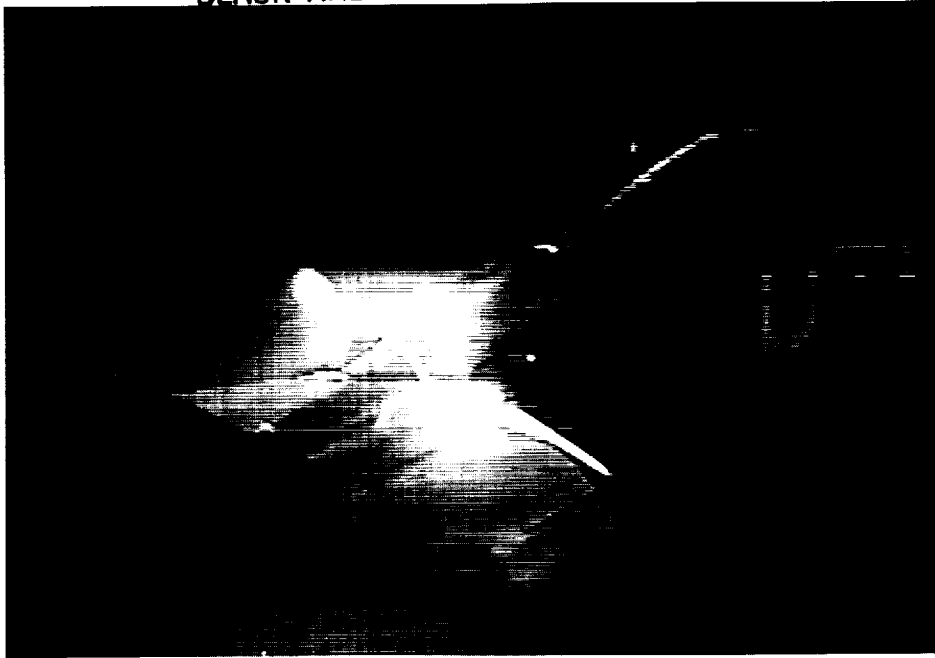


(a) LEX fence; FS 411 (24.66).



(b) Baseline; FS 411 (24.66).

Figure 62. Laser vapor screen flow visualizations on LEX fence and baseline configurations at  $M_\infty = 0.40$ ,  $Re_c = 1.75 \times 10^6$ , and  $\alpha = 20^\circ$ . Dimensions are in inches full scale (0.06 scale).

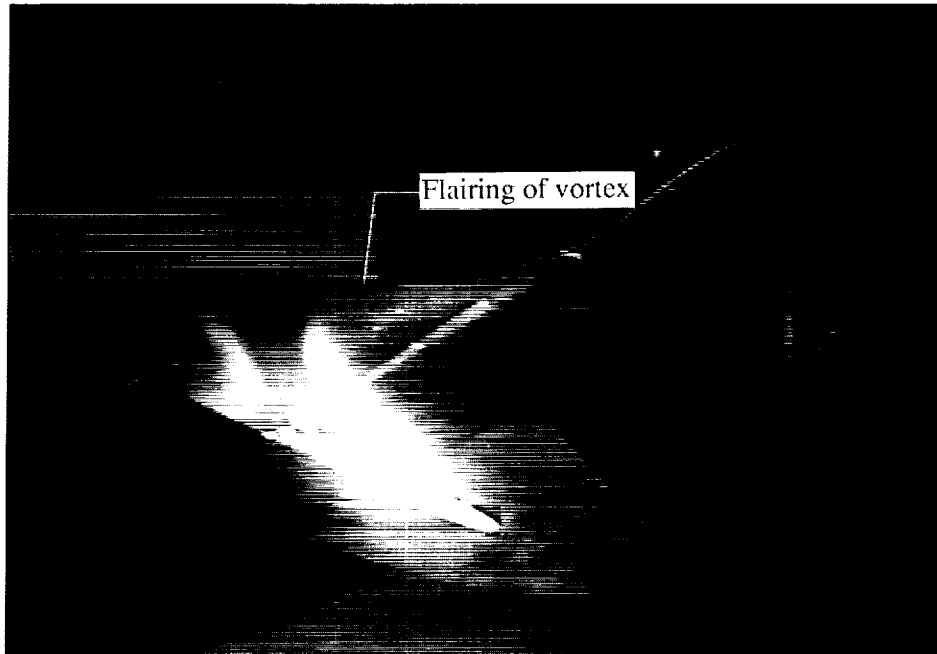


(c) LEX fence; FS 450 (27.00).



(d) Baseline; FS 450 (27.00).

Figure 62. Continued.



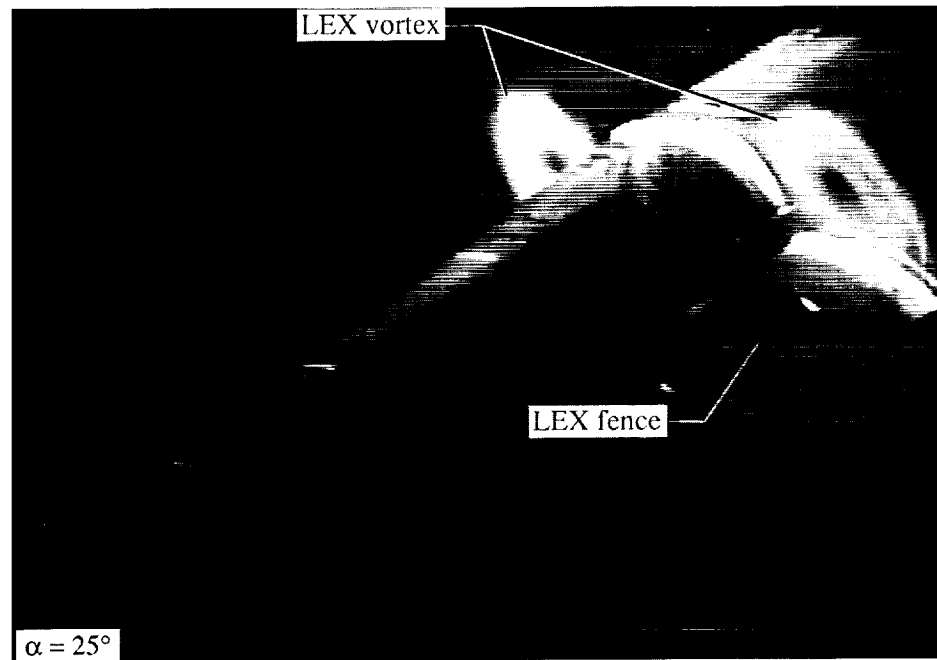
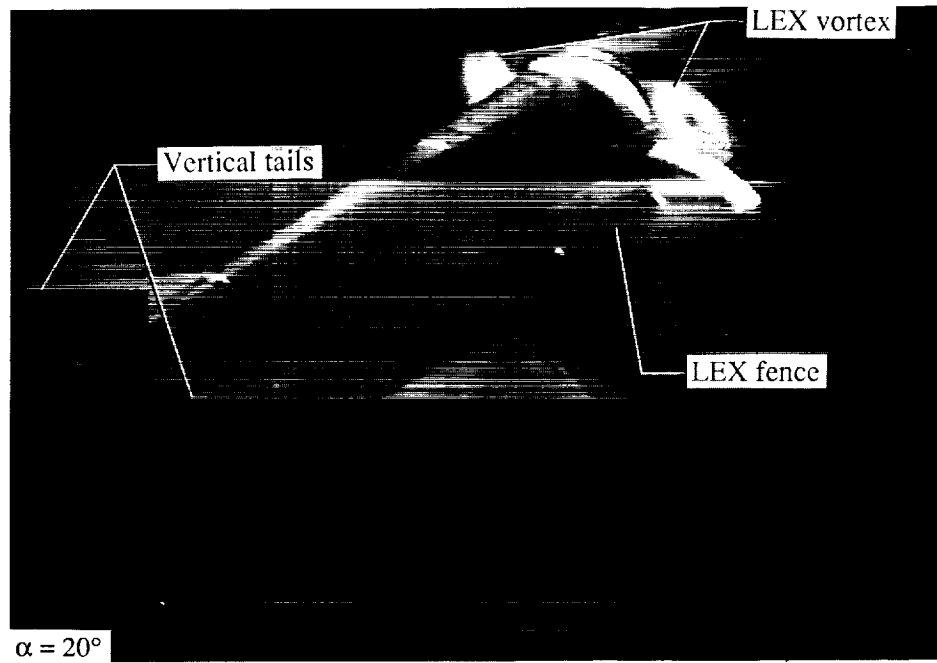
(e) LEX fence; FS 525 (31.50).



(f) Baseline; FS 525 (31.50).

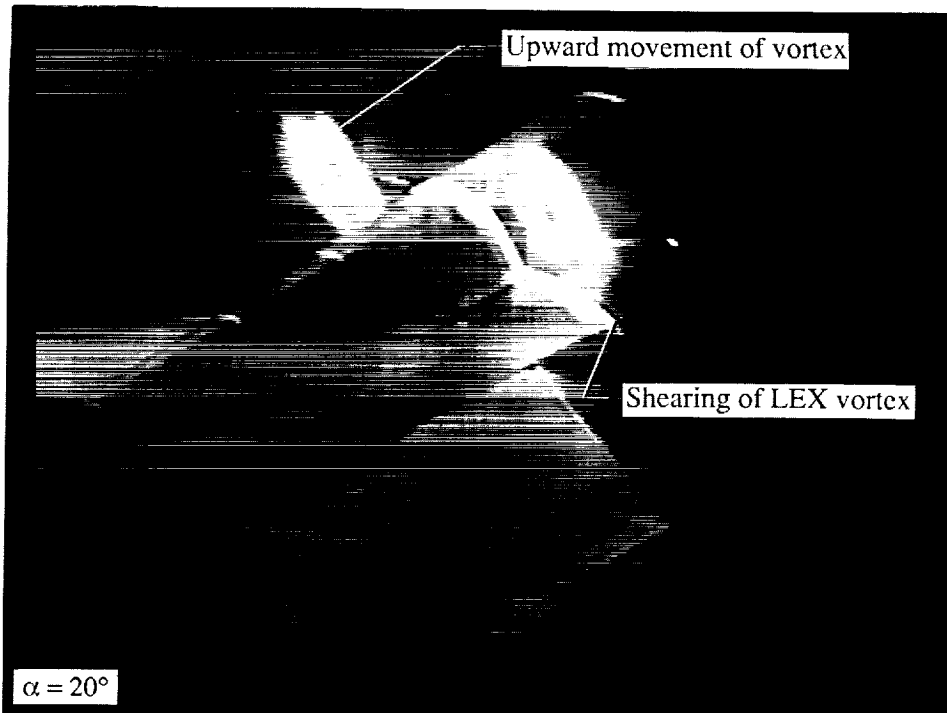
Figure 62. Concluded.

ORIGINAL PAGE  
BLACK AND WHITE PHOTOGRAPH

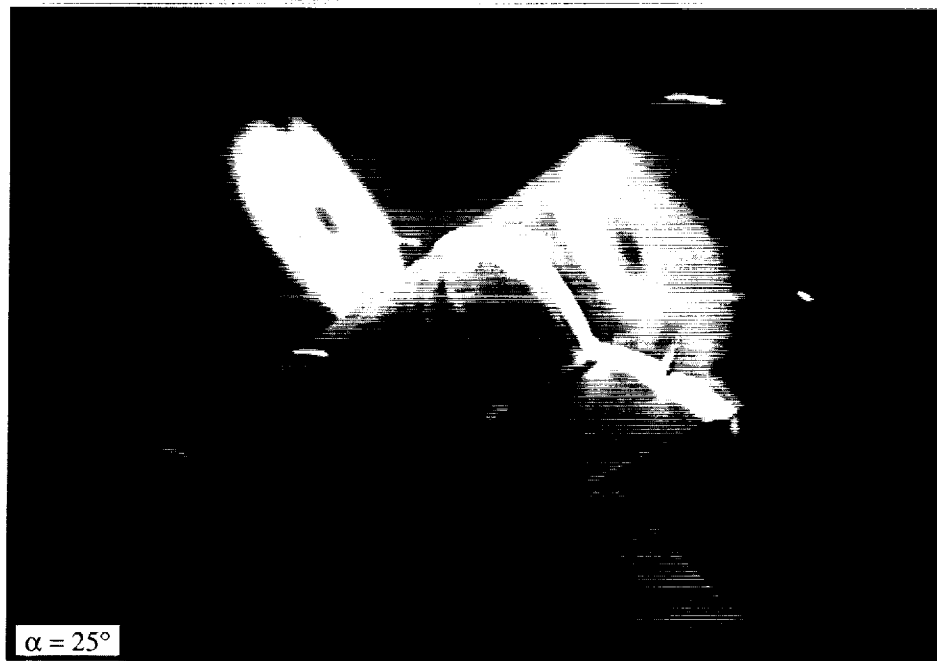


(a)  $FS \approx 357$  (21.42).

Figure 63. Close-ups of cross flow about LEX fence configuration at  $M_\infty = 0.60$  and  $Re_c = 1.32 \times 10^6$ .  
Dimensions are in inches full scale (0.06 scale).

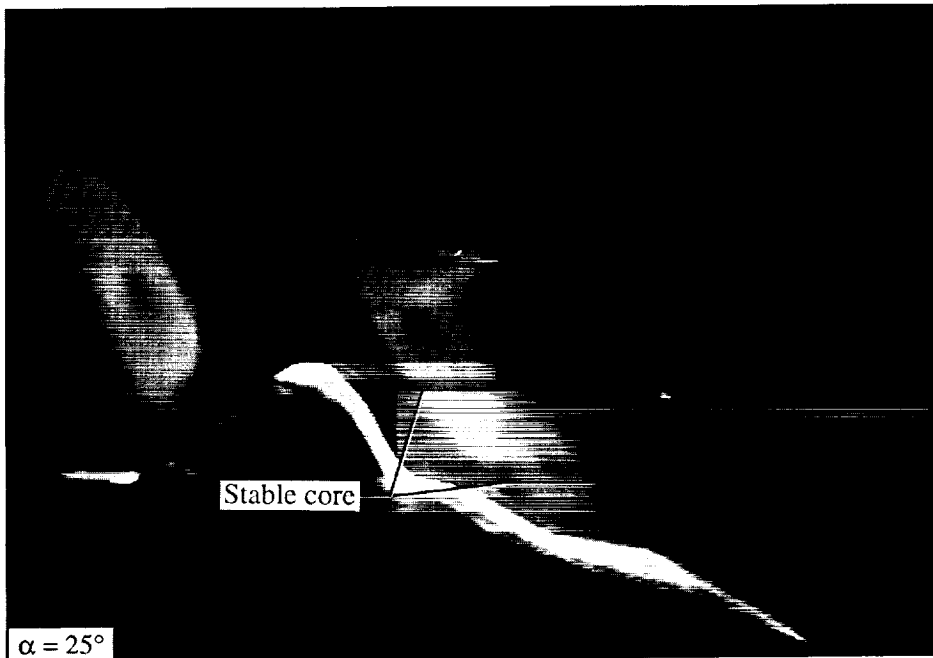
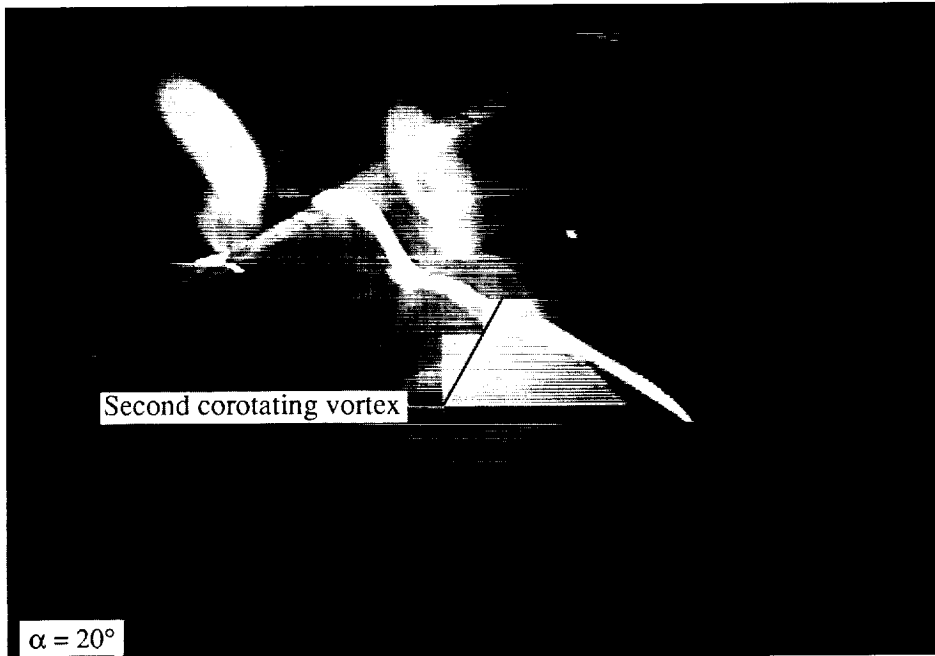


ORIGINAL PAGE  
BLACK AND WHITE PHOTOGRAPH



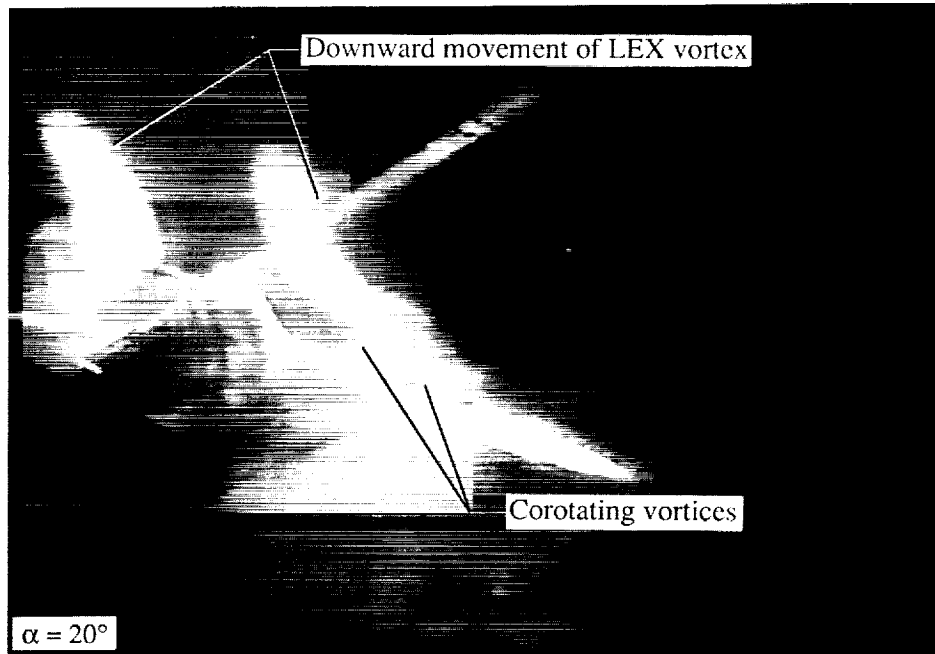
(b) FS  $\approx$  411 (24.66).

Figure 63. Continued.

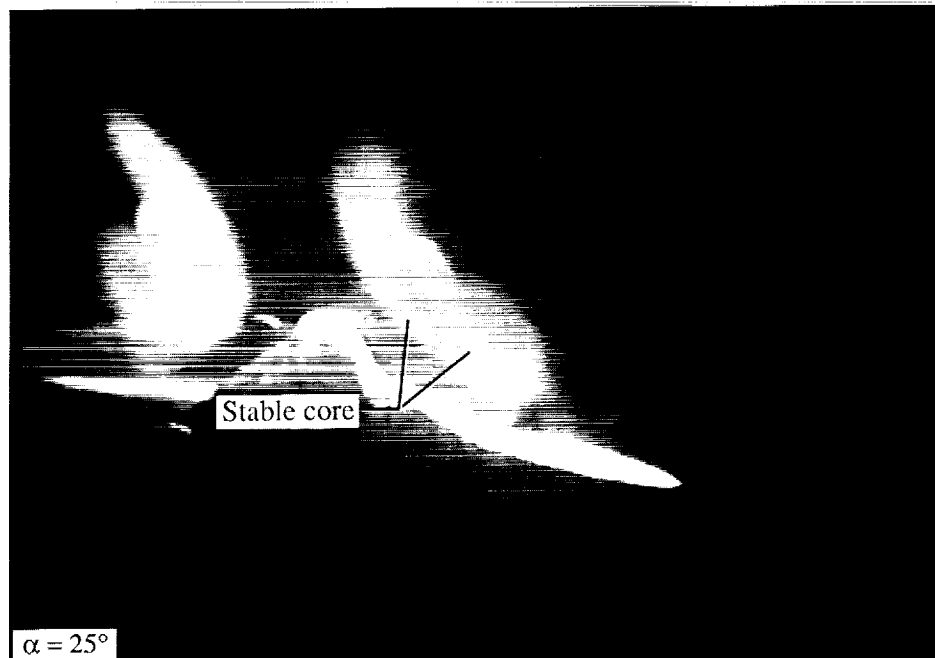


(c)  $FS \approx 450$  (27.00).

Figure 63. Continued.



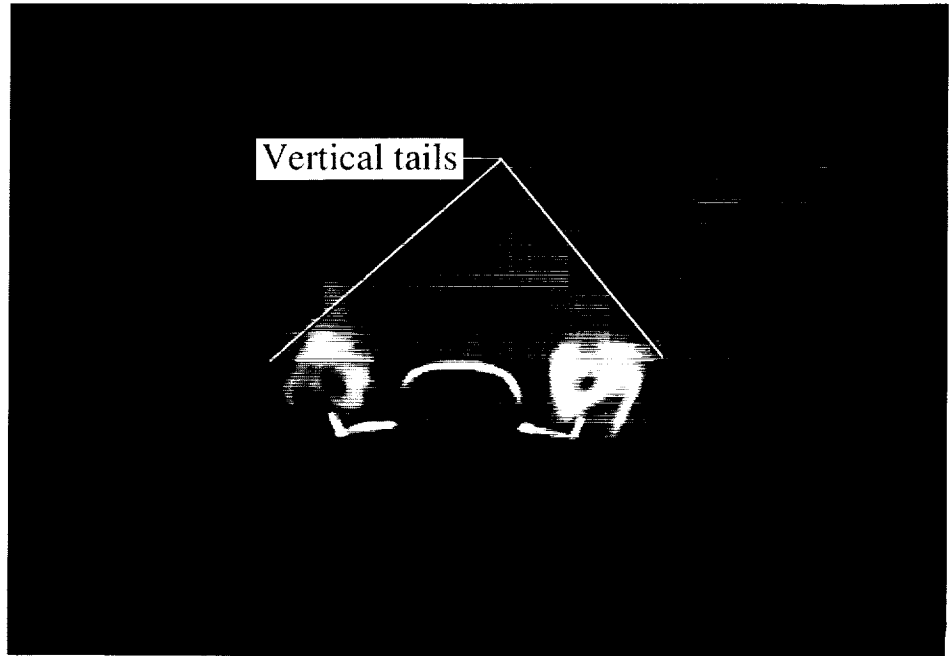
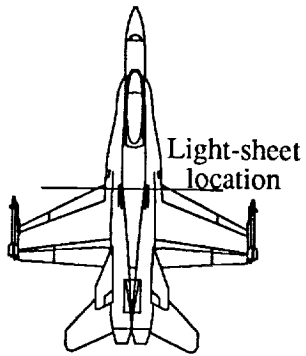
ORIGINAL PAGE  
BLACK AND WHITE PHOTOGRAPH



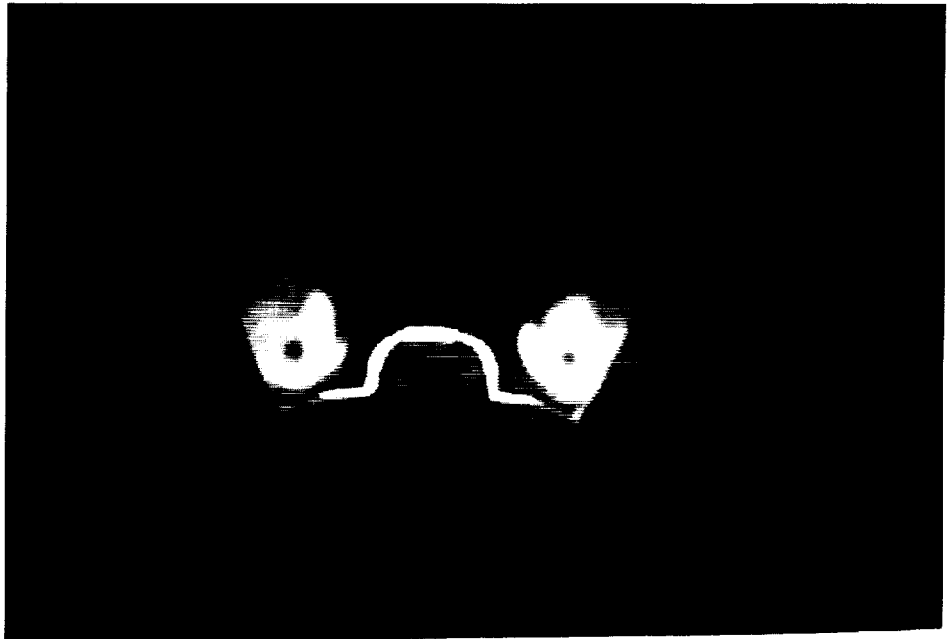
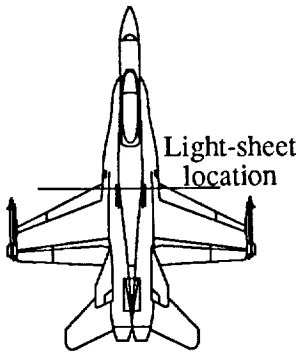
(d)  $FS \approx 483$  (28.98).

Figure 63. Concluded.



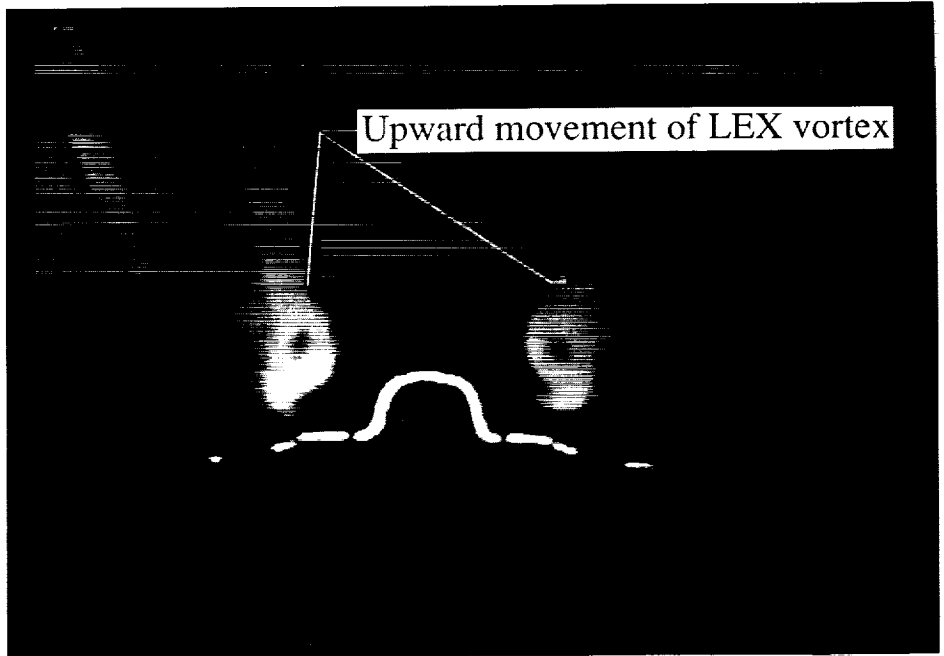
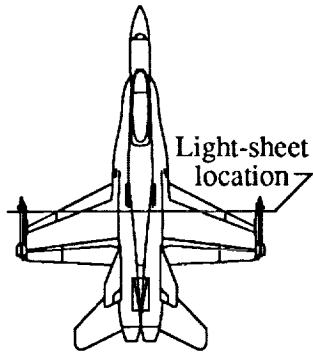


(a) LEX fence; FS 411 (24.66).

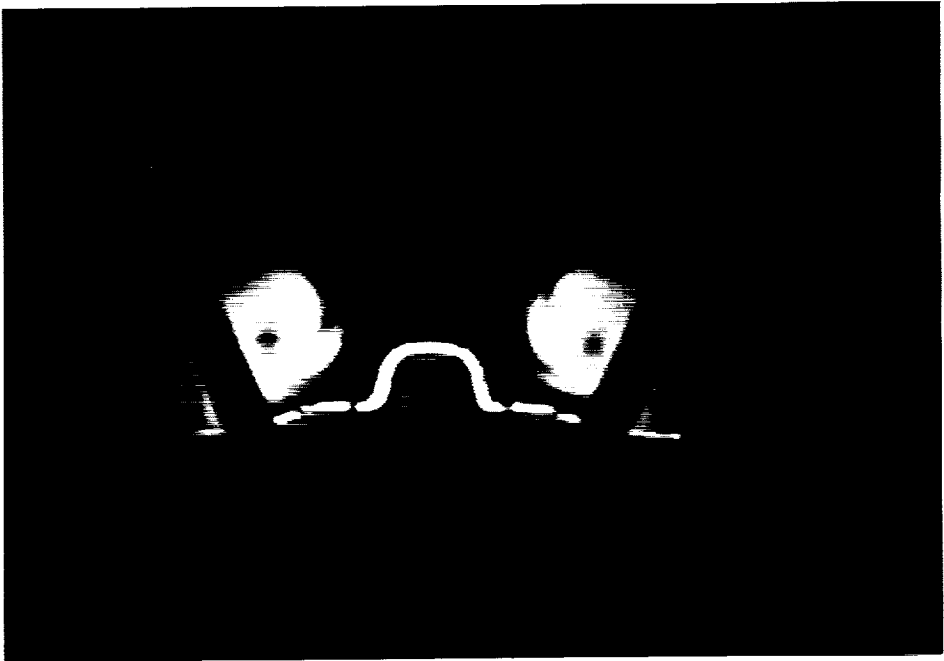
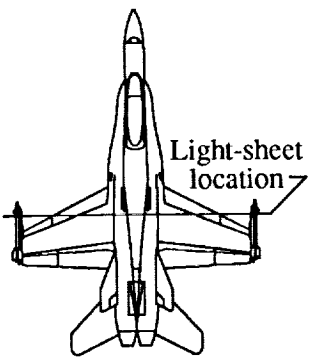


(b) Baseline; FS 411 (24.66).

Figure 64. Cross flow about LEX fence and baseline configurations at  $M_\infty = 0.60$ ,  $Re_c = 1.32 \times 10^6$ , and  $\alpha = 20^\circ$ . Dimensions are in inches full scale (0.06 scale).

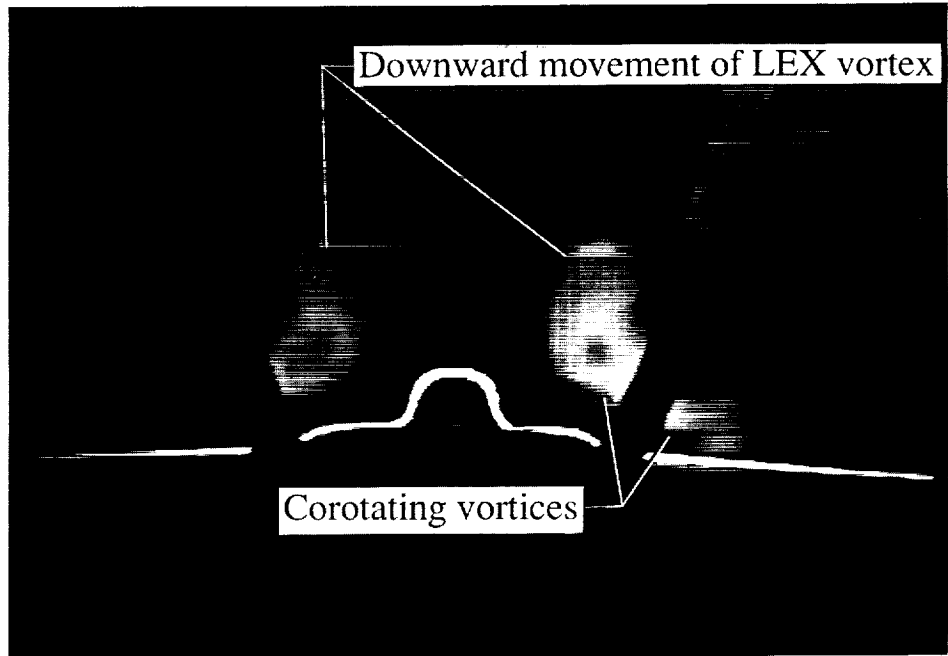
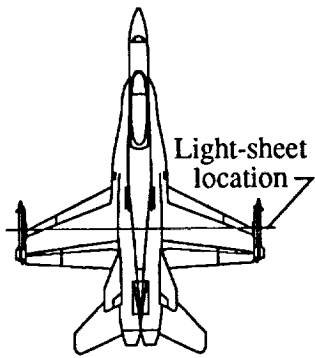


(c) LEX fence; FS 450 (27.00).

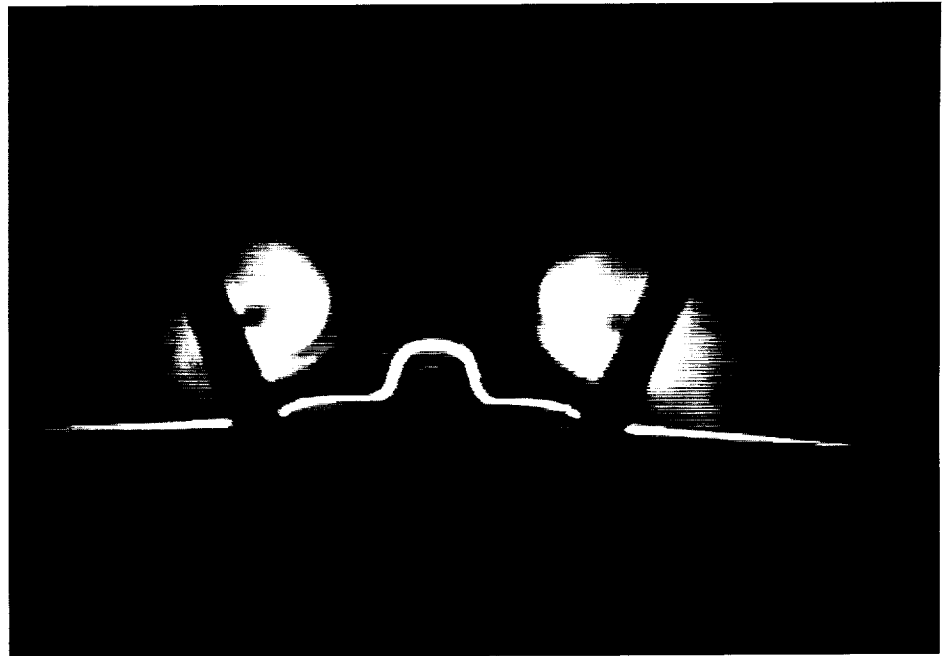
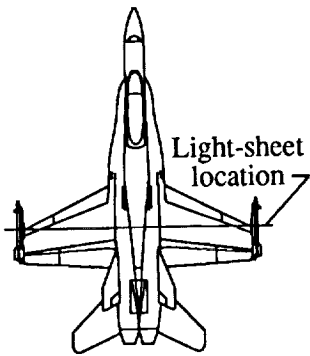


(d) Baseline; FS 450 (27.00).

Figure 64. Continued.

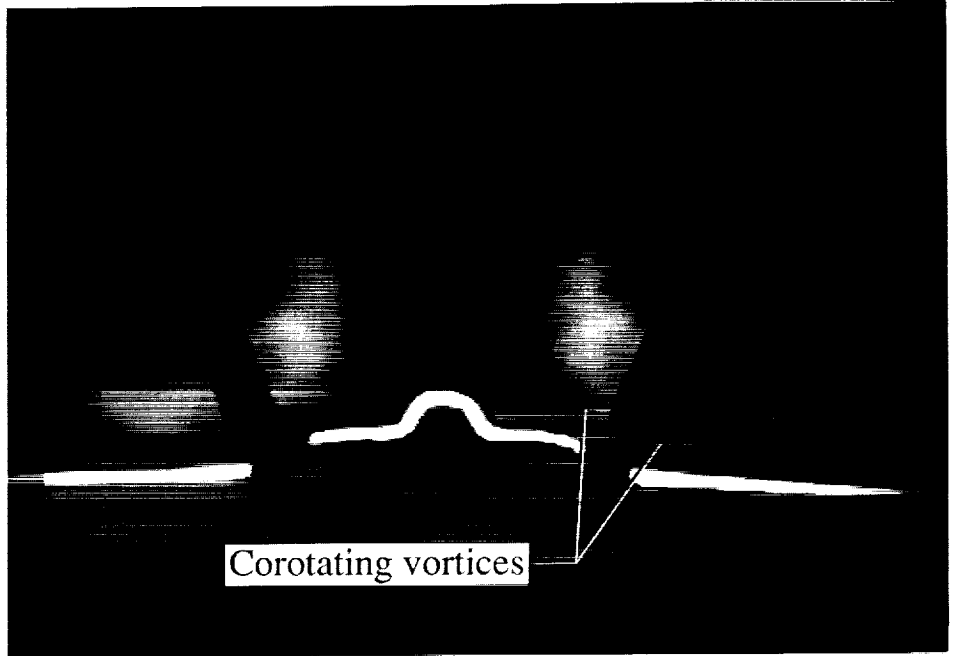
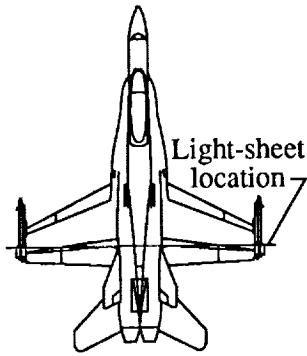


(e) LEX fence; FS 483 (28.98).

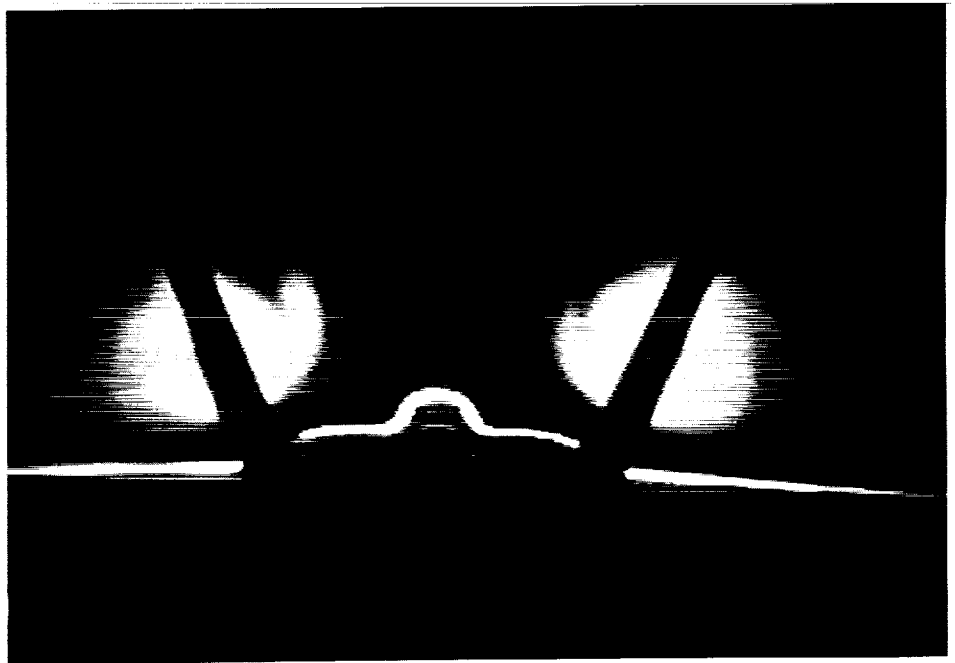
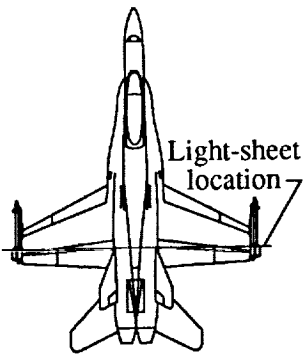


(f) Baseline; FS 483 (28.98).

Figure 64. Continued.

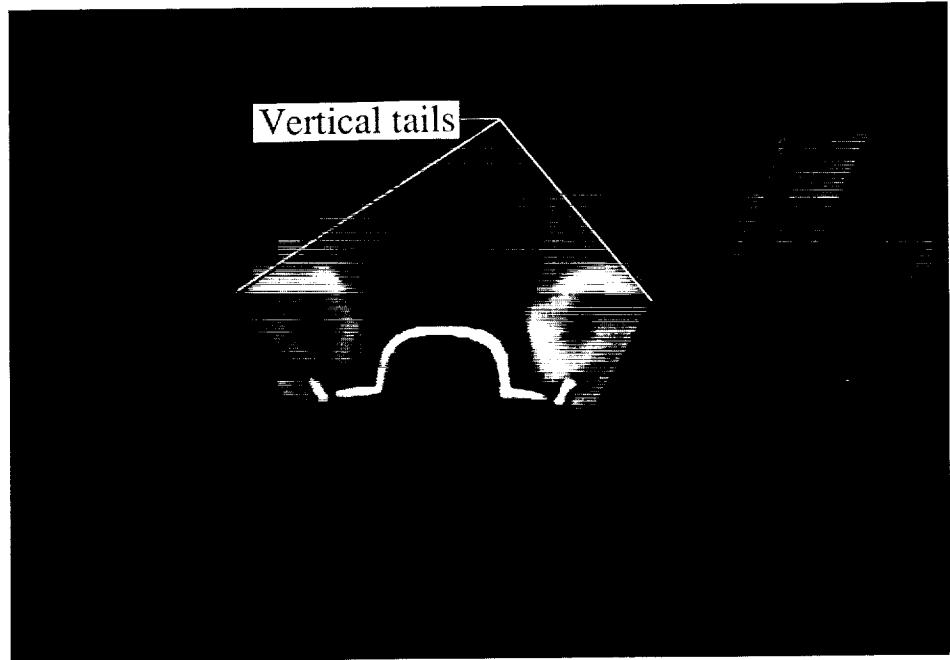
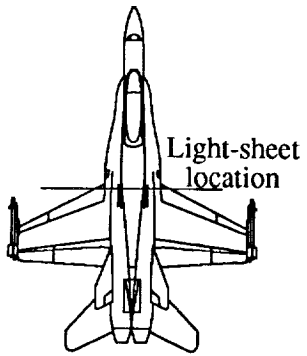


(g) LEX fence; FS 525 (31.50).

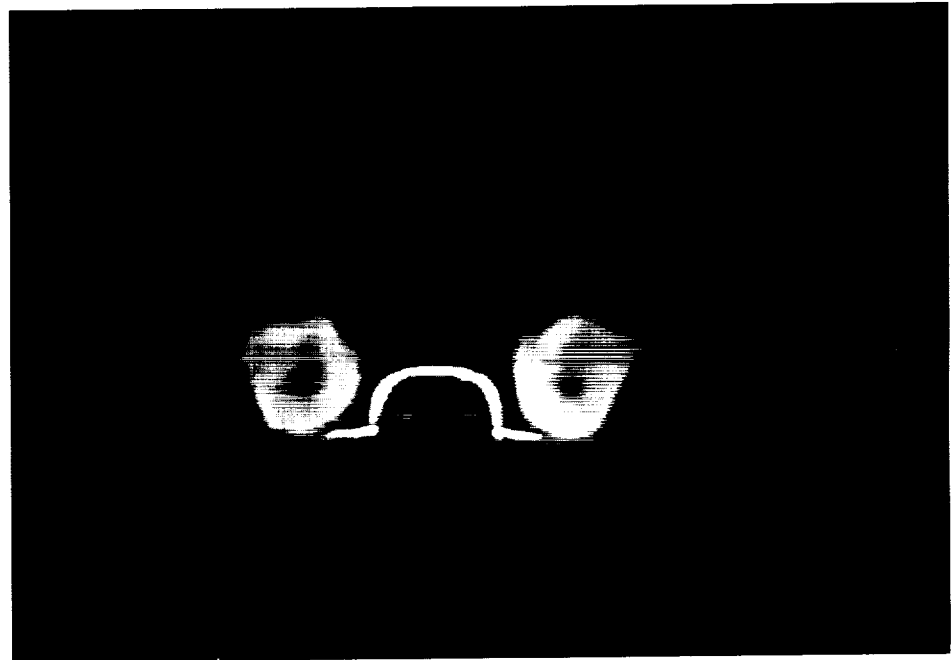
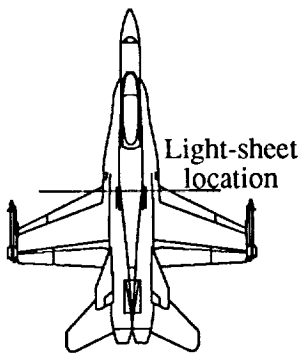


(h) Baseline; FS 525 (31.50).

Figure 64. Concluded.

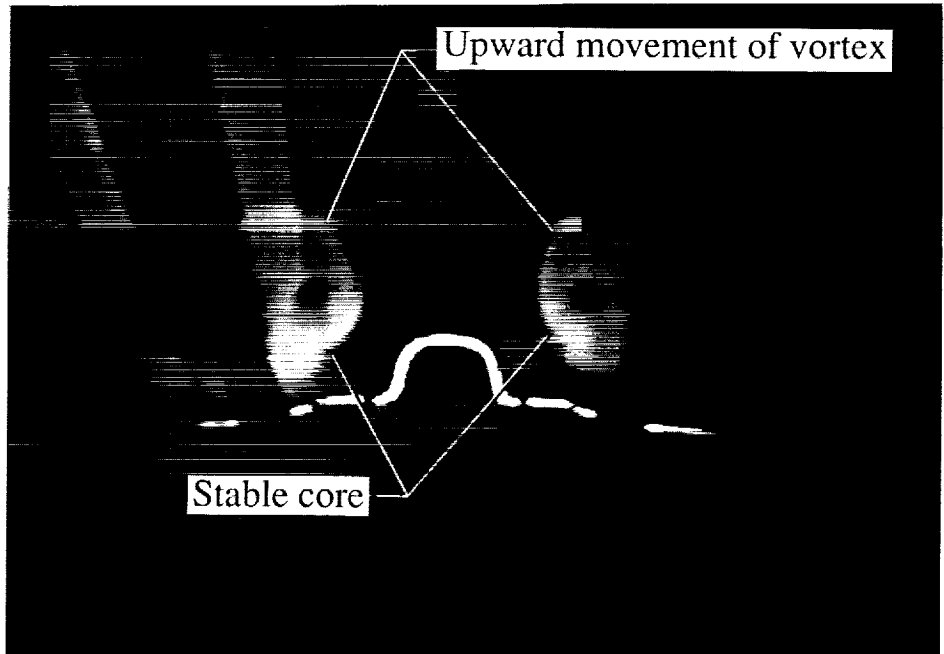
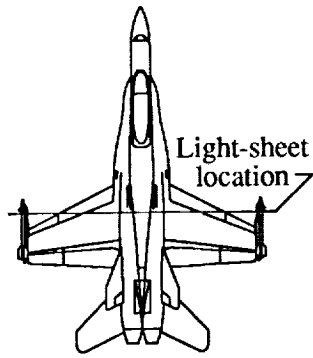


(a) LEX fence; FS 411 (24.66).

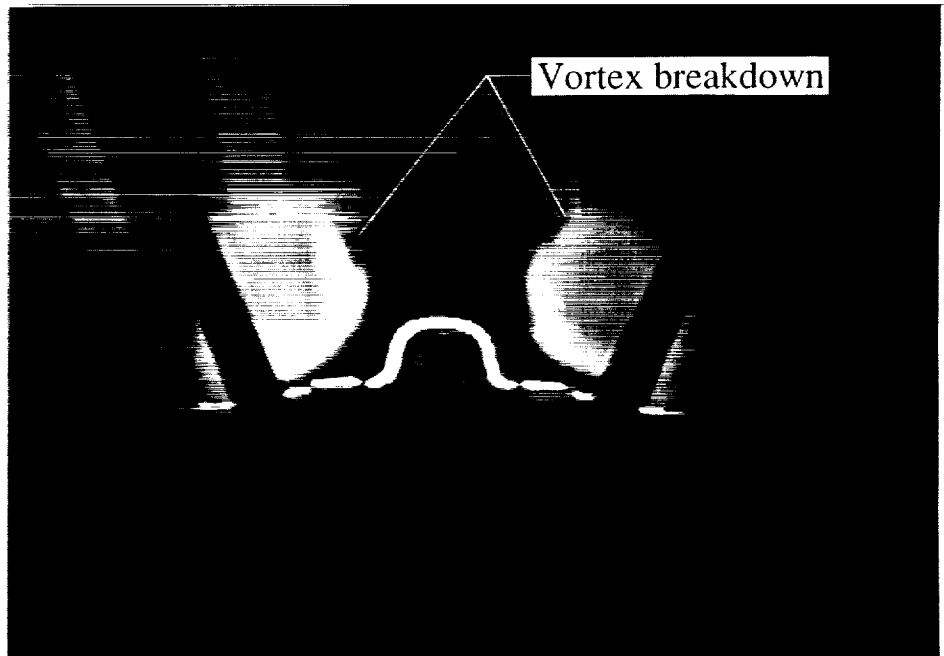
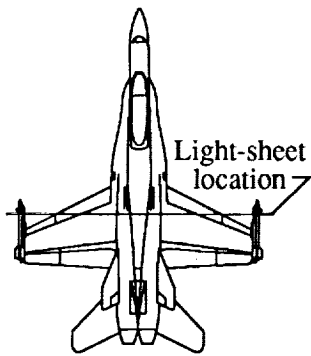


(b) Baseline; FS 411 (24.66).

Figure 65. Cross flow about LEX fence and baseline configurations at  $M_\infty = 0.60$ ,  $Re_{\bar{c}} = 1.32 \times 10^6$ , and  $\alpha = 25^\circ$ . Dimensions are in inches full scale (0.06 scale).

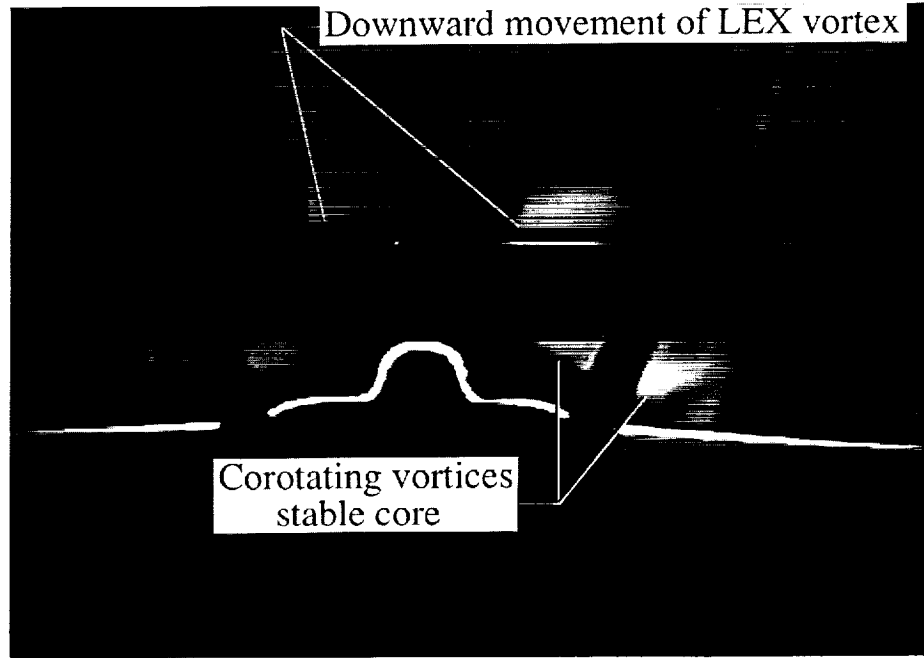
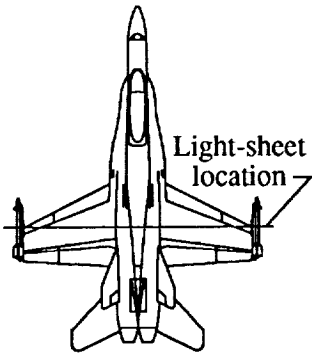


(c) LEX fence; FS 450 (27.00).

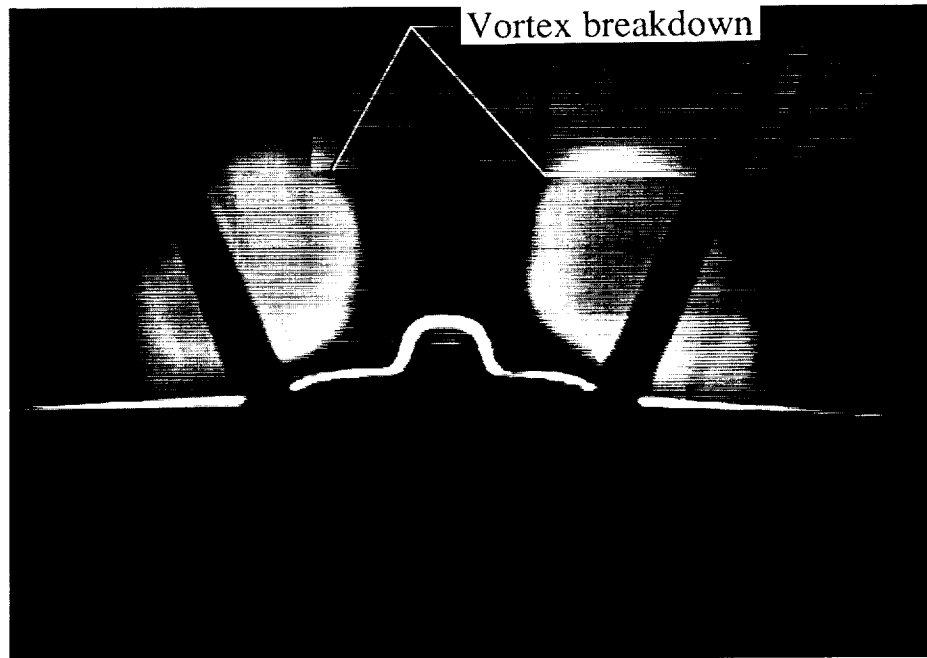
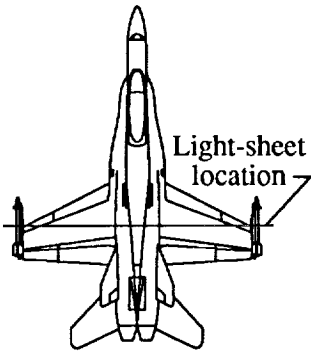


(d) Baseline; FS 450 (27.00).

Figure 65. Continued.

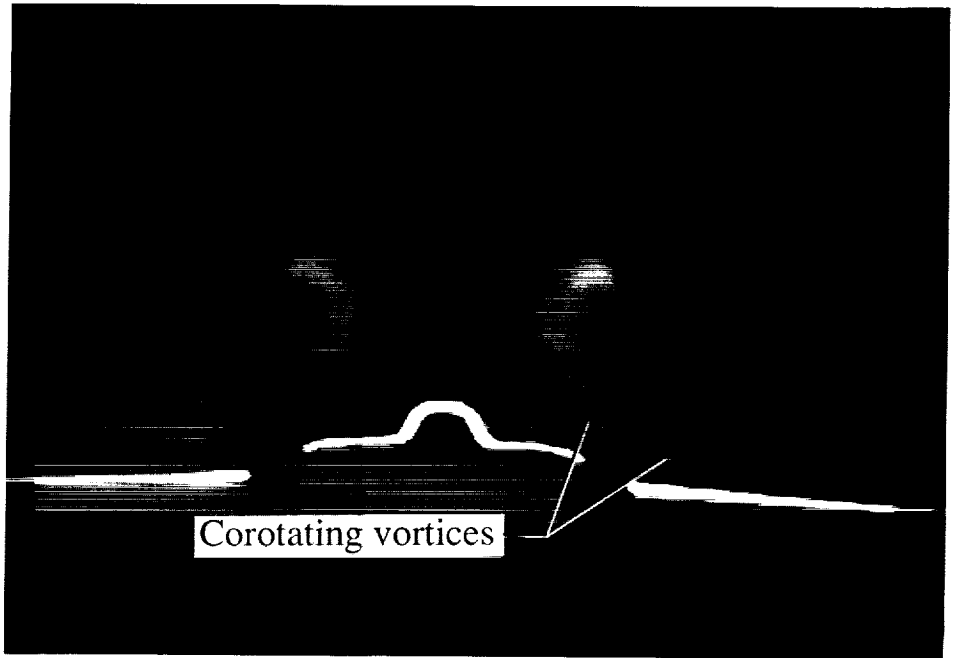
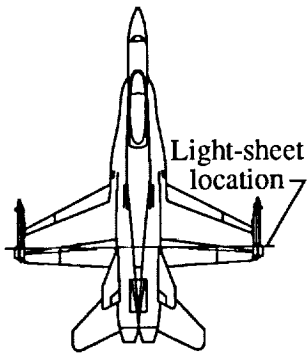


(e) LEX fence; FS 483 (28.98).

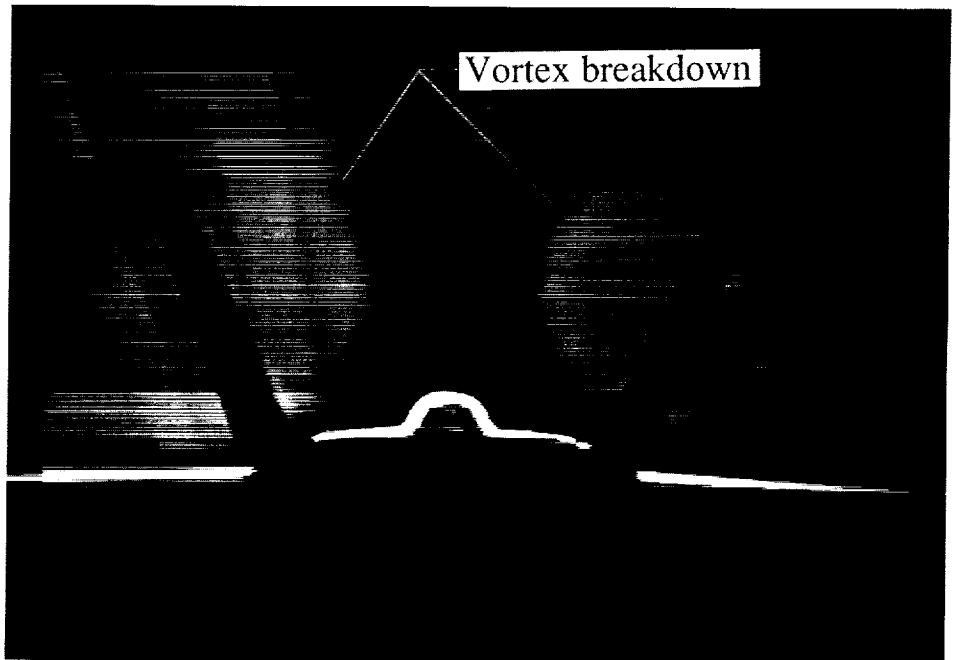
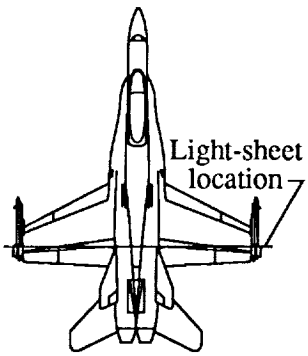


(f) Baseline; FS 483 (28.98).

Figure 65. Continued.



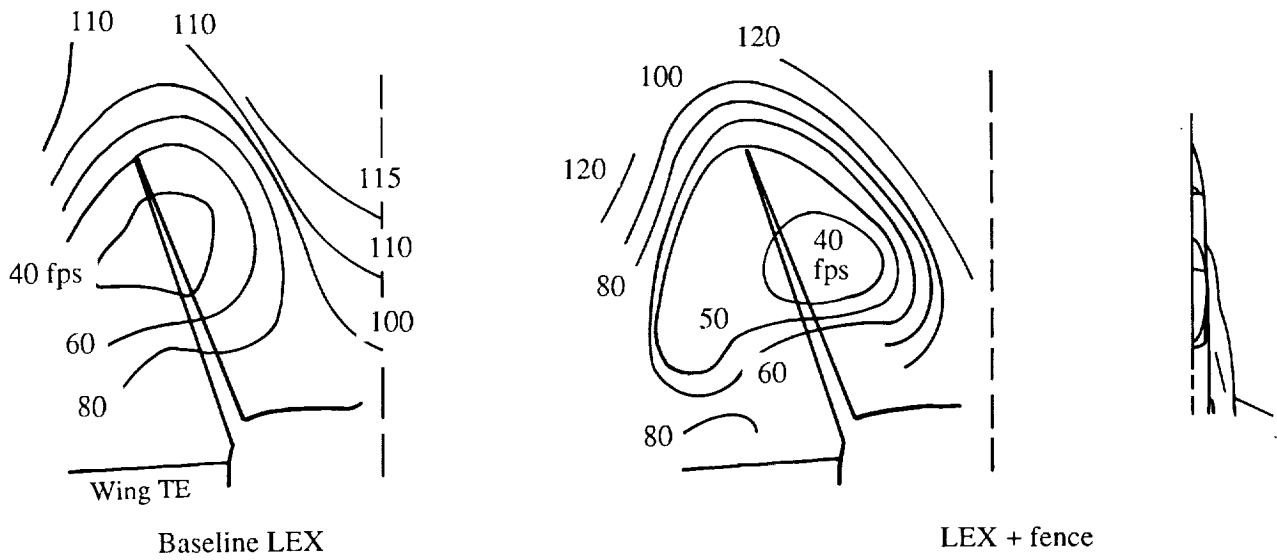
(g) LEX fence; FS 525 (31.50).



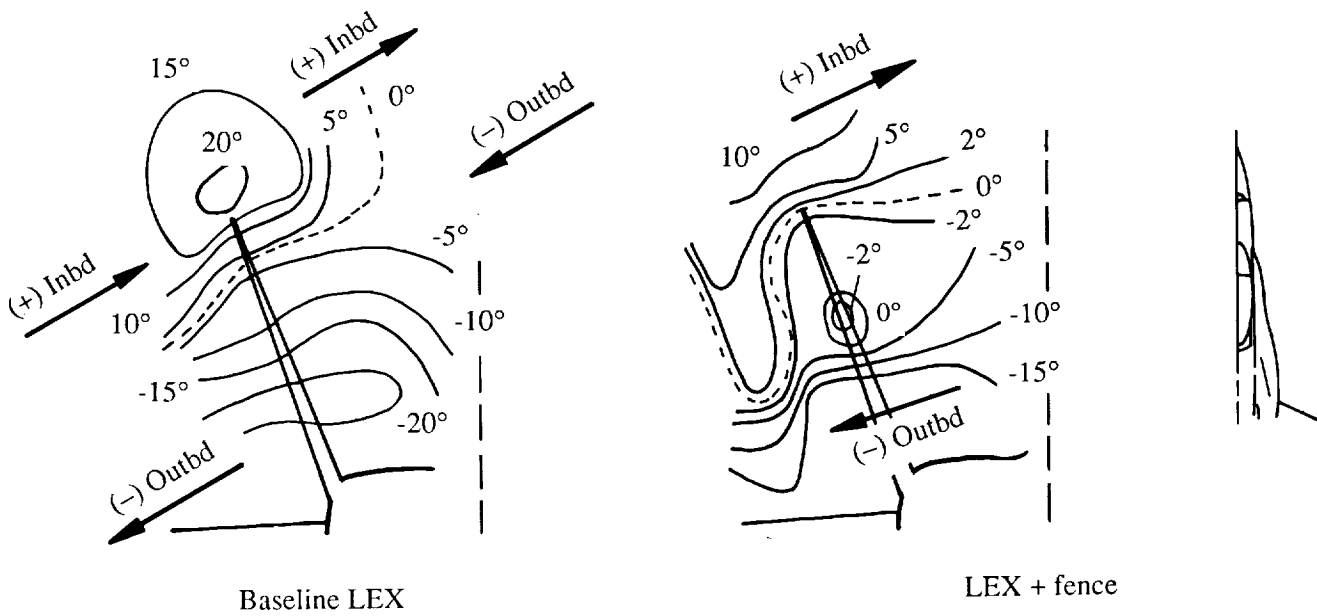
(h) Baseline; FS 525 (31.50).

Figure 65. Concluded.





(a) Mean velocity contours.



(b) Angularity contours.

Figure 66. Effect of mean velocity and flow angularity contours near vertical tails of 0.083-scale F/A-18 model at  $M_\infty = 0.07$  and  $\alpha \approx 29^\circ$ . (Unpublished McDonnell Douglas data.)

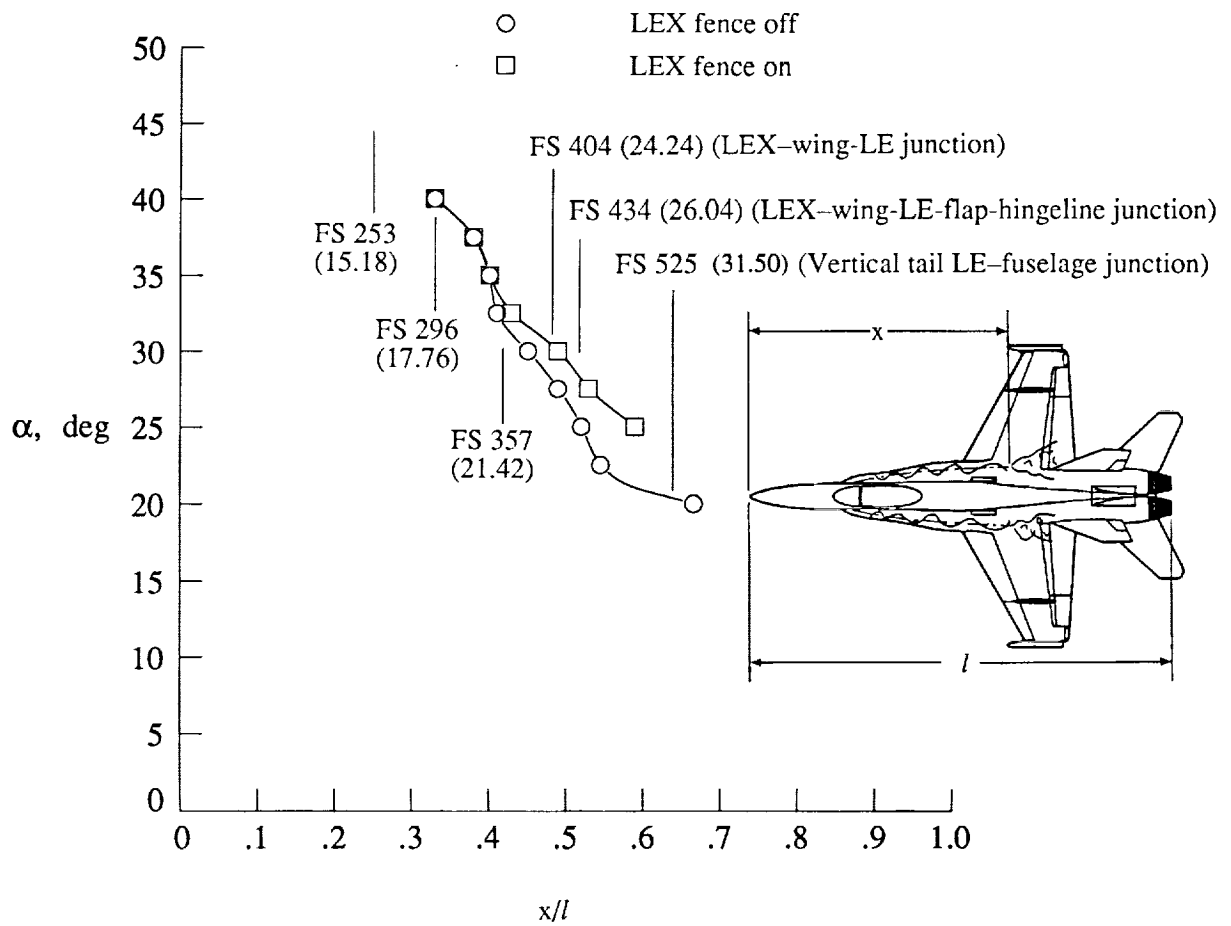
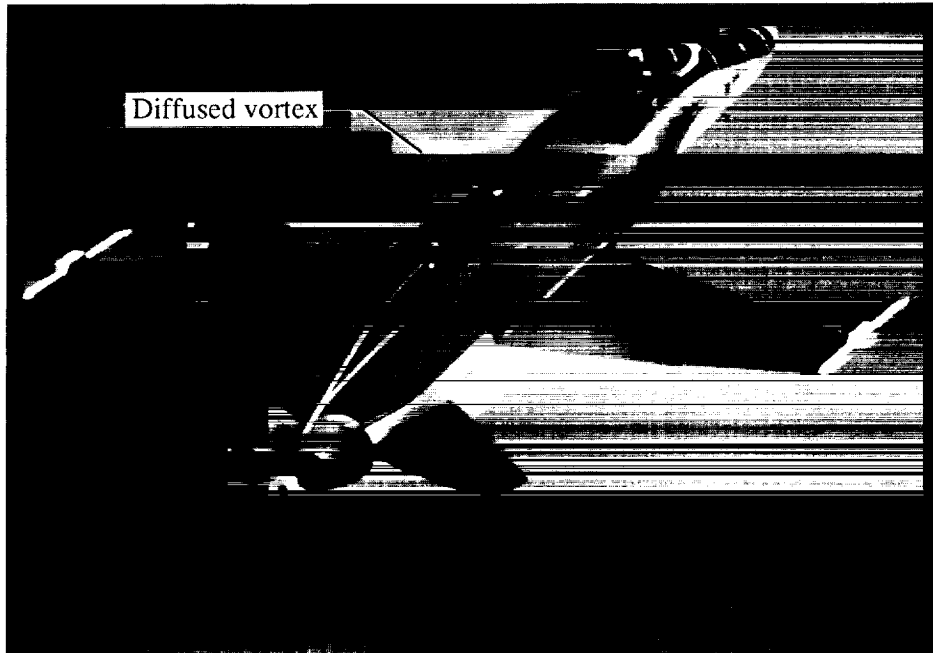
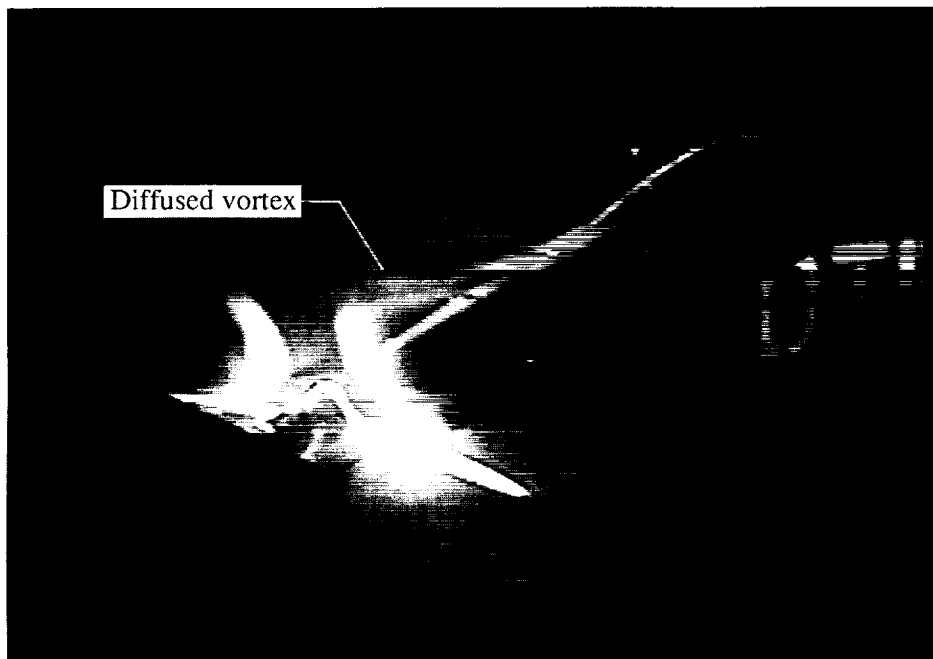


Figure 67. Effect of LEX fence on vortex breakdown progression with angle of attack at  $M_\infty = 0.60$  and  $Re_{\bar{c}} = 1.32 \times 10^6$ . Dimensions are in inches full scale (0.06 scale).

ORIGINAL PAGE  
BLACK AND WHITE PHOTOGRAPH



(a) F-18 HARV;  $M_\infty \approx 0.27$ ;  $Re_{\bar{c}} \approx 13 \times 10^6$ .



(b) 0.06-scale F/A-18;  $M_\infty = 0.40$ ;  $Re_{\bar{c}} = 1.75 \times 10^6$ .

Figure 68. Flight and wind tunnel flow visualizations at  $\alpha = 20^\circ$  with LEX fences on.

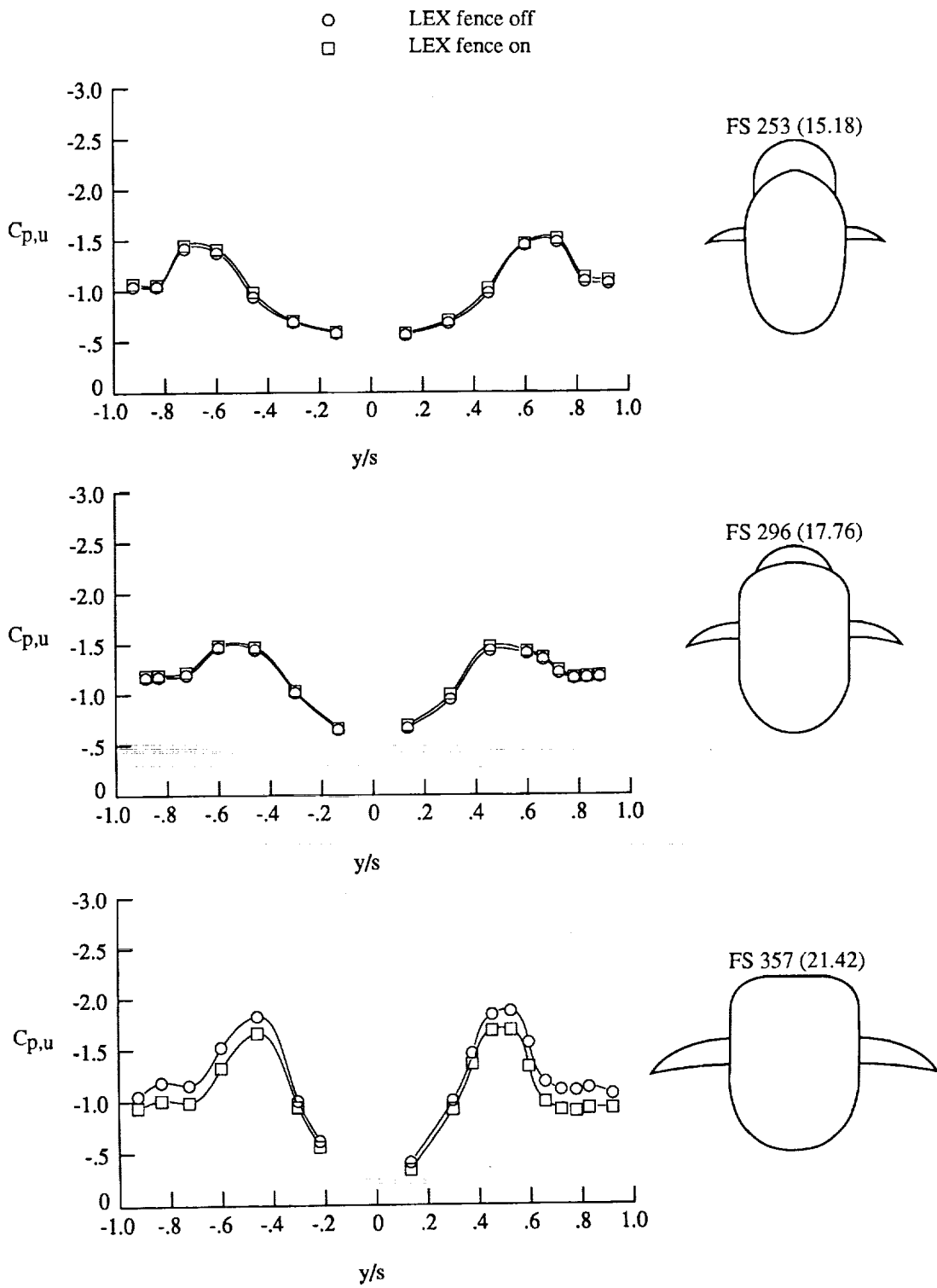
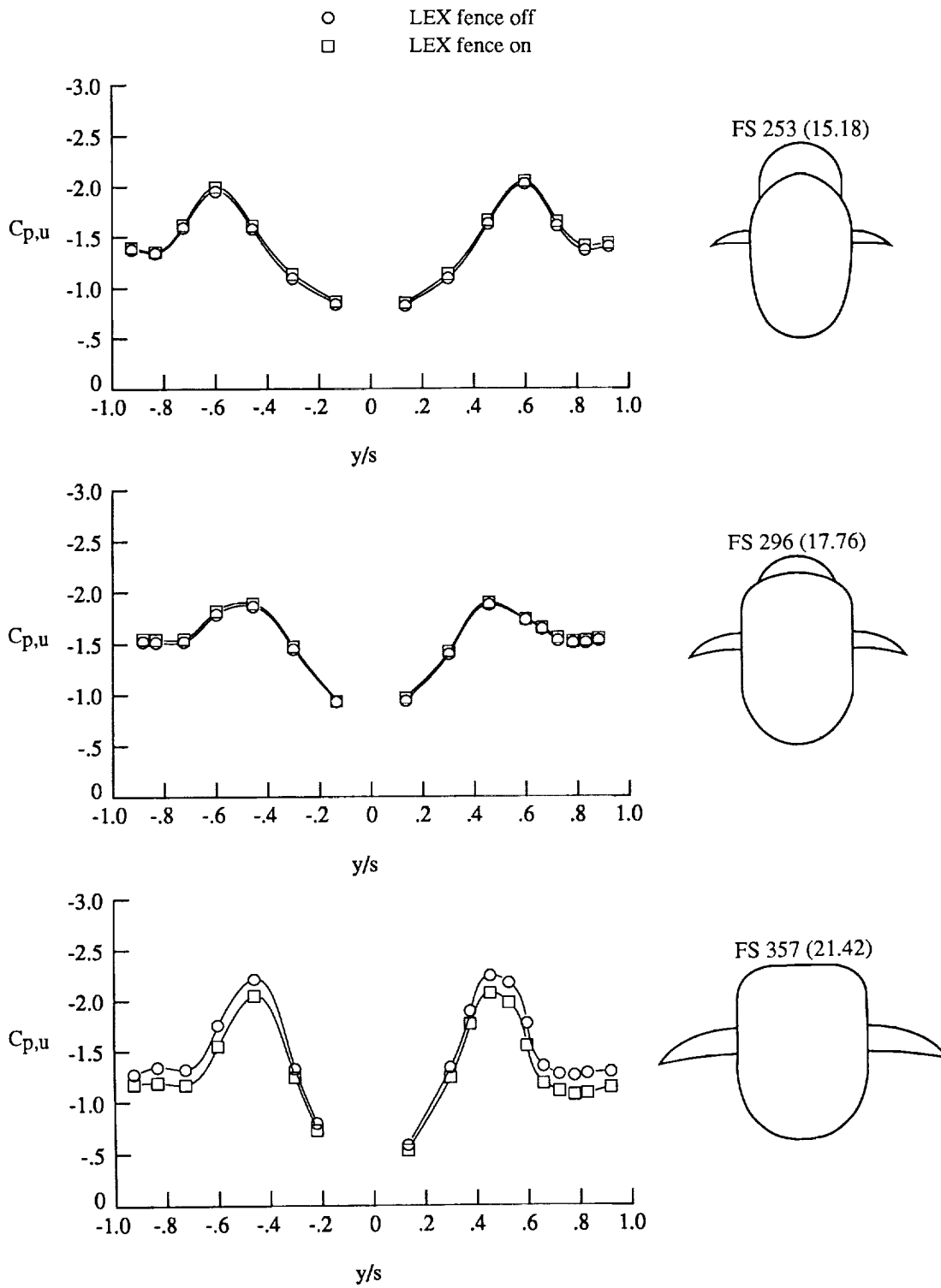
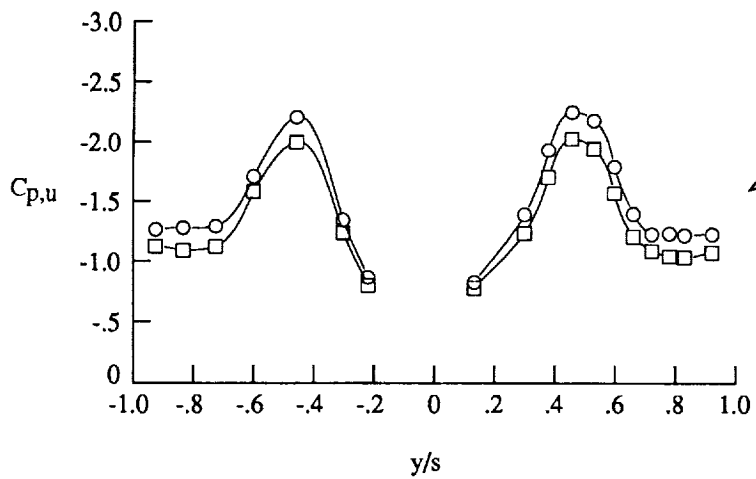
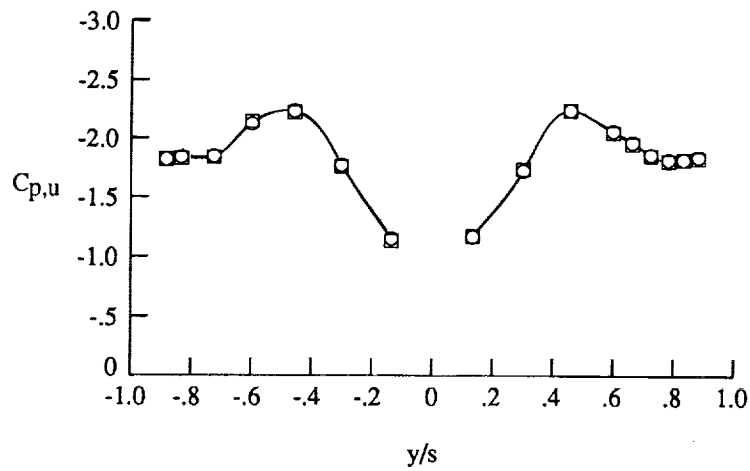
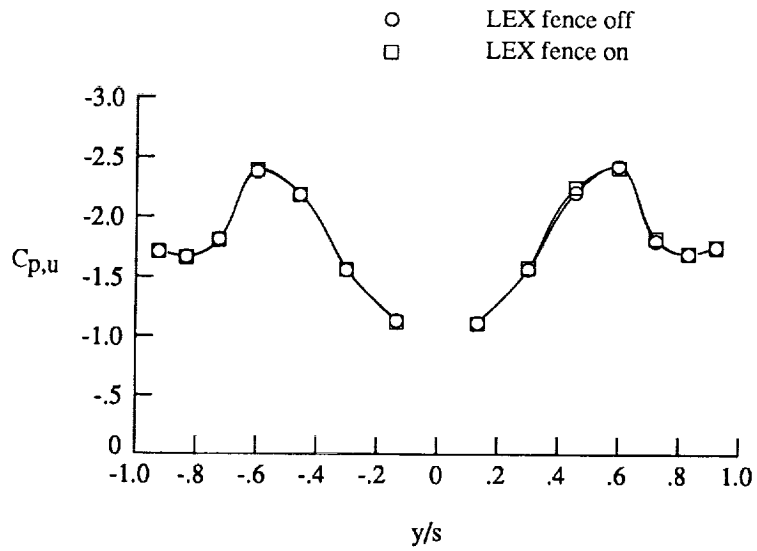


Figure 69. Effect of LEX fence on LEX surface static pressures at  $M_\infty = 0.30$  and  $Re_c = 1.40 \times 10^6$ . Dimensions are in inches full scale (0.06 scale).



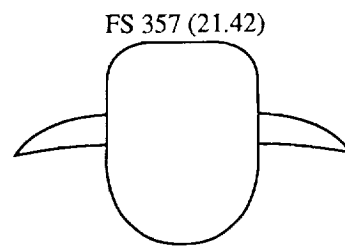
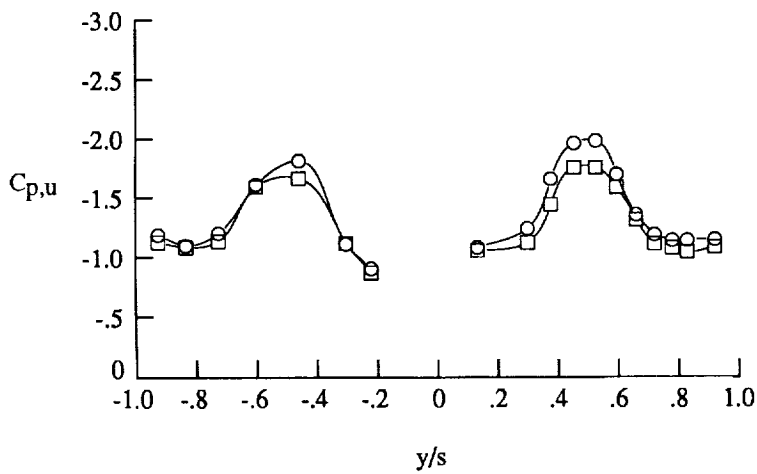
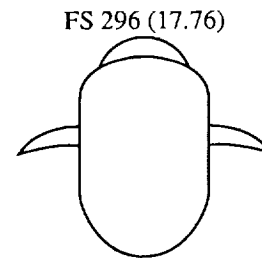
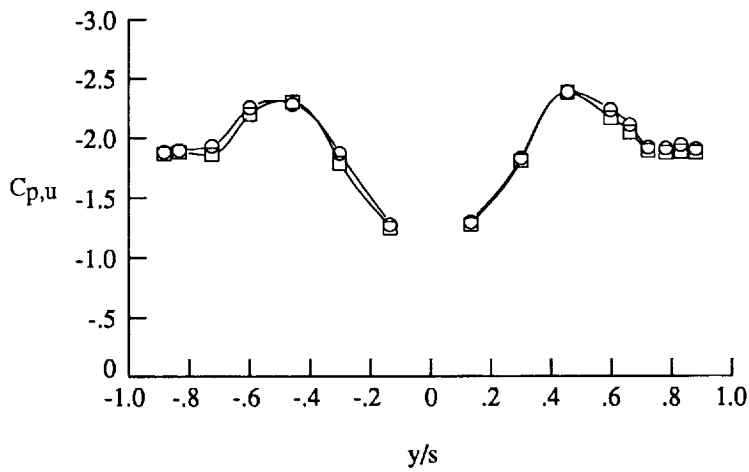
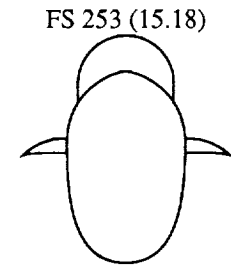
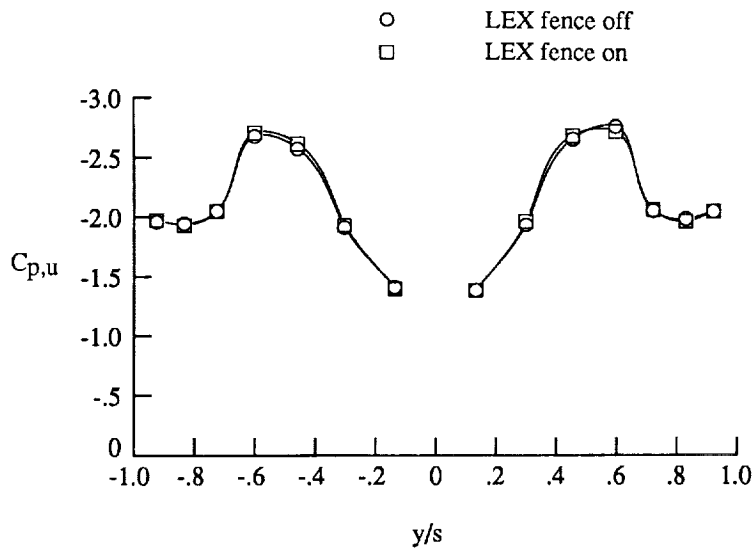
(b)  $\alpha = 25^\circ$ .

Figure 69. Continued.



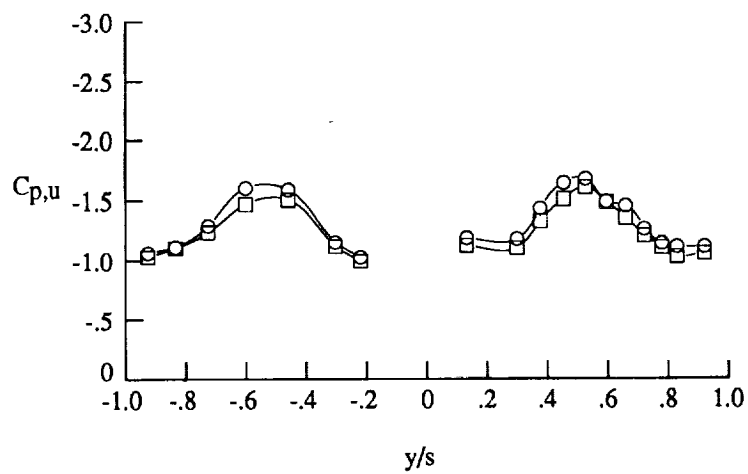
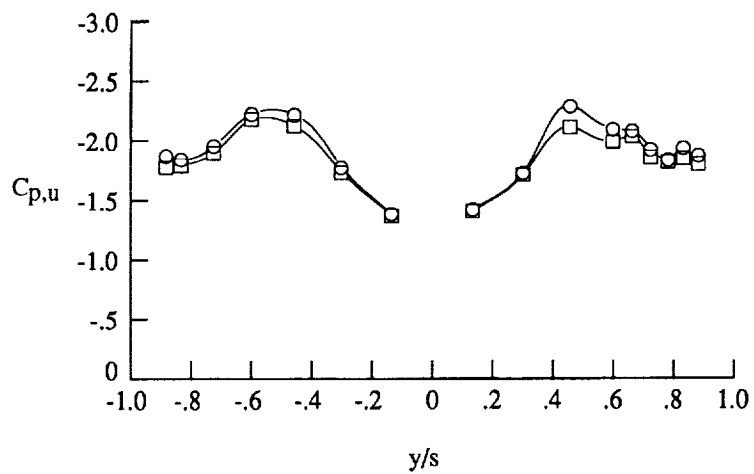
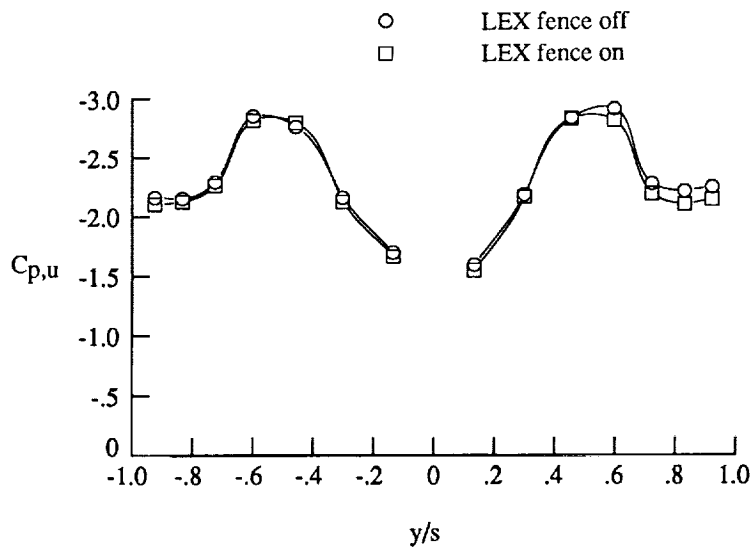
(c)  $\alpha = 30^\circ$

Figure 69. Continued.



(d)  $\alpha = 35^\circ$ .

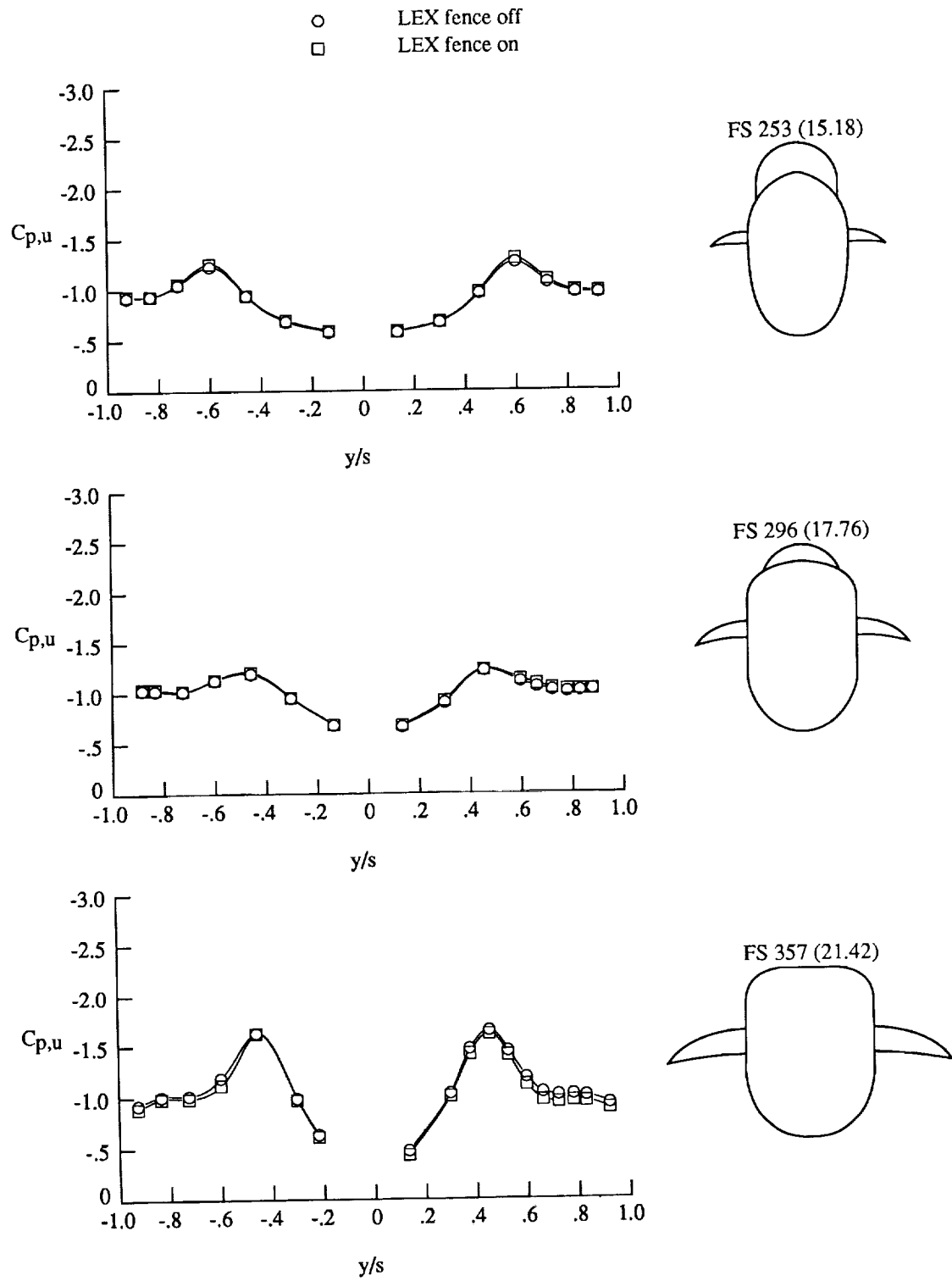
Figure 69. Continued.



(e)  $\alpha = 40^\circ$ .

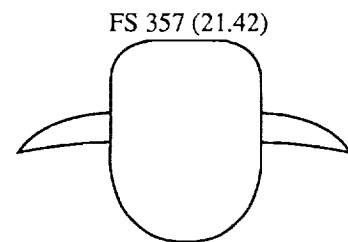
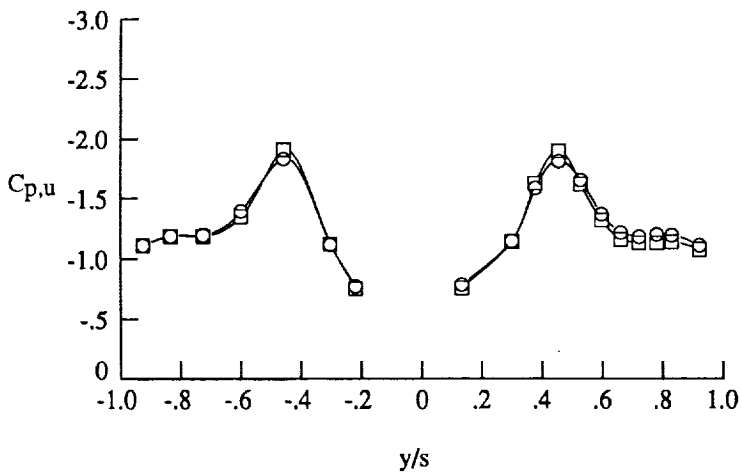
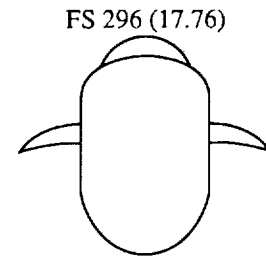
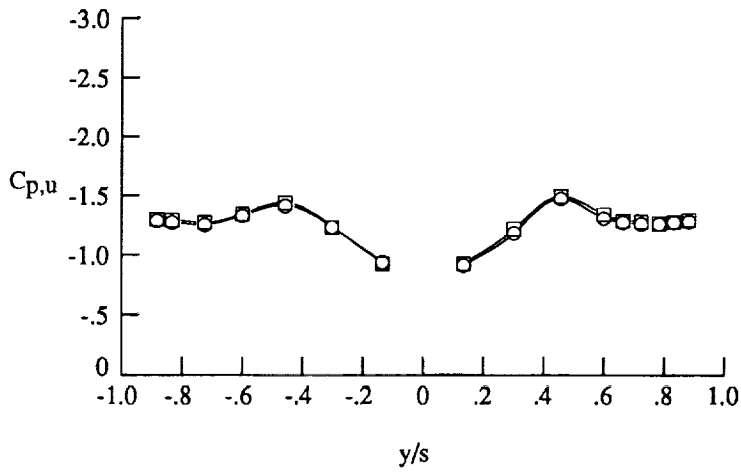
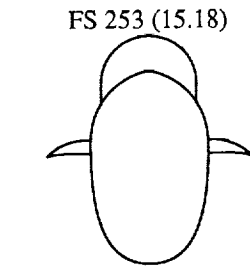
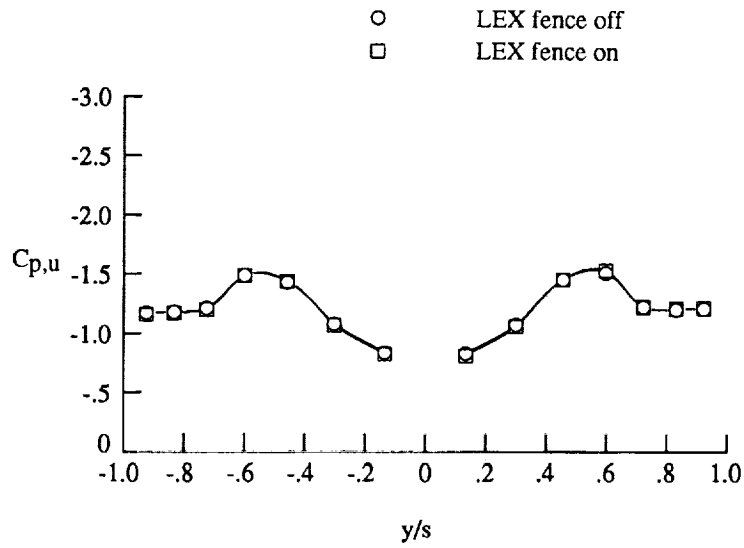
Figure 69. Concluded.





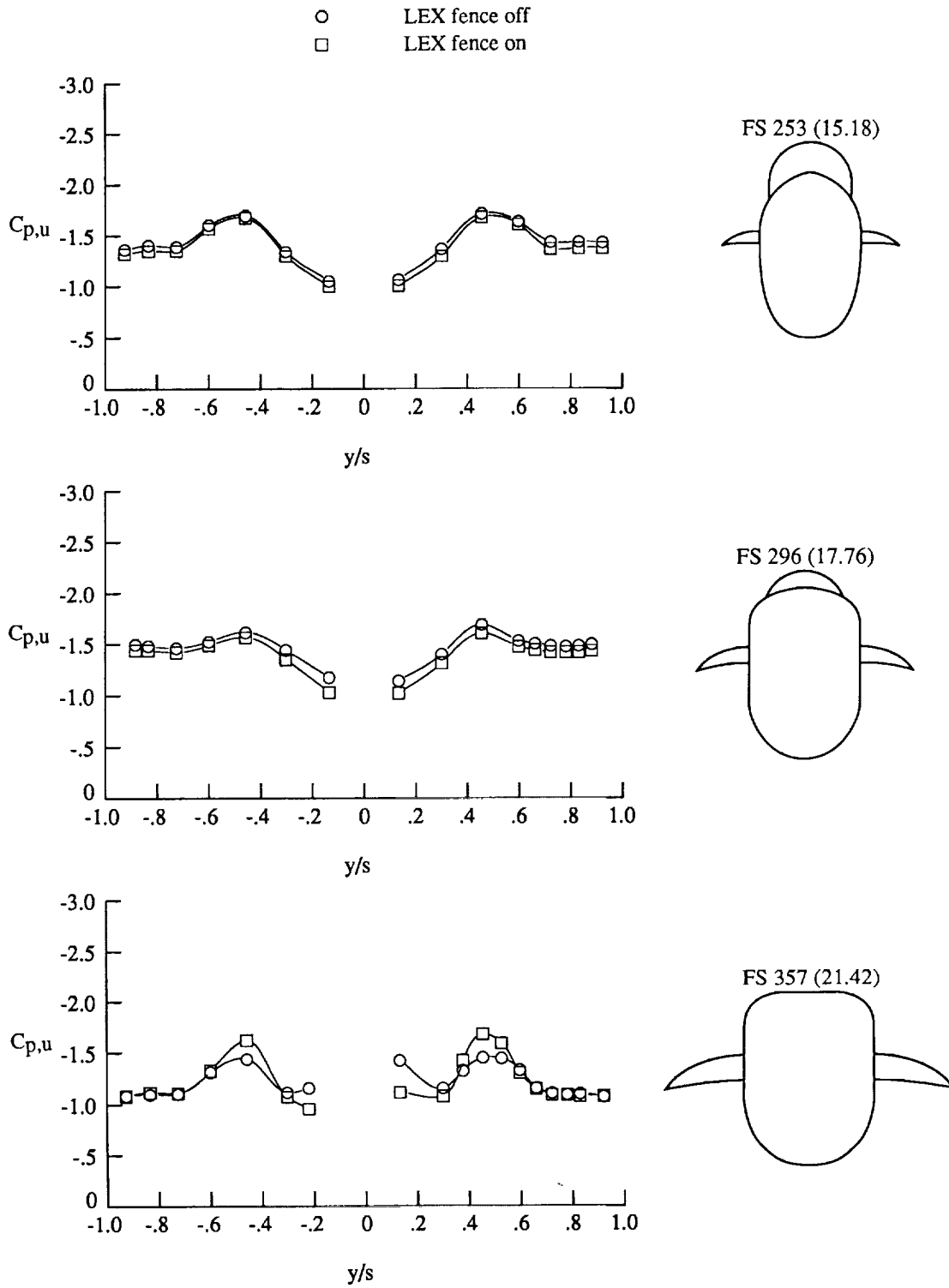
(a)  $\alpha = 20^\circ$ .

Figure 70. Effect of LEX fence on LEX surface static pressures at  $M_\infty = 0.60$  and  $Re_c = 1.32 \times 10^6$ . Dimensions are in inches full scale (0.06 scale).



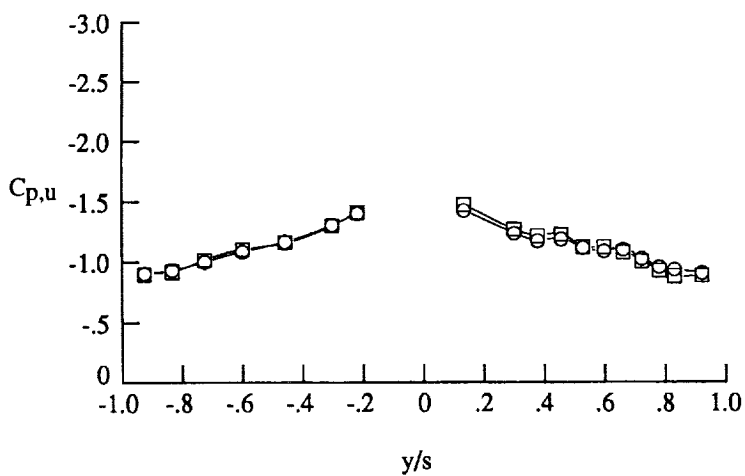
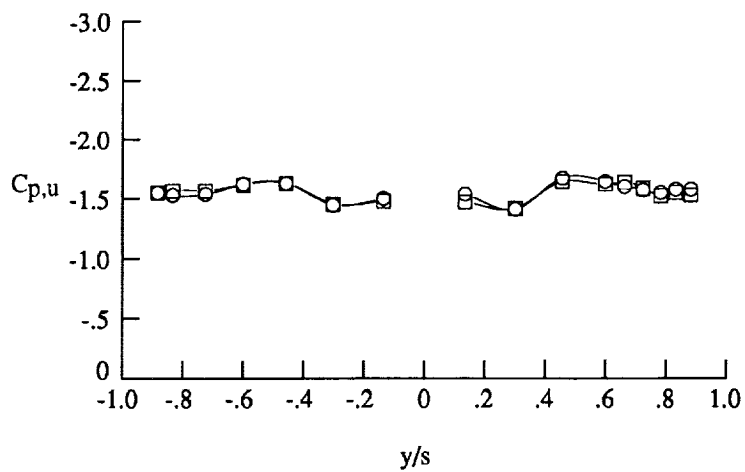
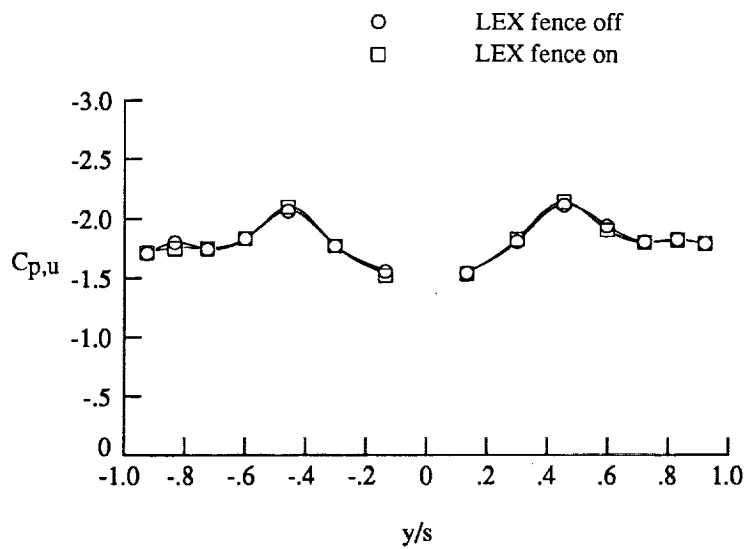
(b)  $\alpha = 25^\circ$ .

Figure 70. Continued.



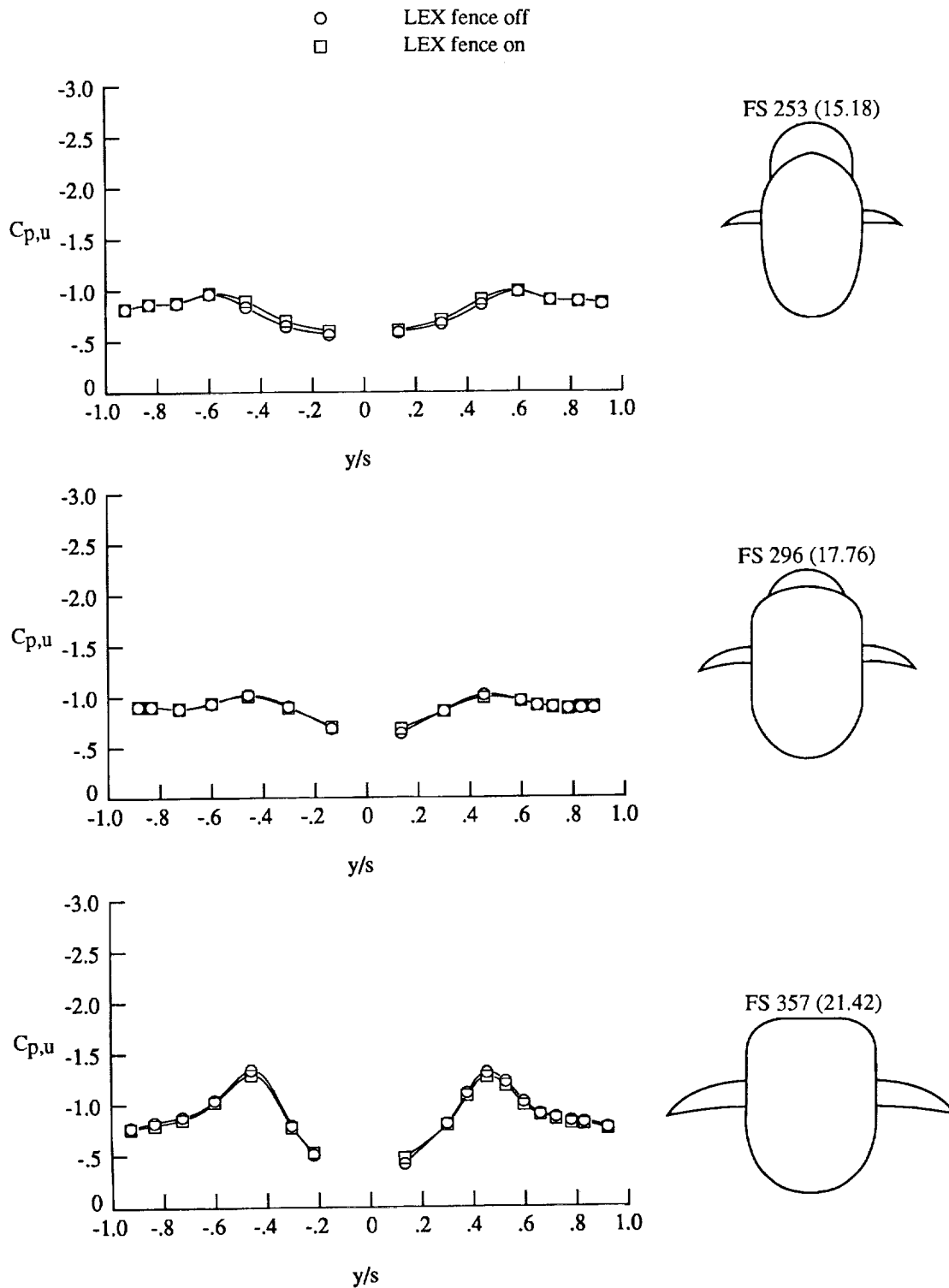
(c)  $\alpha = 30^\circ$ .

Figure 70. Continued.



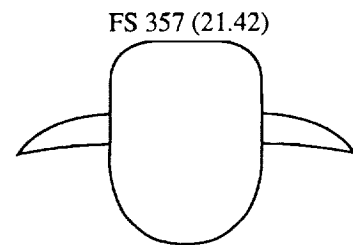
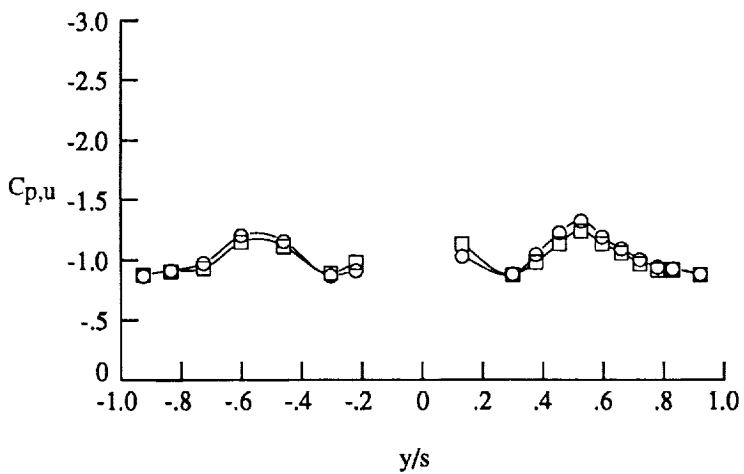
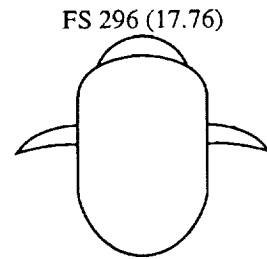
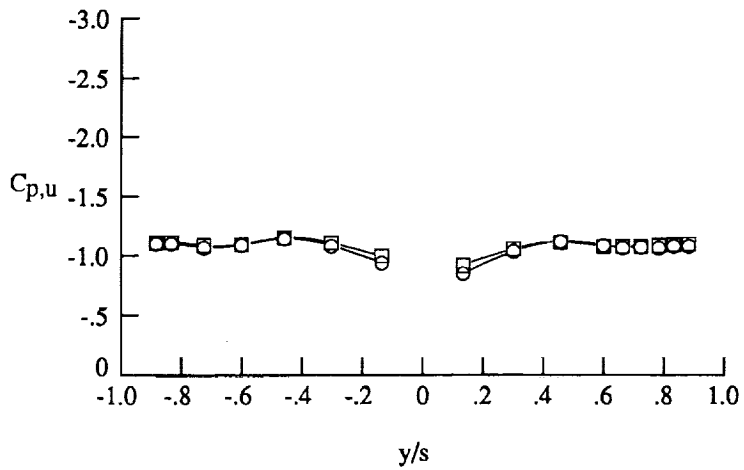
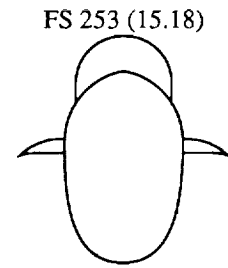
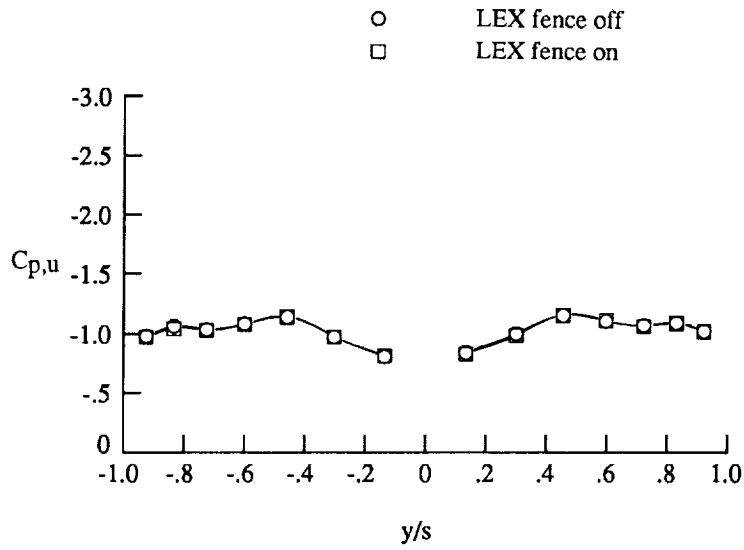
(d)  $\alpha = 40^\circ$ .

Figure 70. Concluded.



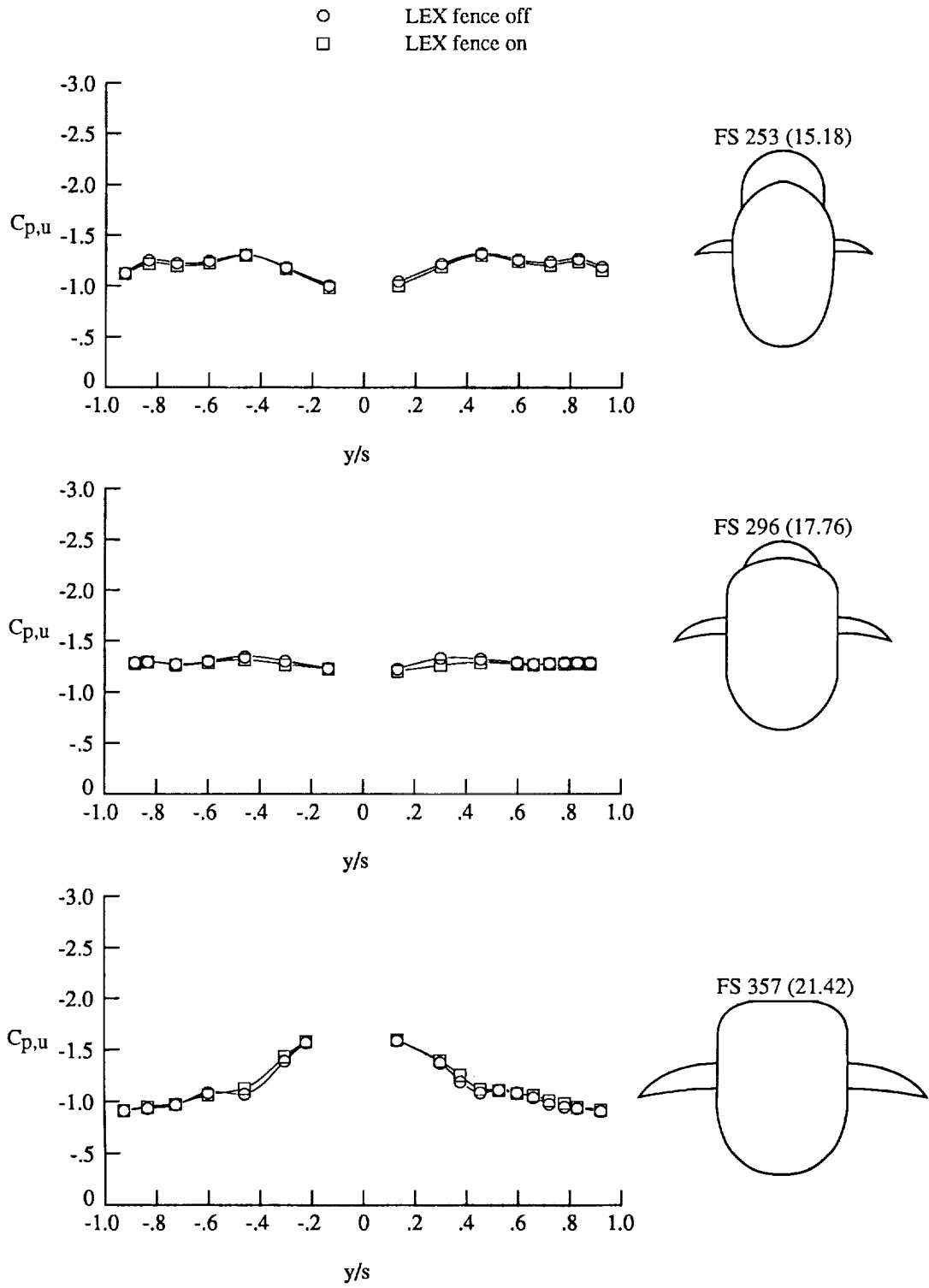
(a)  $\alpha = 20^\circ$ .

Figure 71. Effect of LEX fence on LEX surface static pressures at  $M_\infty = 0.80$  and  $Re_c = 1.02 \times 10^6$ . Dimensions are in inches full scale (0.06 scale).



(b)  $\alpha = 25^\circ$ .

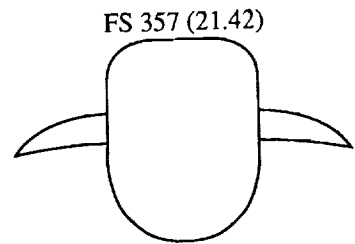
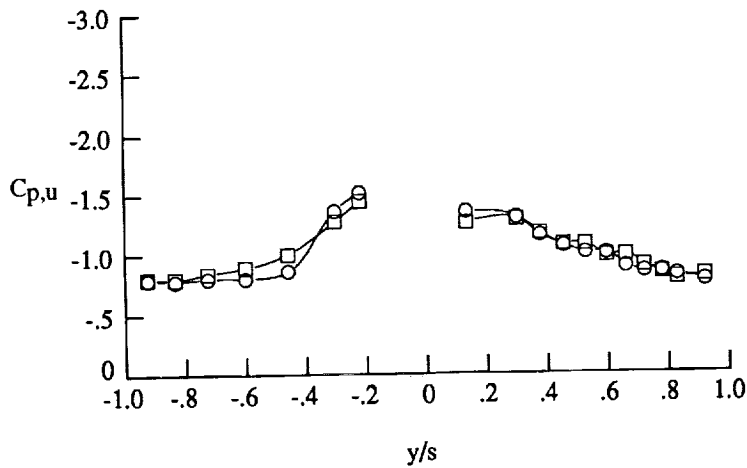
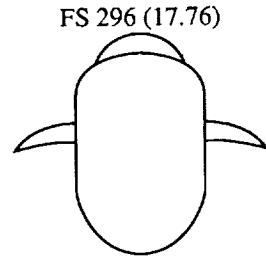
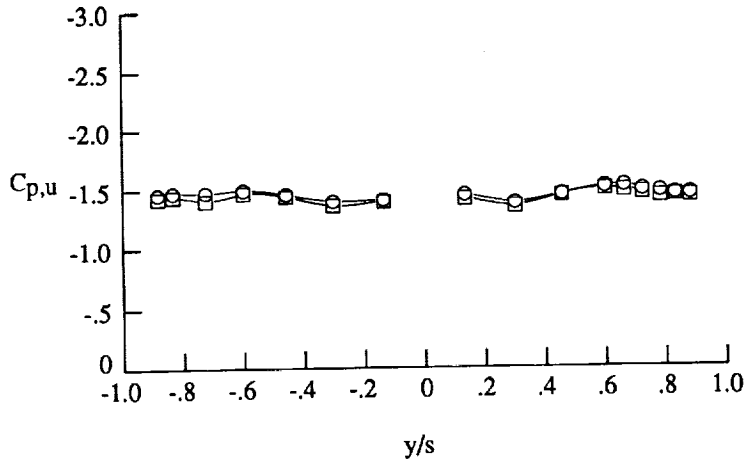
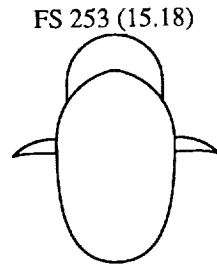
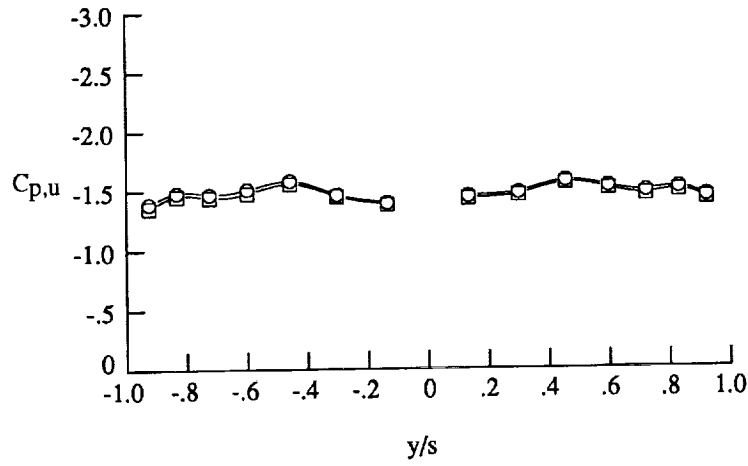
Figure 71. Continued.



(c)  $\alpha = 30^\circ$ .

Figure 71. Continued.

○ LEX fence off  
 □ LEX fence on



(d)  $\alpha = 40^\circ$ .

Figure 71. Concluded.



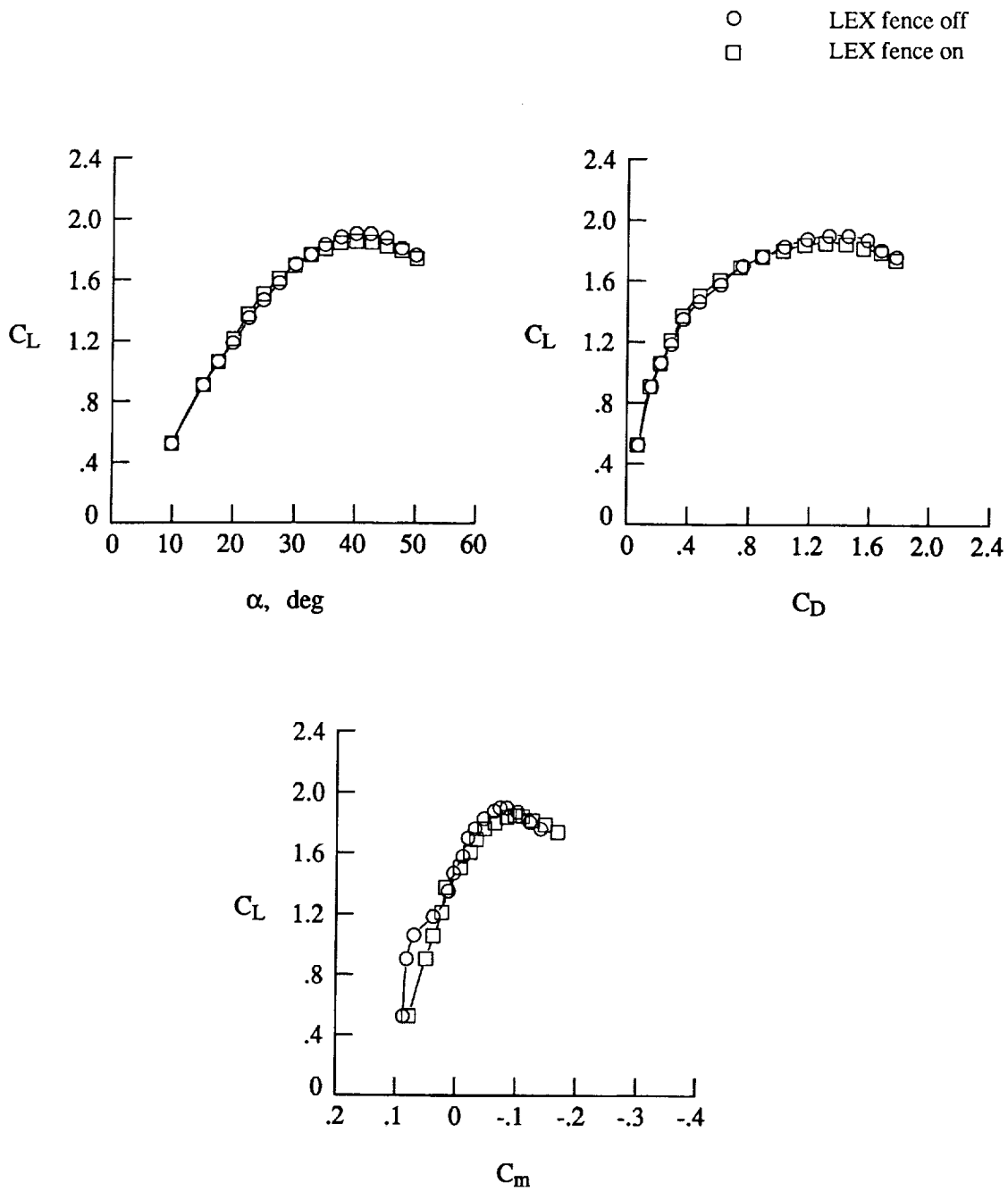


Figure 72. Effect of LEX fence on lift, drag, and pitching-moment characteristics at  $M_\infty = 0.30$  and  $Re_c = 1.40 \times 10^6$ .

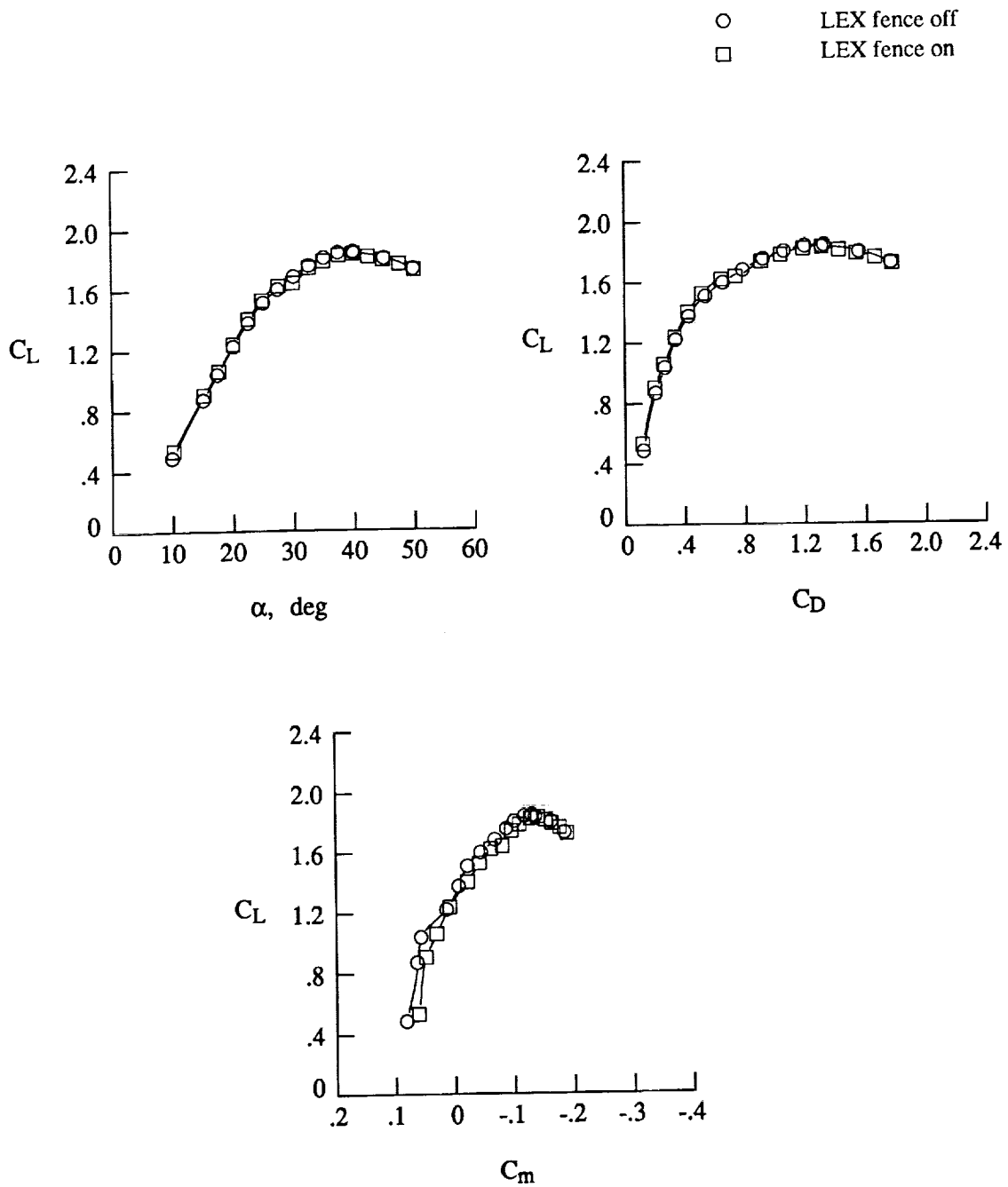


Figure 73. Effect of LEX fence on lift, drag, and pitching-moment characteristics at  $M_\infty = 0.60$  and  $Re_c = 1.32 \times 10^6$ .

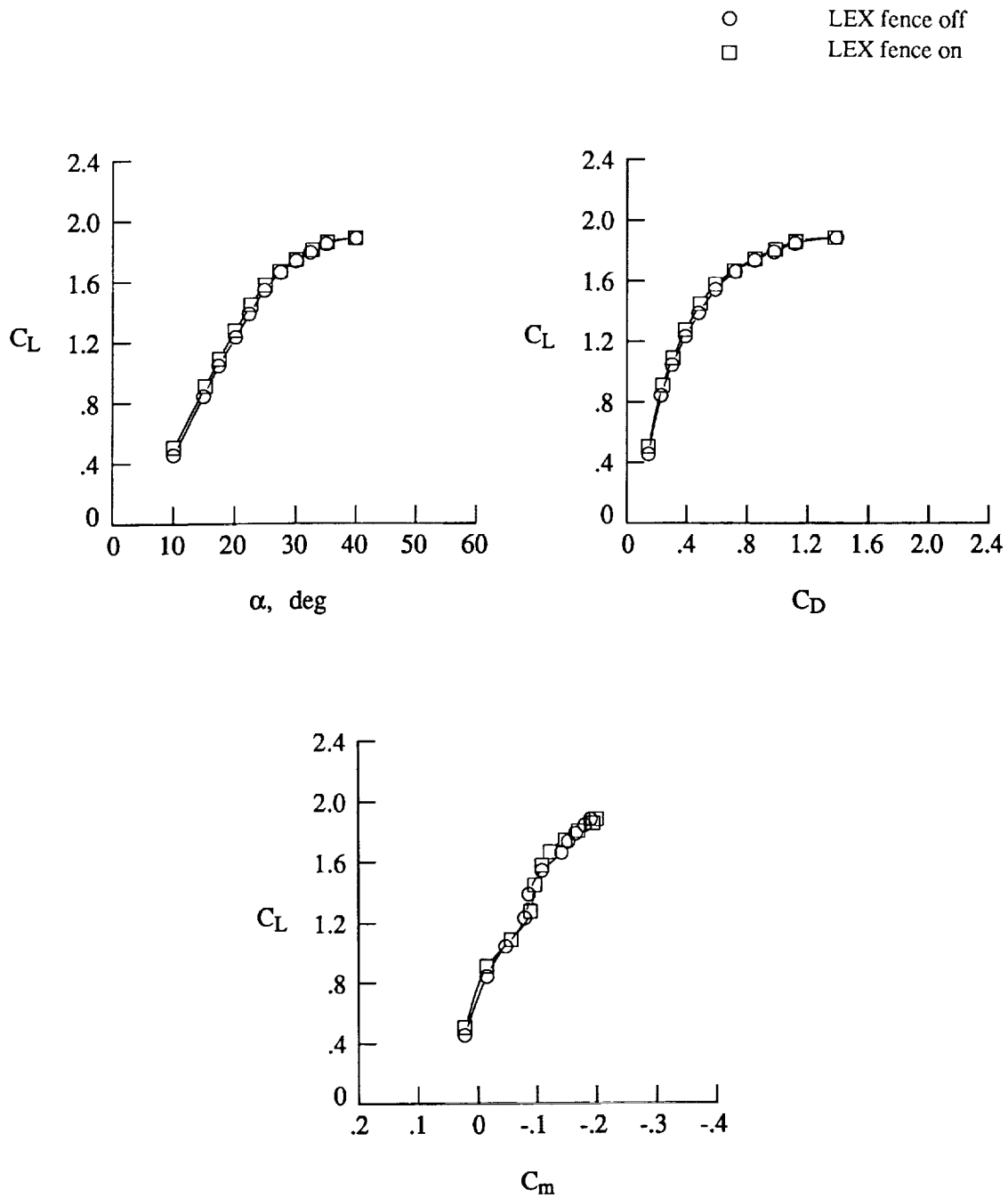
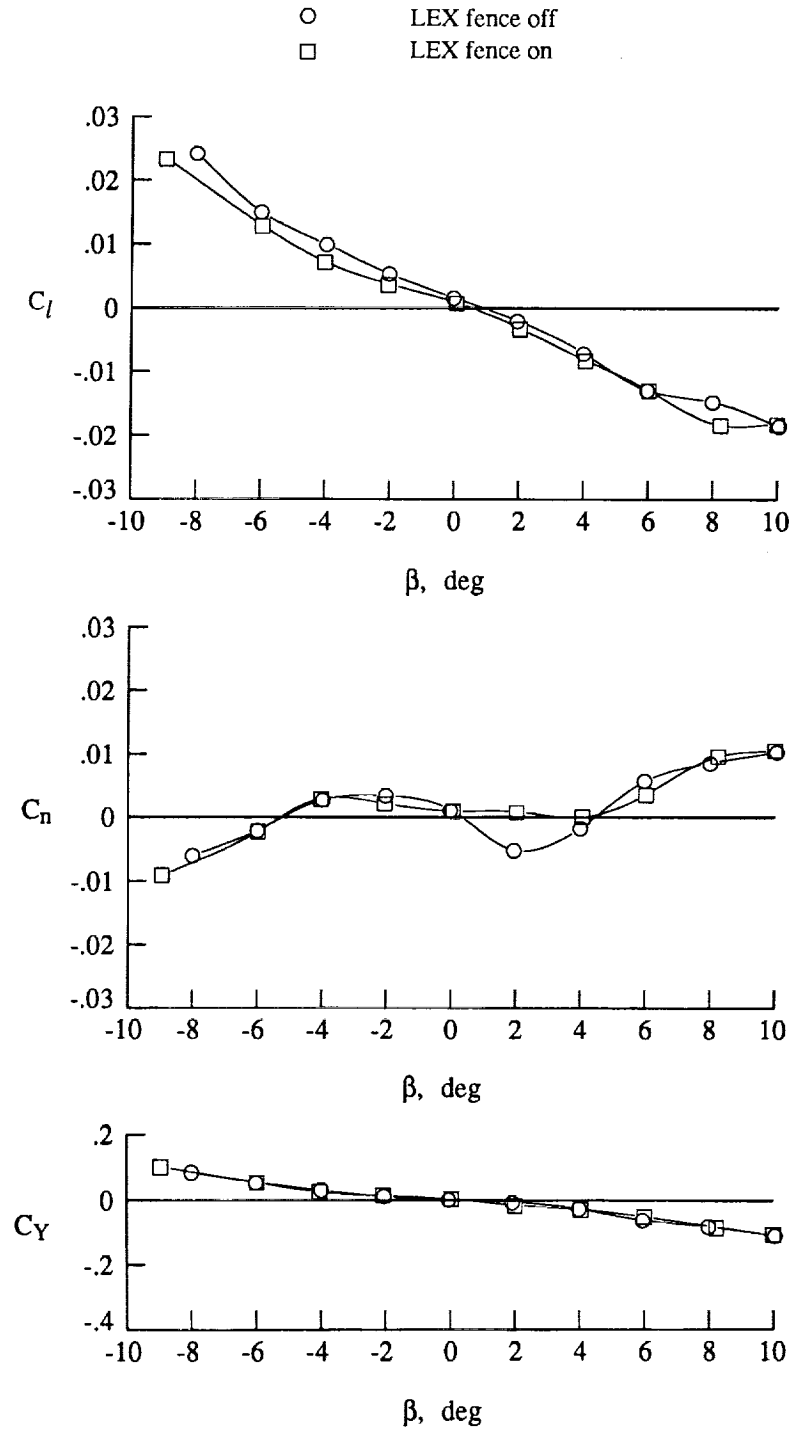


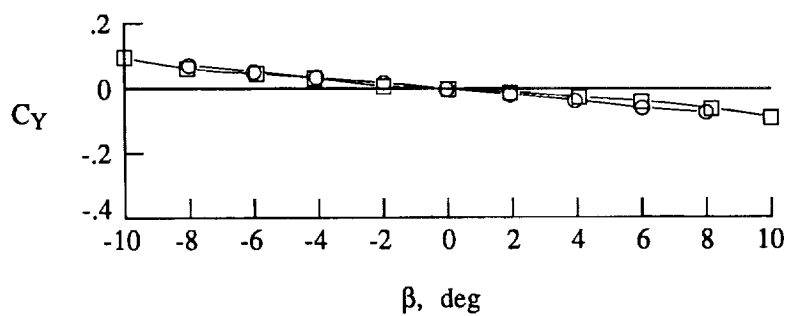
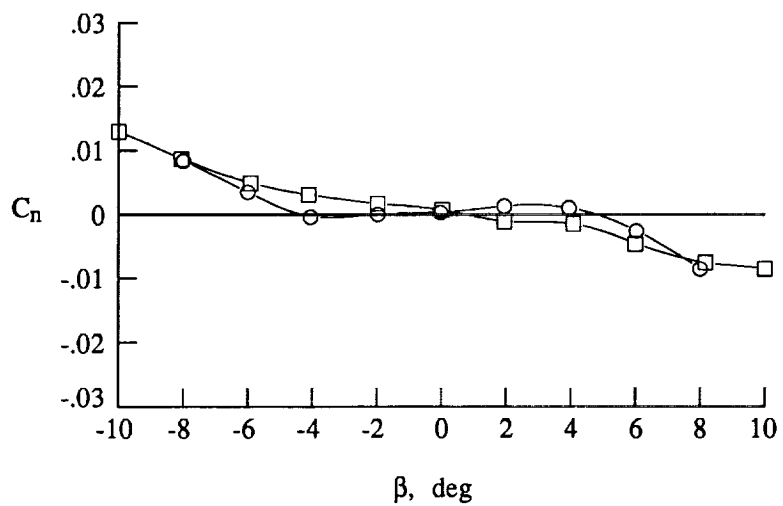
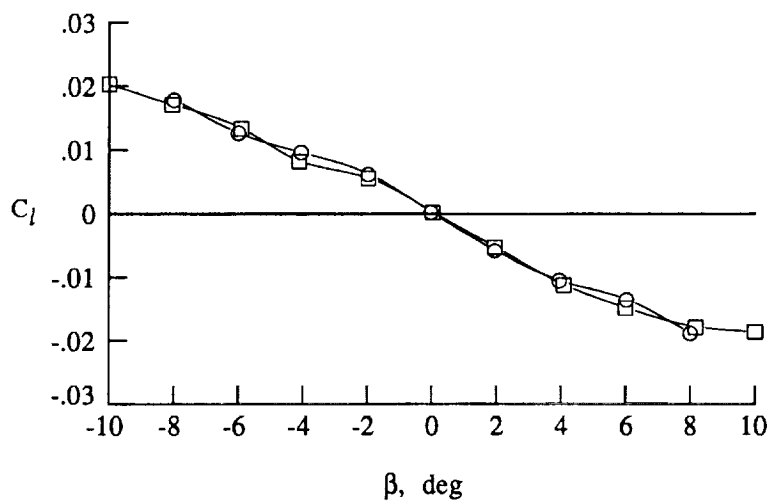
Figure 74. Effect of LEX fence on lift, drag, and pitching-moment characteristics at  $M_\infty = 0.80$  and  $Re_{\bar{c}} = 1.02 \times 10^6$ .



(a)  $\alpha = 20^\circ$ .

Figure 75. Effect of LEX fence on rolling-moment, yawing-moment, and side-force coefficient variations with sideslip at  $M_\infty = 0.60$  and  $Re_{\bar{c}} = 1.32 \times 10^6$ .

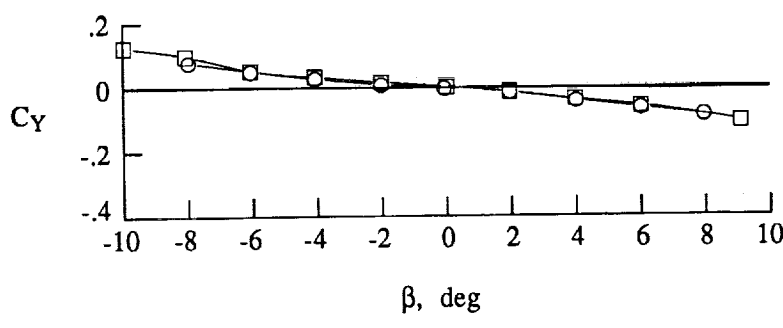
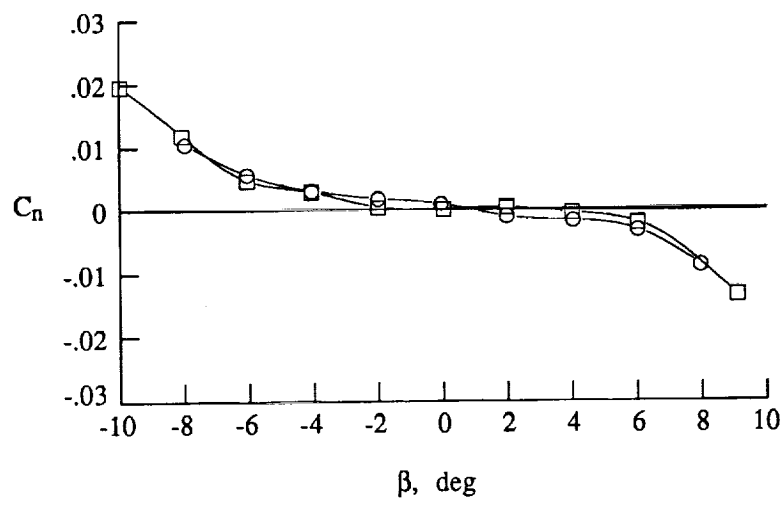
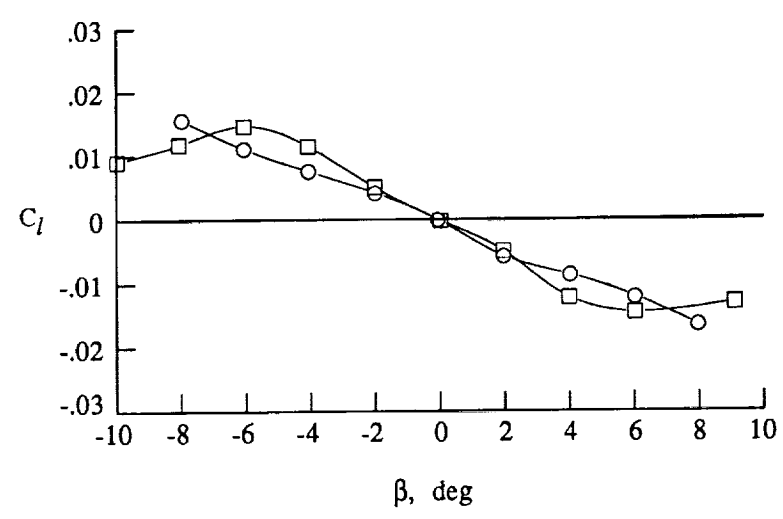
○ LEX fence off  
 □ LEX fence on



(b)  $\alpha = 25^\circ$ .

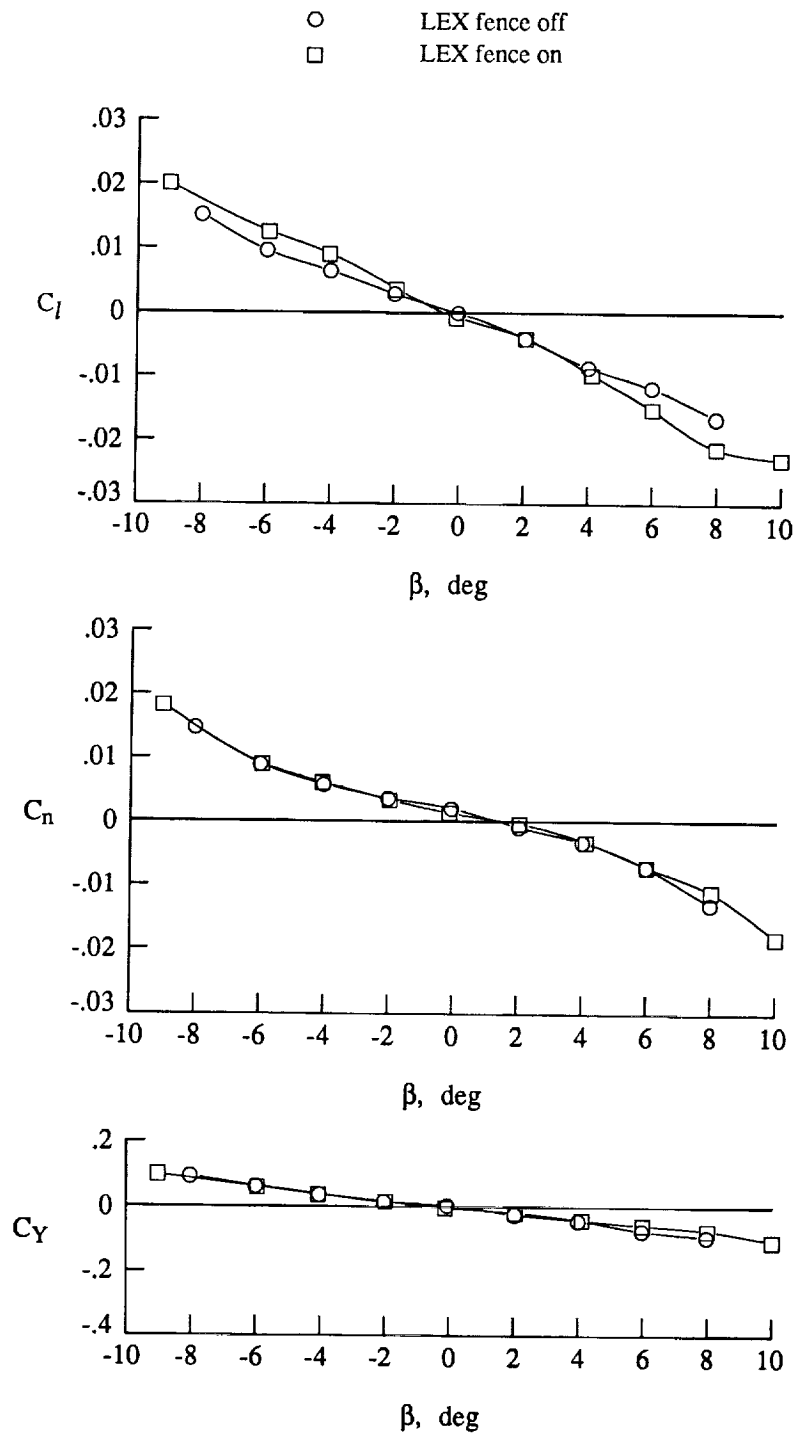
Figure 75. Continued.

○ LEX fence off  
 □ LEX fence on



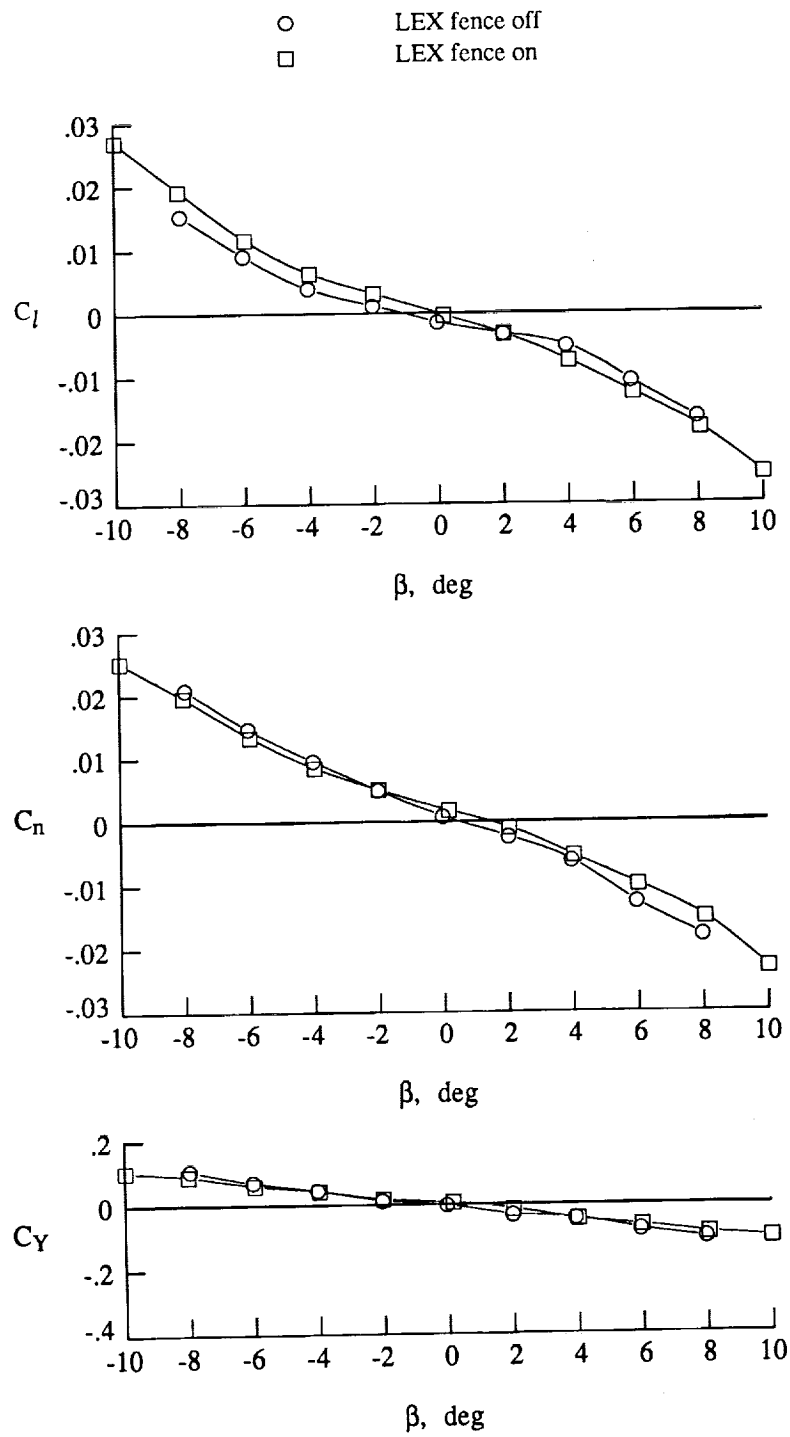
(c)  $\alpha = 30^\circ$ .

Figure 75. Continued.



(d)  $\alpha = 35^\circ$ .

Figure 75. Continued.

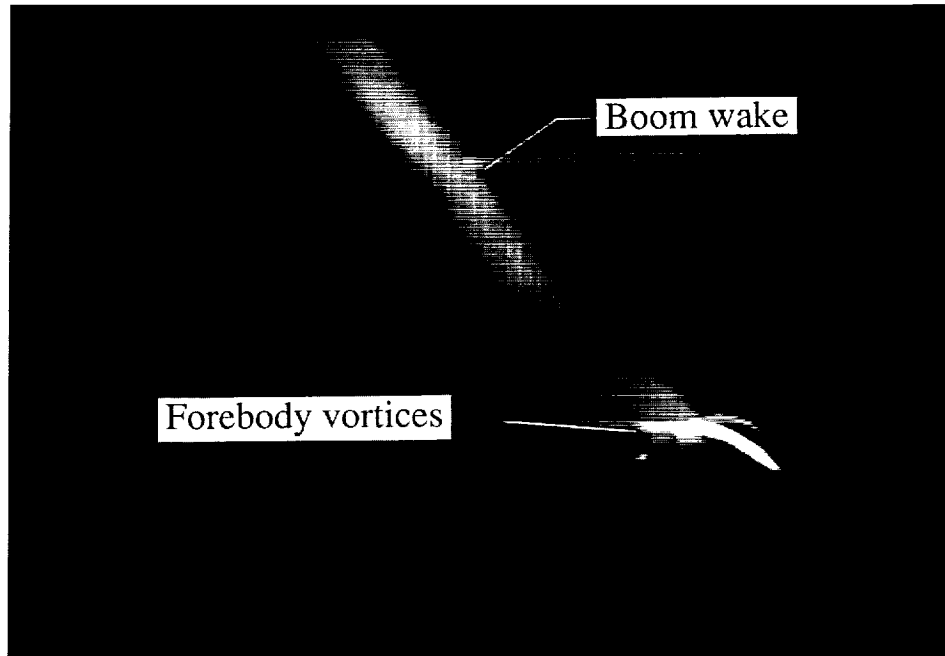
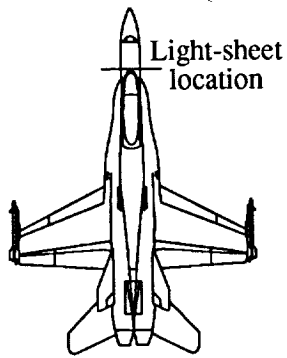


(e)  $\alpha = 40^\circ$ .

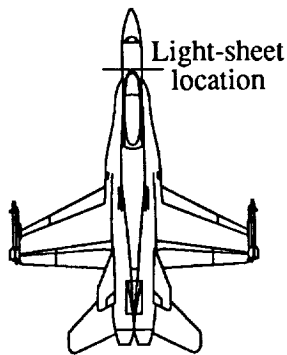
Figure 75. Concluded.



ORIGINAL PAGE  
BLACK AND WHITE PHOTOGRAPH

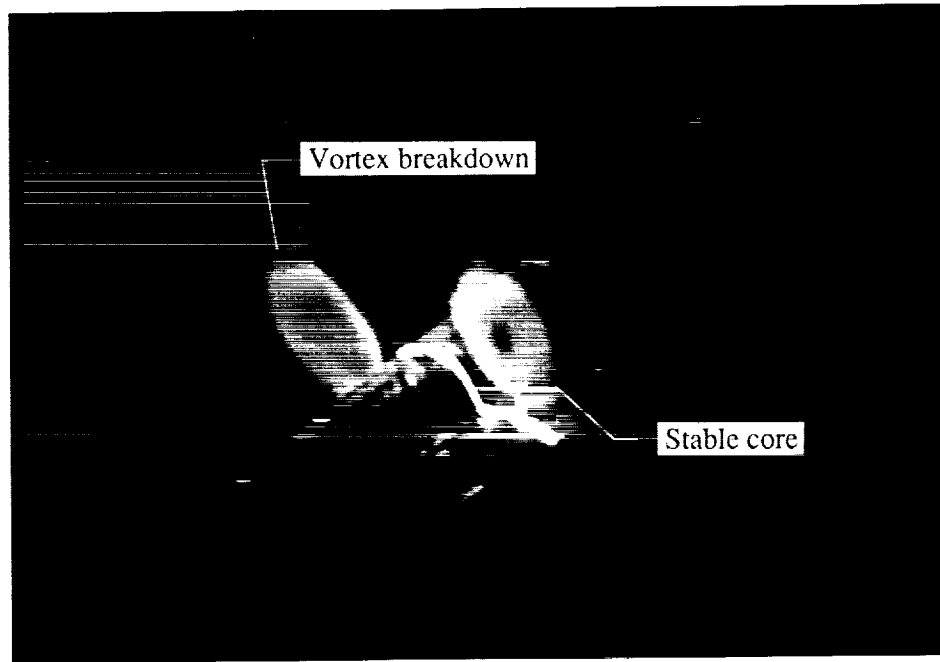


(a) Nose boom on.

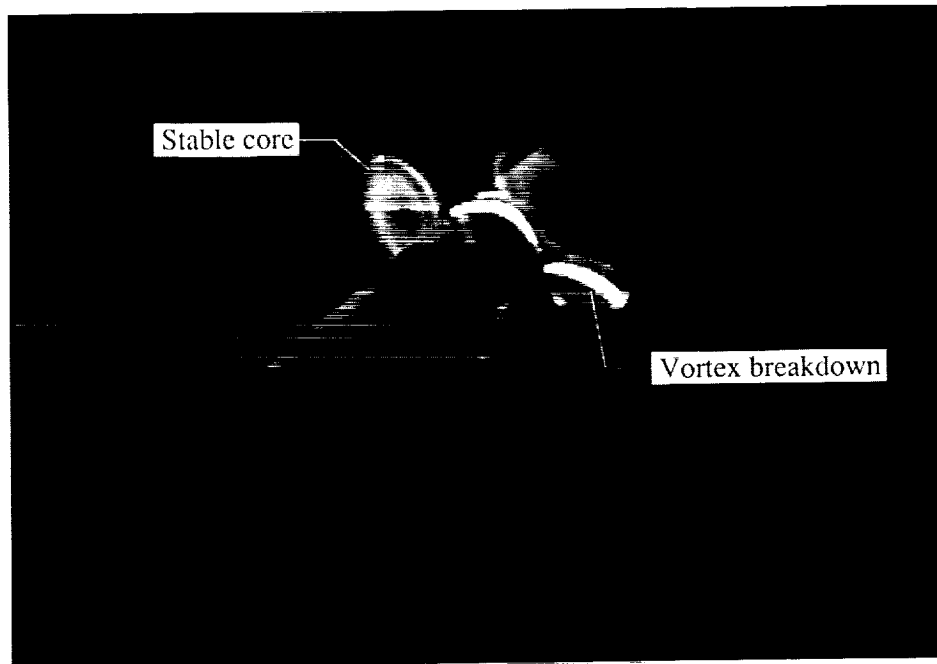


(b) Nose boom off.

Figure 76. Laser vapor screen flow visualizations with nose boom on and off at  $M_\infty = 0.60$ ,  $Re_c = 1.32 \times 10^6$ ,  $\alpha = 50^\circ$ , and FS 184 (11.04). Dimensions are in inches full scale (0.06 scale).



(a)  $\alpha = 30^\circ$ ; FS 411 (24.66).



(b)  $\alpha = 32.5^\circ$ ; FS 357 (21.42).

Figure 77. LEX vortex breakdown asymmetries at  $M_\infty = 0.60$  and  $Re_{\bar{c}} = 1.32 \times 10^6$  with nose boom and LEX fences on. Dimensions are in inches full scale (0.06 scale).

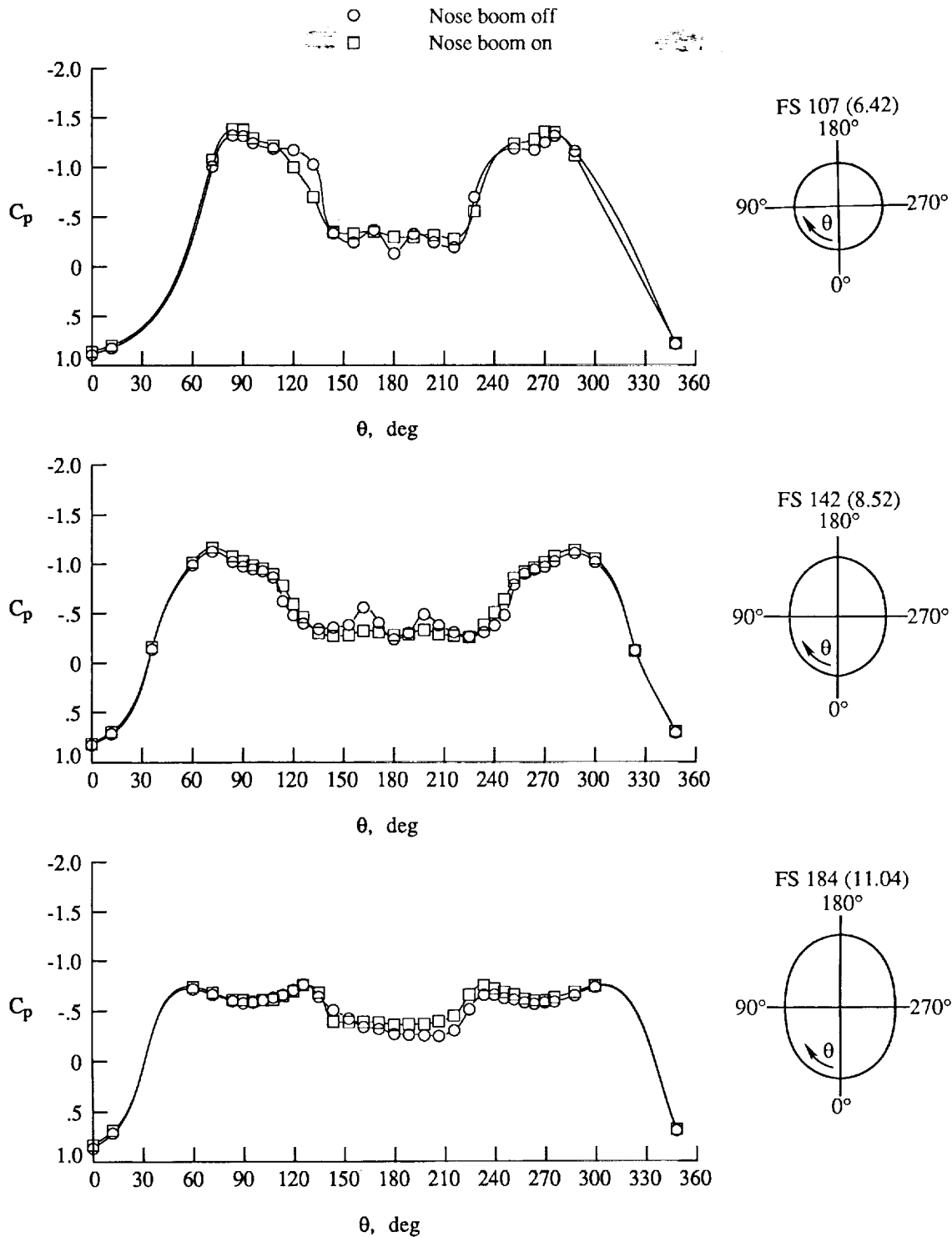


Figure 78. Effect of nose boom on forebody surface static pressures at  $M_\infty = 0.60$ ;  $Re_c = 1.32 \times 10^6$ , and  $\alpha = 50^\circ$ . Dimensions are in inches full scale (0.06 scale).

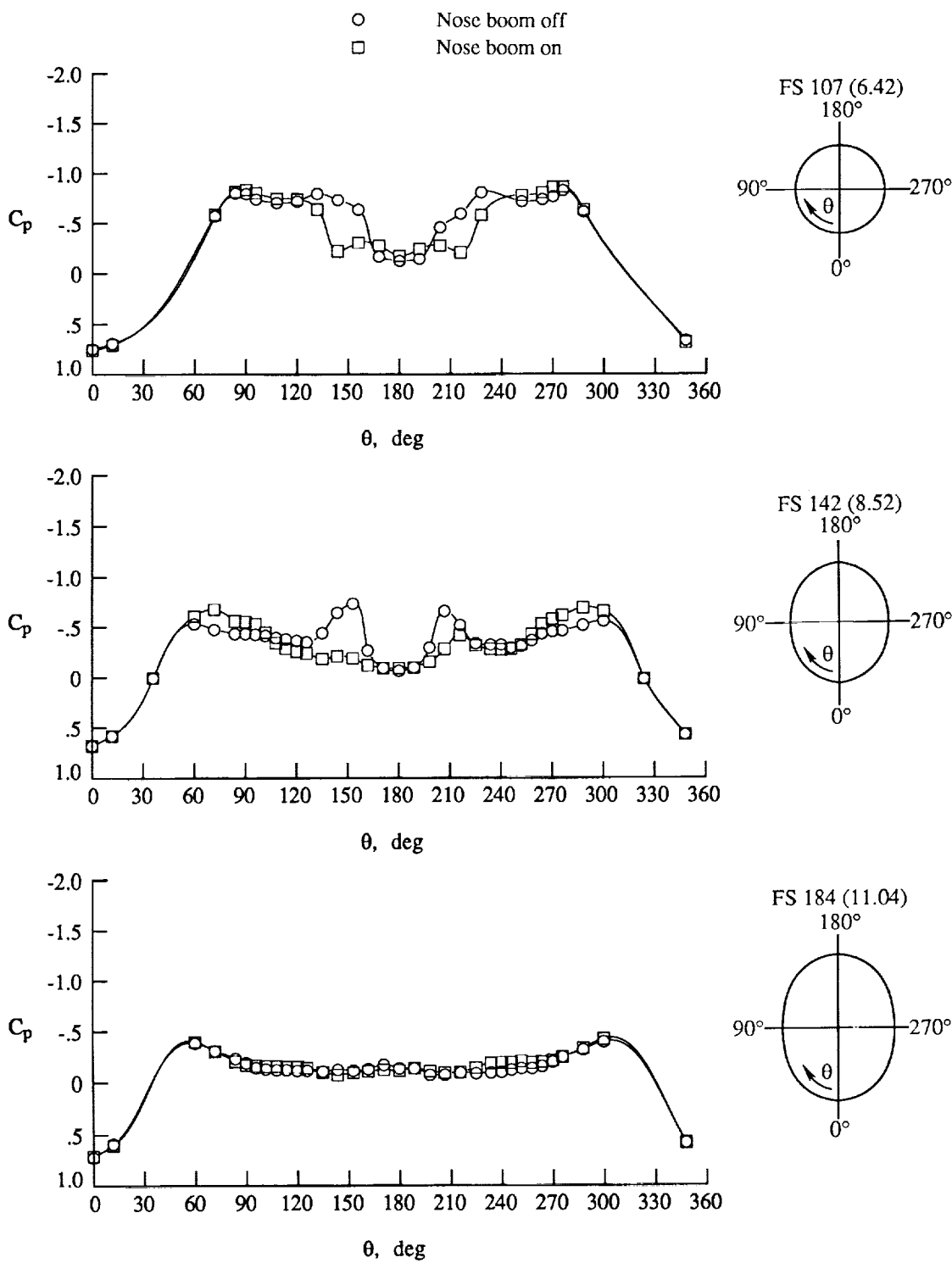


Figure 79. Effect of nose boom on forebody surface static pressures at  $M_\infty = 0.80$ ;  $Re_{\bar{c}} = 1.02 \times 10^6$ , and  $\alpha = 40^\circ$ . Dimensions are in inches full scale (0.06 scale).

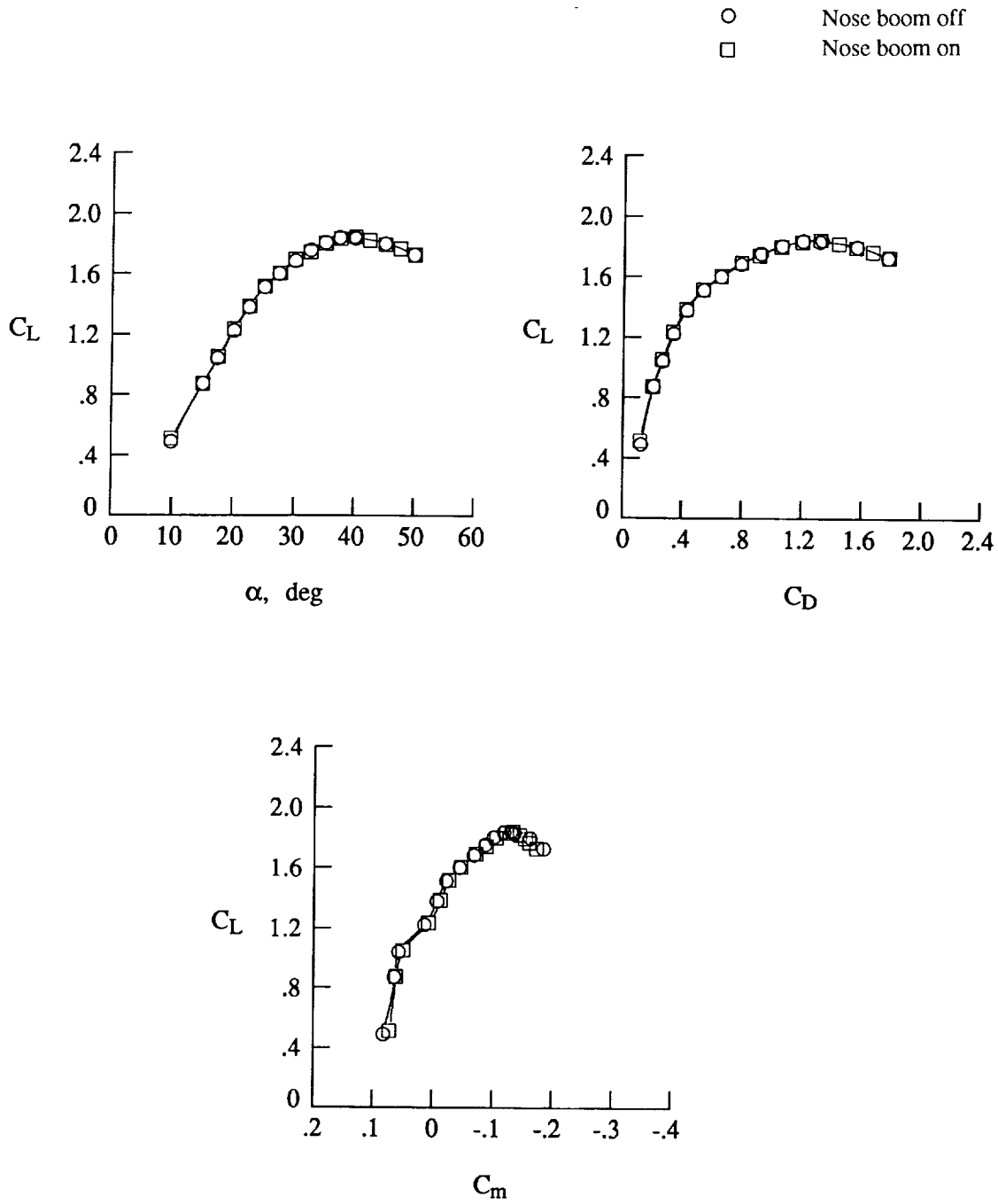


Figure 80. Effect of nose boom on lift, drag, and pitching-moment characteristics at  $M_\infty = 0.60$  and  $Re_{\bar{c}} = 1.32 \times 10^6$ .

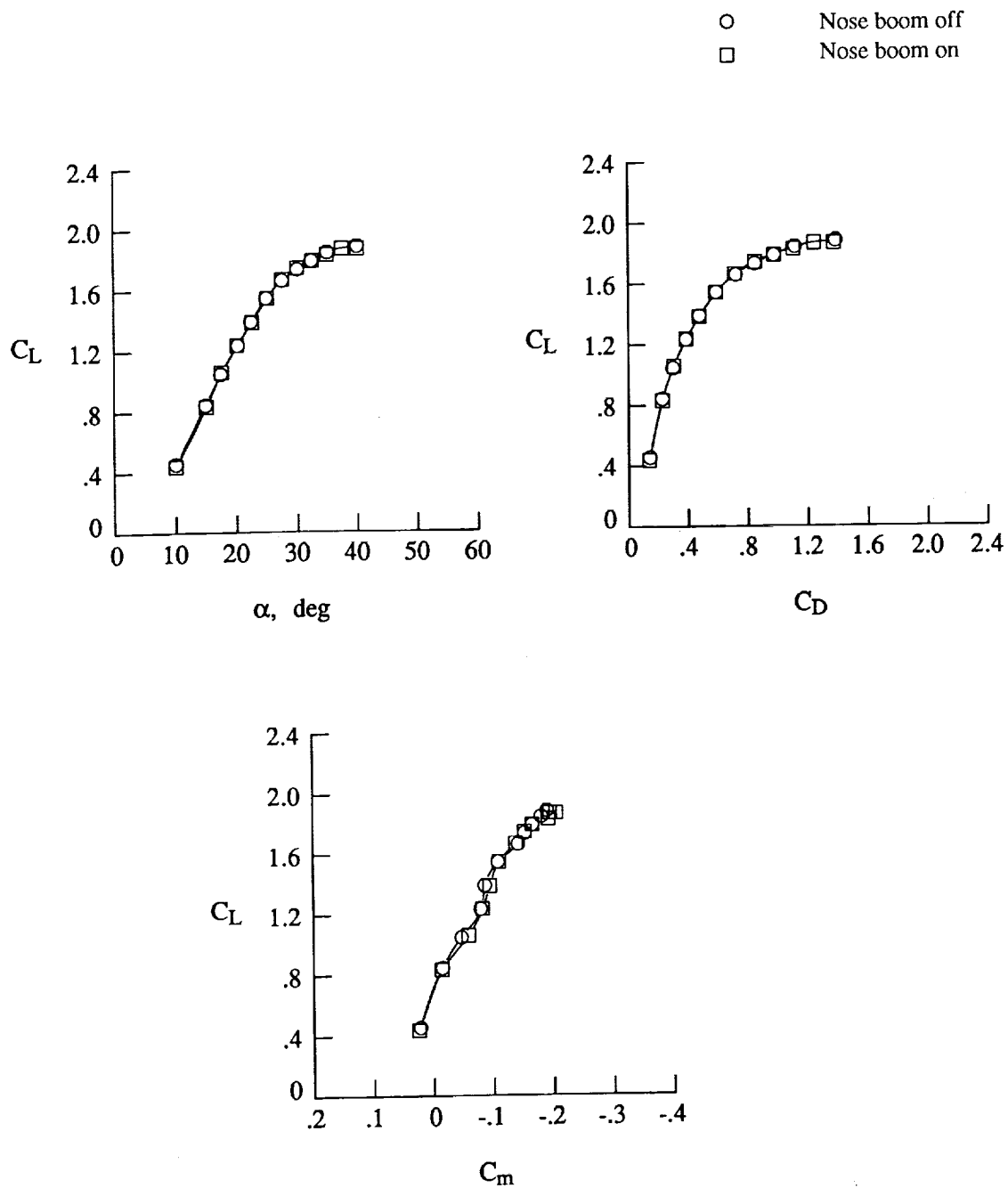


Figure 81. Effect of nose boom on lift, drag, and pitching-moment characteristics at  $M_\infty = 0.80$  and  $Re_{\bar{c}} = 1.02 \times 10^6$ .

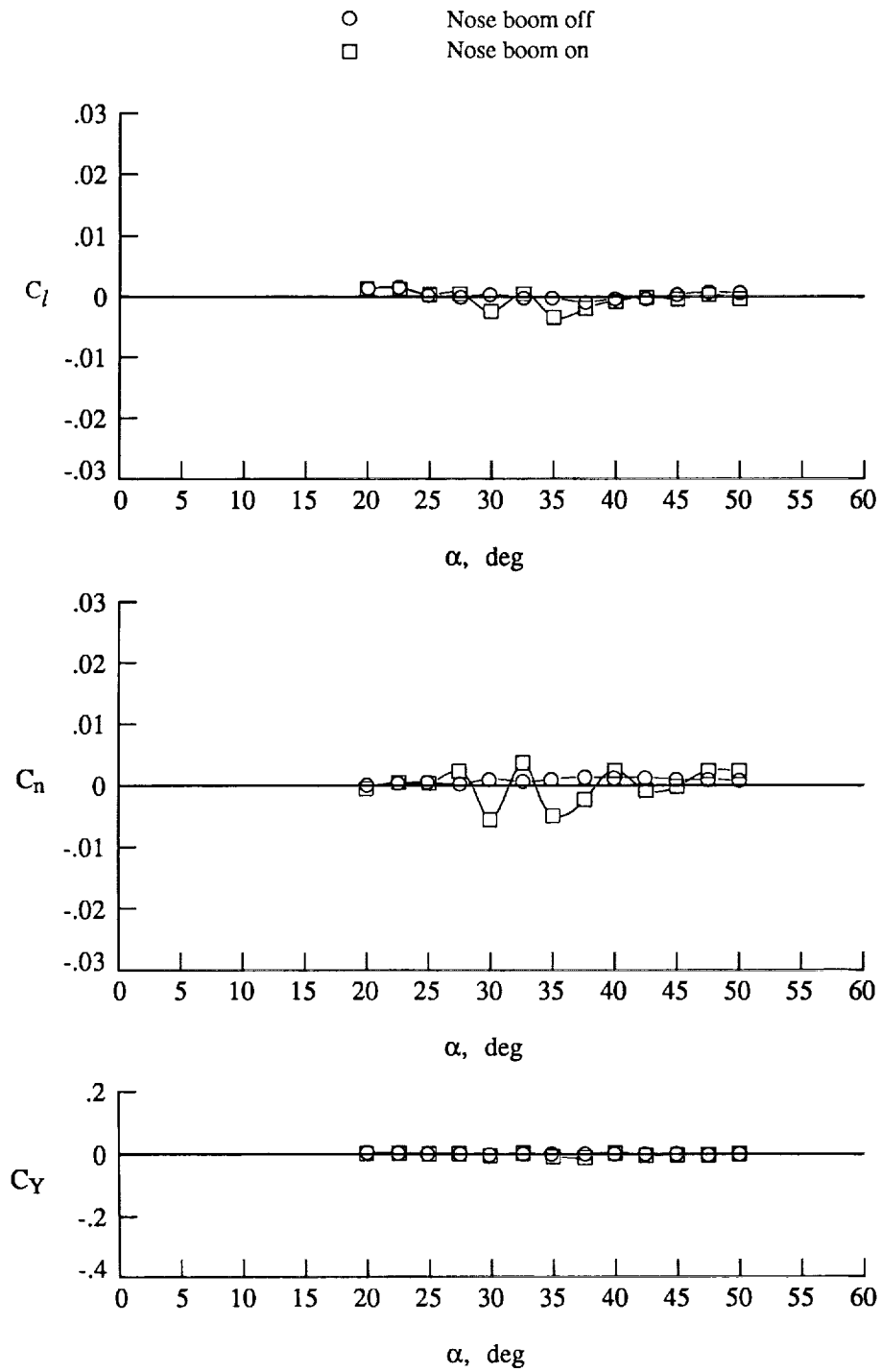
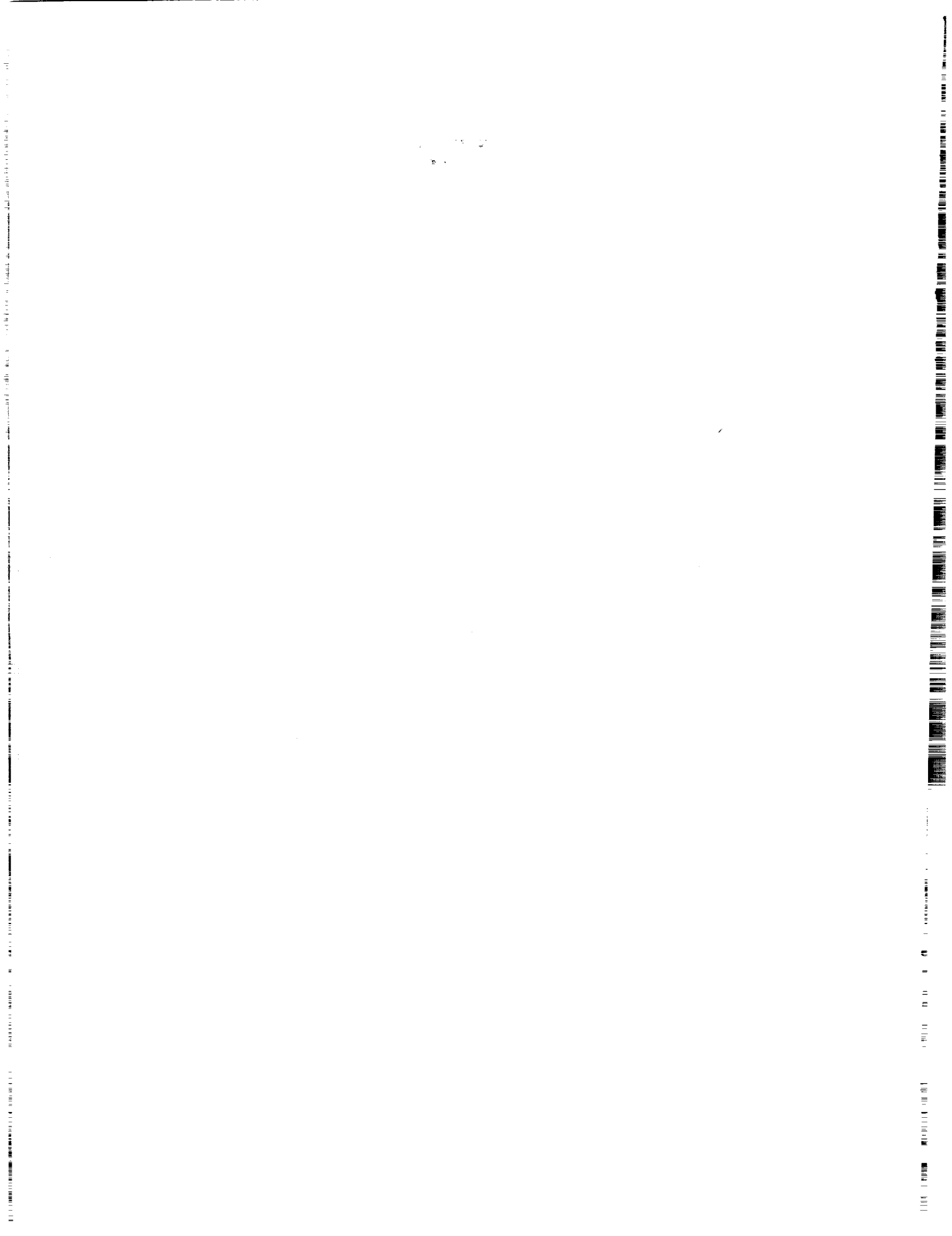


Figure 82. Effect of nose boom on lateral-directional characteristics at  $M_\infty = 0.60$ ,  $Re_{\bar{c}} = 1.32 \times 10^6$ , and  $\beta = 0^\circ$ .





REPORT DOCUMENTATION PAGE			Form Approved OMB No. 0704-0188	
Public reporting burden for this collection of information is estimated to average 1 hour per response, including the time for reviewing instructions, searching existing data sources, gathering and maintaining the data needed, and completing and reviewing the collection of information. Send comments regarding this burden estimate or any other aspect of this collection of information, including suggestions for reducing this burden, to Washington Headquarters Services, Directorate for Information Operations and Reports, 1215 Jefferson Davis Highway, Suite 1204, Arlington, VA 22202 4302, and to the Office of Management and Budget, Paperwork Reduction Project (0704-0188), Washington, DC 20503				
1. AGENCY USE ONLY (Leave blank)	2. REPORT DATE December 1991	3. REPORT TYPE AND DATES COVERED Technical Paper		
4. TITLE AND SUBTITLE Wind Tunnel Investigation of Vortex Flows on F/A-18 at Subsonic Through Transonic Speeds		5. FUNDING NUMBERS WU 505-68-30-03		
6. AUTHOR(S) Gary E. Erickson				
7. PERFORMING ORGANIZATION NAME(S) AND ADDRESS(ES) NASA Langley Research Center Hampton, VA 23665-5225		8. PERFORMING ORGANIZATION REPORT NUMBER L-16799		
9. SPONSORING/MONITORING AGENCY NAME(S) AND ADDRESS(ES) National Aeronautics and Space Administration Washington, DC 20546-0001		10. SPONSORING/MONITORING AGENCY REPORT NUMBER NASA TP-3111		
11. SUPPLEMENTARY NOTES				
12a. DISTRIBUTION/AVAILABILITY STATEMENT  Unclassified Unlimited  Subject Category 02			12b. DISTRIBUTION CODE	
13. ABSTRACT (Maximum 200 words) A wind tunnel experiment was conducted in the 7- by 10-Foot Transonic Tunnel at the David Taylor Research Center of the wing leading-edge extension (LEX) and forebody vortex flows at subsonic and transonic speeds about a 0.06-scale model of the F/A-18. The primary goal was to improve the understanding and control of the vortical flows, including the phenomena of vortex breakdown and vortex interactions with the vertical tails. The wind tunnel results were correlated with in-flight flow visualization and handling qualities trends obtained by NASA using an F-18 High-Alpha Research Vehicle (HARV) and by the U.S. Navy and McDonnell Douglas Corp. on an F-18 airplane with LEX fences added to improve the vertical tail buffet environment. Key issues that were addressed include the sensitivity of the vortical flows to the Reynolds number and Mach number; the reduced vertical tail excitation, and the corresponding flow mechanism, in the presence of the LEX fence; the repeatability of data obtained during high-angle-of-attack wind tunnel testing of F/A-18 models; the effect of particle seeding for flow visualization on the quantitative model measurements; and the interpretation of off-body flow visualizations obtained with different illumination and particle seeding techniques.				
14. SUBJECT TERMS Vortex flows; Subsonic flow; Transonic flow; Fighter aircraft; Forebody; Vertical tail buffet; Vortex breakdown; Flow visualization; Leading-edge extension			15. NUMBER OF PAGES 164	16. PRICE CODE A08
17. SECURITY CLASSIFICATION OF REPORT Unclassified	18. SECURITY CLASSIFICATION OF THIS PAGE Unclassified	19. SECURITY CLASSIFICATION OF ABSTRACT	20. LIMITATION OF ABSTRACT	

